COLLEGE DOCTORAL PAYS DE LA LOIRE
ED SCIENCES DE L'INGENIERIE ET DES SYSTEMES

CENTRALE NANTES

MEMOIRE DE DOCTORAT DE

L'ECOLE CENTRALE DE NANTES

ECOLE DOCTORALE N° 602
Sciences de l'Ingénierie et des Systèmes
Spécialité : Mécanique des Milieux Fluides

Par

Mathieu LANDREAU

Multiscale analysis of sea breezes and low-level jets in a coastal area

Projet de recherche doctoral présenté et soutenu à Nantes, le 16 décembre 2025
Unité de recherche : UMR 6598, Laboratoire de recherche en Hydrodynamique, Énergétique et Environnement Atmosphérique (LHEEA)

Rapporteurs avant soutenance :

Christine Lac	Directrice de recherche, Météo-France Toulouse
Sukanta Basu	Full professor, University at Albany, The State University of New-York, États-Unis

Composition du Jury :

Président :	Christine Lac	Directrice de recherche, Météo-France Toulouse
Examinateurs :	Sukanta Basu	Full professor, University at Albany, The State University of New-York, États-Unis
	Wim Munters	Associate professor, von Karman Institute for Fluid Dynamics, Belgique
	Chantal Staquet	Professeure des universités, Université Grenoble Alpes
Directrice de recherches doctorales :	Isabelle Calmet	Professeur des universités, École Centrale de Nantes
Co-enc. de recherches doctorales :	Boris Conan	Maître de Conférences, École Centrale de Nantes

Remerciements

À Boris et Isabelle, mes parents de thèse, pour avoir donné vie à cette expérience, pour m'avoir fait grandir, pour m'avoir suivi dans mes idées éparpillées, pour m'avoir encadré avec la rigueur et l'intégrité scientifique que j'espérais, et plus généralement pour votre travail sans faille,

À la Région Pays-de-la-Loire et à l'École Centrale de Nantes pour avoir permis la réalisation de cette thèse,

À Christine Lac, Sukanta Basu, Chantal Staquet, et Wim Munters, pour avoir lu et écouté attentivement les résultats de ces 3 années de recherches, pour la précision de leur questions attestant de l'intérêt qu'ils y ont portés, et pour leurs précieux commentaires,

À Benjamin, pour m'avoir donné l'impulsion, pour la motivation et pour l'envie manifeste de faire avancer la science sans attendre de retour,

À Quentin et Robin, mes frères de bureau, pour l'accompagnement quotidien, l'entraide désintéressée, et les promenades dans le campus,

À toute l'équipe DAUC et au LHEEA pour le Concours de Flans, le tournoi de palet et de babyfoot, et plus particulièrement à ses (post-) doctorants, Quentin, William, Antonin, Titouan, Clément, Rishab, Nikos, Thomas, et tant d'autres, pour les phrases sans contexte, et la bonne humeur au quotidien,
À Guillaume, pour le happiness management,
À la fine équipe de football de Centrale qui a donné de la couleur (quelques bleus notamment, désolé Jérôme) à ces trois années,
À Discobol, et au pas-tout-à-fait tiramisù,

À Pau, pour l'amour et la joie au quotidien malgré la fatigue des soirs d'hiver, pour m'apprendre la vie en dehors de la science, pour les muettes, les moix, les bisoux et le chocolat, pour les molens, les pâtes, le chocomel et le gorgonzola, pour les bads, les abdals, les footings et les pizzas, pour nous, pour toi,

À Papa et Maman, mes parents de la vie, pour m'avoir donné les clés pour arriver jusqu'ici, pour m'avoir fait réciter mes leçons, m'avoir appris à travailler avec ma tête quelque soit la situation, à ne pas abandonner tant que le travail n'est pas fini, mais aussi à faire des pauses quand il est nécessaire.
À Jérémy et Quentin, mes frères de la vie, pour m'avoir accompagné là où les parents se sentaient dépassés, pour le pouvoir des trois,
À Vy, Tino et Maia, pour la vie et la joie de vivre, le retour à l'essentiel,

table of content

À tout l'entourage, les immuables Macairois, les jeunes mariés et leur troupe, la compagnie de Polytech, pour toutes leurs questions et leurs encouragements, et pour m'avoir changé les idées régulièrement,

Merci mille fois.

Table des matières

Introduction **1**

1 Literature review **3**
1.1 Atmospheric boundary layer . . . 3
1.1.1 Earth atmospheric layers . . . 3
1.1.2 Far-inland ABL . . . 3
1.1.3 Monin-Obukhov similarity theory . . . 3
1.1.4 Convective boundary layer . . . 5
1.1.5 Stable boundary layer . . . 5
1.1.6 Residual layer . . . 6
1.1.7 Far-offshore ABL . . . 6
1.2 Coastal atmospheric boundary layer . . . 6
1.2.1 Baroclinic pressure gradient . . . 7
1.2.2 Internal boundary layer . . . 7
1.2.3 Inertial Oscillations . . . 8
1.3 Sea-breeze . . . 9
1.3.1 Description . . . 9
1.3.2 Life cycle . . . 11
1.3.3 External parameters . . . 11
1.3.4 Offshore extent . . . 12
1.3.5 Turbulence and waves in a sea breeze . . . 14
1.3.6 Gaps in knowledge . . . 16
1.4 Low-level jet . . . 16
1.4.1 Definition . . . 16
1.4.2 Mechanisms . . . 17
1.4.3 Evolution of a jet characteristics . . . 18
1.4.4 Turbulence and waves in a jet . . . 19
1.4.5 LLJ in coastal areas . . . 20
1.4.6 Gaps in knowledge . . . 21
1.5 Waves, bores, and rolls in the atmospheric boundary layer . . . 21
1.5.1 Kelvin-Helmholtz waves . . . 21
1.5.2 Gravity waves . . . 22
1.5.3 Bores . . . 23
1.5.4 Streaks and rolls . . . 25
1.5.5 Gaps in knowledge . . . 27
1.6 Numerical simulations . . . 27
1.6.1 Realistic mesoscale simulations . . . 27
1.6.2 Turbulence modeling and grey zone . . . 28

2 Method **29**
2.1 Study area . . . 29
2.2 Datasets . . . 30
2.2.1 LiDAR measurements and virtual mast . . . 30
2.2.2 Temperature measurements . . . 31
2.2.3 AROME dataset . . . 31
2.3 Numerical simulations . . . 32
2.3.1 WRF model . . . 32
2.3.2 Domains and mesh . . . 32
2.3.3 Boundary conditions . . . 34
2.3.4 Spin-up time . . . 35
2.3.5 Physics schemes . . . 35
2.4 Post-processing . . . 39
2.4.1 Statistics in LES . . . 39
2.4.2 TKE budget . . . 40
2.4.3 Horizontal filter . . . 41
2.4.4 Trajectories . . . 42
2.5 Model assessment . . . 42
2.5.1 Synoptic conditions and thermal forcing . . . 42
2.5.2 Wind evolution in LiDAR measurements . . . 44
2.5.3 Evaluation of the mean quantities . . . 45
2.5.4 Evaluation of the turbulent statistics and the TKE budget . 50
2.6 Conclusion . . . 54

3 Analysis of the sea breezes near a complex coastline **55**
3.1 Sea-breeze scale and extent . . . 56
3.1.1 Qualitative description of the wind direction . . . 56
3.1.2 Coast orientation at a given scale . . . 57
3.1.3 Sea-breeze orientation . . . 59
3.1.4 Sea-breeze scale . . . 61
3.1.5 Sea-breeze extent . . . 63
3.2 Interactions of local sea breezes during initiation near a peninsula . . 68
3.2.1 Local sea breezes and secondary interfaces . . . 68
3.2.2 Evidence of an undular bore in WRF results . . . 70
3.2.3 Evidence of gravity waves in LiDAR measurements . . . 71
3.2.4 Evolution of the gravity waves characteristics . . . 74
3.2.5 Absence of gravity waves on May 18 . . . 76
3.3 Conclusion of the chapter . . . 78

4 Turbulence characteristics in a sea breeze and influence of gravity waves **83**
4.1 Wind and TKE profiles in the sea-breeze . . . 83
4.1.1 Wind profiles in the sea-breeze . . . 84
4.1.2 TKE profiles in the sea-breeze . . . 86

4.2 Analysis of the turbulence in the center of the sea-breeze cell 87
4.2.1 Height and occurrence of the turbulence peak 87
4.2.2 Kelvin-Helmholtz instability 90
4.2.3 Turbulence in the Kelvin-Helmholtz billows 92
4.3 Impact of gravity waves on the turbulent kinetic energy 94
4.3.1 Turbulence out of the gravity waves 95
4.3.2 Variance induced by the waves' motion 96
4.3.3 Turbulence within the gravity waves 97
4.3.4 Turbulent kinetic energy budget within the gravity waves . . 99
4.4 Analysis of the turbulence in the sea-breeze return current 104
4.4.1 Evolution of the turbulence with offshore distance 104
4.4.2 Performance of the models 105
4.4.3 Comparison of the parameters 108
4.5 Conclusion of the chapter 109

5 Analysis of the low-level jet around the land-sea transition 113
5.1 Nocturnal low-level jet at Le Croisic 114
5.1.1 Detection and definition of the LLJ characteristics 114
5.1.2 Comparison of the LLJ characteristics at Le Croisic 115
5.1.3 Transition from sea breeze to low-level jet 117
5.2 Initiation of the nocturnal low-level jet 119
5.3 Evolution of the low-level jet characteristics around the land-sea transition 122
5.4 TKE in the low-level jet around the land-sea transition 125
5.5 Organized structures in the low-level jet 131
5.5.1 Convective rolls in the TIBL 131
5.5.2 Kelvin-Helmholtz waves above the jet core 135
5.5.3 Kelvin-Helmholtz waves below the jet core 137
5.6 Conclusion of the chapter 139

6 General conclusions and perspectives 143
6.1 On the methodology 143
6.2 On the impact of a multiscale coastline on the ABL 145
6.3 On the waves and turbulence in a coastal area 146
6.4 On the implications for wind energy 148
6.5 Perspectives 150

Bibliographie 153

A WRF referential frame and prognostic equations 175
A.1 WRF referential frame 175
A.1.1 notation 175
A.1.2 Jacobian 175
A.1.3 partial derivatives 176

A.1.4 velocities 177
A.2 WRF prognostic equations 177
A.2.1 Transforming a flux-form equation from R_c to R_w 177
A.2.2 Navier-Stokes in WRF referential frame 178
A.2.3 LES subgrid turbulent mixing 180

B TKE budget calculation in WRF **181**

C Calculation of G **183**

D Turbulence decay models in logarithmic form **185**

Appendices **175**

Nomenclature

Variables and Abbreviations

A	Advection rate of TKE	$m^2.s^{-3}$
ABL	Atmospheric Boundary Layer	-
AEP	Annual Energy Production	-
ARW	Advanced Research WRF	-
α_c	Direction across the coastline	-
α_{GW}	Direction across the GW	-
α_{KH}	Direction across the KHW	-
α_{SB}	Direction of the SB, defined from the shear direction	-
B	Buoyancy production of TKE	$m^2.s^{-3}$
CBL	Convective Boundary Layer	-
CI	Capping Inversion	-
c_p	Specific heat capacity at constant pressure	$J.kg^{-1}.K^{-1}$
δ_{SB}	Deviation of α_{SB} compared to CO	-
ECMWF	European Centre for Medium-range Weather Forecasts	-
ERA5	ECMWF ReAnalysis v5	-
ε	Dissipation rate of TKE	$m^2.s^{-3}$
f_c	Coriolis frequency	s^{-1}
g	Acceleration due to gravity	$m.s^{-2}$
G	Kinetic energy induced by the GW motion	$m^2.s^{-2}$
G_U	Variance of u induced by the GW motion	$m^2.s^{-2}$
G_V	Variance of v induced by the GW motion	$m^2.s^{-2}$
G_W	Variance of w induced by the GW motion	$m^2.s^{-2}$
GW	Gravity Waves	-
HCR	Horizontal Convective Rolls	-
η	Vertical displacement in the GW	m
IBL	Internal Boundary Layer	-
IO	Inertial Oscillations	-
k	Turbulent kinetic energy	$m^2.s^{-2}$
k^*	Normalized TKE in the decay	-
k_{calc}	TKE calculated from the model	$m^2.s^{-2}$
KH	Kelvin-Helmholtz	-
KHW	Kelvin-Helmholtz Waves	-
k_{sgs}	10-minute averaged subgrid TKE	$m^2.s^{-2}$
k_{tot}	Total TKE from the model	$m^2.s^{-2}$
κ	Von Karman constant	-
LES	Large-Eddy Simulations	-
LiDAR	Light Detection And Ranging	-
LIST	Local Intermittent Strength of Turbulence	-
LLJ	Low-Level Jet	-
LSM	Land-Surface Model	-

table of content

λ	Wavelength	m
λ_{GW}	GW wavelength	m
λ_{HCR}	HCR wavelength	m
λ_{KH}	KHW wavelength	m
MOST	Monin-Obukhov Similarity Theory	-
NCAR	National Center for Atmospheric Research	-
N_{BV}	Brunt-Väisälä frequency	s^{-1}
NWP	Numerical Weather Prediction	-
p	Pressure	Pa
P	Shear production of TKE	$m^2.s^{-3}$
PBL	Planetary Boundary Layer	-
PPI	Plan Position Indicator	-
P_{u1}	Longitudinal production terms of TKE in the X_{GW} direction	$m^2.s^{-3}$
P_{v3}	Vertical production terms of TKE in the Y_{GW} direction	$m^2.s^{-3}$
q	Surface sensible heat flux	$W.m^{-2}$
RANS	Reynolds-Averaged Navier-Stokes	-
Ri	Gradient Richardson number	-
Ri_f	Flux Richardson number	-
RMSE	Root Mean Square Error	-
RRTMG	Rapid Radiative Transfer Model for GCMs	-
RWS	Radial Wind Speed (LiDAR measurements)	$m.s^{-1}$
ρ	Density	$kg.m^{-3}$
s	Scale parameter	m
SB	Sea Breeze	-
SBF	Sea-Breeze Front	-
SBH	Sea-Breeze Head	-
SBL	Stable Boundary Layer	-
S_{GW}	Motion speed of the GW	$m.s^{-1}$
s_{SB}	Scale of the sea-breeze	m
SST	Sea-Surface Temperature	-
t	Time	s
TIBL	Thermal Internal Boundary Layer	-
TKE	Turbulent Kinetic Energy	-
T_P	Pressure transport of TKE	$m^2.s^{-3}$
T_{Pb}	Boussinesq pressure transport of TKE	$m^2.s^{-3}$
T_T	Turbulent transport of TKE	$m^2.s^{-3}$
θ_v	Virtual potential temperature	K
UTC	Coordinated Universal Time	-
u	instantaneous easting wind component	$m.s^{-1}$
U	10-minute averaged easting wind component	$m.s^{-1}$
U_c	U oriented across the coastline	$m.s^{-1}$
U_c	U oriented across the coastline	$m.s^{-1}$
u_g	Geostrophic easting wind speed	$m.s^{-1}$
u_{GW}	u oriented across the GW	$m.s^{-1}$

table of content

U_{GW}	U oriented across the GW	$\mathrm{m.s^{-1}}$
u_{KH}	u oriented across the KHW	$\mathrm{m.s^{-1}}$
U_{KH}	U oriented across the KHW	$\mathrm{m.s^{-1}}$
U_{sine}	Model of U in the GW	$\mathrm{m.s^{-1}}$
v	instantaneous northing wind component	$\mathrm{m.s^{-1}}$
V	10-minute averaged v	$\mathrm{m.s^{-1}}$
V_c	V oriented along the coastline	$\mathrm{m.s^{-1}}$
v_g	Geostrophic northing wind speed	$\mathrm{m.s^{-1}}$
v_{GW}	v oriented along the GW	$\mathrm{m.s^{-1}}$
V_{GW}	V oriented along the GW	$\mathrm{m.s^{-1}}$
v_{KH}	v oriented along the KHW	$\mathrm{m.s^{-1}}$
V_{KH}	V oriented along the KHW	$\mathrm{m.s^{-1}}$
V_{sine}	Model of V in the GW	$\mathrm{m.s^{-1}}$
w	instantaneous vertical wind component	$\mathrm{m.s^{-1}}$
W	10-minute averaged vertical wind component	$\mathrm{m.s^{-1}}$
WPS	WRF Preprocessing System	-
WRF	Weather Research and Forecasting	-
WS	Horizontal wind speed	$\mathrm{m.s^{-1}}$
WS_{SB}	SB gravity current speed	$\mathrm{m.s^{-1}}$
WS_{LLJ}	LLJ core speed	$\mathrm{m.s^{-1}}$
WD	Wind direction	$^\circ$
WD_{LLJ}	Wind direction at the LLJ core height	$^\circ$
X	Easting coordinate	km
X_c	Cross-coast coordinate	km
Y	Northing coordinate	km
y_b	Anisotropy parameter	-
Z	Vertical coordinate	m
Z_{CBL}	CBL thickness	m
Z_{LLJ}	LLJ core height	m
z_{LLJ}	instantaneous LLJ core height	m
Z^*_{RC}	Z normalized in the SB return current	-
Z_{SB}	SB gravity current thickness	m
Z^*_{SB}	Z normalized with Z_{SB}	-
Z_{TIBL}	TIBL thickness	m
z_{TIBL}	Instantaneous TIBL thickness	m

Operators

$\overline{\cdot}$	10-minute time-averaging operator	-
$\cdot'$	Fluctuation around the 10-minute averaged quantity	-
$\partial_t(\cdot)$	Time partial derivative	-
$\partial_{x_i}(\cdot)$	Space partial derivative in Cartesian referential frame	-
$\partial_{\chi_i}(\cdot)$	Space partial derivative in WRF referential frame	-
$\widetilde{\cdot}$	Spatial filtering operator	-

table of content

Liste des tableaux

2.1 Characteristics of the simulation domains 33
2.2 LSM datasets used in RANS and LES domains, and their resolution 38

6.1 Characteristics of the waves and oscillations detected the study where the KHW in the SB, below, and above the jet core are numbered 1, 2, and 3, respectively. The period related to their passage at a fixed location is estimated by dividing the wavelength by their speed for GW, or the wind speed for the KHW2. For the HCR, the KHW1, and the KHW3, it is estimated from Figures 5.18, 4.13, and 5.21, respectively. 146

Table des figures

1.1 Schematic of the diurnal cycle of the inland ABL during summer months, based on Stull (2017). 4
1.2 Schematic view of a baroclinic ABL around the land-sea interface during the day. Black lines represent isobaric lines and arrows show the mesoscale pressure force direction. 7
1.3 Schematic view of an inertial oscillation in the Northern hemisphere where the black arrows are the velocity at different times, the dotted circle show its evolution, and the green, red, and blue arrows shows the pressure, Coriolis and the resulting forces respectively. The grey arrow is the equilibrium geostrophic velocity. 9
1.4 Schematic of a sea breeze cell (Stull, 2017). 10
1.5 Schematic of the Blackadar's mechanism, based on Van de Wiel et al. (2010), where the solid gray line shows the initial wind speed, the black line shows the wind profile during the IO around the equilibrium wind profile represented by the dashed gray line. 18
1.6 Schematic of the different regimes of a two-layer flow over an obstacle, taken from Rottman and Simpson (1989) 24
1.7 Schematic of the lab experiment on a bore generated by a gravity current, realized by Rottman and Simpson (1989) 24
1.8 Cross section of the buoyancy field from type I (top) to V (bottom) based on 2D simulation results from White and Helfrich (2012). The figure is build from Figures 5 to 9 of their paper. 25

2.1 Map of the study area (source : https ://www.geoportail.gouv.fr/). . 29
2.2 (a) Photography of the Scanning LiDAR at Le Croisic taken from Paskin et al. (2022) and (b) example of the distribution of *RWS* on a horizontal PPI scan. 30
2.3 Map of the WRF d04 domain with the location of (blue) the meteo mast and (red) the SEM-REV buoy used for comparison in Section 2.5.3. 31
2.4 Terrain map of (a) d01, (b) d03, (c) d04, and (d) d05. White rectangles are inner domains. Red squares are used in Figure 2.9. In d05, green lines outline the LiDAR measurements area. Green and red "+" indicate the virtual mast location and the closest AROME grid cell, respectively. 33
2.5 Vertical mesh in (a) RANS and (b) LES domains. Blue "+" markers correspond to the height of the middle of the cell and orange "x" markers show the thickness of the cell over the sea (terrain height = 0 m). 34

2.6 Schematic of the interactions between physics schemes (Skamarock et al., 2019) where SH, LH, SW, LW, T, and Q_v stand for sensible heat, latent heat, shortwave, longwave, the temperature and humidity, respectively. 36
2.7 Sea-level pressure averaged over 24 h on (a) May 17 and (b) May 18, based on WRF d01 results 42
2.8 Wind speed at 2000 m above sea level averaged over 24 h on (a) May 17 and (b) May 18, based on WRF d02 results 43
2.9 Evolution of the temperature of the sea surface and the land surface, based on d04 results averaged over the red-square areas in Figure 2.1c. The yellow and dark blue colors, at the bottom of this figure and following figures, indicate the daytime and nighttime, respectively. 43
2.10 Evolution of (top) *WS* and (bottom) *WD* in the LiDAR data at 21, 54, 105, 154, and 297 m high. The brown dashed vertical lines indicate 1500 UTC on May 17 and 0300 UTC on May 18, the dates of the profiles shown in Figure 2.12. 44
2.11 (top, middle) Same as Figure 2.10, comparing the different datasets at 21 m high. (bottom) Evolution of the sea-surface temperature and the air temperature at 2 m high at the two points shown in Figure 2.3, based on WRF d04 results, buoy (sea) and meteo mast (land) measurements. 46
2.12 (a, d) *WS* and (b, e) *WD* and (d, f) θ_v profiles at the virtual mast, at (a, b, c) 1500 UTC on May 17 and (d, e, f) 0300 UTC on May 18. 48
2.13 Taylor diagram of WRF results and AROME data, with LiDAR data as the reference, for the variables (a) U and (b) V. The statistics are calculated using hourly data (1 point out of 6 for WRF and LiDAR) from 0900 UTC on May 17 to 0800 UTC on May 19, at the 27 virtual mast heights. 49
2.14 (a) *WD* at 10 m high at 1300 UTC on May 17 in d06 results and (b) profiles of θ_v from 1000 UTC to 1300 UTC averaged within the black square area shown in (a) 51
2.15 Comparison between the k_{calc} budget terms of (a) Pino and Vilà-Guerau De Arellano (2008), (b) the WRF budget, and (c) the Boussinesq budget. The terms are normalized by w^{*3}/Z_{CBL} and plotted as a function of Z^*_{CBL}. In (b) and (c), the terms are averaged in the black area from Figure 2.14a between 1000 UTC and 1300 UTC on May 17. 52
2.16 (a) Spectra of the velocity component in the mean wind direction, at the location indicated by a "+" in Figure 2.14a between 1000 and 1300 UTC on May 17 at 3 different heights. (b) Comparison of the dissipation profiles between the spectral method and the two budget methods. 53

3.1 Spatial distribution of *WD* at 10 m high on May 17 between 1100 and 1600 UTC, based on d04 results. 56

3.2 (a) Land-sea mask in d03 filtered with a 20-km gaussian filter. The red line shows the calculated smoothed coastline (where the filtered mask equals 0.5) and the arrows represent the gradient of the filtered mask. (b) Same as (a) in d05 with a 5-km filter. The "+" shows the position of the LiDAR virtual mast. 58

3.3 Evolution of α_c as a function of s at the LiDAR virtual mast location. 58

3.4 (a) Position of the four points defined in the text : (blue) P1, (orange) P2, (green) P3 and (red) P4, and (b) the coast orientation as a function of the scale s at these locations. 59

3.5 (a-d) Evolution of the wind profile hodographs at (a) P1, (b) P2, (c) P3, and (d) P4 between 1100 UTC and 1900 UTC on May 17, where a circle the circle corresponds to 10 m high and the dots to higher levels. The synoptic wind (see Figure 2.8) is displayed as a blue circle, and the 25-km coastline as a black line. (e-f) Evolution the (e) *WS* and (f) *WD* profiles at P4 over the same period. 60

3.6 Evolution of the SB orientation at points P1 to P4 on May 17. . . . 61

3.7 Standard deviation of δ within the white area defined in Figure 3.4a, as a function of s at different times on May 17. The vertical lines depict s_{SB} at each time. 62

3.8 Evolution of (a) s_{SB} and (b) δ_{SB} over time on May 17 and May 18. Dashed lines in (b) indicate +/- the standard deviation of δ 62

3.9 Spatial distribution of (a) WS_{SB} and (b) Z_{SB} at 1500 UTC based on d03 results computed with $s = 50$ km. 63

3.10 (a-d) Evolution of WS_{SB} in domain d03 on May 17 between 1200 and 1800 UTC. The green line indicates the limits of the SB as defined in the text and the red area is used in Figure 3.11. (e) Vertical cross-section of U_c at 1400 UTC on May 17 on the orange line shown in (b). The contours of 0 and 1 m.s^{-1} are indicated in black and green, respectively. 65

3.11 (a) SB inland and offshore extents in the red areas defined in Figure 3.10 on May 17 and May 18. The dashed lines show linear fits. (b) Same figure taken from Finkele (1998), based on ideal simulations with a cross-coast geostrophic wind speed of (dashed, thin lines) -2.5 m.s $^{-1}$ and (thick line) -5 m.s $^{-1}$. Markers are based on aircraft measurements. 66

3.12 Comparison between the SB offshore extent and s_{SB}. 66

3.13 (a) Map of the Guérande peninsula where the four dashed green lines are coastal segments mentioned in the text. (b-f) Color plot of the 21 m *WD* on May 17 based on d05 results. White arrows show the 21 m wind. Green thin lines near coord. (0,0) correspond to the LiDAR measurement area. Bold green lines are (solid) convergent and (dashed) divergent interfaces separating different areas, letters are explained in the text. 69

3.14 (a) Schematic to explain the convergence area leading to a secondary front between two local SB, and (b-c) Horizontal wind divergence based on d04 results at 10 m high (1st cell) on (b) May 17 and (c) May 18. Before computing the divergence, velocity fields are 1-km filtered and averaged over 2 hours between 1100 and 1300 UTC. . . 69

3.15 Horizontal cross-section of W at 150 m at (a) 1200, (b) 1330, and (c) 1430 UTC on May 17 based on d05 results. Arrows represent the horizontal velocity at (black) 150 m and (green) 550 m. The black line in (a) indicates the vertical cross-section used in Figure 3.16 and the black dot corresponds to X_{GW}=0. The black line and the black and green rectangles in (c) are used to study the GW characteristics. 71

3.16 Vertical cross-section of (a) U_{GW}, (b) θ_v, and (c) Ri based on d05 results at 1200 UTC on May 17. The position of the vertical cross-section is shown in Figure 3.15a. 71

3.17 *RWS* measured by the LiDAR at 21 m high on May 17 between 0931 and 1100 UTC. The time step between consecutive figures is approximately 7 minutes. For clarity, black arrows represent the wind vector reconstructed at several ranges based only on the instantaneous data. The virtual mast position corresponds to (X, Y) = (0, 0) . . . 72

3.18 Time-height plot of W on May 17 at LiDAR location in LiDAR measurements (a) and in WRF d05 results (b). WRF results are averaged over 10-min windows whereas LiDAR measurements are taken only during 5 seconds. The grey area indicates discarded data due to a poor CNR. Letters, corresponding to the zones defined in Figure 3.13, are explained in the text 73

3.19 (a) Temporal evolution of the gravity wave characteristics between 1200 and 1600 UTC on May 17 : (blue) S_{GW}, (orange) λ_{GW}, and (green) A_W. (b) Same as (a) for (red) α_{GW} and (black) α_{SB} 74

3.20 (a) Color plot and isocontours of the gravity wave amplitude (A_{GW}) as a function of time and distance from the coast on May 17. (b) A_{GW} as a function of the normal wind speed difference across the front at 10 m, ΔU_{10}. A_{GW} is the maximum value of the A_W profile. Colors indicate the distance from the coast. 75

3.21 (a) Same as Figure 3.16a at 1000 UTC on May 18 and (b) same as Figure 3.15a on May 18 76

3.22 Comparison of the offshore θ_v profiles on (a) May 17 and (b) May 18 and vertical cross-section of Ri at (c) 0900 UTC, (d) 1000 UTC, and (e) 1100 UTC on May 18. The line of the cross section is shown in Figure 3.21b and the location of the profiles is indicated with a "+" in Figure 3.21b and with a dashed vertical line in (c), (d), (e), and Figure 3.21a. 77

3.23 Backward trajectories ending at different heights at 0900 UTC on (a) May 17 and (b) May 18 close to Le Croisic. The color shows the evolution of θ_v in the trajectory and the final height (in m) of each trajectories is written in black. The first point of the trajectories (if still in the domain) is at 1500 UTC on the previous day. 78

4.1 Division of the domain d06 into different zones based on the distance from the 1-km coastline shown as a red line. The zones are 3 km long. 84

4.2 Evolution of the profiles of (a, d) WS, (b, e) WD and (c, f) θ_v as a function of the distance from coastline (X_c in km) on May 18 at (a, b, c) 1200 UTC and (d, e, f) 1500 UTC. 84

4.3 Evolution of (a) WS_{SB} and (b) Z_{SB} as a function of X_c at different times on May 18. (c-f) Spatial distribution of U_c at 10 m high in d06 at (c) 1200, (d) 1300, (e) 1400, and (f) 1500 UTC. 85

4.4 Same as Figure 4.2 but for (a, d) k_{calc}, (b, e) the wind shear and (c, f) Ri. 86

4.5 (a) Division of the domain d06 into 122 blocks based on the distance from the 1-km coastline (red line). (b) Time-distance plot of the detected peaks in the k_{tot} profiles on May 18. The color indicates the peak value and white dots correspond to the absence of a peak. The position of the dots is slightly shifted to improve readability, and no dot is shown where there is no SB (bottom right). (c,d) Scatter plot of the height of the detected peaks of k_{tot} as a function of Z_{SB} for blocks that are located at least 2 km offshore. The color indicates the distance from coastline in (a, c) and the hour of the day in (d). The size of the dots is proportional to the intensity of the peak as shown in the legend of (c). The dashed lines correspond to Z_{SB} +/- 50 m. . 88

4.6 Spatial distribution of k_{tot} in d06 at 130 m high, at (a) 1510 UTC, (b) 1610 UTC and (c) 1620 UTC. The circles denotes the position of the offshore patches. The "+" is referred to in Figure 4.10. The squares are used to average the profiles at 1620 UTC shown in Figure 4.7. . 89

4.7 Comparison of the TKE profiles within and outside the patch (the two squares in Figure 4.6) at 1620 UTC on May 18. The horizontal line shows the height of the cross-section in Figure 4.6 89

4.8 Proportion of the total TKE generated by the most turbulent events. 90

4.9 Spatial distribution of the instantaneous vertical wind speed w in d06 at 130 m high, at (a) 1510 UTC, (b) 1610 UTC and (c) 1620 UTC. The "+" is referred to in Figure 4.10. The squares are used to average the profiles shown in Figures 4.7 and 4.12. The green lines are used to determine λ_{KH} and α_{KH} 90

4.10 Time-height evolution of (a) the instantaneous θ_v, (b) k_{tot}, and (c) the instantaneous Ri, at the location of the "+" shown in Figure 4.6. 91

4.11 Hodograph of the wind profile between the green lines of Figure 4.9a and 4.9c, from 110 m high (biggest dot) to 250 m high. The dotted lines show the waves direction, perpendicular to the green lines. . . . 92

4.12 Profiles of $\overline{u'^2_{KH}}$, $\overline{v'^2_{KH}}$, $\overline{w'^2}$, and k_{calc} averaged over the squares, shown in Figure 4.9c, (a) within and (b) outside of the KH waves, at 1620 UTC on May 18. 93

4.13 (a) Same as Figure 4.10 for u_{KH}, and (b) time evolution of u_{KH} at 30 m and 151 m high at the same location. The two horizontal lines in (a) are at 30 m and 151 m high. 94

4.14 Spatial distribution of the instantaneous w at 150 m high in d06 at (a) 1200, (b) 1330, and (c) 1400 UTC on May 17. The rectangles depict the regions and blocks used in this section. 95

4.15 (a) k_{tot} profile at (left) 1200 and (right) 1400 UTC, in two different blocks in the region without gravity waves shown in Figure 4.14. (b) Evolution of the height of the detected peaks in the k_{tot} profile (as described in the text) as a function of Z_{SB}. The size of the markers is proportional to k_{tot} at the peak and the color indicates the distance from the coastline. A bit of randomness, between -5 and +5 m, is added to both heights to improve readability. 96

4.16 (a) W and U as a function of X_{GW} at 300 m on the same cross-section as in Figure 3.16 at 1300 UTC. The solid line represents the WRF output, the dashed line is the spatially-filtered output, and the dotted solid line is the sine-wave reconstruction. (b) Variance of W and U on the same section as (a). The solid line is the WRF output and the dotted solid line is the GW related variance. (c) TKE contribution profiles at 1300 and 1400 UTC averaged over the green-box region defined in Figure 4.14. 97

4.17 (a) Schematic explaining the calculation of Z_0, Z_{SB}, Z_{SB0} and Z^*_{SB}. Details are in the text. (b) k profiles as a function of Z^*_{SB} and the GW phase, averaged between 1230 and 1430 UTC in the green-box region depicted in Figure 4.14. As shown in the wave diagram in the bottom right corner, orange and green represent the ascending phases (A), purple and brown correspond to the crests (C), grey and olive represent the descending phases (D), and light and dark blues correspond to the troughs (T). The black line shows the same profile averaged over the region outside the GW. (c-e) Same as (b) for (c) k between 1230 and 1330 UTC, (d) k_{tot} between 1230 and 1330 UTC, (e) k_{tot} between 1340 and 1430 UTC. 99

4.18 Same as 4.17b for (a) $\overline{u'^2_{GW}}$, (b) $\overline{v'^2_{GW}}$, and (c) $\overline{w'^2}$. The time averaging is realized between 1340 and 1400 UTC when the GW are stationary. 100

4.19 Evolution of (a) k_{tot}, (b) P, (c) B, (d) A, (e) T_P, and (f) $-\varepsilon$ as a function of Z^*_{SB} and the GW phase, averaged between 1340 and 1430 UTC in the green-box region shown in Figure 4.14. iso-k lines and U_{GW} vectors are shown in each figure. 101

4.20 Same as Figure 4.19 for (a) P_{23}, and (b) P_{11}. 102

4.21 Same as Figure 4.19 for (a) $\overline{v'_{GW}w'}$, (b) $\overline{w'\theta'_v}$, (c) $\frac{\partial W}{\partial X_{GW}}\frac{\partial V_{GW}}{\partial X_{GW}}$, and (d) $\frac{\partial W}{\partial X_{GW}}\frac{\partial \theta_v}{\partial X_{GW}}$. 102

4.22 (a) Map of d06 showing the rectangular zones in which k_{calc} is averaged in (b) and (c). The lines show iso values of X_c which is positive inland and negative offshore. (b,c) Evolution of k_{calc} as a function of X_c on May 18 (b) at 618 m high at different times and (c) at 1200 UTC at different heights. The circle indicates X_{SBF}. The horizontal lines shows k_0, the average k_{calc} between X_{SBF} - 2 and X_{SBF} + 1, as depicted by the short lines at the bottom. 104

4.23 (a) Profiles of k_0 at different times. (b) Same as (a) where the height and k_0 are normalized with Z_{CBL} and w^{*2}, respectively. (c) Time evolution of Z_{CBL} and Z_{SB} where Z_{SB} is determined based on the profile of U_c at X_c = -5 km shown in (d). 105

4.24 Fit of $\log(k^*)(X_c - X_0)$ at the same time and height than in (a, b, c) Figure 4.22b and (d, e, f) Figure 4.22c with (a, d) model 1, (b, e) model 2, and (c, f) model 3. The area where the fit is made is depicted by the horizontal lines at the bottom. and the vertical lines in (c, f) separate the 3 parts of model 3. 106

4.25 (a) Comparison of the RMSE of the modeled $\log(k^*)$ compared to the simulated one, as a function of $X_c - X_{SBF}$. The right axis shows the exponential of this RMSE which represents the average factor between the modeled k^* and the simulated one. (b) Profile of $X_0 - X_{SBF}$, averaged between 1000 and 1400 UTC, for each model. The shaded area shows +/- the standard deviation. 107

4.26 Comparison of the various length scales for each fit between 1000 and 1400 UTC : (a) $L_{\varepsilon 1}$ and Z_{CBL}, (b) $L_{\varepsilon 2}$ and Z_{CBL}, (c) $L_{\varepsilon 3a}$ and Z_{CBL}, (d) $L_{\varepsilon 2}$ and $L_{\varepsilon 1}$, and (e) $L_{\varepsilon 2}$ and $L_{\varepsilon 3a}$. The color indicates Z^*_{RC} 108

4.27 Schematic of the offshore turbulence within the SB in this case study. Numbered layers correspond to (1) the near-surface gravity current offshore, influenced by the waves from above, (2) the center of the SB cell featuring KHW, and (3) the return current where the turbulence is a residual from the CBL. The blue and red lines are profiles of U_c and θ_v, respectively. 109

5.1 Evolution of (a) Z_{LLJ}, (b) WS_{LLJ}, (c) WD_{LLJ}, (d) the LLJ width, and (e) the LLJ prominence, on May 17 and 18. 116

5.2 Evolution of (left) θ_v and (right) the horizontal wind curl at 100 m high between 1800 UTC on May 17 and 0300 UTC on May 18 based on d03 results. The curl is computed with U and V horizontally filtered with a 10-km Gaussian filter. Lines separates Zones E, F, and G explained in the text. Grey dots correspond to the trajectories introduced later in Figure 5.4 and the big green dot is the location of the air mas at the time indicated on the Figure. 118

5.3 Spatial distribution of (a) WS_{LLJ} and (b) Z_{LLJ} on May 18 at 0300 UTC based on WRF d02. No LLJ is detected in the grey area. The arrows indicate the 150 m wind vector and the green lines delimits the three Zones defined in Figure 5.2. 119

5.4 Profiles of WS (a-c), WD (d-f), and θ_v (g-i) on the three trajectories shown in (j), based on domain d03 results. The color indicates the hour of the day. The three trajectories crosses the green smoothed coastline at 0000 UTC on May 18, and corresponds from top-left to bottom-right to (a, d, g), (b, e, h), and (c, f, i). The dots at the top of (a-f) show the value at 2000 m high. 120

5.5 Hodographs of the wind over time between 2100 UTC (large dot) and 0100 UTC, at several heights, in the black rectangle shown in Figure 5.4j. 121

5.6 Spatial evolution of (a, b) WS_{LLJ} and (c, d) the LLJ prominence on the trajectories that crossed the coastline at (a, c) 0000 UTC and (b, d) 0200 UTC on May 18, based on domain d03 results. Isolines of time are shown every 3 hours in black. 123

5.7 Same as Figure 5.6 for (a, b) Z_{LLJ} and (c, d) the LLJ width 124

5.8 (a) Evolution of the ${N_{BV}}^2$ profile as a function of the distance from the coast along the trajectory T2 (X_{ct}, negative in the offshore direction). The green and red curves show Z_{LLJ} and the TIBL height Z_{TIBL}, respectively. (b) Scatter plot of Z_{LLJ} as a function of Z_{TIBL} on all the trajectories used to draw Figures 5.6 and 5.7. 125

5.9 Same as Figure 5.4, offshore 126

5.10 Evolution of the profiles of (a, d) WS, (b, e) WD and (c, f) θ_v as a function of the distance from coastline (X_c in km) on May 18 at (a, b, c) 0000 UTC and (d, e, f) 0300 UTC, based on domain d06 results. The circles indicate Z_{LLJ} and the triangles indicate Z_{TIBL}. 127

5.11 Evolution of (a) WS_{LLJ} and (b) Z_{LLJ} as a function of X_c at different times on May 18, based on domain d06 results. 128

5.12 Same as Figure 5.10 for (a, d) k_{calc}, (b, e) k_{tot} and (c, f) Ri where the vertical black line indicates 0.25. 128

5.13 Same as Figure 5.12 but for (a, d) $\overline{u'^2_{45}}$, (b, e) $\overline{v'^2_{45}}$ and (c, f) $\overline{w'^2}$. . . . 129

5.14 TKE budget at X_c = (a, d) -6, (b, e) -9, and (c, f) -12 km at (a, b, c) 0000 and (d, e, f) 0300 UTC, based on domain d06 results. The horizontal green and red lines indicate Z_{LLJ} and Z_{TIBL}, respectively. The advection term A is separated into the horizontal advection (A_1 + A_2) and the vertical advection (A_3). Due to their suspicious behavior the horizontal pressure terms are discarded and are not taken into account in the calculation of ε. Only the vertical pressure term T_{p3} is shown. 130

5.15 Distribution of (a) k_{calc} at 110 m high and (b-d) w at (b) 50 m, (c) 110 m , and (d) 410 m high, at 0040 on May 18, based on domain d06 results. 132

5.16 Distribution of (a) w^*, (b) u^*, and (c) u^*/w^* at 0240 UTC on May 18 based on domain d06 results. The "+" shows the position of the time series in Figure 5.18. 132

5.17 Distribution of w at 50 m high at (a) 0300 UTC. (b-e) Same as (a) zoomed over the square area at (b) 0220, (c) 0230, (d) 0240, (e) 0250, and (f) 0300 UTC. The "+" and the lines in (a) are used in Figures 5.18 and 5.19 133

5.18 Time-height plot of (a) w, (b) u_{45}, and (c) v_{45}, between 0220 and 0300 UTC on May 18, at the location of the "+" in Figure 5.17. The green and red lines correspond to the instantaneous z_{LLJ} and z_{TIBL} (calculated with the instantaneous profiles), respectively. The arrows depict the (v_{45}, w) vector field. 134

5.19 (a) Vertical cross section of w along the solid black oriented northwest-southeast shown in Figure 5.17c at 0300 on May 18. The green and red lines correspond to Z_{LLJ} and Z_{TIBL}, respectively. (b) Hodograph of the wind profile between 10 (large dot) and 190 m high, averaged in the square shown in Figure 5.17c, at 0300 UTC. The solid and dashed lines have the same orientation as in Figure 5.17c. 135

5.20 Distribution of w at 410 m high at (a) 0020, (b) 0030, and (c) 0040 UTC on May 18 based on domain d06 results. The "+", the square and the lines are used in Figures 5.21 and 5.22. 135

5.21 Time-height plot of (a) w, (b) θ_v, and (c) the instantaneous Ri, between 0020 and 0050 UTC on May 18, at the location of the "+" in Figure 5.20. The green and red lines correspond to z_{LLJ} and z_{TIBL}, respectively. 136
5.22 (a) Vertical cross section of w along the solid black oriented northwest-southeast shown in Figure 5.20c at 0040 on May 18. The green and red lines correspond to Z_{LLJ} and Z_{TIBL}, respectively. (b) Hodograph of the wind profile between 10 and 510 m high (black), and between 330 and 430 m high (red), averaged in the square shown in Figure 5.20c, at 0040 UTC. The solid and dashed lines have the same orientation as in Figure 5.20c. 137
5.23 (a) Distribution of w at 110 m high at 0030 UTC. (b) Same as (a) but zoomed on the square region shown in (a). The lines are used in Figure 5.24. 137
5.24 (a) Profile of Ri in the square region shown in Figure 5.23a and (b) vertical cross section of w along the solid black oriented northeast-southwest shown in Figure 5.23b at 0030 on May 18. The green and red lines correspond to Z_{LLJ} and Z_{TIBL}, respectively. 138
5.25 Distribution of Ri at 170 m high at 0030 UTC. The square is the same as in Figure 5.23a. 138
5.26 Schematic summarizing the structure of the offshore ABL during the LLJ event. The blue curves show the LLJ wind profile. Layers L1, L2, and L3 correspond respectively to the TIBL, the intermediate layer between the TIBL and the LLJ core, and the layer above the LLJ core. 141

6.1 Turbulence anisotropy as a function of the height and the state of the ABL, visualized on a barycentric map where x_b and y_b are the coordinates (Stiperski and Calaf, 2018), and where 1C, 2C, and 3C correspond to a turbulence dominated by one component, by two components, and to an isotropic turbulence, respectively. The LLJ profile is taken at X_c = -9 at 0300 UTC (Figure 5.13), the SB profiles with and without KH are those of Figure 4.12. The CBL profiles are averaged in the same period and area as the TKE budget terms in Section 2.5.4. 148

Introduction

The coastal areas have a particular importance for human activities as more than 2 billion people live within 100 km of the coast (Reimann et al., 2023). In this area, several activities are impacted by the state of the atmospheric boundary layer (ABL), e.g. fishing, tourism, nautical activities, and pollutant dispersion. The recent development of marine wind energy triggered an increasing interest to characterizing the offshore wind resource that has been identified as one of the main scientific challenges for the scientific community (Veers et al., 2022). For all these reasons, understanding the phenomena occurring in the coastal ABL (CABL) appears to be of primary importance to address socio-economic challenges.

The CABL is characterized by the large difference in roughness and temperature between the sea surface and the land surface. This heterogeneity of surface conditions can drive or influence several complex mesoscale phenomena, such as sea breezes (SB), internal boundary layers (IBL), or low-level jets (LLJ).
SBs were studied essentially above land so that the wind and turbulence in their offshore part are still poorly documented. In addition, its development along a coastline that features complexities at several scales (hereafter called a multiscale coastline) has been documented only qualitatively and no consistent method to describe the SB near a multiscale coastline has been proposed.
Whereas the LLJ is not necessarily a coastal phenomenon, its appearance and evolution is governed by variations of the surface temperature over time or space, so that the land-sea interface influences its characteristics. In the case of a nocturnal LLJ crossing the coastline from land to sea, a convective IBL develops over the sea. The evolution of the LLJ with offshore distance, its interaction with a convective IBL and the nature of turbulence during such an event remain unknown.
Stable and sheared layers are characteristic of SB and LLJ. In such stable layers, the turbulence is sometimes intermittent in space and time, and several sub-mesoscale motions such as gravity waves (GW) or Kelvin-Helmholtz waves (KHW) can be observed. The influence of these structures on turbulence is still poorly understood which limits the knowledge of the turbulence in stably-stratified flows (Sun et al., 2015b).

Performing offshore field measurements is expensive and technically difficult so that there is a lack of experimental data of the offshore CABL, which results in a gap in the knowledge of the CABL flows. Moreover, the broad range of scales involved in the coastal phenomena makes them hard to analyze from measurements at a single location. Therefore, mesoscale-to-microscale numerical simulations represent a powerful complementary tool to study CABL flows as they can resolve phenomena at different scales and give information on several quantities over a large area.

table of content

In this context, the first objective of this work is to assess how a particularly complex coastline influences the offshore wind field and the main characteristics of SBs and LLJs. The second objective is to document the nature and intensity of turbulence within an offshore CABL during these particular events.

The thesis presents an in-depth analysis of the CABL near the French Atlantic coast which is complex at several scales. It focuses on two days, on May 17 and 18, 2020, when an alternation of SB and LLJ events was identified by a scanning LiDAR deployed in this region. The results presented in this manuscript are based on a realistic numerical simulation performed using the Weather Research and Forecasting (WRF) code, which allows for a progressive downscaling from mesoscale to microscale resolutions. With this method, processes ranging from mesoscale to the largest scales of turbulence can be resolved. In addition, the complexity of the coastline and the associated wind field led to the development of several tools and methods for the analysis of the simulation results.

The manuscript starts with a literature review in Chapter 1, about the CABL, the SB, the LLJ, several organized structures, and atmospheric simulations. Then, Chapter 2 presents the methods used in this study, including a description of the LiDAR measurements, the simulation set-up, post-processing tools, and an evaluation of the simulation results. In Chapter 3, the mesoscale characteristics of the SB and its interaction with a multiscale complex coastline are investigated, as well as an offshore atmospheric undular bore identified during SB initiation. Then, in Chapter 4, the offshore turbulence profiles within the SB are studied using the LES results, with a focus on the center of the SB cell within and outside the undular bore, and on the turbulent kinetic energy (TKE) decay in the return current. Chapter 5 focuses on the LLJ observed during nighttime, the evolution of its characteristics in the CABL, and the offshore turbulence during this event. Finally, Chapter 6 presents the general conclusions of the thesis, with a discussion on implications for offshore wind energy, and perspectives for future research.

Chapitre 1

Literature review

1.1 Atmospheric boundary layer

1.1.1 Earth atmospheric layers

The Earth atmosphere is composed of 5 main layers that are, from the highest to the lowest, the exosphere, the mesosphere, the thermosphere, the stratosphere, and the troposphere. The latter extends from the surface up to about 11 km, although this height varies with latitude and seasons. The atmospheric boundary layer (ABL), on which the thesis focuses, corresponds to the few lowest kilometers of the troposphere. The ABL is defined as the atmospheric layer that is directly influenced by the roughness, topography, and thermal forcing at the Earth surface. It is characterized by important variations at short time scales and the strong influence of turbulence. The bottom of the ABL, between the surface and about a hundred meters, is the atmospheric surface layer (ASL), while at the top of the ABL, a shallow and strongly stable layer named the capping inversion (CI) significantly inhibits exchanges of heat and momentum with the rest of the atmosphere (free atmosphere).

1.1.2 Far-inland ABL

The far-inland ABL exhibits a strong diurnal cycle, represented in Figure 1.1. During daytime, the land surface is heated up more rapidly than the atmosphere by the downward radiative heat flux from the sun. A part of this energy is released upward as a sensible heat flux to the ABL. Thus, the ABL is warmed up from the bottom, the vertical gradient of the virtual potential temperature (θ_v) is negative in the surface layer, resulting in a thermally unstable ABL named the convective boundary layer (CBL). At night, the surface cools down by upward radiative flux more rapidly than the atmosphere, so that a stable boundary layer (SBL) develops from the surface. This stable layer is less turbulent, and thickens more slowly than the CBL. As a consequence, a residual layer (RL) forms between the SBL and the CI.

1.1.3 Monin-Obukhov similarity theory

The most popular theory for the description of the ASL is the Monin-Obukhov Similarity Theory (MOST) (Monin and Obukhov, 1954), which applies for steady and horizontally-homogeneous flows. This theory assumes that the vertical fluxes

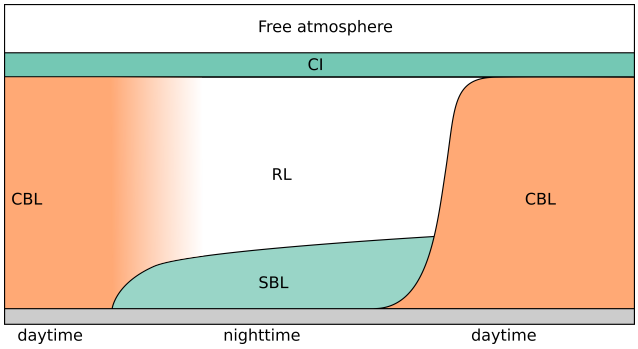

FIGURE 1.1 – Schematic of the diurnal cycle of the inland ABL during summer months, based on Stull (2017).

of momentum τ and temperature H are constant with height (and humidity as well but it is neglected in this explanation). Close to the surface, in the roughness sublayer, these fluxes are the sum of a turbulent flux and a molecular flux. Above the roughness sublayer, the molecular flux is negligible so that the fluxes are solely turbulent and write

$$\tau = \rho\sqrt{\overline{u'w'}^2 + \overline{v'w'}^2} \tag{1.1}$$

$$H = \rho c_p \overline{w'\theta'_v} \tag{1.2}$$

with u, v, and w the zonal, meridional, and vertical wind components, respectively, ρ the density, and c_p the thermal capacity. A velocity scale u^* and a temperature scale θ_v^* can be defined from these fluxes as

$$u^* = \sqrt{\frac{\tau}{\rho}} \tag{1.3}$$

$$\theta_v^* = \frac{H}{\rho c_p u^*}. \tag{1.4}$$

From these parameters, the Monin-Obukhov length scale can be defined as

$$L_{MO} = \frac{-u^{*2}}{\kappa\beta\theta_v^*} \tag{1.5}$$

where $\kappa \approx 0.4$ is the Von Kàrmàn constant, and $\beta = g/\theta_v$ is the buoyancy coefficient with g the gravity acceleration. The MOST assumes that all the vertical derivatives of mean quantities normalized by u^*, θ_v^*, z, and L_{MO} are function of the variable $\zeta = z/L_{MO}$, so that

$$\frac{\partial U}{\partial z} = \frac{u^*}{\kappa z}\phi_U(\zeta) \tag{1.6}$$

$$\frac{\partial \theta_v}{\partial z} = \frac{\theta_v^*}{\kappa z}\phi_\theta(\zeta) \tag{1.7}$$

where ϕ_U and ϕ_θ are universal functions defined experimentally. To calculate the profiles of U and θ, these gradients are integrated from a given height down to

the surface. A length parameter z_0 emerges from this calculation. This parameter depends on the nature of the surface and is larger (lower) for a rough (smooth) surface so that it is called the roughness length.

1.1.4 Convective boundary layer

Above the ASL, the CBL exhibits a well-mixed layer where the velocity, temperature, and humidity are almost constant with height. The turbulence and the fluxes follow the mixed-layer similarity theory (Deardorff, 1980) where the main parameters are the CBL thickness, Z_{CBL}, and the convective velocity scale, w^*, defined as

$$w^* = \left(\frac{\beta H}{\rho c_p} Z_{CBL}\right)^{1/3}. \tag{1.8}$$

In a sheared CBL, two stability parameters are defined to determine the relative contribution of shear and convection to the state of the ABL : u^*/w^* and $-Z_{CBL}/L_{MO}$ (Moeng and Sullivan, 1994; Stoll et al., 2020). These two parameters are related through the relationship

$$-\frac{Z_{CBL}}{L_{MO}} = \kappa \left(\frac{u^*}{w^*}\right)^{-3}. \tag{1.9}$$

They determine the relative contribution of shear production and buoyancy production in the TKE budget (Pino and Vilà-Guerau De Arellano, 2008) and the nature of the largest turbulent structures in the ABL, i.e. convective cells or convective rolls (reviewed in Section 1.5.4).

1.1.5 Stable boundary layer

In the SBL, the turbulence intensity is much lower than in the CBL, because the buoyancy effect tends to suppress vertical motions. Two regimes are commonly identified (Ren et al., 2025). In the first regime, the *weakly SBL* is coupled with the surface, and the local similarity theory, a theory close to the MOST but scaled with local fluxes, can be applied (Nieuwstadt, 1984). In the second regime, the *very SBL* is decoupled from the surface and the classical similarity theories fail at describing the vertical fluxes. In the very SBL, turbulence is intermittent, partly because of the presence of a large variety of sub-mesoscale motions (Sun et al., 2015b), such as gravity waves or Kelvin-Helmholtz billows (described in Sections 1.5.2 and 1.5.1, respectively). Ren et al. (2019) introduced the local intermittent strength indicator (LIST) indicator, defined as the square-roots of the ratio of the TKE to the total (turbulent + sub-mesoscale) fluctuations energy, to quantify the level of intermittency of the flow. When the LIST is close to 1, the turbulence dominates over the sub-mesoscale motions so that the intermittency is weaker, whereas when the LIST is closer to 0, the intermittency is stronger.

table of content

The low turbulence in the SBL reduces the mixing, allowing for large wind shear. In particular, the presence of low-level jets (reviewed in Section 1.4) is common in the nocturnal SBL (Aird et al., 2022).

1.1.6 Residual layer

The RL is a residual from the CBL (Figure 1.1), that is decoupled from the surface after the sunset, due to the presence of the underlying SBL. Thus, the RL exhibits well mixed profiles of velocity and temperature, but the turbulence is progressively decaying over time. More about the turbulence decay can be found in Section 1.3.5.

1.1.7 Far-offshore ABL

The marine ABL has several differences compared to the land ABL. On the one hand, the sea-surface roughness length is relatively low, which results in average in a higher wind speed and a lower turbulence than over land (Barthelmie et al., 1999). However, as the sea surface influences the ABL, the air flow, in return, also modifies the sea-surface properties, generating waves and swell that affect the roughness length z_0. In many atmospheric models, this two-way interaction is modeled based on the theory of Charnock (1955). On the other hand, because of the large water thermal capacity, the sea temperature is only slowly affected by solar radiation, so that the diurnal cycle is less pronounced than over land (Huang et al., 2024a). The seasonal pattern, however can be more pronounced. Ma et al. (2016) found more unstable atmospheric conditions in winter than in summer in the Pacific Ocean whereas the opposite is observed in the North Sea by Sathe et al. (2011). Holtslag (2016) states that the stability over the ocean is also influenced by the North-South air advection.

1.2 Coastal atmospheric boundary layer

This thesis focuses on the coastal ABL, where the atmospheric conditions are influenced by the presence of both the land surface and the sea surface. There, the ABL characteristics strongly depend on the wind direction (i.e. land wind or sea wind). There is no clear agreement on the maximal offshore distance under which land have an influence on the marine ABL. According to Barthelmie et al. (1999), the land effects can be detected within 40 km of the coastline. Pollak et al. (2014) studied wind statistics dependency on wind direction and found that the fetch had a great impact on the offshore turbulence intensity (TI), with TI decreasing with distance from land up to 50 km and then increasing for higher distance. The offshore extent of the sea-breeze (reviewed in Section 1.3), being of the order of several tens of kilometers also inform about the extent of the coastal ABL. Some mechanisms at

play in the coastal ABL, and encountered in this study, are presented hereafter.

1.2.1 Baroclinic pressure gradient

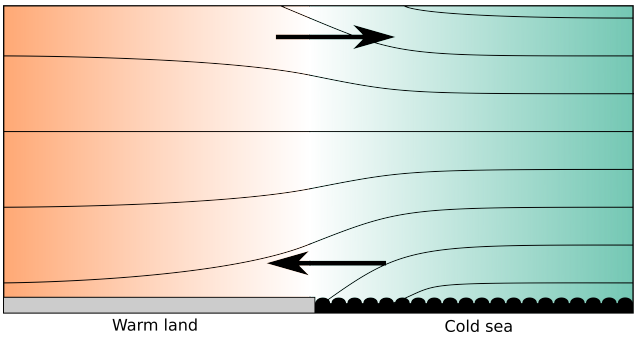

FIGURE 1.2 – Schematic view of a baroclinic ABL around the land-sea interface during the day. Black lines represent isobaric lines and arrows show the mesoscale pressure force direction.

The diurnal cycle of surface temperature is much more pronounced inland than offshore so that, during daytime, the land surface is generally warmer than the sea surface, whereas the opposite occurs during nighttime. This results in a significant horizontal temperature gradient, and thus a horizontal density gradient, with a lower density (ρ) on the warmer side than on the colder side. The vertical pressure gradient is mainly governed by the hydrostatic equation :

$$\frac{\partial p}{\partial z} = -\rho g \tag{1.10}$$

where p is the pressure and z the vertical coordinate. Thus, during the day, the isobaric lines are more spaced on the warmer land side than on the colder sea side, as shown in Figure 1.2. Such an atmosphere necessarily features a horizontal pressure gradient varying with height, called a baroclinic pressure gradient. Under weak synoptic winds, the baroclinic pressure gradient can generate land breezes or sea breezes (reviewed in Section 1.3).

1.2.2 Internal boundary layer

In coastal areas, the surface characteristics (roughness, temperature) are highly heterogeneous. When air is advected through the coastline, it requires some time for the wind and temperature profiles to reach the equilibrium associated to the new surface forcing. Just after the transition, the air flow is separated into two layers : an internal boundary layer (IBL) close to the surface where the various quantities are influenced by the new surface forcing, and a layer above it, where the conditions are unchanged.

IBLs were studied downstream a roughness transition in neutral boundary layers. The change of roughness results in the acceleration (rough to smooth) or deceleration

(smooth to rough) of the air within the IBL (Kaimal and Finnigan, 1994). The evolution of the IBL depth is often found to be a power function of the distance from the transition (e.g. an exponent of 0.8 according to Elliott (1958) but other values can be found in the literature).

When the two surfaces have different temperatures, the IBL is referred to as a thermal IBL (TIBL). If the transition occurs from a cold to a warm (from a warm to a cold) surface, the TIBL is convective (stable). The characteristics of the convective and stable TIBLs are similar to that of the CBL (Section 1.1.4) and the SBL (Section 1.1.5), respectively. The convective TIBL is usually composed of a thermally unstable surface layer topped by a mixed layer, and grows faster than the stable TIBL, which therefore extends farther from the transition (Kaimal and Finnigan, 1994). In addition, the development of a stable IBL is often associated with a frictional decoupling both within and above the IBL, which can generate inertial oscillations (reviewed in Section 1.2.3).

The marine stable TIBL has been studied by Jiang and Wang (2021) using large-eddy simulations. They defined 3 zones based on the advection time (function of the distance) and the turbulent dissipation time : the near-shore zone where the advection is predominant, the intermediate offshore zone where the advection is less important but still non-negligible, and the far-offshore zone where the flow is adjusted to the new surface and MOST is applicable. Mahrt et al. (2014) describe two positive feedback loops causing the rapid decrease of turbulence in a marine stable TIBL. The first one is thermal : as the turbulence decreases, the mixing diminishes so that the thermal stability strengthens which further reduce the turbulence. The second one is mechanical : as the turbulence decreases, the surface waves grow less, which reduces the sea-surface roughness length and thus reduces the turbulence.

1.2.3 Inertial Oscillations

Atmospheric flows are most exclusively studied in a non-Galilean ground-based referential frame in which the Earth rotation induces a Coriolis force that acts perpendicularly to the velocity vector and proportionally to its magnitude. Above the ABL, where the turbulence is relatively low, the wind is mostly governed by the pressure force and the Coriolis force so that

$$\frac{\partial u}{\partial t} = -\frac{1}{\rho}\frac{\partial p}{\partial x} + f_c v \tag{1.11}$$

$$\frac{\partial v}{\partial t} = -\frac{1}{\rho}\frac{\partial p}{\partial y} - f_c u \tag{1.12}$$

with t the time and f_c the Coriolis frequency. Thus, the equilibrium geostrophic wind vector (u_g, v_g) equals $(-\frac{f_c}{\rho}\frac{\partial p}{\partial y}, \frac{f_c}{\rho}\frac{\partial p}{\partial x})$ (Stull, 2017).

table of content

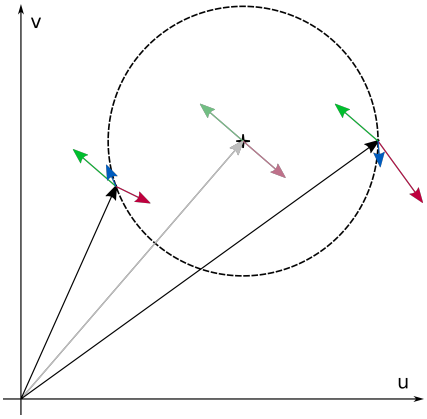

FIGURE 1.3 – Schematic view of an inertial oscillation in the Northern hemisphere where the black arrows are the velocity at different times, the dotted circle show its evolution, and the green, red, and blue arrows shows the pressure, Coriolis and the resulting forces respectively. The grey arrow is the equilibrium geostrophic velocity.

Following this hypothesis, any departure of the wind from its geostrophic equilibrium results in circular inertial oscillations (IO) of the wind vector around the geostrophic wind. These oscillations are represented in the (u, v) plane in Figure 1.3 where the pressure force (green arrow) is constant and the variation of the Coriolis force (red arrow) results in a force (blue arrow) tangent to the circle. The IO period is $\frac{2\pi}{f_c}$ (Blackadar, 1957) which is about 16 hours at 47 °N where this study is made. Theoretically (following Equations 1.11 and 1.12), they never stop but in practice the non-zero turbulence tends to damp the oscillations toward the equilibrium wind (Stull, 2017).

In the ABL, the turbulent mixing force is non-negligible. Therefore, the equilibrium wind speed in the CBL is lower than the geostrophic equilibrium. When the surface conditions rapidly transition from unstable to stable, e.g. at sunset or in a stable TIBL, the equilibrium wind speed changes. Van de Wiel et al. (2010) extended the IO theory, and showed that in this case, the wind vector tends to rotate around its new equilibrium wind. IO are an important mechanism responsible for the generation of low-level jets (reviewed in Section 1.4).

1.3 Sea-breeze

1.3.1 Description

A *sea breeze* (SB) is a local circulation driven by the baroclinic pressure gradient (Section 1.2.1) resulting from the higher temperature of the land surface compared to that of the sea surface during daytime. Therefore, a SB is characterized by a cold and humid *gravity current* propagating near the surface toward land and a warmer *return current* propagating aloft toward the sea (Stull, 2017). During nighttime,

the radiative cooling tends to cool land surface faster than sea surface, so that the opposite circulation can occur and is referred to as a *land breeze*.

SBs have been widely studied over time (Abbs and Physick, 1992; Miller et al., 2003; Crosman and Horel, 2010). Stull (2017) summarized the main characteristics of SBs in a schematic shown in Figure 1.4. After crossing the coastline, the gravity current propagates above a warmer surface resulting in a convective TIBL (represented with a dashed line), and forms a front (SBF) at the interface with the CBL over land. The SBF is a horizontally convergent area with strong updrafts and large temperature, density, and velocity gradients (Kraus et al., 1990). At the top of the SBF, the lifted air forms the SB head (SBH). Kelvin-Helmholtz waves (KHW) can form at the interface between the gravity current and the return current.

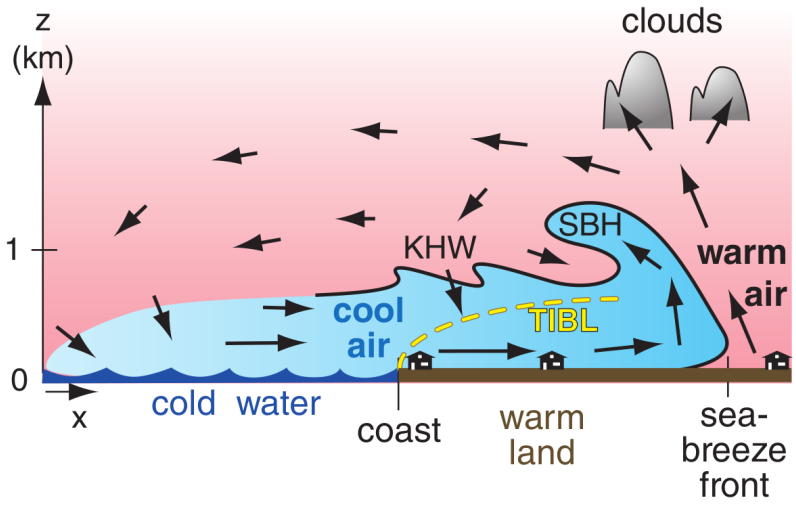

FIGURE 1.4 – Schematic of a sea breeze cell (Stull, 2017).

To study the SB, the velocity field is divided into the cross-coast component U_c, and the along-coast component V_c (Paul et al., 2021), where U_c is positive for sea winds. Thus, U_c is positive in the gravity current, with a maximum value, WS_{SB}, generally between 5 and 10 m.s^{-1}. Its characteristic height, Z_{SB}, is the height at which $U_c = 0$ (Rizza et al., 2015), corresponding to the interface between the gravity current and the return current. The typical value of Z_{SB} is between 100 m and 1 km (Simpson, 1994).

The horizontal extent of the breeze is divided into two parts. The inland extent (the distance between the coastline and the SBF) usually reaches a few tens of kilometers in late afternoon (Stull, 2017). In Australia and India, SB events have been observed more than 100 km inland (Simpson, 1994). Abbs and Physick (1992) note that this extent is generally larger in tropical areas where it can reach a few hundred kilometers. The offshore extent, i.e. the distance between the coastline and

the offshore limit, has been less studied and is reviewed in Section 1.3.4.

1.3.2 Life cycle

The SB life time follows several stages, briefly summarized hereafter using the vocabulary of Cuxart et al. (2014) and Clarke (1984). In the preparatory stage, after the sunrise, the baroclinic pressure gradient installs. If the synoptic wind is from land (as often during SB events), the near-surface wind decelerates, resulting in a calm area offshore. The SB onset occurs when the gravity current establishes, i.e. when U_c becomes positive close to the surface. Then, during the development stage, the SB thickens, expands horizontally, and U_c increases over time. A SB can be seen as the early stage of an IO (Section 1.2.3) : when the baroclinic pressure gradient installs, the equilibrium wind changes, initiating a rotation of the wind vector around this new equilibrium. Thus, the wind acceleration is associated with a veering under Coriolis force, following the IO (Haurwitz, 1947). During the mature phase, Cuxart et al. (2014) observed, from numerical simulation, a nearly steady SB when the pressure gradient is approximately balanced by turbulent drag above land and by advection over the sea. In the late afternoon, the land surface cools rapidly and the baroclinic pressure gradient decreases. As a result, the SB decays. Depending on the external forcings, the SB may revert to a land breeze at night, or, as related by Clarke (1984), the SBF may detach from the SB cell, and propagate in the nocturnal stable layer as an atmospheric bore (reviewed in Section 1.5.3).

1.3.3 External parameters

The sensible heat flux is the main forcing of the SB. Based on idealized LES, Antonelli and Rotunno (2007) showed that both Z_{SB} and WS_{SB} are proportional to the time integral of the land sensible heat flux. The temperature difference between the land surface and the sea surface, being easier to measure than the surface heat flux, is often used as a criteria to detect SB events. For example, Grau et al. (2021) consider that this difference must be larger than 5 °C for a SB to install.

The synoptic wind, and especially its cross-coast component, also have a strong influence on the SB development. A light synoptic wind from land is the most favorable for the SB initiation (e.g. between 0 and 2 m.s^{-1} for Arritt (1993)). When it increases, Z_{SB} decreases and the SB cell is shifted offshore (Steele et al., 2013; Gahmberg et al., 2010). When the synoptic wind is from the sea, the maximal thermal wind in the gravity current decreases with increasing synoptic velocity. In this case, the return current fails to install, so that the baroclinic gravity current cannot really be considered as a SB but rather as a *thermal reinforcement* or a *synoptic breeze* (Mestayer et al., 2018).
The along-shore component of the synoptic wind also has an impact on the SB

development and is often used to classify SB as pure, corkscrew, and backdoor (Miller et al., 2003; Steele et al., 2013, 2015). The *pure SB* corresponds to the case with no along-shore component. In the Northern hemisphere, when the synoptic wind has a westerly or easterly component (for a case where the land is to the north and the sea to the south) the SB is described as *corkscrew* or *backdoor*, respectively. Corkscrew SBs are more frequent and stronger than backdoor SBs (Gahmberg et al., 2010; Steele et al., 2015). This is explained by the fact that for a corkscrew (backdoor) SB, the synoptic pressure gradient is oriented in the same direction as (opposed to) the mesoscale thermally-induced pressure gradient (Miller et al., 2003). Another argument is that the divergence area above the sea in corkscrew conditions also enhance the SB onset, whereas the convergence area in backdoor conditions tends to inhibit the SBF propagation (Mestayer et al., 2018).

Most of the SB studies, especially numerical ones, focused on simple straight coastlines. However, near a complex coastline, the relevant coast orientation is hard to determine (Shen and Zhao, 2020), and the coastline complexity can strongly influence the behavior of a SB. Bays and peninsulas have an impact on vertical velocity (Arritt, 1989), wind direction (Calmet et al., 2018), precipitations (Baker et al., 2001), and deep-convection events (Fu et al., 2021) during SB events. Zhong and Takle (1992) observed that in early morning, breezes can form both at the coastline and at the river boundaries and later merge into a bigger scale breeze. They also suggested that the presence of a river might tend to speed up the SBF by reducing the turbulent drag in the TIBL. Simpson (1996) showed that the evolution of wind direction during a SB event can be influenced by the transition from the local SB to a regional SB (which he calls *continental SB*) associated to a larger-scale land mass.

Rotunno (1983) gathered several analytical models of the SB in a unified linear theory, and showed that the aspect ratio of the SB (ratio of its horizontal extent to its depth) depends on the latitude and the initial stability. The simulation results of Arritt (1989) are in agreement with this theory. The influence of other external parameters are reviewed by Crosman and Horel (2010).

1.3.4 Offshore extent

In the offshore part of the breeze the baroclinic pressure force is mainly balanced by advection so that it is characterized by a continuous acceleration in the gravity current (Cuxart et al., 2014). Therefore, there is a horizontal divergence that is compensated by a low subsidence in a large area. The wind aloft is warmer and dryer as it has been transported from land in the return current.

Whereas the inland limit of the SB is clearly defined by the SBF, the offshore limit is unclear. Several studies defined a limit based on a threshold on U_c (Arritt, 1989; Finkele, 1998; Zhong and Takle, 1992; Steele et al., 2013). The threshold of 1

m/s proposed by Arritt (1989) is the most commonly used (hereafter referred to as Arritt's extent). This definition have a few limitations. First, Steele et al. (2013) note that the extent value is highly dependent on the threshold value (a threshold of 1.5 m/s results in a 33 % difference in extent). Second, as reported by Arritt (1993) himself, this limit is undefined when the synoptic wind is from the sea. Third, the definition of "cross-coast component" for a point located tens of kilometers offshore needs to be clarified especially near complex coastlines. Fourth, the definition is not applied the same way in all studies. Arritt (1989) initially suggested this threshold for an atmosphere initially at rest. Under light synoptic wind, he rather apply the threshold to the departure from the synoptic wind whereas Finkele (1998) and Steele et al. (2013) applied this threshold to U_c at 47 m and 10 m high, respectively.
Other definitions for the offshore limit include the observation of a cloud-free area which corresponds to the extent of the subsidence area (Stevenson, 1969; Simpson, 1994). Aparna et al. (2005) proposed a statistical definition based on the probability that the surface wind at a given distance is correlated with the SB surface wind. They showed that this probability gradually decreases with distance from coast. Using an arbitrary threshold, they were able to define a statistical limit to the SB. However, this definition cannot be applied to a single case-study.

Studies from Dixit and Nicholson (1964) and Finkele et al. (1995) present a complete cross-section of the SB wind field. Arritt's extent can be estimated to 32 km in the former and 28 km at 1119 local time (LST) in the latter (Figure 3 in their paper). The buoy from Zhong and Takle (1992) observed SB at 40 km offshore while the ship from Subrahamanyam et al. (2001) detected inversion of the wind direction at 80 km offshore during 4 SB days but didn't detect change in wind direction at 100 km offshore during 4 similar SB days. All this measurements give an idea of typical extent of the SB. However they do not inform about the maximal extent of the observed SB and the offshore expansion speed. The statistical method proposed by Aparna et al. (2005) gives an average extent of 180 km, but it is difficult to compare this value to other measurements.

Arritt (1989) was one of the first authors to study the sensitivity of the offshore extent on different parameters. He performed ideal-case numerical simulations and obtained the following results : (i) with initial atmosphere at rest, the offshore extent reached 113 km at 40 °N, (ii) the offshore extent is greater than onshore extent, (iii) the SST has only a little impact on the offshore extent unless it is sufficiently warm to initiate convection offshore, (iv) increasing the initial stability tends to increase slightly the offshore extent and decrease the SB depth so that the Rotunno's linear theory is roughly valid, (v) similarly, the latitude impacts both the extent and the depth of the SB so that the linear theory is valid, and (vi) the synoptic wind has an impact on the offshore extent (applying the threshold to the departure from synoptic wind), i.e. under light land wind, it is much larger than under light sea wind. Finkele (1998) performed idealized simulations to study the SB propagation speed both inland and offshore and compared with aircraft measurements. She found

that the offshore extent is similar under offshore synoptic winds of 2.5 $m.s^{-1}$ and 5 $m.s^{-1}$, reaching a maximal value of 70 to 80 km, and that the offshore propagation speed had a constant value of 3.4 $m.s^{-1}$. The independence of the offshore extent on the synoptic wind found by Finkele (1998) is not in good agreement with Arritt (1989) statement. However, the threshold is applied to the absolute wind speed by the former and to the departure from synoptic wind by the latter.

1.3.5 Turbulence and waves in a sea breeze

Gravity waves (GW, reviewed in Section 1.5.2), have been observed during SB events in previous studies. First, according to the linear theory of Rotunno (1983), the SB initiation features GW at equatorial latitudes (between 30 °N and 30 °S). These GW propagate both onshore and offshore, and may trigger rainfall (Fang and Du, 2022). Furthermore, at a very late stage, the interaction of a degenerate SBF with the nocturnal SBL or other mesoscale fronts can generate a bore and gravity waves, responsible for example for the famous Morning Glory cloud pattern (Thomsen and Smith, 2006; Huang et al., 2024b; Noonan and Smith, 1986).

Kelvin-Helmholtz (KH) billows (reviewed in Section 1.5.1) have been observed by several authors seaward of the SBF (Wood et al., 1999; Plant and Keith, 2007). These waves were reproduced in a water tank by Britter and Simpson (1978) and were also observed in the simulations of Sha et al. (1991) and Rizza et al. (2015). The KH billows are generated by the shear in the middle of the cell where the gravity current and the return current move in opposite direction. Simpson and Britter (1980), in water tanks experiments, found that the KH billows wavelength (λ_{KH}) was 1.7 times larger than their vertical amplitude, defined as the difference between the height of the SB head and that of the steady gravity current, which gives typical values around 500 m. Plant and Keith (2007) listed several studies on KH billows during SB events where the wavelength, if determined, is between 500 m and 3 km.

In the land convective TIBL (Figure 1.4), Shao et al. (1991) showed that the scaling laws for vertical velocity and potential temperature are similar to the CBL ones (Kaimal and Finnigan, 1994) and depend on the TIBL height. Moreover, the TKE budget within the TIBL computed by Cuxart et al. (2014) strongly resembles that of a sheared CBL e.g. in Pino and Vilà-Guerau De Arellano (2008).

In the return current, the air comes from the CBL and is decoupled from the surface after crossing the SBF (upper part in Figure 1.4). Thus, the return current can be considered as a residual layer where the turbulence decays with distance from the SBF (Briere, 1987; Kitada, 1987; Wood et al., 1999). However, the behavior of this decay has been poorly studied. Nieuwstadt and Brost (1986) and Sorbjan (1997) studied numerically the decay of turbulence from the CBL when the surface heat flux

is instantaneously set to zero. Although their works aimed at modeling the evening decay of turbulence at sunset, they might be applicable to a land-sea transition and to the SB return current. Several models emerged to describe this decay. As discussed by Nieuwstadt and Brost (1986), the first simple approach to model the turbulence decay is based on the assumption used for isotropic homogeneous turbulence that

$$\frac{\partial k}{\partial t} = -\varepsilon \tag{1.13}$$

where k is the TKE and ε its dissipation rate.

A first model, hereafter called model 1, suppose that ε is proportional to k so that

$$\varepsilon = \frac{k}{t_{\varepsilon 1}} \tag{1.14}$$

where $t_{\varepsilon 1}$ is a decay time scale. Injecting Equation 1.14 into Equation 1.13 results in an exponential decay of k as

$$k(t) = k_0 \exp^{-\frac{t}{t_{\varepsilon 1}}} \tag{1.15}$$

$$\varepsilon(t) = \varepsilon_0 \exp^{-\frac{t}{t_{\varepsilon 1}}} \tag{1.16}$$

where t is the time since the decoupling occurred and the subscript $\cdot_0$ denotes the initial value in the CBL.

A second model, hereafter called model 2, suppose that ε is proportional to $k^{3/2}$ so that

$$\varepsilon = \frac{k^{3/2}}{L_{\varepsilon 2}} \tag{1.17}$$

where $L_{\varepsilon 2}$ is a decay length scale. Injecting Equation 1.17 into Equation 1.13 gives the following solution

$$k(t) = k_0(1 + \frac{1}{2}\frac{\sqrt{k_0}}{L_{\varepsilon 2}}t)^{-2} \tag{1.18}$$

$$\varepsilon(t) = \varepsilon_0(1 + \frac{1}{2}\frac{\sqrt{k_0}}{L_{\varepsilon 2}}t)^{-3}. \tag{1.19}$$

Model 2 is inspired by the CBL similarity theory (Section 1.1.4), where k_0 and ε_0 are parameterized as

$$k_0 = C_k w^{*2} \tag{1.20}$$

$$\varepsilon_0 = C_\varepsilon \frac{w^{*3}}{Z_{CBL}}. \tag{1.21}$$

with C_k and C_ε two constants, so that

$$\varepsilon_0 = \frac{k_0^{3/2}}{\frac{Z_{CBL} C_k^{3/2}}{C_\varepsilon}} \tag{1.22}$$

table of content

which, combining with Equation 1.17, gives

$$L_{\varepsilon 2} = Z_{CBL}\frac{C_k^{3/2}}{C_\varepsilon} \tag{1.23}$$

and, injecting into Equation 1.18,

$$k(t) = k_0(1 + \frac{1}{2}\frac{C_\varepsilon w^*}{C_k Z_{CBL}}t)^{-2} \tag{1.24}$$

$$\varepsilon(t) = \varepsilon_0(1 + \frac{1}{2}\frac{C_\varepsilon w^*}{C_k Z_{CBL}}t)^{-3}. \tag{1.25}$$

Nieuwstadt and Brost (1986) compared this model to the LES results of an idealized decoupled CBL and found that it was not able to properly represent the decay, primarily because the assumption of Equation 1.13 is not correct : the buoyancy mechanism continues to have a non negligible influence on the evolution of k. They found, however, that a good similarity is obtained between simulations with different initial conditions, using the CBL parameters to scale the TKE as $\frac{k}{w^{*2}}$ and the time as $t^* = \frac{tw^*}{Z_{CBL}}$. Nieuwstadt and Brost (1986) and Sorbjan (1997) found that for $t^* > 1$, $\frac{k}{w^{*2}}$ decays as $t^{*-1.2}$. This model is hereafter called model 3. More recently, El Guernaoui et al. (2019) showed that this exponent, determined in a log-log representation, is dependent on the choice of the initial decoupling time. These 3 models, designed for a theoretical decay of turbulence, have not been applied to the SB return current yet, except by Wood et al. (1999) who used model 1 to fit the decay of ε in the SB return current. This fit roughly represented the decay up to 10 km from the SBF.

1.3.6 Gaps in knowledge

Despite the extensive literature, some gaps remain in the knowledge of sea breezes. First, no consistent method to study SBs near complex coastlines was proposed. Former studies considering non-rectilinear coastlines have described qualitatively the resulting phenomenon (Mestayer et al., 2018; Calmet and Mestayer, 2015; Arritt, 1989; Simpson, 1996) but did not propose methods to quantify them. Second, since turbulence in a breeze has been studied almost exclusively in the TIBL inland, there is a lack of turbulence characterization in the return current and in the offshore part of SBs.

1.4 Low-level jet

1.4.1 Definition

The term *low-level jet* (LLJ) describes a wind-speed profile exhibiting a local maximum located at low altitude, typically between 100 m and 1 km high (Nunalee

and Basu, 2014). Such a maximum is in contradiction with the monotonic wind profiles described by the MOST. LLJs regularly occur in the nocturnal SBL and in coastal area (Luiz and Fiedler, 2024).

LLJs are generally characterized by strong wind shear, being positive below and negative above the core. For example, Wagner et al. (2019) measured an averaged wind shear of 20 $m.s^{-1}.km^{-1}$ with extreme values of 70 $m.s^{-1}.km^{-1}$. Such large wind shears are of interest for wind energy as they generate load and fatigue on wind-turbine blades (Holtslag et al., 2016; Kosović et al., 2025).

In most of the studies, the LLJ is defined solely based on a peak in the wind speed (WS) profile with a criteria on the absolute or relative difference between the LLJ core wind speed (WS_{LLJ}) and the minimum WS above it (Aird et al., 2022; Visich and Conan, 2025). Different arbitrary criteria are chosen by authors to exclude too small maxima that can occur for example in a mixed layer. Alternatively, the LLJ can also be defined based on the maximum and minimum shear in a wind profile (Hallgren et al., 2023). Other criteria can be used depending on the type of jet observed, e.g. a late evening acceleration (Banta, 2008).

1.4.2 Mechanisms

Different mechanisms can generate a LLJ involving either heterogeneous or unsteady conditions (Liu et al., 2014). Some of them are described hereafter.

Blackadar (1957) suggested that LLJs in the Great Plains, USA, originate from a frictional decoupling in the ABL after sunset, due to the change from unstable to stable ABL. The reduced turbulence in the SBL induces a frictional decoupling resulting in IO of the wind velocity around the equilibrium velocity (Van de Wiel et al., 2010) (see Section 1.2.3). At some point of these oscillations, generally in late night or early morning, the wind speed exceeds the geostrophic wind speed, thus forming a low-level jet. This effect, sometimes referred to as "inertial jet" is summarized in Figure 1.5.

A similar mechanism was proposed by Högström and Smedman-Högström (1984) based on offshore LLJ observations where the frictional decoupling is caused by the transition from a warm land to a colder sea rather than the daytime-nighttime transition. Their hypothesis was confirmed by an idealized numerical simulation and is a common explanation for the presence of LLJs over the Baltic Sea (Wagner et al., 2019). This LLJ can exist as far as 200 km offshore.

As mentioned in Sections 1.2.1 and 1.3, a baroclinic pressure gradient generates a thermal wind that can result in a SB, a land breeze, or a thermal reinforcement. The definition of a low-level jet is broad enough to include these three types of flow,

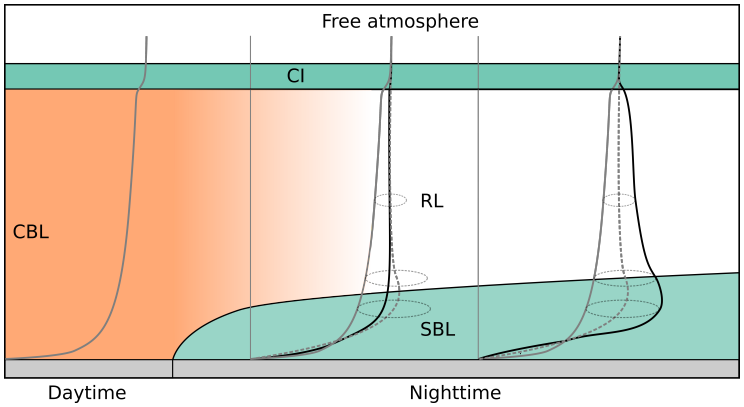

FIGURE 1.5 – Schematic of the Blackadar's mechanism, based on Van de Wiel et al. (2010), where the solid gray line shows the initial wind speed, the black line shows the wind profile during the IO around the equilibrium wind profile represented by the dashed gray line.

which indeed present a wind speed maximum at low-level (Kalverla et al., 2019). This mechanism is responsible for the LLJs observed for example by Burk and Thompson (1996) at the Californian coast and Colle and Novak (2010) in the New-York Bight. LLJs were also observed close to a sea-surface thermal front (Vihma et al., 1998). Baroclinicity can also result from temperature variations over a sloped terrain, as suggested by Holton (1967) : anabatic and katabatic winds can be considered as LLJ.

A few other mechanisms are known to generate LLJs such as convergence due to blockage effect by mountain chains (Jiang et al., 2010), the interaction with upper jet streams (Stensrud, 1996), or frontal passage (Wagner et al., 2019; Baki et al., 2025).

The determination of the LLJ initiation mechanism is quite difficult, and is often limited to showing the existence of a baroclinic area, circular oscillations of the wind vector to suggest the presence of IO, or a change in stability to suggest a frictional decoupling. In coastal areas, the inertial and baroclinic mechanisms generally act at the same time (Wagner et al., 2019). In an inertial-jet case caused by warm air advection over colder sea surface, Mahrt et al. (2014) mentioned that the baroclinic pressure gradient is opposed to the LLJ development. They found higher core speed farther offshore than near the coast, which can be attributed either to the baroclinic deceleration or the IO requiring distance to generate a LLJ.

1.4.3 Evolution of a jet characteristics

The LLJ core speed (WS_{LLJ}) in the ABL is generally of the order of 10 to 20 m.s^{-1} (Banta, 2008; Aird et al., 2022), although much faster jets can be observed, e.g. up to 40 m.s^{-1} for Quint et al. (2025).
For a baroclinic LLJ, the maximum LLJ speed is reached when the angle of the

oscillations around the thermal wind is roughly aligned with the synoptic wind. This occurs a few hours after the maximal baroclinic conditions in the studies of Burk and Thompson (1996) and Wagner et al. (2019). This delay can be explained by the synoptic wind being mainly along-shore, while the early response to the land-sea baroclinicity is a cross-shore wind component (as an SB).
For an inertial LLJ, there is theoretically a delay of $\frac{\pi}{f_c}$ (half IO) between the frictional decoupling and the wind speed maximum (Van de Wiel et al., 2010).

The LLJ core height (Z_{LLJ}) can vary significantly between observations. Aird et al. (2022) found a median LLJ height of 150 m, whereas in a long term measurement campaign at FINO1, Wagner et al. (2019) find that most of the detected LLJs core height is between 200 and 300 m. In several studies the research of a wind maximum is restricted to the first hundreds of meters due to a specific interest in this layer (wind energy application) or to the limited extent of the measurements (e.g. with a profiler LiDAR).
For the inertial LLJ in the weakly stable regime, Banta (2008) finds that Z_{LLJ} increases with WS_{LLJ} so that the shear is roughly constant in the subjet layer. Several authors note that Z_{LLJ} decreases with increasing stability (Banta, 2008; Mahrt et al., 2014; Céspedes et al., 2024). For the baroclinic LLJ of Burk and Thompson (1996), the core is found at the top of the near-neutral marine ABL that varies with the offshore distance. When a nocturnal LLJ moves over a urban area, the mixing in the urban boundary layer tends to increase the jet height (Tsiringakis et al., 2022). Similarly, Quint et al. (2025) found that Z_{LLJ} is higher in the presence of wind farms. Thus, a mixed layer below the jet tends to increase its height.

1.4.4 Turbulence and waves in a jet

Banta et al. (2006) observed inertial LLJs during 6 nights when they computed the velocity variance in the direction of the jet ($\overline{u'^2_{LLJ}}$) arguing that it is very close to the TKE. They found different structures of the $\overline{u'^2_{LLJ}}$ profiles below Z_{LLJ}, depending on the thermal stability defined by a modified bulk Richardson number

$$Ri_B = \frac{g}{\theta}\frac{\Delta\theta}{\Delta z} \Big/ \left(\frac{WS_{LLJ}}{Z_{LLJ}}\right)^2 . \tag{1.26}$$

For Ri_B around 0.15, $\overline{u'^2_{LLJ}}$ decreases with height from the surface up to Z_{LLJ} where it reaches a minimum. This minimum is also measured by Smedman et al. (1993) for offshore inertial LLJ events and simulated by Cuxart and Jiménez (2007).
For Ri_B around 0.19, the maximum of $\overline{u'^2_{LLJ}}$ is found aloft, and the turbulence is transported downward. This case is referred to as the "upside-down boundary layer".

Banta et al. (2006) also found that the near-surface value of $\overline{u'^2_{LLJ}}$ scales with WS_{LLJ} as

$$\frac{\sqrt{\overline{u'^2_{LLJ}}}}{WS_{LLJ}} \approx 0.05 . \tag{1.27}$$

table of content

The same order of magnitude is found offshore from the aircraft measurements of Smedman (1988) (their ratios of the turbulent velocity scale to the wind speed scale are between 0.04 and 0.11), and the turbulence intensity measured below the LLJ core by Christakos et al. (2014) (5 to 11 %) and Thomasson (2021) (2 to 6 %).

Below Z_{LLJ}, the large shear can trigger KHW (Newsom and Banta, 2003; Nakanishi et al., 2014). Above Z_{LLJ}, Smedman et al. (1993) observed a strong maximum of TKE in the high negative shear region in 3 out of 4 cases, which could also be caused by KHW. This is less obvious but also observable in the weakly stable regime of Banta (2008) whereas Céspedes et al. (2024) find that $\overline{w'^2}$ is negligible above Z_{LLJ}. Svensson et al. (2019) performed LiDAR measurements and numerical simulations and found, as expected, a downward momentum flux below the jet core where the shear is positive and an upward flux above it where the shear is negative.

The TKE budget measured by Smedman et al. (1993, 1995) in the inertial LLJ was dominated by the balance between shear production and dissipation, and it is suggested that the pressure term, computed as a residual, distributes the TKE at all heights, whereas in the LES of Cuxart and Jiménez (2007), the TKE budget is balanced by the shear production, the negative buoyancy and the dissipation.

1.4.5 LLJ in coastal areas

Several authors studied offshore LLJs in coastal areas, mostly for wind energy applications. Luiz and Fiedler (2024) performed a global 30-year analysis using ERA5 and determined that LLJs occur 19 % of the time in a coastal area, with higher frequency to the west of continents (maximum of 90 % at the African Atlantic coast). These LLJs are, for most cases, parallel to the coast and located at the top of an unstable or neutral boundary layer capped by a strongly stable layer. Sheridan et al. (2024) found a majority of LLJs under along-coast winds at the US west coast whereas Wagner et al. (2019) found that most events occur under land winds in the North Sea. Despite a linear decrease of LLJ frequency with offshore distance, some LLJ events are detected by Aird et al. (2022) as far as 300 km offshore on daytime during summer months. Far offshore (200-300 km), WS_{LLJ} is well correlated with Z_{LLJ} whereas this correlation is less clear close to the coastline. Djath et al. (2022) analyzed the evolution of the near-surface wind speed in a coastal area using SAR observation, and found several events when the speed decreases with increasing offshore distance in stable conditions. They suggested that this behavior correspond to the weakening of LLJs in the convective TIBL that form at the land-sea transition. Finally, Wagner et al. (2019) analyzed two cases using WRF simulations to determine their initiation mechanisms and found a contribution of both the baroclinicity and the inertial oscillations.

table of content

1.4.6 Gaps in knowledge

While the LLJ is not necessarily a coastal phenomenon, its appearance and evolution are closely related to thermal effects through stability and baroclinicity. Therefore, it is of high interest to document the possible mechanism driving a LLJ in coastal areas. Moreover, to the author's knowledge, there is no study on the evolution of a nocturnal jet initiated over land that crosses the coastline. In such a case, a convective TIBL would develop under the LLJ core, modify its characteristics, and affect the turbulence. The interaction between a LLJ and a convective TIBL has not been documented yet.

1.5 Waves, bores, and rolls in the atmospheric boundary layer

Several types of oscillating structures can develop in the ABL with wavelengths ranging from tens of meters to a few kilometers. At different stages of this thesis, some of these structures are detected and analyzed. For that reason, an overview is provided in the present section. Sun et al. (2015b) reviewed the different types of waves in the SBL, based on particular solutions of the 2D Taylor-Goldstein dispersion relation :

$$k_z^2 = \frac{{N_{BV}}^2 k_x^2}{(\omega - U k_x)^2} + \frac{\partial^2 U}{\partial z^2}\frac{k_x}{(\omega - U k_x)} - \frac{k_x}{H_s(\omega - U k_x)}\frac{\partial U}{\partial z} - \frac{1}{4H_s^2} - k_x^2 \qquad (1.28)$$

where k_x, k_z, and ω are the horizontal and vertical wave number and the wave frequency, respectively, N_{BV} is the mean Brunt-Väisälä frequency, U is the horizontal mean wind speed, and H_s the scale height. This theoretical equation relates the wave number to the mean characteristics of the atmosphere to determine the range of waves that can exist in a given atmosphere. Following the classification of Sun et al. (2015b), we separate the vorticity waves generated by shear instability (referred to as Kelvin-Helmholtz waves) described in Section 1.5.1 from the buoyancy waves (referred to as gravity waves) described in Section 1.5.2. Then, a particular type of gravity waves, the bore waves, is described in Section 1.5.3. Finally, as the study also deals with convective layer structures, a short review on the convective rolls is given in Section 1.5.4.

1.5.1 Kelvin-Helmholtz waves

The *Kelvin-Helmholtz waves* (KHW) are waves that are generated by the Kelvin-Helmholtz instability, which occurs when the shear destabilization overcomes the buoyancy stability. The common criteria for the existence of KHW is

$$Ri = \frac{\frac{g}{\theta_v}\frac{\partial \theta_v}{\partial z}}{(\frac{\partial U}{\partial z})^2 + (\frac{\partial V}{\partial z})^2} < 0.25 \qquad (1.29)$$

table of content

where Ri is the gradient Richardson number, and U and V are the horizontal mean wind components (Plant and Keith, 2007). According to Turner (1979), the most unstable KH wavelength, λ_{KH}, is 7.5 times the thickness of the layer where $Ri < 0.25$. The KH waves are rapidly non-linear and diverge from the Taylor-Goldstein framework. Exchange of momentum with the sheared background flow leads to the transformation of the waves into vortex rolls called the KH billows. The breaking of KHW is one of the major cause of the generation of turbulence in stably stratified layers (Thorpe, 2012).

In the atmosphere, KHW are observed during SB events (Figure 1.4), at the top of the CBL (Kallistratova et al., 2019), or during LLJ events (Newsom and Banta, 2003; Nakanishi et al., 2014).

1.5.2 Gravity waves

Gravity waves (GW) arise from a disturbance in the hydrostatic equilibrium of a stably stratified fluid. The distinction is made between surface gravity waves, which propagate at the interface between two layers with different densities, and internal gravity waves (IGW) propagating within a stable layer.

Based on the sign of k_z^2 in the Taylor-Goldstein equation, IGWs can either propagate vertically ($k_z^2 > 0$) or be "trapped" or "evanescent" ($k_z^2 < 0$). Under the assumption that (i) $\omega/k_x << U$ and (ii) the third and fourth terms of the right-hand side of Equation 1.28 are negligible, Scorer (1949) simplified the system to derive a dispersion relation involving the Scorer parameter l_S that determines whether the waves will propagate vertically or become evanescent :

$$k_z^2 = \frac{{N_{BV}}^2}{U^2} - \frac{1}{U}\frac{\partial^2 U}{\partial z^2} - k_x^2 = l_S^2 - k_x^2. \tag{1.30}$$

Thus, if $k_x > l_S$, the wave is evanescent, whereas if $k_x < l_S$, the wave propagates vertically. If l_S decreases with height, the GW may be trapped within a certain layer (Johnson et al., 2018).

In the ABL, GW can be generated in baroclinic area (Rotunno, 1983) (See Section 1.3.5), by the interaction with orography (orographic gravity waves) (Teixeira, 2014), or by the propagation of an underlying gravity current (bore waves in Section 1.5.3).

GW can destabilize and break, which can enhance a significant level of turbulence (Staquet and Sommeria, 2002). For non-breaking GW, Sun et al. (2015a) observed near-surface oscillations of turbulent mixing related to the oscillations of the velocity components within the GW. They suggested that these turbulent mixing oscillations, in turn, modified the velocity components. They called this phenomenon turbulence-forced oscillations. Roy et al. (2021) measured near-surface (10 m high) wind speed

with a sonic anemometer during a GW event onshore. They noticed higher wind fluctuations as well as larger turbulent eddies at crests than at troughs. For short waves, turbulence scales and wave scales can overlap (Mahrt, 2014), which further increases the complexity of studying turbulence within GW.

1.5.3 Bores

To understand the nature of a bore, one needs to introduce the criticality of a shallow-layer flow. Consider a thin layer of a dense fluid lying beneath a lighter fluid. According to Stull (2017), the intrinsic velocity c_0 of a surface gravity wave at the interface between the two fluids is expressed as :

$$c_0 = \sqrt{g' h_0} \tag{1.31}$$

where h_0 is the thickness of the denser fluid, and g' is the reduced gravity acceleration that depends on the density difference between the two fluids. Two flow regimes exist based on the Froude number Fr, defined as

$$Fr = \frac{U}{c_0} \tag{1.32}$$

where U is the mean velocity of the fluid. When $Fr < 1$ ($Fr > 1$), the fluid moves slower (faster) than the gravity waves, and the flow is referred to as subcritical (supercritical).

As the flow crosses an obstacle of height d_0, the observed behavior depends on Fr and the height ratio d_0/h_0. Rottman and Simpson (1989) summarized the various laminar regimes in Figure 1.6. Regions (a) and (d) represent flows that are entirely supercritical or subcritical, respectively. In the supercritical regime, the interface between the two fluids bulges above the obstacle, while in the subcritical regime, the interface dips and the flow velocity increases over the obstacle. When the d_0/h_0 increases, the flow becomes partially blocked. In this case (b), the local Froude number changes as the fluid passes the obstacle, forming a hydraulic jump. Finally, when the dense fluid height is less than the obstacle height and its kinetic energy is low, the flow is entirely blocked by the obstacle (c).

When a gravity current propagates beneath the aforementioned two-layer fluid, it behaves as an obstacle. This phenomenon was experimentally studied by Rottman and Simpson (1989), as shown in Figure 1.7. The experiment involved creating a gravity current of density ρ_0 in a resting environment formed by two layers (1 and 2) of densities ρ_1 and ρ_2 with $\rho_0 > \rho_1 > \rho_2$. The propagation of the gravity current disturbs the initial stratified environment, generating various phenomena depending on its depth d_0 and velocity U.

Based on idealized simulation, White and Helfrich (2012) described five different regimes, determined by the Froude number Fr and the ratio of height d_0/h_0, where d_0 is the depth of the gravity current. Figure 1.8 shows a vertical cross-section of the buoyancy field for the five different regimes. Layers red, green and blue correspond respectively to the gravity current, layer 1 and layer 2. The five regimes are :

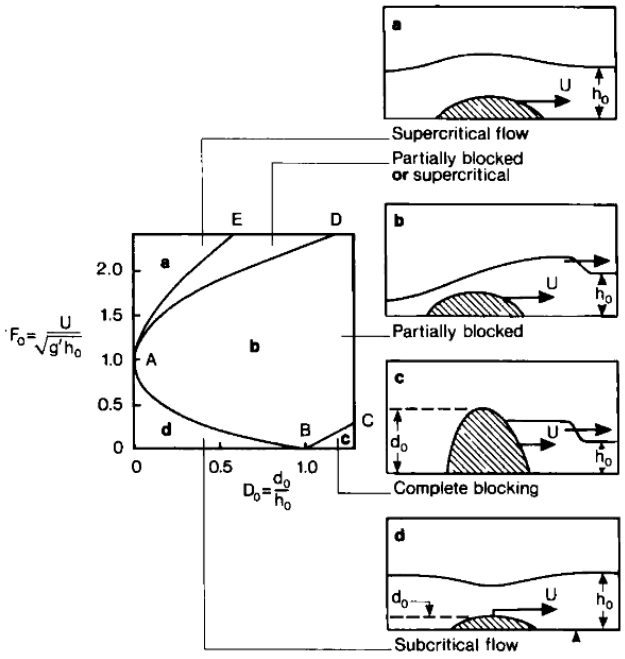

FIGURE 1.6 – Schematic of the different regimes of a two-layer flow over an obstacle, taken from Rottman and Simpson (1989)

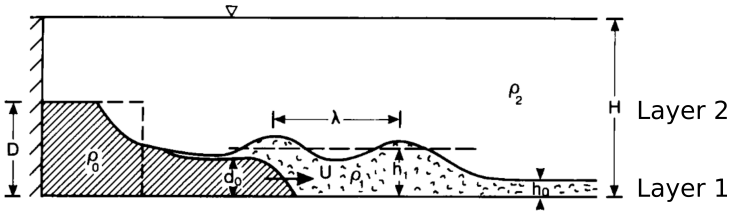

FIGURE 1.7 – Schematic of the lab experiment on a bore generated by a gravity current, realized by Rottman and Simpson (1989)

I - "Subcritical currents" : This regime is similar to the subcritical currents above an obstacle. The flow in layer 1 is accelerated but remains subcritical which results in a small dip at the interface 1-2. Flow remains laminar, there is almost no mixing between layers

II - "Currents that generate upstream undular bores" : The gravity current generate resonant undular bores that move faster than the front. Those waves are continuously generated by the front. They grow in height and increase in speed until they detach from the front.

III - "Currents that generate an upstream monotonic bore connected by a rarefaction" : The bore is travelling upstream faster than the gravity current, but it stays connected to the gravity current.

IV - "Supercritical fronts with a large-amplitude trapped solitary-wave-like disturbance" : A single solitary wave is generated whose amplitude grows

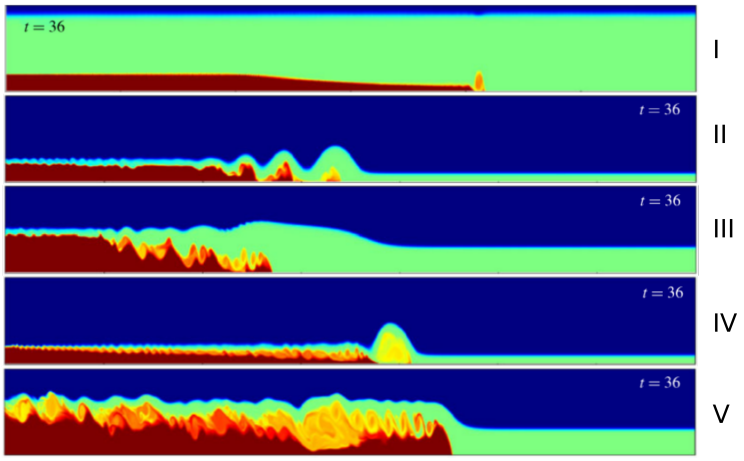

FIGURE 1.8 – Cross section of the buoyancy field from type I (top) to V (bottom) based on 2D simulation results from White and Helfrich (2012). The figure is build from Figures 5 to 9 of their paper.

with time by entraining dense fluid in the recirculation until it reaches its maximal size. After this time it remains constant.

V - "Supercritical gravity currents" : The thickness of each fluid is constant behind the front. Shear instability generates important mixing between the gravity current and fluid 1.

In some specific regimes, the bore features GW (e.g. type II), in which case it is called an *undular bore*.

In the atmosphere, a mesoscale cold front moving into a stable layer can generate a bore (Haghi et al., 2019). The known mechanisms for bore generation include cold pool intrusion (Zhang et al., 2024) and the interaction of a degenerate SBF with the nocturnal SBL or other fronts (Thomsen and Smith, 2006; Huang et al., 2024b; Noonan and Smith, 1986). The presence of an atmospheric bore is often revealed by horizontal bands of clouds such as the famous Morning Glory cloud pattern in Australia (Clarke et al., 1981). Bores can also be observed in vertical scans of radar reflectivity, temperature, and humidity (Johnson and Wang, 2019). The application of hydraulic theory to the observation of an atmospheric bore is not straightforward due to ABL complexity such as the variation with height of thermal stability and wind, and the interactions with other phenomena (Haghi et al., 2019). Thus, studying atmospheric bores remains a challenge.

1.5.4 Streaks and rolls

The neutral sheared boundary layer features several particular structures such as streaks and longitudinal roll vortices, known as rolls (Young et al., 2002). According to Waleffe and Kim (1998), a streaky flow is a flow where the wind speed varies

essentially along to the vertical and transverse direction. On a horizontal plane, streaks correspond to longitudinal bands of higher or lower wind speed than the average. Rolls describe an alternation of contra-rotating vortical structures with their axis oriented in the longitudinal direction. Waleffe and Kim (1998) explain that the streaks and the rolls are closely related : the rolls transport the low wind speed from the surface upward, and transport back high wind speed downward. Thus, updrafts are associated with higher wind speeds, and downdrafts with larger wind speeds. In the atmosphere, streaks are generally constrained to the ASL, where the shear is the largest.

In convective sheared boundary layers, the buoyancy effect also contributes to the formation of rolls, thus referred to as horizontal convective rolls (HCR). Young et al. (2002), in a review, identified 5 different types of rolls : (i) shear-driven turbulence in the neutral ASL, (ii) buoyantly-driven rolls in the sheared convective ASL, (iii) rolls in the mixed layer type A, (iv) rolls in the mixed layer type B, and (v) GW-induced rolls. Types A and B differ by the dependency or not of their aspect ratio on the boundary layer height. However, it is often difficult to determine the type of rolls based on a single observation. According to Drobinski and Foster (2003), HCR differ from the streaks as they span the whole PBL and persist for hours, whereas the streaks are located in the ASL and have a shorter lifetime of the order of several tens of minutes. HCR can also be observed in convective TIBL, such as over land within the SB gravity current (Iwai et al., 2008).

The pure canonical CBL (no shear) exhibits convective cells rather than rolls. As introduced in Section 1.1.5, the presence of cells or rolls is governed by the relative contribution of shear and buoyancy, described either by u^*/w^* or $-Z_{CBL}/L_{MO}$. For clarity, all the criteria are here converted in term of u^*/w^*. Based on LES results, Sykes and Henn (1989) found rolls only for $u^*/w^* > 0.35$, whereas Moeng and Sullivan (1994) found a limit at 0.7. From field measurements, Iwai et al. (2008) observed convective rolls at $u^*/w^* = 0.61$. More recently, Jayaraman and Brasseur (2021) performed LES with u^*/w^* varying from 0.51 to $+\infty$ (sheared neutral ABL) and observed rolls in every simulation. They studied the progressive transition from shear-driven rolls (high values of u^*/w^*) to HCR (moderate values of u^*/w^*), and identified several regimes transitioning at $u^*/w^* = 0.97$ and 0.72. Below 0.72, the state of the CBL evolves toward the canonical moderately convective ABL.

The wavelength of the HCR is defined as the distance between two updraft regions, i.e. the width of two contra-rotating vortices (LeMone, 1973). Their aspect ratio, i.e. the ratio of their wavelength to the boundary layer height, is generally between 2 and 10 according to several observations reported by (Young et al., 2002).

table of content

1.5.5 Gaps in knowledge

The bores and GW interact with turbulence but this interaction is still poorly documented, except in cases involving wave breaking. In particular, Kosović et al. (2025) reminds that their impact on near-surface turbulence remains largely unknown. Moreover, the KHW detected during SB events have been observed just downstream of the SBF, and it remains unclear whether they can also develop farther offshore. Finally, the literature about KHW during LLJ events remains sparse, and further observations are needed to better assess their frequency and characteristics.

1.6 Numerical simulations

1.6.1 Realistic mesoscale simulations

Numerical simulations are a powerful tool for the study of the ABL. Two types of ABL simulation can be distinguished : the idealized and the realistic simulations. The term *idealized simulations* describe simulations featuring simple geometries and idealized input data. They are used to perform sensitivity analysis or to study specific atmospheric flows in controlled conditions. In contrast, *realistic simulations* aim at reproducing the state of the atmosphere at a specific location and date. They can be used as a precious complement to measurements by providing information on many quantities over a large area.

As the atmosphere has no horizontal limits, a correct modeling requires first a *global model*, i.e. a model covering the whole Earth. Global models are generally nudged with observational data. They can be applied for weather forecasts, for future climate projections, or for past reanalyses (e.g. ERA5).

However, the current computing capacities limit the resolution of the global models to horizontal grid sizes (Δ_X) to some tens of kilometers, which is too large to properly resolve mesoscale structures. Thus, mesoscale meteorology studies rely on *limited area models* (LAM), i.e. models covering only a specific region. Such models can use finer grids but need data from larger models to obtain realistic boundary conditions. To resolve small-scale structures in a specific area, several LAM use the nested-domains method, consisting of using successively or simultaneously several simulation domains with increasing resolution and decreasing horizontal extent, where the boundary conditions are forced by the preceding domain.

Several LAMs exist, e.g. the Advanced Regional Prediction System (ARPS) (Xue et al., 2000), Meso-NH (Lafore et al., 1998), or the fifth-generation Penn State/NCAR Mesoscale Model (MM5) (Grell et al., 1994). The most widely used LAM for research application is maybe the Weather Research and Forecasting model (WRF) (Skamarock et al., 2019). This latter model is used in this study (Section 2.3).

table of content

1.6.2 Turbulence modeling and grey zone

ABL flows are characterized by the strong influence of turbulence (Section 1.1.2). The coarse grids of LAMs used at mesoscale do not allow for the resolution of turbulence. Thus, the mixing induced by turbulence is fully modeled using planetary boundary layer (PBL) models, i.e. Reynolds-averaged Navier-Stokes (RANS) models specifically designed for the ABL. These models can be used for horizontal grid sizes larger than about one kilometer. For finer resolution simulations, the large eddies of turbulence are resolved and the effect of subgrid turbulence can be modeled using a LES model. Current LES models assume that the turbulence is resolved down to a scale belonging to the inertial range of the Kolmogorov cascade. In theory, this would limit the use of LES models to small grid size, i.e. lower than about a 100 m in the CBL (Honnert et al., 2020) and about 2 m in the SBL (Beare et al., 2006). Unfortunately, there is a grey zone (or terra incognita) where neither the RANS approach nor the LES approach are entirely suitable (Wyngaard, 2004; Honnert et al., 2020).

Two methods are used in the literature to deal with the grey zone. The first one consists of jumping over it, i.e. downscaling from a RANS-resolution domain to a LES-resolution domain, which requires a factor larger than 10 between the grid sizes of the two domains. With such a large factor, the inflow in the LES domain is very smooth, and turbulence needs considerable space to develop. For that reason, this method requires generation of turbulence in the inflow, e.g. with the cell-perturbation method (Munoz-Esparza et al., 2014). The second method relies on a progressive downscaling with at least one domain in the grey zone. Bauer et al. (2020) and Liu et al. (2020) used RANS and LES models in the grey zone ($\Delta_X = 300$ and 333 m, respectively) and found better results with LES models. This latter method is used in this study (Section 2.3). Some authors recently proposed turbulence models designed for grey-zone resolution, e.g. Juliano et al. (2022), but this is still an active field of research.

Chapitre 2

Method

Introduction

The study focuses on a two-day period, May 17 and May 18, 2020, during which a succession of complex events occurred near the Atlantic coastline. These events were observed with a scanning LiDAR and numerically reproduced with a WRF simulation.
The following sections present the study area (Section 2.1), the LiDAR measurements and analysis method (Section 2.2), the WRF simulation settings, and post-processing methods that are used throughout the thesis (Section 2.4). Finally, in Section 2.5, the succession of phenomena is introduced and the simulation is evaluated through a comparison with the LiDAR measurements and a meteorological dataset.

2.1 Study area

The study focuses on the area around the city of Le Croisic (France), located along the French Atlantic coastline. This area, shown in Figure 2.1, is geographically intricate at different scales.



Figure 2.1 – Map of the study area (source : https ://www.geoportail.gouv.fr/).

At the mesoscale, Le Croisic is located to the south of Brittany, a 100-km wide peninsula, bounded by the Channel sea to the north and the Atlantic to the

southwest.

At the local-scale, Le Croisic is located near the tip of the Guérande peninsula, a 20-km wide peninsula lying between the estuaries of the Loire River to the south and the Vilaine River to the north. The coastline is very complex with an alternance of sand beaches, rocky coasts, and a series of small bays and coves. It also includes several islands, the largest being Belle-Île-en-Mer to the west, and the Gulf of Morbihan to the north. The terrain is quite flat in the Guérande peninsula, as displayed in Figure 2.4c, except for a 50-meter hill oriented northwest-southeast, parallel to the coast close to Le Croisic (Figure 2.4d).

All along the thesis, the dates and hours are given in the coordinated universal time (UTC). At Le Croisic (-2.524 °E), there is a negligible difference of 11 minutes between the UTC and the local solar time.

2.2 Datasets

2.2.1 LiDAR measurements and virtual mast

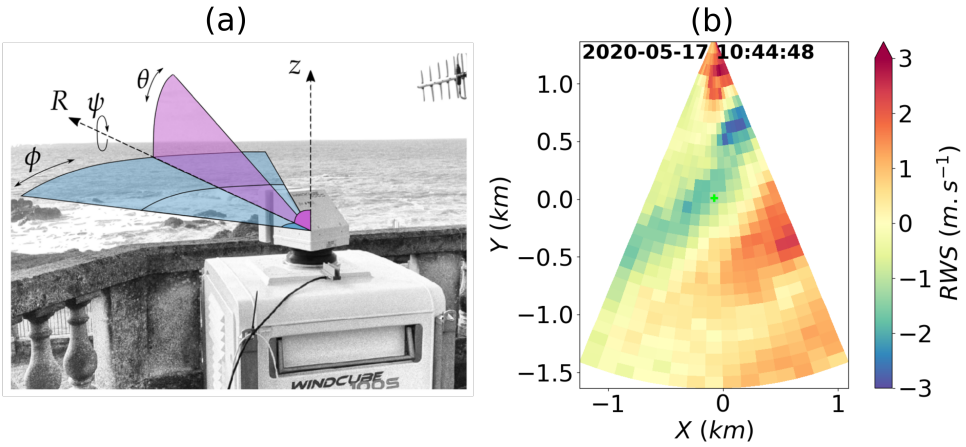

FIGURE 2.2 – (a) Photography of the Scanning LiDAR at Le Croisic taken from Paskin et al. (2022) and (b) example of the distribution of *RWS* on a horizontal PPI scan.

A scanning LiDAR (Vaisala WindCube Scanning LiDAR 100S) was deployed from March to September 2020 near Le Croisic, approximately 100 m from the sea (Figure 2.2a). Its scanning head allows for measuring simultaneously 25 points along its line of sight at given azimuth (ϕ) and elevation angles (θ), with a maximum range of 3 km. The site and the experimental setup are described by Paskin et al. (2022). The LiDAR performed azimuthal scans (known as PPI, Plan Position Indicator) that measure the radial wind speed (RWS) as a function of ϕ at a given θ. The measurement domain covered by the PPI scans is outlined in Figure 2.4d by two

green lines, crossing at the LiDAR position. Raw horizontal PPI scans corresponding to the 21 m horizontal plane and shown in Figure 2.2b, are analyzed in Section 3.2.3. A series of six PPI scans at different elevations θ are used to produce a 10-minute averaged profile of the horizontal wind components (U, V) at 27 heights between 21 and 450 m. It is referred to as the "virtual mast" and is located 1.4 km offshore (Visich and Conan, 2025). In addition to the PPI scans, a fixed vertical scan is taken every 10 minutes to measure the vertical wind speed W. This scan lasts 5 s, and is located onshore at the LiDAR position (not at the virtual mast).

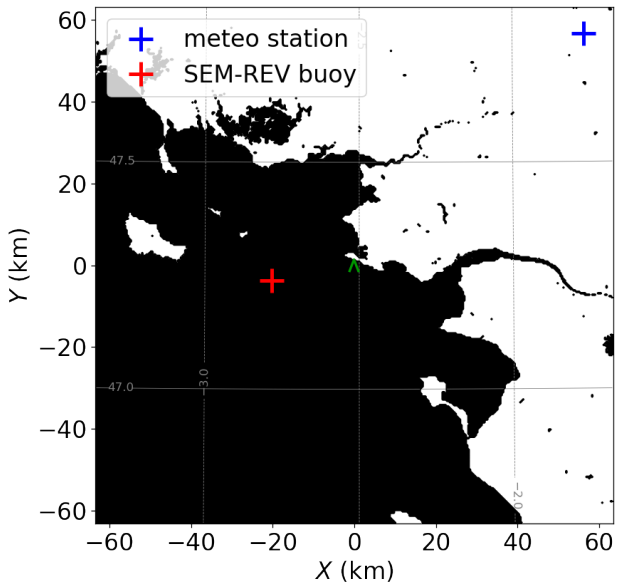

FIGURE 2.3 – Map of the WRF d04 domain with the location of (blue) the meteo mast and (red) the SEM-REV buoy used for comparison in Section 2.5.3.

2.2.2 Temperature measurements

Two temperature datasets are used in Section 2.5.3 to evaluate the thermal forcing in the simulation. The first dataset is based on buoy measurements of the sea-surface temperature (SST) at the SEM-REV experimental site (47.238 °N, -2.786 °E, red "+" in Figure 2.3). The second dataset is based on meteo-station measurements of the air temperature over land at 2 m high at La-Noë-Blanche (47.780 °N, -1.765 °E, blue "+" in Figure 2.3). This station is chosen to be sufficiently far from the coast so that the SB has little influence on the measurements.

2.2.3 AROME dataset

AROME analysis data have been used for a complementary comparison with WRF results and LiDAR measurements. AROME is a limited-area weather predic-

tion model focused on France (Seity et al., 2011), with a horizontal resolution of 0.025° (approximately 2.5 km). AROME data provide hourly saved meteorological variables at 25 fixed heights above surface level. The first 10 heights are 10, 20, 35, 50, 75, 100, 150, 200, 250, and 375 m. Jourdier (2020) found a good agreement between AROME results and field measurements in France.

2.3 Numerical simulations

Realistic mesoscale-to-microscale simulations were performed using the Advanced Research (ARW) configuration of the Weather Research and Forecasting (WRF) model version 5.1 (Skamarock et al., 2019).

2.3.1 WRF model

WRF is a 3D, compressible and non-hydrostatic atmospheric model developed at the National Center for Atmospheric Research (NCAR). Its prognostic variables are the velocity component in Cartesian coordinates (u, v, and w), the moist potential temperature, the perturbation of geopotential, the dry air surface pressure, and the mixing ratios of water vapor, rain, and other species. The prognostic equations are detailed in Appendix A.

WRF uses an Arakawa C staggered grid with the velocity components computed on the cell faces and the scalars computed at the center of the cells. The vertical coordinate system is a terrain-following hybrid sigma-pressure coordinate (Skamarock et al., 2019). It is based on the dry hydrostatic pressure so that the cells height z can evolve with time. Momentum and scalar variables are advected using 5th-order schemes in horizontal direction and 3rd-order schemes in the vertical direction. The time integration is done with a 3rd-order Runge-Kutta scheme. No additional numerical diffusion term is used.

2.3.2 Domains and mesh

The simulation is conducted across six concurrent one-way nested domains (d01 - d06) illustrated in Figure 2.4, with the characteristics detailed in Table 2.1. The horizontal grid size (Δ_X, Δ_Y) is refined from 9.5 km to 39 m with a ratio of 3 for each pair of domains. The three largest domains (d01, d02, and d03) are referred to as RANS domains whereas the three smallest (d04, d05, and d06) are referred to as LES domains. For each domain, the horizontal mesh is composed of $N_X = N_Y = 360$ cells, except for d06 where $N_X = N_Y = 600$ cells.

In RANS domains, the vertical mesh is composed of 52 cells between the surface and the 5000 Pa level with a first cell thickness of $\Delta_Z = 20$ m and a constant

	Domain	**1**	**2**	**3**	**4**	**5**	**6**
Space	(Δ_X, Δ_Y) (m)	9477	3159	1053	351	117	39
	N_X, N_Y	360					600
	N_Z	52			139		
	Δ_{Zmin} (m)	20					
Time	Δ_t (s)	60	20	6.67	2.22	0.74	0.25
	Total duration (j)	4			3		2
Physics	Turbulence	MYJ (RANS)			TKE 1.5 (LES)		
	Surface layer	Eta similarity (MOST)					
	Radiations	RRTMG					
	Microphysics	WSM6					
	Land surface model	Noah LSM					
	Cumulus scheme	Kain-Fritsch	None				

TABLE 2.1 – Characteristics of the simulation domains

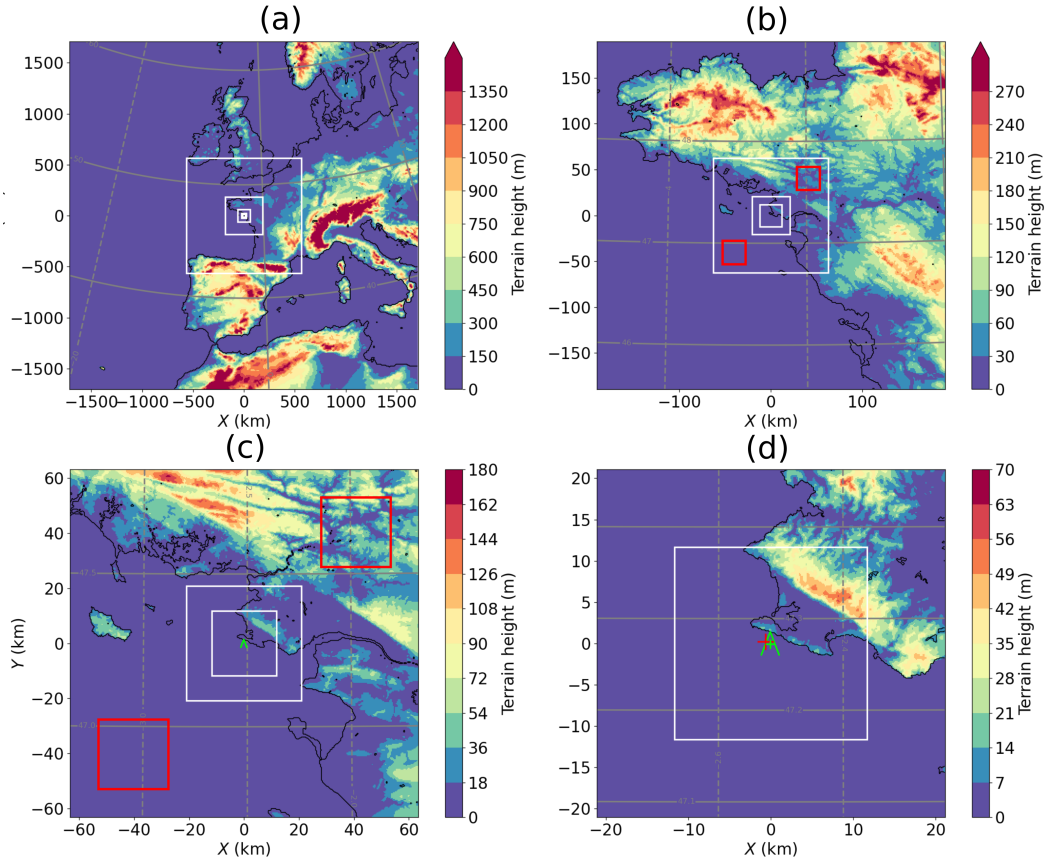

FIGURE 2.4 – Terrain map of (a) d01, (b) d03, (c) d04, and (d) d05. White rectangles are inner domains. Red squares are used in Figure 2.9. In d05, green lines outline the LiDAR measurements area. Green and red "+" indicate the virtual mast location and the closest AROME grid cell, respectively.

table of content

grid stretching with a ratio of 1.1 until a grid size of 1 km is reached. A vertical grid refinement between domains d03 and d04 is applied to increase the vertical resolution in LES domains in which a constant grid size of 20 m is chosen up to 1 km and a grid stretching with a ratio of 1.05 is applied above. The vertical mesh is represented in Figure 2.5a for RANS domains and in Figure 2.5b for LES domains, by showing the average cells thickness and height (Z).

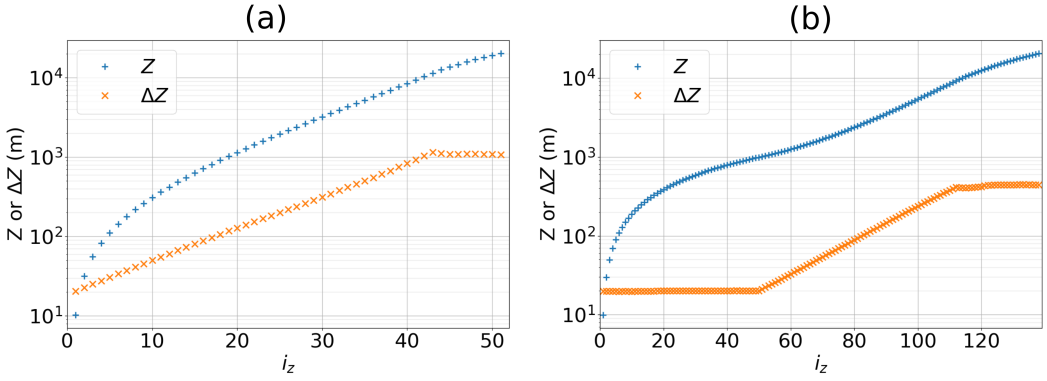

FIGURE 2.5 – Vertical mesh in (a) RANS and (b) LES domains. Blue "+" markers correspond to the height of the middle of the cell and orange "x" markers show the thickness of the cell over the sea (terrain height = 0 m).

The Lambert-conformal conic map projection is used in this study. According to the ArcGIS website, it is suited for mid-latitude areas without a too large north-south extent. Three values are needed to describe a projection : the standard longitude, the true latitude 1, and the true latitude 2. The standard longitude used in this study is -2.516 °E. The two latitude values should correspond to about one sixth of the domain from the top and from the bottom. The chosen values are 44.273 °N and 50.273 °N, which correspond to the one sixth proportion for domain d02. The projection is centered on the LiDAR virtual mast position (47.273°N, -2.516°E). The coordinates X and Y used throughout this study, are the west-east and south-north coordinates, respectively, in this projection with the origin at the virtual mast location (Figure 2.4).

2.3.3 Boundary conditions

The lateral boundary conditions of domain d01 are forced with hourly reanalysis data from the ECMWF ERA5 product interpolated on 37 pressure levels with a spatial resolution of 31 km (Hersbach et al., 2023). According to Sheridan et al. (2021), who performed a comparison between reanalysis data and LiDAR measurements in the coastal and marine ABL in the USA, ERA5 has a better correlation with measurements than the NARR (North American Regional Reanalysis) product. They showed however that ERA5 tends to underestimate the wind speed at hub height (90 m) during SB events.

table of content

The bottom boundary conditions are managed by the surface layer scheme and will be further detailed in Section 2.3.5.3. A 5-km Rayleigh damping layer is applied at the top of the domain to avoid the reflection of gravity waves.

2.3.4 Spin-up time

Because the soil characteristics (e.g. thermal conduction, heat capacity) in ERA5 do not match those in WRF at a given location, a spin-up period is required for the soil temperature and moisture to adjust to the WRF characteristics. The length of this period depends on the quantity and on the soil layer depth : close to the surface, a variable adjusts within a few days, whereas deeper in the soil, it can take several years to properly adjust (Cosgrove et al., 2003). In this 2-day study, a spin-up period of 2 days is chosen for the RANS domains (starting on May 15 0800 UTC), allowing for the adjustment of the near-surface layers. As suggested by Angevine et al. (2014), the deep soil layers are weakly coupled with the surface and it is expected that they do not significantly influence the results within a couple of days.

In domains d04, d05 (starting on May 16, 0800 UTC), and especially d06 (starting on May 17, 0800 UTC), the spin-up period is shortened to save computational time. A shortened spin-up time is acceptable for atmospheric quantities, because they are initialized with their parent-domain results, and because the horizontal extent of these domains is reduced. However, in the current version of WRF, the soil quantities cannot be initialized from the parent domains but are instead initialized with the input meteorological dataset (here ERA5). As a spin-up of only a few hours in domain d06 is not very satisfying for adjusting soil quantities under these conditions, a method has been implemented to initialize all the soil and surface quantities of a nested domain from its parent domain. This method uses functions available in the WRF Preprocessing System (WPS), which are now directly used in the code. Thanks to this implementation, small domains benefit from the spin-up of their parent domain.

2.3.5 Physics schemes

WRF takes into account several physical processes through different categories of schemes : e.g. turbulence, microphysics, radiation, land surface, cumulus. Theses schemes are not fully separated but have crossed impacts on each other, as represented in Figure 2.6.

2.3.5.1 Turbulence

In the three largest domains the horizontal grid size is larger than 1 km. At these scales, planetary boundary layer (PBL) models are considered as valid. Many authors studied the sensitivity of the simulation results to the several PBL models that are available in WRF. Shin and Hong (2011) compared the temperature,

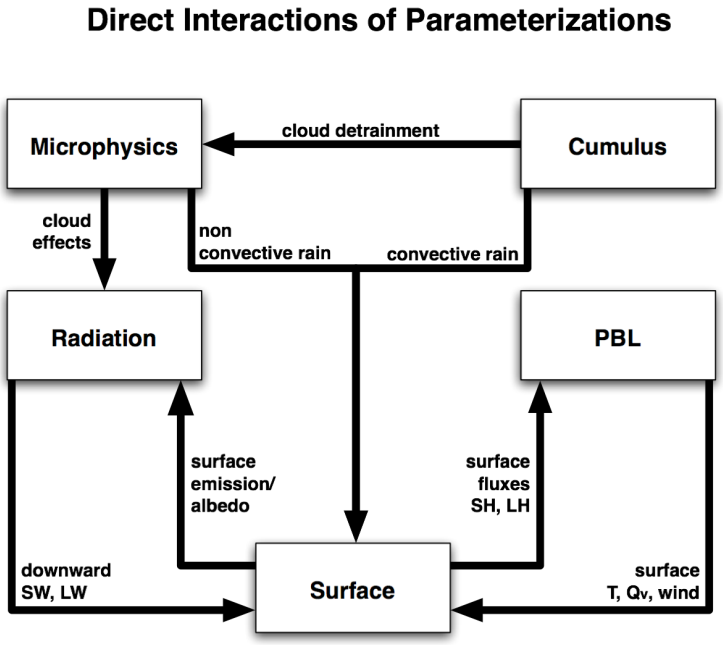

FIGURE 2.6 – Schematic of the interactions between physics schemes (Skamarock et al., 2019) where SH, LH, SW, LW, T, and Q_v stand for sensible heat, latent heat, shortwave, longwave, the temperature and humidity, respectively.

humidity and wind profiles obtained for a stable and a convective case using 5 PBL models. They observed that non-local schemes offer more realistic profiles under unstable conditions. However, under stable conditions, TKE closure schemes perform better than first-order-closure schemes. Nunalee and Basu (2014) compared 6 commonly used PBL schemes for a coastal LLJ event case and concluded that the model solutions are strongly sensitive to the choice of the PBL scheme and that the estimation of a wind turbine annual energy production (AEP) can vary by a factor of two. Mirocha et al. (2016) tested 54 model configurations to assess the sensitivity to the PBL model, the horizontal and vertical grid sizes and the land surface model. In the case of a LLJ in the Great Plains, they concluded that although some configurations perform better at some times, none performs better in overall. For the present study, the Mellor-Yamada-Janjic (MYJ) TKE-closure scheme is used (Janjić, 1994) as it was one of the most accurate in modeling a coastal LLJ profile in the study of Nunalee and Basu (2014).

To reach a LES resolution, a *progressive downscaling* method is used so that, depending on the stability conditions, one or several domains are in the grey zone where only the very large scales of turbulence are resolved (Section 1.6.2). Bauer et al. (2020) found that using a LES model performed better than using a PBL model at a resolution of 300 m for a simulation of the CBL. Udina et al. (2020) also chose to apply LES closure at resolutions of 333 m. Following these studies, the TKE1.5

subgrid-scale model is used in domains d04 to d06 (Deardorff, 1980). Therefore, these three domains are referred to as LES domains. Several recent studies obtained interesting results with similar configurations (Liu et al., 2020; Bauer et al., 2023).

In the 6 domains, the turbulent mixing terms are evaluated in physical space (diff_opt = 2), and vertical diffusion acts on full fields (mix_full_fields = .true.), as in the simulation of Bauer et al. (2023).

2.3.5.2 Microphysics

Water cycle is a very impacting feature of atmospheric flows in many aspects : the evapotranspiration process modifies the Bowen ratio between sensible and latent heat fluxes and strongly influence the air temperature near the surface ; cloud acts on the radiation fluxes ; snow coverage generally increases the albedo of the surface ; phase transition of water implies an absorption or a release of energy which modifies the temperature of the medium. Since the scale of the water vapor physics is far below the grid size, these processes are modeled with a microphysics scheme in which the prognostic variables are the mixing ratios of the different states of water.

The WSM6 (WRF Single-Moment 6-class) scheme is chosen for this study. It models rain, vapor, cloud water, cloud ice, snow and graupel mixing ratios. Skamarock et al. (2019) mention a better performance of WSM6 than other WSM models for cloud-resolving grids. Thus it seems to be the most adapted for a WRF-LES simulation. This scheme has been used in several previous studies (Segura et al., 2021) and gave better results in the bore simulation of Johnson et al. (2018) than other microphysics model.

2.3.5.3 Atmospheric surface layer and land surface model

The ASL is characterized by strong vertical gradients of atmospheric variables and it would therefore require a very high resolution to resolve properly the near-surface flow. A common approach is to model the near-surface exchanges. The model used in this study is based on the MOST (Section 1.1.2).

The land-surface model (LSM) simulates the exchanges of heat, moisture, and momentum between the soil layers and the ASL. Among the WRF available schemes, the Noah LSM is the most widely used (Talbot et al., 2012; Giannakopoulou and Nhili, 2014; Aird et al., 2021; Dy and Fung, 2016; Liu et al., 2020). It uses 4 soil layers for moisture and temperature and simulates evapotranspiration, drainage, runoff, root zone.
LSM schemes need several datasets describing soil and surface characteristics. The datasets used in this study are described in Table 2.2. The highest resolution

available in WPS datasets is 30 arc-second (approximately 900 m), which is finer than the RANS grids but coarser than the LES ones. Liu et al. (2020) noticed a stronger sensitivity of LES results to the topography dataset resolution than to the choice of the PBL or subgrid-scale model for a complex topography in near-neutral atmospheric conditions (Chinese mountains). Although the present case deals with a smoother topography, the 25 m European Digital Elevation Model (EU-DEM) v1.1 (European Environment Agency, 2016) is used for the LES domains. A finer land-use dataset is also necessary, especially to refine the coastline description. The 2018 Corine Land Cover (CLC) product (European Environment Agency, 2019) at the resolution of 100 m is used in all domains. It is composed of 44 classes that are converted to the 21 MODIS land-use classes following Vogel et al. (2022). CLC is applied to all domains in France, and the MODIS dataset is used to supplement land-use data outside of France for the RANS domains. Both the EU-DEM and CLC datasets are reprojected to the WRF Preprocessing System (WPS) coordinate system (EPSG :4326) and converted to WPS binary format using QGIS version 3.26 with the GIS4WRF plug-in. To improve the accuracy of the surface boundary conditions, the Leaf Area Index (LAI) and Fraction of Vegetation Coverage (FCOVER) from the PROBA-V GEOV3 product (European Union's Copernicus Land Monitoring Service information, 2017b,a), available at a resolution of 333 m every 10 days, are preferred over the standard monthly MODIS datasets. The data from May 20, 2020, are reprojected onto the simulation grids using a Python script with a nearest-neighbor algorithm and incorporated into the input files for each domain.

	RANS		**LES**	
elevation	GMTED2010	900 m	EU-DEM	**25 m**
soil	10-category soil type	900 m	same	900 m
land cover	CLC + MODIS	**100 m**+900 m	CLC	**100 m**
FCOVER	PROBA-V FCOVER	**333 m**	same	**333 m**
LAI	PROBA-V LAI	**333 m**	same	**333 m**
SST	ERA5	31 km	same	31 km

TABLE 2.2 – LSM datasets used in RANS and LES domains, and their resolution

Over the sea, a Charnock's model is used to account for the modification of the sea-surface roughness under the action of wind (Charnock, 1955). The sea-surface temperature (SST) is forced with ERA5 data interpolated to WRF grids. The SST field in ERA5 varies only once per day at 2200 UTC (as shown in Figure 2.9). Moreover, due to the coarse resolution of ERA5 (31 km), the small-scale heterogeneities of the sea-surface temperature, e.g. near river deltas, are not represented.

table of content

2.3.5.4 Radiation

The radiation schemes simulate the downward and upward energy fluxes between space, atmosphere and Earth surface including emission, absorption and reflection processes. Radiation physics is divided into two categories : longwave and shortwave radiations. Shortwave radiation is the direct visible and ultraviolet light from the sun while longwave radiation corresponds to the infrared radiation emitted by the Earth surface and by the atmosphere. Radiation processes are highly influenced by microphysics, greenhouse gases, and surface characteristics (e.g. temperature, albedo). In the present study, the RRTMG (Radiative Transfer Model for GCMs, Iacono et al. (2008)) is used for both longwaves and shortwaves radiation. This is a widely-used scheme (Liu et al., 2020; Xia et al., 2022; Talbot et al., 2012).

2.3.5.5 Orography wave drag

A gravity-wave drag model is applied only in the largest domain to account for the drag induced by the orographic gravity waves (Choi and Hong, 2015). This model utilizes a separate orography dataset that is provided at a resolution of 10 arc-minute in WPS.

2.4 Post-processing

2.4.1 Statistics in LES

In a LES, the largest scales of turbulence are resolved. The classical approach to analyze LES results is based on the Reynolds decomposition of any instantaneous variable (e.g. u) as the sum of a time-averaged component ($\overline{u}$, denoted U) and a fluctuating component (u'). Computing time averages of the turbulent quantities in post processing in the whole domain is technically impossible because it would require an extremely large storage capacity. Thus, an online averaging method was implemented, based on the WRFlux project of Göbel (2024), to calculate the 10-minute averages of the wind components (U, V, W), the virtual potential temperature (θ_v), the water vapor mixing ratio, the height (Z), and products of variables (e.g. $\overline{uv}$). These calculations are performed at the center of each grid cell where the velocity components are interpolated. Unless otherwise specified, the simulated quantities presented in this thesis are 10-minute averaged.

Variances and covariances of the velocity components are computed in post-processing (only in LES domains), for example as $\overline{u'v'} = \overline{uv} - \overline{u}.\overline{v}$. The resolved TKE ($k_{calc}$) is computed as

$$k_{calc} = \frac{1}{2}(\overline{u'^2} + \overline{v'^2} + \overline{w'^2}) \tag{2.1}$$

table of content

and the total simulated TKE is

$$k_{tot} = k_{calc} + k_{sgs} \tag{2.2}$$

where k_{sgs} is the 10-minute averaged subgrid TKE. The resolved TKE calculated with Equation 2.1 may include the variance induced by the motion of various sub-mesoscale structures, especially in stable conditions, which do not exactly correspond to the definition of turbulence (Durden et al., 2013; Ren et al., 2025). However, the terms "resolved TKE" and "total TKE" are used to describe k_{calc} and k_{tot}, respectively, as it is usually done in LES studies.

2.4.2 TKE budget

An analysis of the TKE budget is performed at different stages of this thesis. The most common approach to compute the TKE budget in the ABL follows the Boussinesq approximation (Rai et al., 2017; Rohanizadegan et al., 2025). In this approach, the term of the momentum equation containing the density and the pressure gradient is decoupled into a pressure perturbation and a buoyancy terms as

$$-\frac{1}{\rho}\partial_{x_i}(p) - g = -\frac{1}{\rho_0}\partial_{x_i}(p_1) + \frac{g}{\theta_v}(\theta_v - \theta_{v0})\delta_{i3} \tag{2.3}$$

where ρ_0 and θ_{v0} are the base state density and temperature depending only on z, and p_1 is the difference between the pressure p and the base state pressure p_0. The variations of density are here transformed into variations of the temperature θ_v. The k_{calc} budget in the Boussinesq approximation can be written as

$$\partial_{t_c}(k_{calc}) = \underbrace{-U_j\partial_{x_j}(k_{calc})}_{A}\underbrace{-\overline{u_i'u_j'}\partial_{x_j}(U_i)}_{P}\underbrace{-\partial_{x_j}\overline{u_j'k_{calc}'}}_{T_T}\underbrace{-\frac{1}{\overline{\rho}}\partial_{x_j}\overline{u_j'p'}}_{T_{Pb}}\underbrace{+\frac{g}{\theta_v}\overline{w'\theta_v'}\delta_{i3}}_{B} - \varepsilon_b \tag{2.4}$$

where A is the advection by the mean flow, P the shear production, T_T the turbulent transport, T_{Pb} the Boussinesq pressure transport, B the buoyancy production, and ε_b the dissipation computed as a residual. Without the Boussinesq approximation, the "exact" TKE budget is

$$\partial_{t_c}(k_{calc}) = \underbrace{-U_j\partial_{x_j}(k_{calc})}_{A}\underbrace{-\overline{u_i'u_j'}\partial_{x_j}(U_i)}_{P}\underbrace{-\partial_{x_j}\overline{u_j'k_{calc}'}}_{T_T}\underbrace{-\overline{a_i'u_i'}}_{PB} - \varepsilon \tag{2.5}$$

where $a_i = \frac{1}{\rho}\partial_{x_i}(p)$. In this budget, the fluctuations of pressure and density are coupled in the pressure-buoyancy term PB. In this work, the TKE budget is computed as

$$\partial_{t_c}(k_{calc}) = A + P + T_T + \underbrace{(PB - B)}_{T_P} + B\underbrace{-D - E}_{-\varepsilon} \tag{2.6}$$

table of content

where the pressure transport T_P is calculated as the difference between PB and B, and the dissipation ε is decomposed into an explicit dissipation from the subgrid-scale model (D) and a numerical dissipation (E) calculated as a residual. More details about this budget can be found in Appendix B.

A first motivation for computing the exact pressure term is based on Rai et al. (2017) who explained that for their case, the pressure and the density were too much coupled so that the Boussinesq approximation was invalid. Another motivation is related to the WRF vertical coordinate that is based on the dry-hydrostatic pressure, so that z fluctuates over time (see Appendix A). In both budgets, it is supposed that the fluctuations of z do not affect the variances and covariances computation. However the vertical pressure gradient is very large in the atmosphere so that a fluctuation of z could result in a pressure fluctuation noticeably stronger than the pressure fluctuation at a constant height. A comparison between the Boussinesq TKE budget (Equation 2.4) and the budget of Equation 2.6 (referred to as the WRF TKE budget) is given in Section 2.5.4.

2.4.3 Horizontal filter

The present study deals with both unsteady and inhomogeneous phenomena occuring at different scales. To analyze various processes, a horizontal Gaussian filter is sometimes applied on the simulation results (e.g. in Section 5.3). This filtering is used either to filter out small-scale perturbations in order to highlight the large-scale variations or to help the 10-minute averages to converge toward ensemble averages, as hypothesized in the TKE budget equation. The Gaussian filter is applied using the Scipy *gaussian_filter* function. This method requires a scale parameter s corresponding to the standard deviation of the filter function f_f

$$f_f(x) = \frac{1}{s\sqrt{2\pi}} e^{-x^2/(2s^2)}. \tag{2.7}$$

Thus, a "1-km Gaussian filter" refers to a Gaussian filter with $s = 1$ km. Filtered variables are denoted by $\widetilde{\cdot}$. The horizontal gradient (e.g. the land-sea mask in Section 3.1.2) can be computed at the same time as the filtering using the argument *order = 1* of the *gaussian_filter* function.

A filtered quantity at a given location is a kind of spatial averaging of the original field around this location. Thus, near the domain boundaries the filtering is not reliable. The width of the non-reliable boundary area is proportional to s so that using a too large value of s compared to the domain width would give a wrong result within the whole domain. In addition, s can not be lower than the grid size. It will be shown in Section 3.1.2 that satisfying results are obtained when (i) $s > 4\Delta_X$ and (ii) s is lower than 3 times the distance to the nearest domain boundary.

table of content

2.4.4 Trajectories

At different stages of this study, trajectories are computed to analyze the time evolution of air parcels in the Lagrangian framework (e.g. in Section 3.2.5). These trajectories are computed using the Python library from Gowan (2019), modified to compute both forward and backward trajectories in the WRF coordinate system. The trajectories are computed using a 1st-order Euler method, with a time step smaller than the WRF output time step (10 minutes) assuming a linear variation of the wind field between two time steps. This method contains inevitably small errors but the trajectories aims at following the global path of a mesoscale air parcel rather than the turbulent motions of a small-scale air parcel. For that, the wind field is horizontally filtered before computing the trajectory (Section 2.4.3). The combination of the horizontal filtering with the small time step of the computation helps stabilizing the trajectories, reducing the dependency on the initial location and time.

2.5 Model assessment

In this section the simulation results are evaluated. First, a description of the synoptic conditions and the thermal forcing as well as a description of the LiDAR data are given, providing a knowledge of the phenomena occurring during May 17 and May 18. This helps the analysis of the mean quantities differences between the simulation, the measurements and AROME data, given in Section 2.5.3. Finally, in Section 2.5.4, the TKE budget computation is evaluated within the CBL.

2.5.1 Synoptic conditions and thermal forcing

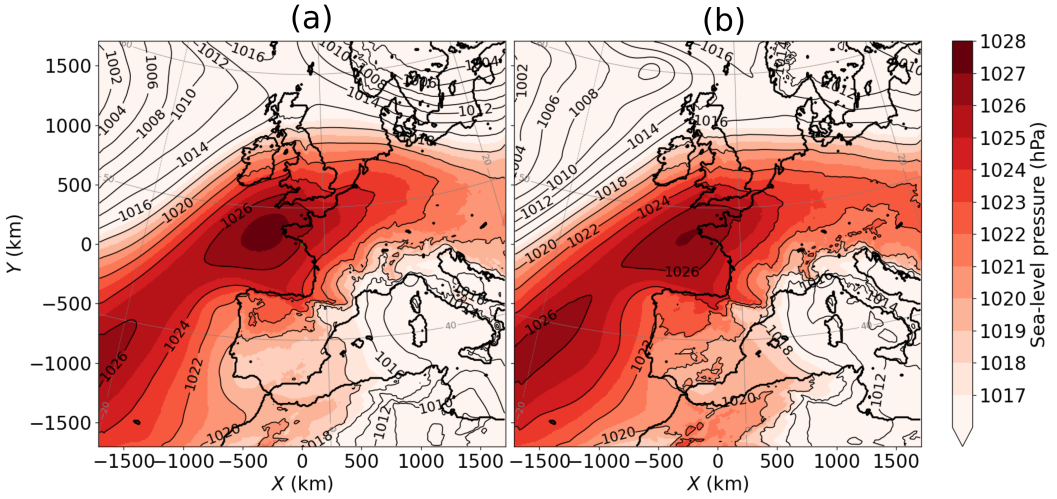

FIGURE 2.7 – Sea-level pressure averaged over 24 h on (a) May 17 and (b) May 18, based on WRF d01 results

table of content

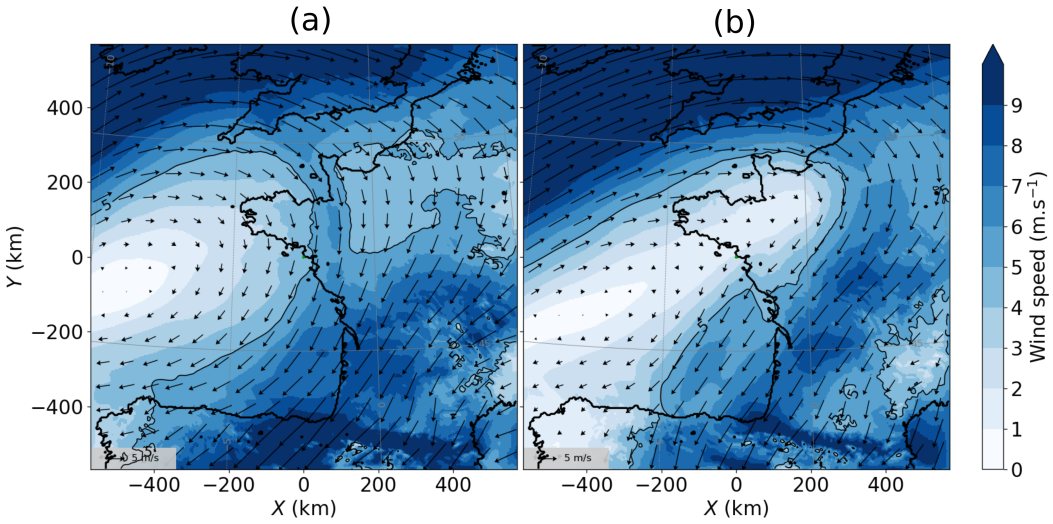

FIGURE 2.8 – Wind speed at 2000 m above sea level averaged over 24 h on (a) May 17 and (b) May 18, based on WRF d02 results

During the period between May 17 and May 18, the meteorological situation is mainly governed by a synoptic high-pressure system centered a few hundred kilometers to the west of Brittany. As depicted in Figure 2.7, which displays the 1-day average sea-level pressure on May 17 (Figure 2.7a) and May 18 (Figure 2.7b), this high-pressure region is slightly stretched in the SW-NE direction, especially on May 18. This high-pressure system results in an anticyclonic synoptic wind, as depicted in Figure 2.8 where the 2000 m wind field rotates clockwise around the high pressure. At Le Croisic (0, 0), the synoptic wind is quite weak and from north-northeast : 5 m.s^{-1} from the north on May 17 (Figure 2.8a), and 2 m.s^{-1} from the north-east on May 18 (Figure 2.8b).

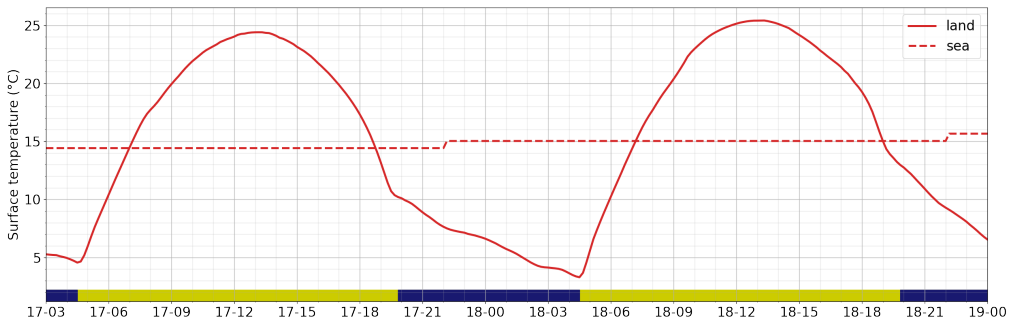

FIGURE 2.9 – Evolution of the temperature of the sea surface and the land surface, based on d04 results averaged over the red-square areas in Figure 2.1c. The yellow and dark blue colors, at the bottom of this figure and following figures, indicate the daytime and nighttime, respectively.

The evolution of the land-surface and sea-surface temperatures is displayed in Figure 2.9. The sea surface temperature, forced with ERA5, is considered constant during a day, whereas the land surface temperature varies between 5 and 25 °C.

table of content

The land-sea temperature difference becomes positive at 0700 UTC, rises up to 10 °C around 1200 UTC, becomes negative at 1900 UTC and reaches a minimum of -10 °C just before the sunrise (0500 UTC).

Overall, during the studied period, there is a light corkscrew synoptic wind, and a land-sea temperature difference of 10 °C, which are two external conditions highly favorable for the development of a SB (Section 1.3).

2.5.2 Wind evolution in LiDAR measurements

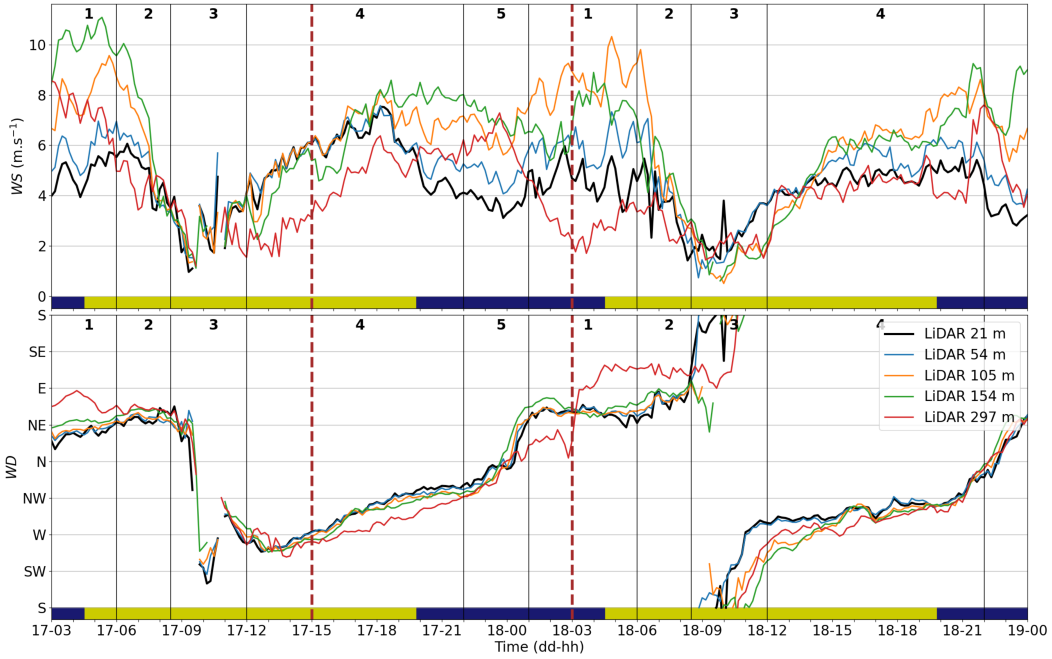

FIGURE 2.10 – Evolution of (top) *WS* and (bottom) *WD* in the LiDAR data at 21, 54, 105, 154, and 297 m high. The brown dashed vertical lines indicate 1500 UTC on May 17 and 0300 UTC on May 18, the dates of the profiles shown in Figure 2.12.

Before comparing with the simulation results, the evolution of the wind speed (*WS*) and the wind direction (*WD*) at 5 heights according to the LiDAR measurements, displayed in Figure 2.10, is analyzed. Discontinuities in the curves are found when the reconstruction of U and V is not valid (Section 2.2.1). The evolution shows a similar pattern between the two studied days, which can be divided into 5 phases with the following characteristics :

Phase 1, 0100-0600 UTC : At night, *WD* is persistently from northeast at every height except for $Z = 257$ m where it is from east. *WS* oscillates around a value constant in time but varying in height. The maximal *WS* is found at 154 m high on May 17, and at 105 m high on May 18, while at 297 m, *WS* is significantly

lower.

Phase 2, 0600-0830 UTC : In the early morning, *WD* remains as in Phase 1, but *WS* decreases rapidly and homogenizes with height.

Phase 3, 0830-1200 UTC : In the late morning, *WS* reaches a minimum of about 2 $m.s^{-1}$ while *WD* rotates from northeast to west. On May 17, this rotation takes place two stages : first a counter-clockwise shift to southwest at 0930 UTC, then a clockwise shift to west-northwest at 1030 UTC. There are missing data during each shift (discontinuities in the lines), indicating that the wind vector reconstruction is discarded due to the failure to meet the horizontal homogeneity assumption. On May 18, *WD* rotates continuously clockwise, with a delay between the lowest and the highest levels.

Phase 4, 1200-2200 UTC : During the afternoon, *WD* turns slowly clockwise, while *WS* increases until 1800 UTC and remains roughly constant afterward. Again, the maximal *WS* is found at 154 m high on May 17 and 105 m high on May 18.

Phase 5, 2200-0100 UTC : Around 0000 UTC, a rapid *WD* shift from northwest to northeast is observed on both days while *WS* remains constant over time. At 297 m high, this shift appears later at 0300 UTC, suggesting a decoupling between the lower and upper layers.

Phases 2, 3, and 4 are consistent with a sea-breeze event. In the morning, the land wind speed decreases during Phase 2, and then shifts to a sea breeze in Phase 3 while the synoptic wind direction remains north-northeast throughout the period (Figure 2.8). At this moment, the land surface is more than 5 °C warmer than the sea surface (Figure 2.9), which is sufficient for the SB to install (Grau et al., 2021). Then, *WS* increases and *WD* gradually veers during Phase 4 (under the Coriolis force). During Phase 1, the flow is referred to as a LLJ because *WS* at 297 m high is significantly lower than below (later confirmed in Figure 2.12e, 2.12f).

2.5.3 Evaluation of the mean quantities

Wind fields of WRF results are compared to LiDAR measurements and AROME analysis data (Section 2.2). For all domains (AROME and WRF), the grid point the closest to the virtual mast is selected for the comparison (Figure 2.4d for AROME), and the U and V components are linearly interpolated to the measurement heights of the virtual mast. Finally, *WS* and *WD* are calculated from the interpolated data.

Figure 2.11 shows the time evolution of *WS* and *WD* at 21 m above mean sea level, obtained from five WRF domains (d01 to d05), LiDAR data, and AROME data on May 17 and 18. Results of domain d06 are not shown as they are very close to that of domain d05. Overall, there is a good agreement between the different datasets with

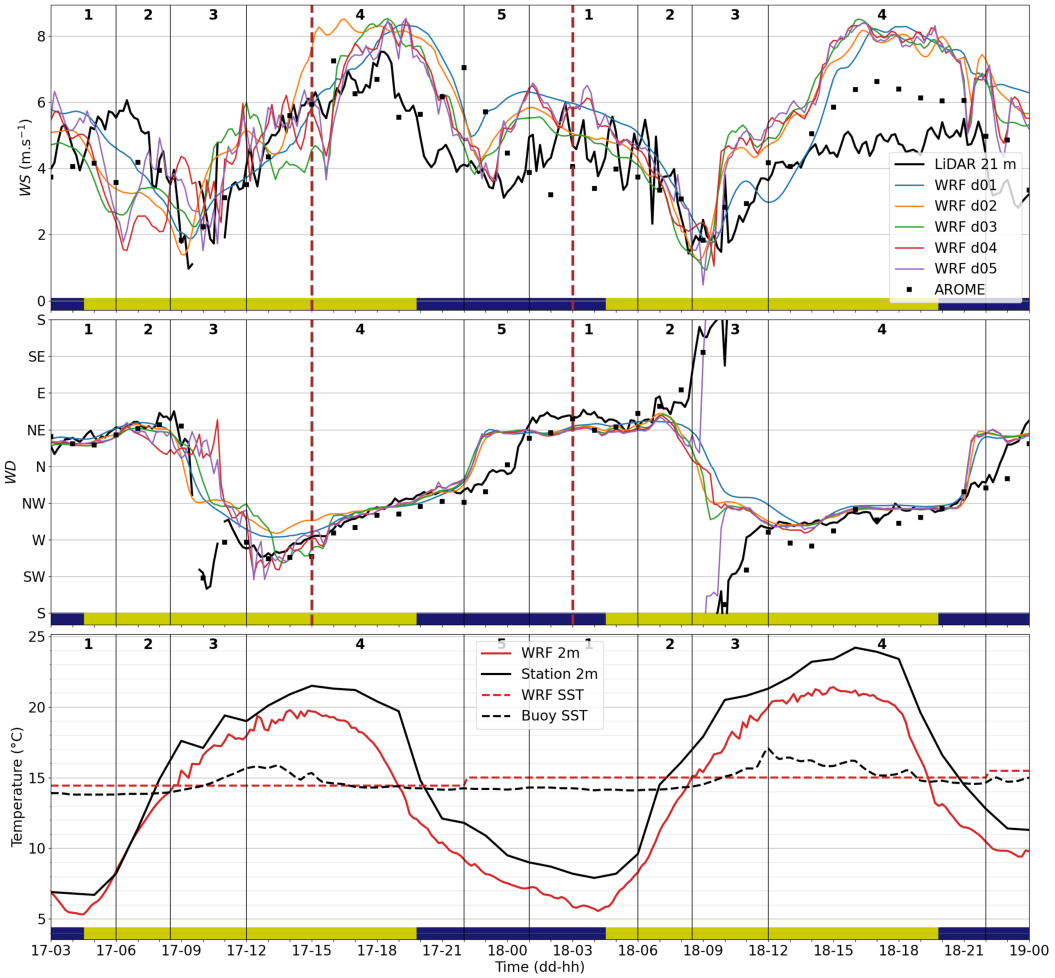

FIGURE 2.11 – (top, middle) Same as Figure 2.10, comparing the different datasets at 21 m high. (bottom) Evolution of the sea-surface temperature and the air temperature at 2 m high at the two points shown in Figure 2.3, based on WRF d04 results, buoy (sea) and meteo mast (land) measurements.

a nearly identical daily cycle following the same 5 phases as described in Section 2.5.2.

Phase 1 : During late night, *WD* is well represented by AROME and WRF despite a slight difference of 20° on May 18. *WS* in WRF is slightly larger than in the measurements and shows fewer oscillations. AROME tends to underestimate *WS* by about 1 $m.s^{-1}$.

Phase 2 : In the early morning, the decrease in *WS* on May 17 occurs 3 hours earlier in the WRF results compared to LiDAR measurements, whereas the speed is very similar between all datasets on May 18.

Phase 3 : This phase shows the largest differences between the two days and

between the 7 datasets, notably between the different WRF domains.
On May 17, AROME reproduces well the two *WD* shifts. In WRF domains d01 and d02, *WD* shifts only once to northwest around 0930 UTC whereas in d03 to d05, two distinct shifts occur respectively around 1030 and 1200 UTC, e.g. later than in the LiDAR measurements. The behavior depends on the grid size, suggesting that the phenomenon is influenced by local-scale features. The wind field during this phase will be analyzed more deeply in Section 3.2.
On May 18, the LES and AROME results reproduce well the clockwise rotation. In RANS domains, the wind rotation is counter-clockwise but *WS* is very low (less than 2 $m.s^{-1}$) so that the wind direction at this time is less significant.
Noticeably stronger *WS* oscillations are observed on May 17 than on May 18 in LiDAR measurements and in LES results as well.

Phase 4 : During the afternoon, *WD* in WRF results is very close to the LiDAR while a small difference is found in AROME. On May 18, there is a strong *WS* overestimation of 3 $m.s^{-1}$ in WRF results, which is less pronounced in AROME. During both days, a sudden increase in *WS* around 1530 UTC is observed in the WRF and AROME results.

Phase 5 : Finally, the *WD* shift in Phase 5 occurs 2 hours sooner in WRF results than in AROME and the LiDAR observations.

The 2 m temperature and the sea-surface temperature in domain d04 are compared with the measurements of the meteorological station and the SEM-REV buoy (Section 2.2.2), respectively (Figure 2.11 bottom). The buoy measurements reveal that the SST has a little diurnal cycle with slightly higher temperature during the daytime than during the nighttime. Despite the constant SST used in WRF, the difference between WRF forcing and the buoy measurements is mainly below 1 °C. The air temperature at 2 m over land exhibits a persistent difference of 2 °C between the simulation results and the measurements. The difference between the air temperature above the land (at 2 m high) and the sea surface temperature becomes positive later in the simulation than in the measurements, which can explain that the SB onset (shifts in *WD*) occurs later in the simulation. In the afternoon, this temperature becomes negative sooner in the simulation than in the measurements, which can explain the sooner *WD* shift in the simulation during Phase 5.

To evaluate the simulation results up to 1 km high, the *WS*, *WD*, and θ_v profiles are presented in Figure 2.12 at 1500 UTC on May 17, which corresponds to Phase 4 when the sea breeze is fully established, and at 0300 UTC on May 18, during the LLJ of Phase 1.

At 1500 UTC on May 17, the *WD* profiles in Figure 2.12b correspond to those of a sea breeze with two layers where the wind comes from almost opposite directions. As the coastline near the LiDAR is approximately oriented from northwest to southeast,

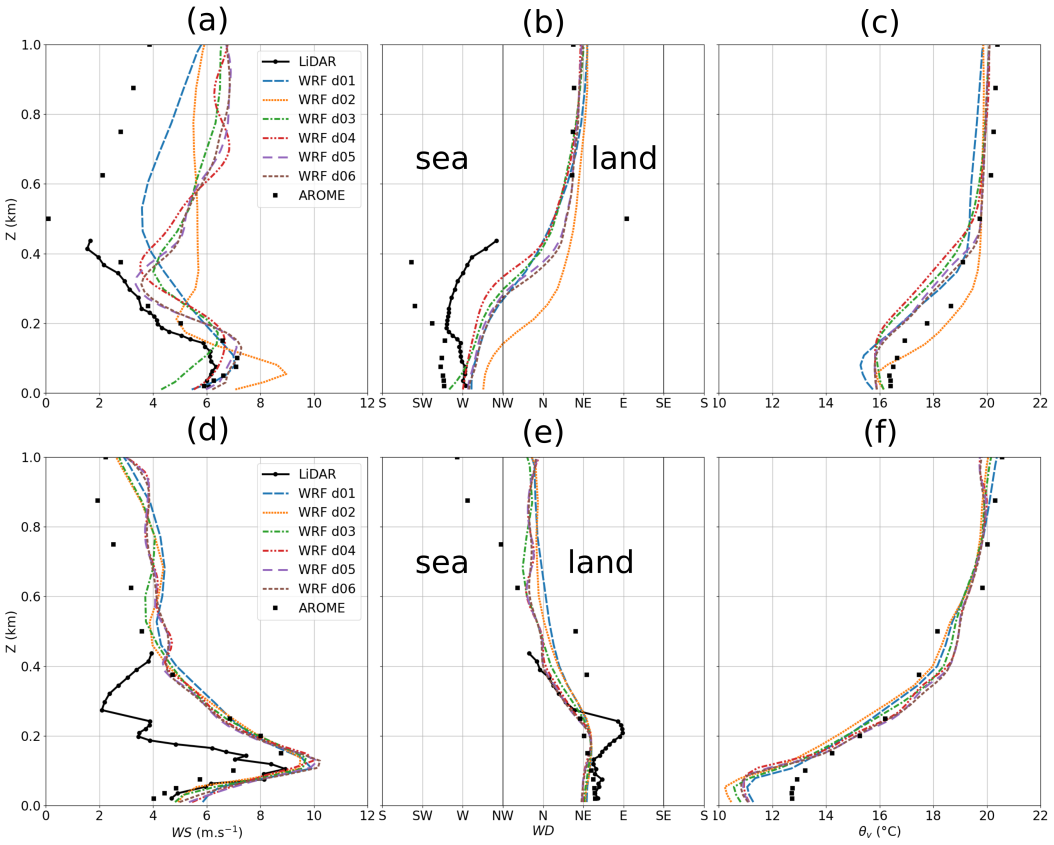

FIGURE 2.12 – (a, d) *WS* and (b, e) *WD* and (d, f) θ_v profiles at the virtual mast, at (a, b, c) 1500 UTC on May 17 and (d, e, f) 0300 UTC on May 18.

the westerly wind up to 400 m high indicates the gravity current and the northeasterly wind the SB return current. The gravity current is shallower in WRF results than in AROME and the LiDAR data. *WD* is generally well reproduced by WRF and AROME near the surface. However, compared to the LiDAR, AROME data exhibit a clockwise deviation, while WRF results show a counterclockwise deviation between 150 and 400 m. At the same time, the *WS* profile (Figure 2.12a) measured by the LiDAR is well reproduced by AROME, despite a slight overestimation at 100 m. In all WRF domains *WS* is overestimated by 1 m.s^{-1} in the gravity current compared to the LiDAR. Above 400 m, *WS* is strongly overestimated in WRF results compared to AROME. The θ_v profiles (Figure 2.12c) also correspond to those of a SB with a cool gravity current and a warmer return current, generating a stable layer in the center of the SB. Below 500 m, θ_v is smaller in WRF results than in AROME, except for domain d02. Domain d02 is clearly the most inaccurate for both *WD* and *WS*, and its θ_v profile deviates from that of the other WRF domains below 400 m.

It will be shown in Section 3.2 that near the LiDAR location during Phases 3 and 4, the wind field is highly heterogeneous at small-scale due to the complexity of the coastline. In domain d02, the particularly inaccurate representation of the sea

table of content

breeze at 1500 UTC is related to some partially resolved phenomena (not shown). Moreover, the presence of the Belle-Île-en-Mer island (Figure 2.1a) to the west of the LiDAR might also influence *WS* and *WD* in the gravity current during Phase 4, when *WD* is from west.

At 0300 UTC on May 18, all the WRF domains show nearly the same profiles, suggesting that they are related to a mesoscale phenomenon. In the LiDAR measurements, *WD* (Figure 2.12e) is nearly constant from east-northeast below 150 m, it slightly veers (clockwise) up to 250 m high and then it backs (counterclockwise) above. The same is observed in the WRF results with an anticlockwise deviation below 250 m. In AROME, the backing is observed above 400 m. Above 600 m high, *WD* is constant from north-northwest in WRF results while it continues to back in AROME so that a west direction is found at 1 km high. The *WS* and θ_v profiles (Figure 2.12d and 2.12e) reveal 3 distinct layers : a nearly neutral layer below 50 m, a strongly stable layer between 50 m and 400 m high with a low-level jet around 150 m high, and a weakly stable layer above where *WS* is nearly constant. Below 50 m, the WRF temperature is 2 °C lower than that of AROME which is in agreement with Figure 2.11 (bottom). The LLJ core is located slightly higher in WRF and AROME than in the LiDAR and the core speed is overestimated by 1 m.s^{-1} in WRF. Above the LLJ core, *WS* decreases brutally in the LiDAR measurements, while the negative shear is less intense in WRF and AROME results. Notably, the *WD* profiles show that a land-breeze return current is found in AROME while it is not present in WRF.

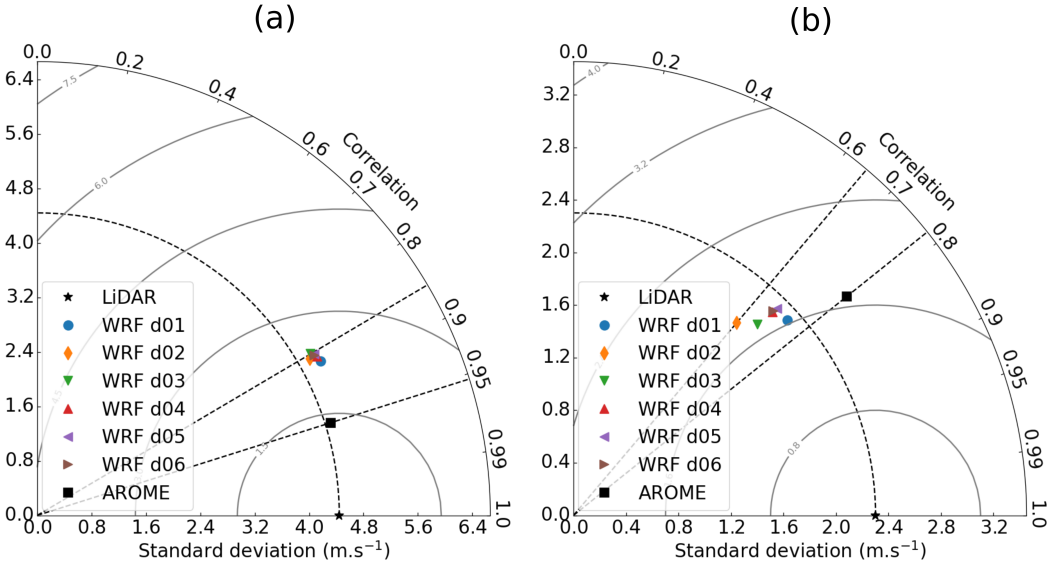

FIGURE 2.13 – Taylor diagram of WRF results and AROME data, with LiDAR data as the reference, for the variables (a) U and (b) V. The statistics are calculated using hourly data (1 point out of 6 for WRF and LiDAR) from 0900 UTC on May 17 to 0800 UTC on May 19, at the 27 virtual mast heights.

table of content

To conclude this comparison, Figure 2.13 shows the Taylor diagram (Taylor, 2001) of WRF and AROME data relative to LiDAR measurements for the variables U (Figure 2.13a) and V (Figure 2.13b). This diagram allows for a more quantitative comparison of the datasets with the standard deviation in the radial coordinate, the Pearson correlation coefficient in the tangential coordinate, and the RMSE relative to the reference (gray lines). There is a good correlation between the WRF simulation and LiDAR measurements. All WRF results show a correlation coefficient around 0.85 for U and 0.7 for V. AROME generally exhibits better correlation than WRF, which can be attributed to the smaller errors at 21 m high during Phase 4 on May 18 (Figure 2.11) or a better timing during Phases 2 and 5. Results obtained on the WRF domains d03 to d06 exhibit nearly identical statistics. This suggests that increasing the horizontal resolution does not significantly change the average comparison between simulation and measurements. The discrepancies are more likely due to large-scale errors in the representation of synoptic conditions, which propagate through all domains, such as the time lag noticed during Phase 5 in all domains (Figure 2.11).

Overall, the comparison between simulation results and observations reveals a good agreement with the presence of SB and LLJ events during both days, attesting the reliability of the numerical simulation and opening the possibility of analyzing in greater depth the dynamical physical processes at play during these days. The few discrepancies between the WRF results and the LiDAR data might be due to a small misrepresentation of the forcing terms : synoptic wind and surface heat fluxes.

2.5.4 Evaluation of the turbulent statistics and the TKE budget

No measurement of turbulent fluxes is available at the time and place of the LES simulation to evaluate the simulated turbulence. However, a part of the domain is located in the land CBL, where the turbulence characteristics are well studied in the literature. Thus, a land area (black square in Figure 2.14a) is selected in domain d06, in which the TKE budget is calculated between 1000 UTC and 1300 UTC on May 17. At 1300 UTC in Figure 2.14a, *WD* in the chosen area is from land while the SB gravity current, depicted by the SW wind direction, has not reached the area yet. The θ_v profiles in Figure 2.14b confirm that the ABL is convective and can thus be qualified as a CBL. Its height (Z_{CBL}), defined as the height at which ${N_{BV}}^2 = \frac{g}{\theta_v}\frac{\partial \theta_v}{\partial Z} = 2.10^{-4} s^{-2}$, is displayed as thin horizontal lines, showing that the CBL is growing between 1000 UTC and 1300 UTC.

The TKE budget terms are compared with the one computed by Pino and Vilà-Guerau De Arellano (2008) (hereafter PV08), who performed LES of the CBL under several geostrophic wind conditions. In their cases, $w^* = 1.5$ m.s^{-1} (Equation 1.8) whereas the friction velocity u^* (Equation 1.3) varies between 0 and 0.8 m.s^{-1}. The case with a geostrophic wind of 5 m.s^{-1} (GC5) is chosen for the comparison because

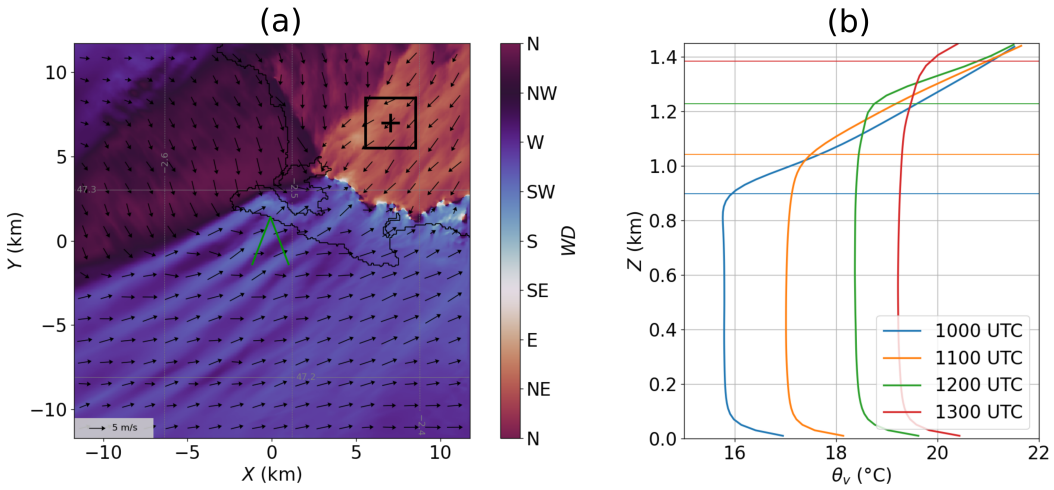

FIGURE 2.14 – (a) *WD* at 10 m high at 1300 UTC on May 17 in d06 results and (b) profiles of θ_v from 1000 UTC to 1300 UTC averaged within the black square area shown in (a)

the ratio w^*/u^*, being equal to 4.76, is the closest to that of the present case (w^*/u^* = 4.26, w^* = 2.05 m.s^{-1}). Thus, Figure 2.15a displays the TKE budget terms taken from PV08 (their Figure 8b), while Figures 2.15b and 2.15c show the same terms computed with the present simulation results using the WRF method (Equation 2.6) and the Boussinesq method (Equation 2.4), respectively. The profiles are plotted as a function of the normalized CBL height $Z^*_{CBL} = Z/Z_{CBL}$, and the budget terms are normalized by w^{*3}/Z_{CBL}, which corresponds to the buoyancy production at the surface, as suggested by Conzemius and Fedorovich (2006) and Luce et al. (2020).

The comparison focuses first on the terms that are similar with both the Boussinesq and the WRF budget methods. $\partial_t(k_{calc})$ is negligible indicating a quasi-steady CBL. In both studies, the buoyancy production exhibits a peak close to the surface and then decreases linearly down to 0 at $Z^*_{CBL} = 0.8$. Above $Z^*_{CBL} = 0.8$, i.e. around the capping inversion (CI), B exhibits a negative peak in PV08, commonly observed in the CBL (Stull, 2017; Kaimal and Finnigan, 1994), but not reproduced by the present simulation. The shear production profiles exhibit the largest value near the surface and a second peak close to the CI, which is smaller in the present case. In the middle of the CBL, P is negligible in PV08 while exhibiting a significant positive value in the present study. The profiles of the shear production and buoyancy terms compares generally well with PV08 below $Z^*_{CBL} = 0.8$ despite a few discrepancies probably due to the present case being non-ideal, with heterogeneous forcing. The CI is noticeably different between the two studies, which could be attributed to a dissimilar initial stability or turbulence above the CBL.

In PV08, the pressure and turbulent transport terms are added together. This total transport term is strongly positive for $Z^*_{CBL} < 0.03$, negative up to the middle of the CBL and positive near the CI. This behavior is well reproduced with the

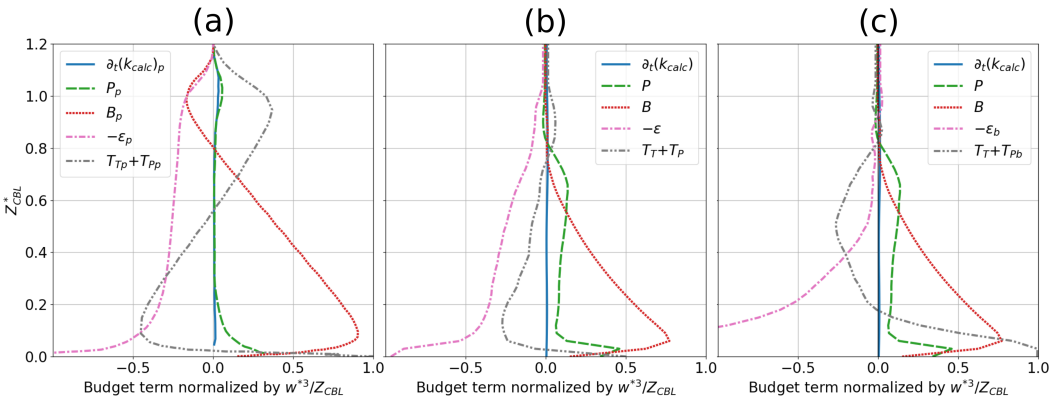

FIGURE 2.15 – Comparison between the k_{calc} budget terms of (a) Pino and Vilà-Guerau De Arellano (2008), (b) the WRF budget, and (c) the Boussinesq budget. The terms are normalized by w^{*3}/Z_{CBL} and plotted as a function of Z^*_{CBL}. In (b) and (c), the terms are averaged in the black area from Figure 2.14a between 1000 UTC and 1300 UTC on May 17.

WRF budget method (Figure 2.15b). The positive values close to the CI are significantly lower, which is coherent with the lower B at the same level. When using the Boussinesq approximation (Figure 2.15c), the transport term is significantly different, being positive up to $Z^*_{CBL} = 0.2$. The dissipation term is also different in the two methods ($\varepsilon \neq \varepsilon_b$), because it is computed as a residual. With the WRF budget, the dissipation profile is similar to the one of PV08 despite a lower value close to the CI, whereas with the Boussinesq budget, ε_b is close to 0 for $Z^*_{CBL} > 0.5$ and too much negative for $Z^*_{CBL} < 0.2$.

The differences between the two budget reveals that the Boussinesq approximation cannot be applied in this case. In Section 2.4.2, two hypothesis that could explain the error introduced by the Boussinesq approach are presented : (i) the possible coupling between the pressure and density perturbations, and (ii) the pressure perturbations caused by the fluctuations of z in the WRF referential frame. It is unlikely that the first hypothesis is responsible for the failure of the Boussinesq approximation in the present case (Figure 2.15c) because the PV08 TKE budget shown as a comparison (Figure 2.15a) uses the Boussinesq approximation. Thus, the errors of the Boussinesq budget are likely not caused by the Boussinesq approximation itself but rather by the numerical errors induced by the WRF vertical coordinate system in the computation of the pressure flux ($\overline{p'u'_i}$ in Equation 2.4). The good agreement between the WRF budget and the PV08 budget suggests that the WRF coordinate system does not generate significant errors in the computation of the other turbulent fluxes.

The dissipation, for now computed as a residual, can also be estimated from the wind speed spectrum. At the location of the black "+" in Figure 2.14a, the time series of the velocity component in the average wind direction are saved using the *wrf_timeseries* feature between 1000 UTC and 1300 UTC. During this period,

the wind profile at this location is nearly stationary. From the time series, the power spectral density (PSD) is calculated using the Welch's method (computed with the *Scipy* library) with a window size of 30 minutes and an overlap of 15 minutes between the windows. The time spectra are then converted to space spectra using the Taylor hypothesis with the mean wind speed of each level. The PSD at three different heights are shown in Figure 2.16a, where it is estimated that the inertial range lies between 0.004 and 0.03 rad.m^{-1}. Then, the spectral dissipation ε_s is estimated based on the -$\frac{5}{3}$ Kolmogorov cascade theory with a constant of 0.49 (Wacławczyk et al., 2017). The fits are shown in Figure 2.16a as dashed lines. Figure 2.16b shows a comparison of the profiles of ε_s, ε_b, and ε. Again, it is clear that the Boussinesq budget residual ε_b does not behave correctly as it is too large for Z^*_{CBL} below 0.2 and a too small above 0.5. Despite strong oscillations in the profile, ε_s is pretty close to ε. The differences between ε_s and ε may be related to the spectral method giving approximate results, and to the fact that ε_s relies on simulation results on a single computational cell where ε is averaged over several hundreds of cells (square in Figure 2.14a).

The profile of $-D$ is also shown in Figure 2.16 as it is the modeled part of the total dissipation ε, the other part being the numerical dissipation E computed as a residual (Equation 2.6). ε is nearly 2 times larger than D at every level, meaning that the residual term $E \approx D$. This is consistent with the results of Kitamura and Nishizawa (2019) who studied the numerical dissipation of the 5th-order WRF advection scheme in a canonical CBL case and found that the numerical dissipation profile is very close to the modeled dissipation (Figure 1 of their paper). These coherent dissipation profiles brings confidence in the WRF budget method.

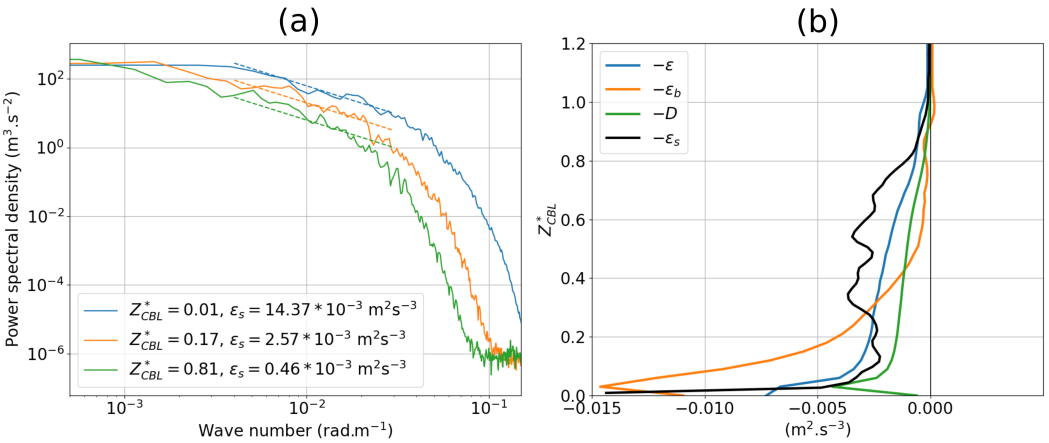

FIGURE 2.16 – (a) Spectra of the velocity component in the mean wind direction, at the location indicated by a "+" in Figure 2.14a between 1000 and 1300 UTC on May 17 at 3 different heights. (b) Comparison of the dissipation profiles between the spectral method and the two budget methods.

Overall, the WRF k_{calc} budget implemented for this study seems to be a reliable

tool in the CBL, allowing the analysis of the TKE in more complex conditions.

2.6 Conclusion

In this chapter, the method employed is presented, including a description of the site, the experimental data, the model set-up, the post-processing tools, and the assessment of the simulation results. The simulation results show a good agreement with the LiDAR data and AROME data. In particular, all datasets reveal the presence of SB events during daytime and LLJ events during nighttime on May 17 and 18. Moreover, the turbulent statistics and the TKE budget computed from the simulation results in the CBL are consistent with the theory and with other studies. These comparisons bring confidence in the realism of the simulation and allow for a deeper analysis of the simulation results as presented in the next chapters.

table of content

Chapitre 3

Analysis of the sea breezes near a complex coastline

Introduction

The wind profiles during daytime (Figures 2.11, 2.12a and 2.12b) revealed the presence of SB events at Le Croisic. This common coastal phenomenon has been studied in the past but several gaps remain in the knowledge of SB (Section 1.3.6), in particular on the offshore part and near complex coastlines.
As shown in Section 2.1, the coastline near Le Croisic is notably intricate and features bays and peninsulas at different scales. However, no consistent method was proposed to describe the SB characteristics near a complex coastline. A first objective of this chapter is to propose a tool to locally describe the coast orientation at a given scale.
Simpson (1996) suggested that the evolution of the wind direction in a SB near a complex coastline is governed first by the coast orientation at small scale and later by the coast orientation at a larger scale. A second objective is to quantify the increasing scale of the coastline "felt" by the SB during its development. For that, the spatial distribution of the SB orientation is studied at several time, and compared with the distribution of the coast orientation at a given scale.
Just a few authors determined the evolution of the SB offshore extent (Section 1.3.4). However, knowing this extent is necessary to estimate the impact of the SB on the offshore wind resource. Thus, a third objective is to study the evolution of the SB offshore extent.
On May 17, an offshore atmospheric undular bore is observed near the Guérande peninsula during SB initiation. Such an observation has never been reported in the literature. The fourth objective of this chapter is to determine the mechanism involved in its generation and to describe its main characteristics. The absence of bore on May 18 is also investigated.
The chapter is organized as follows. Section 3.1 presents the evolution of the SB scale, starting with a qualitative description of the distribution of the wind direction in Section 3.1.1, followed by an introduction of the tool to describe the coast orientation in Section 3.1.2 and a definition of the SB orientation in Section 3.1.3, then the evolution of the SB scale and orientation are calculated in Section 3.1.4, and finally the SB extent is investigated in Section 3.1.5. Then, Section 3.2 investigates the atmospheric bore by describing the initiation of local SBs close to the Guérande peninsula in Section 3.2.1, proving evidence of the presence of a

bore in the simulation results and in the LiDAR measurements in Sections 3.2.2 and 3.2.3, studying the evolution of the main bore characteristics in Section 3.2.4, and finally, investigating the reason for the absence of bore on May 18 in Section 3.2.5.

3.1 Sea-breeze scale and extent

3.1.1 Qualitative description of the wind direction

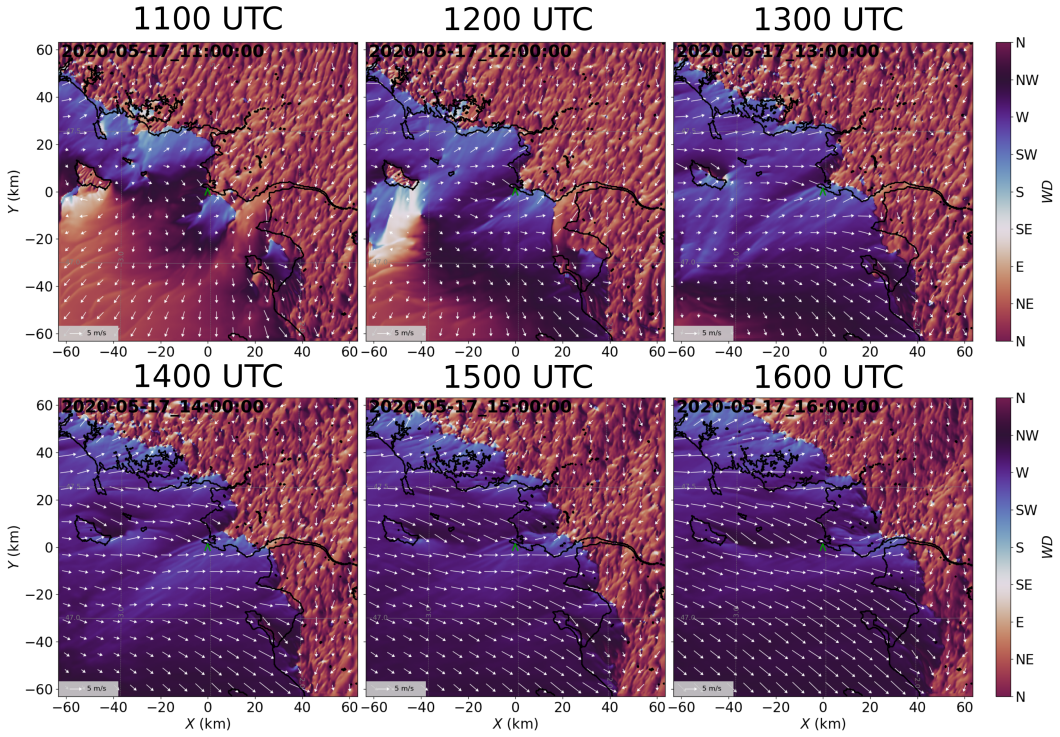

FIGURE 3.1 – Spatial distribution of *WD* at 10 m high on May 17 between 1100 and 1600 UTC, based on d04 results.

This section starts with a qualitative description of the evolution of the wind direction in the SB. Figure 3.1, presents the spatial distribution of *WD* at 10 m high between 1100 and 1600 UTC on May 17. Initially, *WD* is from northeast (land wind) within the whole domain, following the synoptic wind direction (Figure 2.8). At 1100 UTC, the coastal area is divided into several zones with different *WD*, corresponding to the development of local SBs. Local SBs are identified by the sea wind, except at the mouth of the Loire river. At 1200 UTC, the SBs almost cover the entire coastline and extend roughly 20 km offshore. Local SBs can still be distinguished from each other as their direction depends on the local-scale coast orientation. Over time, the SBs spread more rapidly in the offshore direction than inland. At 1600 UTC, *WD* is nearly uniform in the area showing that the local SBs have merged into a regional SB. This direction varies smoothly within the domain from westerly

table of content

wind to the north to northwesterly wind to the south, suggesting that it is related to the large-scale coast orientation that also changes within the domain (Figure 3.2a). Note that *WD* is not perpendicular to the large-scale coastline but deviates by 45 ° clockwise. Overall, the *WD* evolution shows that, in the morning, several local SBs are initiated under the influence of the local-scale coastline, and that over time, they merge into a regional SB that is influenced by a larger scale coast orientation and rotates clockwise. This is in agreement with Simpson (1996) who suggested that the early SB is oriented according to the local-scale coast orientation while the mature SB is oriented according to the large-scale land mass. Thus, an increase of the SB scale influences the spatial distribution of the direction.

The observations suggest that the SB orientation α_{SB} can be decomposed as

$$\alpha_{SB}(X, Y, t) = \alpha_c(X, Y, s) + \delta(X, Y, t) \tag{3.1}$$

where α_c is the coast orientation at a given scale s and location (X, Y), and δ is the deviation angle between the SB and the coast orientation. In the next sections, an attempt to quantify the evolution of the SB scale s_{SB} is proposed, based on the distribution of the SB direction α_{SB}. For this, we assume that the SB scale s_{SB} and deviation δ_{SB} vary with time but are constant in space within the whole SB so that Equation 3.1 can write

$$\alpha_{SB}(X, Y, t) = \alpha_c(X, Y, s_{SB}(t)) + \delta_{SB}(t). \tag{3.2}$$

This assumption is obviously very simplistic and will be discussed later in the conclusion of the chapter.

A method to calculate α_c as a function of a scale parameter s is given in Section 3.1.2, while Section 3.1.3 presents the definition of α_{SB} used in this study. The evolution of the SB scale s_{SB} and deviation δ_{SB} are studied in Section 3.1.4. Finally the evolution of the SB extent and a comparison with s_{SB} are given in Section 3.1.5.

3.1.2 Coast orientation at a given scale

The present study deals with a notably intricate coastline including peninsulas and bays at different scales (Section 2.1). Therefore, the coast orientation depends on the scale considered. Moreover, determining the coast orientation for a point that is located a few kilometers from the coastline is not straightforward. A method is proposed here to calculate the orientation of the coastline at a given location and scale s, by applying a Gaussian filter of size s on the land-sea mask array M, and computing the gradient of the filtered array (Section 2.4.3). M contains a value of 1 for land cells and 0 for sea cells, so that in the filtered mask ($\widetilde{M}$), the coastal cells have real values between 0 and 1. Thus, the gradient of $\widetilde{M}$ points toward land, and the coast orientation (α_c) is locally defined as the direction of this gradient. The method is illustrated in d03 with $s = 20$ km (Figure 3.2a) and in d05 with $s = 5$

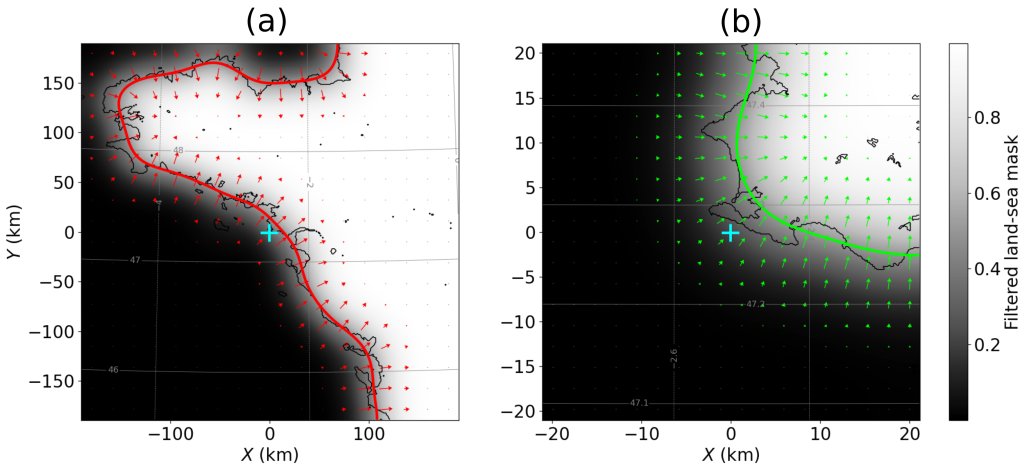

FIGURE 3.2 – (a) Land-sea mask in d03 filtered with a 20-km gaussian filter. The red line shows the calculated smoothed coastline (where the filtered mask equals 0.5) and the arrows represent the gradient of the filtered mask. (b) Same as (a) in d05 with a 5-km filter. The "+" shows the position of the LiDAR virtual mast.

km (Figure 3.2b). The arrow fields represent the gradient of $\widetilde{M}$ and the solid lines are the filtered coastline obtained with $\widetilde{M} = 0.5$.

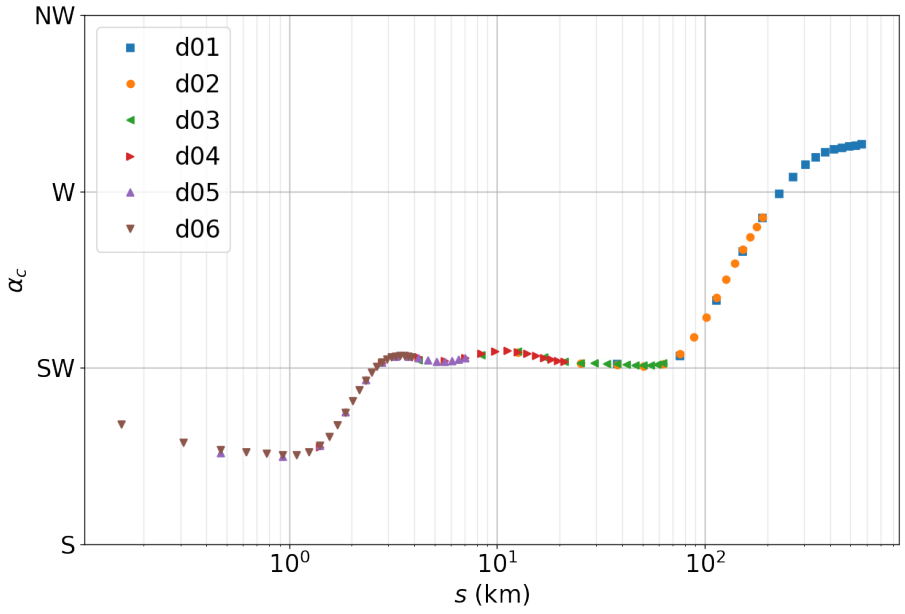

FIGURE 3.3 – Evolution of α_c as a function of s at the LiDAR virtual mast location.

An interesting feature of this method is the scale parameter s. Large values of s better reveal the large-scale land mass and filter out the small-scale tortuosity. For

example, the Guérande peninsula is filtered out in Figure 3.2a ($s = 20$ km) but not in Figure 3.2b ($s = 5$ km). The evolution of α_c at the virtual mast location ("+" in Figure 3.2) as a function of s is shown in Figure 3.3. This curve is calculated using all domains, and for some values of s, α_c can be calculated in several domains. A good continuity is found between the domains when the following conditions are verified : (i) $s > 4\Delta_X$ and (ii) s is lower than 3 times the distance to the nearest domain boundary. Thus, these two conditions are verified in the next sections. The evolution of α_c as a function of s highlights the different scales involved in Le Croisic area. For $s < 2$ km, α_c is related to the local-scale peninsula of Le Croisic oriented south-southwest, for 3 km $< s <$ 70 km, α_c is related to the Guérande peninsula and the Atlantic coastline, and finally for $s > 70$ km, the Brittany peninsula is progressively filtered out so that α_c points toward the large-scale European continent.

3.1.3 Sea-breeze orientation

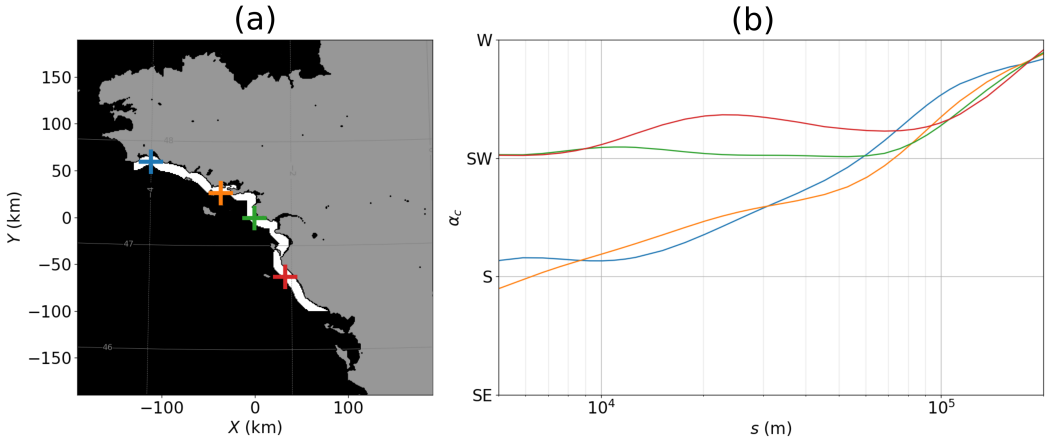

FIGURE 3.4 – (a) Position of the four points defined in the text : (blue) P1, (orange) P2, (green) P3 and (red) P4, and (b) the coast orientation as a function of the scale s at these locations.

To choose a definition for the SB orientation, four points named P1 to P4, shown in Figure 3.4a, are chosen within domain d03, where P3 corresponds to the LiDAR virtual mast location. The evolution of α_c at these points is displayed in Figure 3.4b for s ranging between 5 and 200 km. At P1 and P2, α_c is from the south at local scale and progressively turns toward southwest as s increases whereas at P3 and P4, α_c depends less on the scale. α_c at all four points converges with increasing s.

The evolution of the wind profiles at P1 to P4 is shown in Figure 3.5a to 3.5d, respectively, in the form of hodographs : each line corresponds to a wind profile, showing both *WS* and *WD* at all levels. For illustration, the corresponding *WS* and *WD* profiles at P4 are shown in Figure 3.5e and 3.5f. At the four locations, the wind profiles on the hodographs are forming lines that are oriented, by definition, according to the main shear direction. This direction is roughly perpendicular to the 25-km coastline at 1100 UTC and it tends to rotate clockwise over time. The profiles

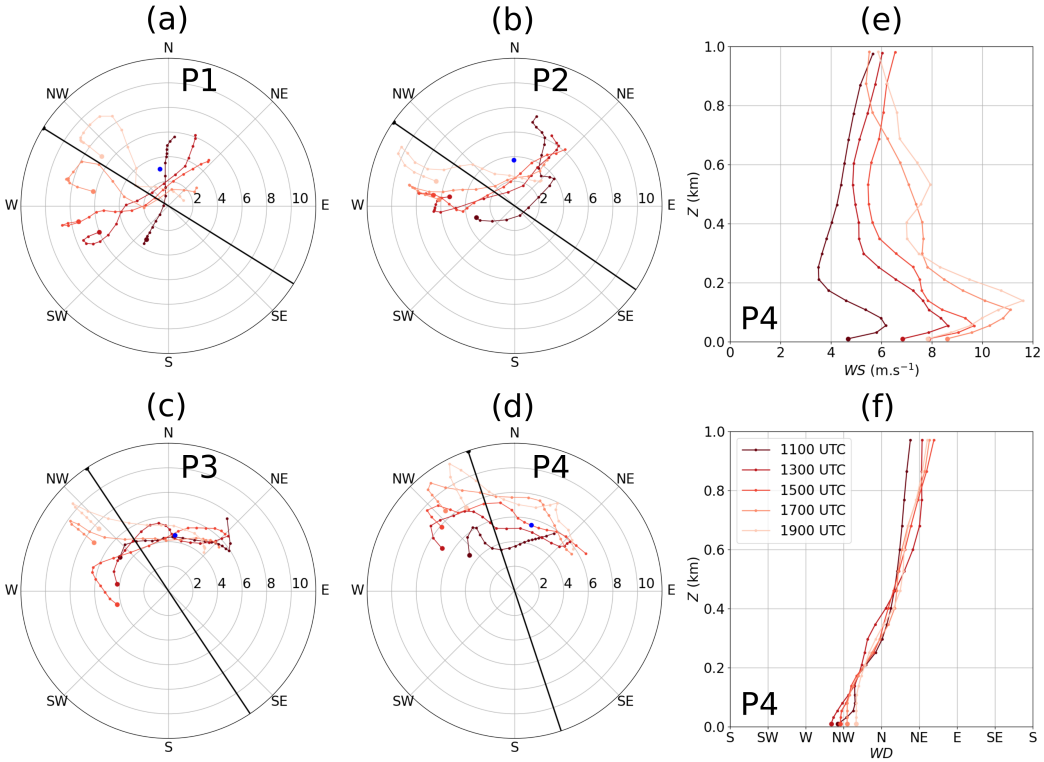

FIGURE 3.5 – (a-d) Evolution of the wind profile hodographs at (a) P1, (b) P2, (c) P3, and (d) P4 between 1100 UTC and 1900 UTC on May 17, where a circle the circle corresponds to 10 m high and the dots to higher levels. The synoptic wind (see Figure 2.8) is displayed as a blue circle, and the 25-km coastline as a black line. (e-f) Evolution the (e) *WS* and (f) *WD* profiles at P4 over the same period.

do not cross the center of the hodographs but are shifted toward the synoptic wind (blue dot), especially at P3 and P4 where the synoptic wind speed is the largest. These hodographs illustrates the difference between *WD* and the shear direction. For example, at P4 at 1100 UTC, *WD* evolves between northwest and northeast in the profile (Figure 3.5f) whereas the main shear direction is about west-east (Figure 3.5d). The particularly pronounced shear, that is not aligned with the synoptic wind direction, is likely related to the vertically non-uniform baroclinic pressure gradient driving the SB (Section 1.2.1). For that reason, in this study, α_{SB} is defined as the main direction of the profile in the hodograph, and is determined by fitting a line on the profile between 50 and 800 m in the (U, V) plane using *Scipy.odr*. We believe that this definition is more robust than *WD* at a given height.

The evolution of α_{SB} over time at the four points is shown in Figure 3.6. At P1 and P2, the clockwise rotation is well pronounced while at P4 the direction is constant. At P3 (the virtual mast location) the direction backs (rotates anti-clockwise) rapidly at 1300 UTC and veers (rotates clockwise) after 1400 UTC. This chaotic behavior is caused by a competition between two local SBs as will be

table of content

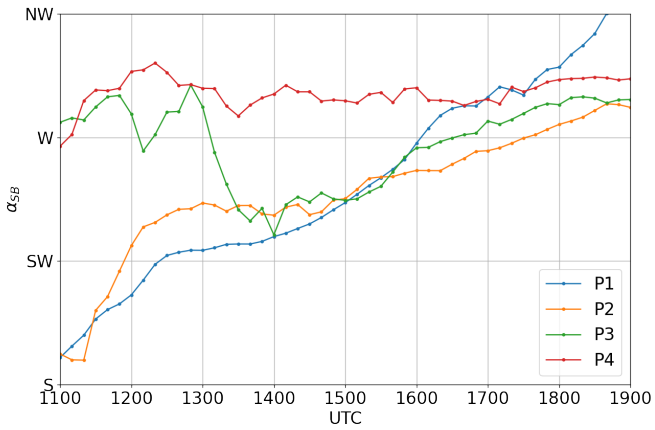

FIGURE 3.6 – Evolution of the SB orientation at points P1 to P4 on May 17.

explained in Section 3.2. The comparison between α_{SB} as a function of time (Figure 3.6) and α_c as a function of s (Figure 3.4b) matches well with the relationship given in Equation 3.2 : the increase of s_{SB} results in a clockwise rotation of the relevant α_c at P1 and P2, that tends to increase the rotation of α_{SB} whereas at P3 and P4, the rotation is slower because α_c depends less on s.

3.1.4 Sea-breeze scale

Based on the definition of α_{SB} and $\alpha_c(s)$ defined in Sections 3.1.2 and 3.1.3, respectively, and on Equation 3.2, a method is proposed to determine both s_{SB} and δ_{SB} at a given time in the white area shown in Figure 3.4a. For each point of this area, $\delta(s)$, the deviation between α_{SB} and $\alpha_c(s)$ (Equation 3.1), is calculated for a range of s values. In Equation 3.2, it is assumed that $\delta(s = s_{SB})$ is a constant over space equal to δ_{SB}. Therefore, the scale s for which the spatial standard deviation of δ is the lowest is taken as s_{SB}, and the spatial average of $\delta(s = s_{SB})$ is taken as δ_{SB}.

The evolution of the standard deviation of δ as a function of s at different times on May 17 is shown in Figure 3.7. All curves show a large standard deviation when considering the coast orientation at a 5-km scale. Then, as s increases, the standard deviation decreases smoothly down to a minimum. The scale associated to this minimum (s_{SB}, denoted by a vertical line) increases over time. Notably, a second minimum is found at larger scales (around 200 and 300 km). For infinite values of s, i.e at infinitely large scale, α_c is by definition invariant in space so that according to Equation 3.1, the spatial standard deviation of δ equals that of α_{SB}. This asymptotic value is calculated and depicted by the horizontal dashed lines. As expected, for s = 400 km, the standard deviation of δ is close to the asymptote.

table of content

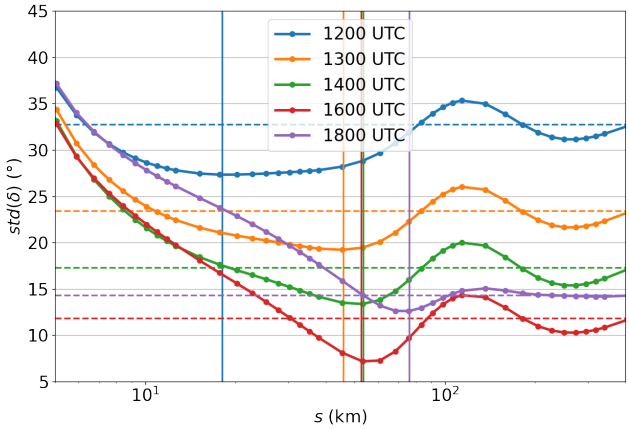

FIGURE 3.7 – Standard deviation of δ within the white area defined in Figure 3.4a, as a function of s at different times on May 17. The vertical lines depict s_{SB} at each time.

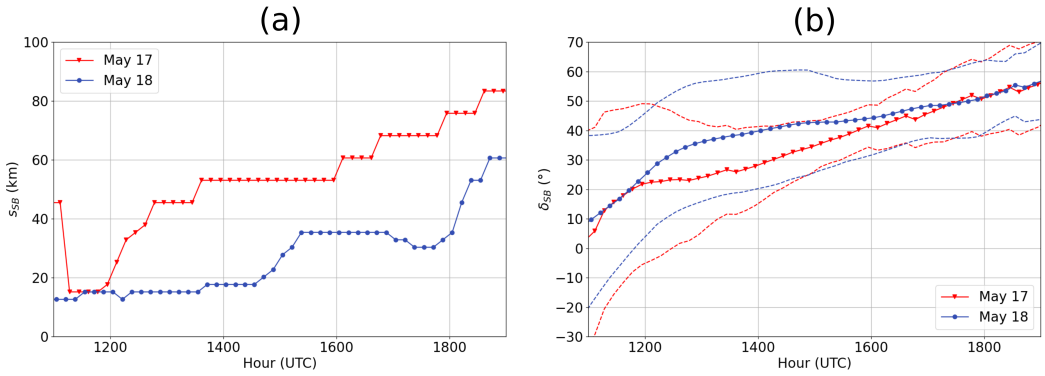

FIGURE 3.8 – Evolution of (a) s_{SB} and (b) δ_{SB} over time on May 17 and May 18. Dashed lines in (b) indicate +/- the standard deviation of δ

The time evolution of s_{SB} is shown in Figure 3.8a. During the SB initiation, at 1200 UTC, the SB scale is about 15 km. On May 17, s_{SB} increases rapidly between 1200 and 1300 UTC and then linearly during the whole afternoon. On May 18, s_{SB} increases more slowly between 1200 and 1700 UTC and even decreases slightly between 1700 and 1800 UTC. After 1800 UTC, it increases rapidly and gets closer to the May-17 values. In Figure 3.8b, the evolution of δ_{SB} is very similar between May 17 and May 18 with a value close to 0 at the SB initiation and a persistent veering during the whole period. The rotation is faster around 1100 UTC (around 15 °.h^{-1}) and slower after 1200 UTC (around 5 °.h^{-1}). This rotation rate is lower than the IO rotation rate (about 22 °.h^{-1} at this latitude).

A few weaknesses of the method used to determine s_{SB} are revealed in Figure 3.7. First, the second minimum value is sometimes very close to the first one, so that s_{SB} could jump from a scale to another. Second, at 1200 UTC, the curve does

table of content

not exhibit a well-pronounced minimum but shows instead a flat area between 15 and 40 km. Moreover this minimum remains above 25 °. A possible cause for this flat minimum lies in the wrong assumption that both s_{SB} and δ_{SB} are constant over space at a given time. Indeed, at this time, the local SBs within the studied area may be at different development stages. In addition, the 1-km resolution of the domain d03 possibly alters the small-scale local SBs, that will be analyzed in the next section based on LES results.

Despite these weaknesses, the time evolution of s_{SB} and δ_{SB} are in good agreement with the behavior described in Section 3.1.1 : the scale of the SB increases over time, meaning that the orientation of the SB is related to the coast orientation at a progressively larger scale, and the deviation angle increases clockwise from nearly 0 ° at 1100 UTC to 45 ° at 1600 UTC. Although the rotation rate is lower than the theoretical IO rotation rate, it is likely that the clockwise rotation is governed by the Coriolis force, as observed in many SB studies (Section 1.3.2).

3.1.5 Sea-breeze extent

Another important scale of the SB is its horizontal extent. In this section, a short description of the SB velocity and height is given, and the evolution of its extent is analyzed around Le Croisic.

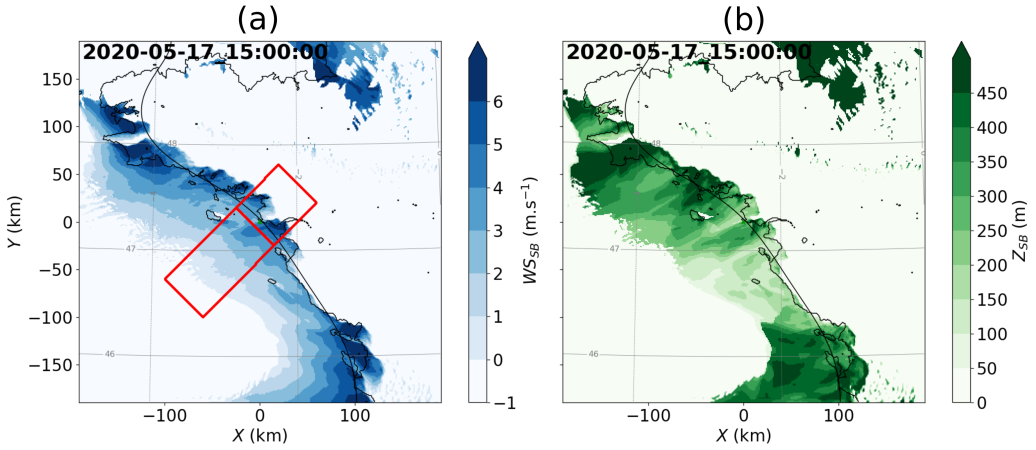

FIGURE 3.9 – Spatial distribution of (a) WS_{SB} and (b) Z_{SB} at 1500 UTC based on d03 results computed with $s = 50$ km.

As in many studies, the cross-coast velocity component (U_c) is defined as the wind components perpendicular to the coastline, i.e. in the direction of α_c (Section 3.1.2). If U_c is positive (sea wind) close to the surface, and negative at some upper level, Z_{SB} is defined as the height at which U_c equals 0. In addition, the speed of the gravity current (WS_{SB}) is defined as the maximal value of U_c below Z_{SB}. The

spatial distribution of WS_{SB} and Z_{SB} at 1500 UTC on May 17 based on d03 results is shown in Figure 3.9a and 3.9b, respectively. These characteristics are computed based on the coast orientation at s = 50 km, which is the value of s_{SB} between 1300 and 1600 UTC on May 17 (Figure 3.8). As in domain d04 (Figure 3.1), the SB is detected all along the Atlantic coastline, with a dissymmetry between the small extent inland and the much larger offshore extent. At the Channel coast, the synoptic wind from the sea (Figure 2.8) inhibits the return current except for a small region at the north-east corner of the domain. The rest of the study focuses on the Atlantic coast. As expected, WS_{SB} decreases with increasing offshore distance (Section 1.3.4). The evolution of Z_{SB} with the offshore distance is less clear. Z_{SB} strongly depends on the along coast coordinate with larger values at Y = 50 km and Y = -150 km than at Y = -60 km.

The extent of the SB is defined here using the 1 m.s^{-1} threshold proposed by Arritt (1989) (see Section 1.3.4), applied on WS_{SB}. To visualize this extent, Figures 3.10a to 3.10d display the distribution of WS_{SB} on May 17, where the limits are depicted as green lines. In addition, the distribution of U_c in a vertical cross-section is shown in Figure 3.10e. Around Le Croisic, two red rectangle regions are defined in Figures 3.9 and 3.10, where the inland and offshore extents are calculated as the median distance between the SB limits and the s = 50 km coastline (black smooth line). The 50-km coastline is preferred over the real coastline because the tortuosity of the real coastline tends to affect the calculation of the inland propagation. The boundary between the two rectangle areas is placed according to the narrow SB during its initiation (Figure 3.10a) so that on May 18, this boundary is placed closer to the land (not shown).

The evolution of the SB extent on May 17 and May 18 is displayed in Figure 3.11a. On both days, the SB expands between 1200 and 1430 UTC. The averaged speed of SB expansion between 1200 and 1430 UTC is determined using linear fits that are displayed as dashed lines. The expansion speed is quite low inland (1.9 m.s^{-1} on May 17 and 0.6 m.s^{-1} on May 18) so that the maximal inland extent is less than 20 km. On May 18, the SBF propagates faster before 1200 UTC but then remains around 15 km. Offshore, the expansion follows closely the linear fit with a larger speed, especially on May 17 (4.8 m.s^{-1} against 3.2 m.s^{-1} on May 18) when the extent reaches 65 km. After 1600 UTC, both the inland and offshore extents decrease. The linear increase of the offshore extent with time compares well with the simulation results of Finkele (1998), shown in Figure 3.11b, which brings confidence in the realism of the simulated SB events.

Both the SB scale and the offshore extent are notably larger on May 17 than on May 18. The comparison between their evolution is shown in Figure 3.12. On May 17, the two quantities are very close to each other during the expansion phase while on May 18, a 50 % difference is observed. At the LiDAR location, the cross-coast component of the synoptic wind speed is -3.5 m.s^{-1} on May 17 and -2.4 m.s^{-1} on

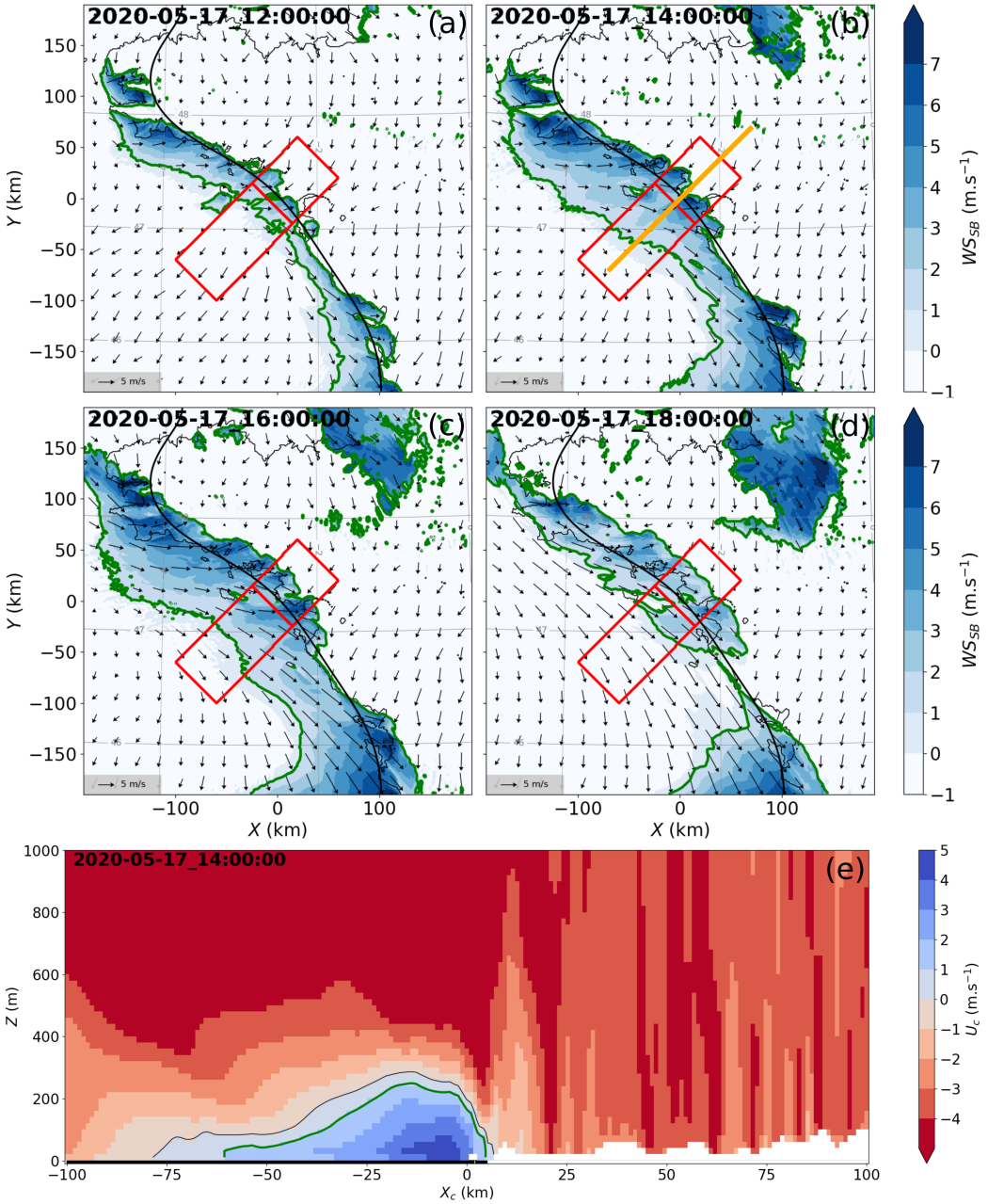

FIGURE 3.10 – (a-d) Evolution of WS_{SB} in domain d03 on May 17 between 1200 and 1800 UTC. The green line indicates the limits of the SB as defined in the text and the red area is used in Figure 3.11. (e) Vertical cross-section of U_c at 1400 UTC on May 17 on the orange line shown in (b). The contours of 0 and 1 m.s^{-1} are indicated in black and green, respectively.

May 18 (Figure 2.8) while the land-sea temperature difference is similar between the two days (Figure 2.9), which suggest that a larger synoptic wind speed accelerates the offshore expansion. This is in contradiction with Finkele (1998) who concluded that the geostrophic wind speed has a little impact on the offshore expansion speed,

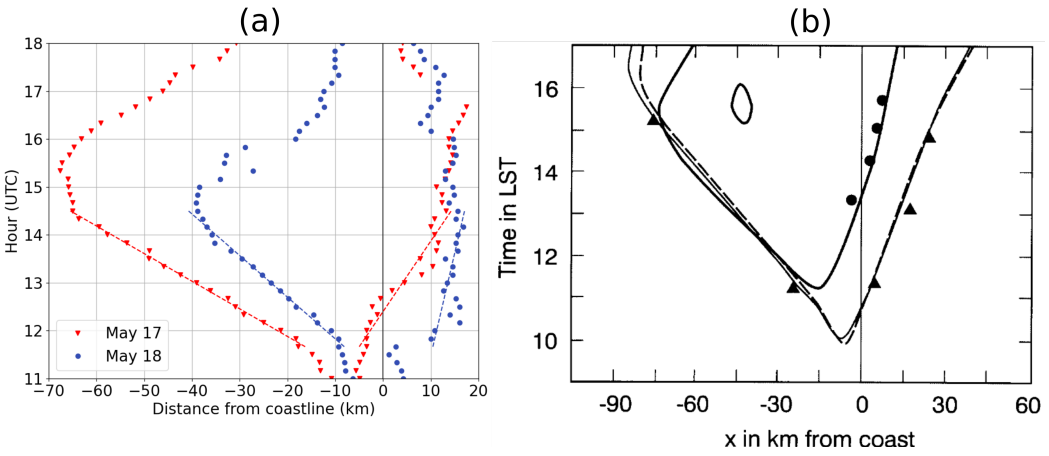

FIGURE 3.11 – (a) SB inland and offshore extents in the red areas defined in Figure 3.10 on May 17 and May 18. The dashed lines show linear fits. (b) Same figure taken from Finkele (1998), based on ideal simulations with a cross-coast geostrophic wind speed of (dashed, thin lines) -2.5 m.s $^{-1}$ and (thick line) -5 m.s $^{-1}$. Markers are based on aircraft measurements.

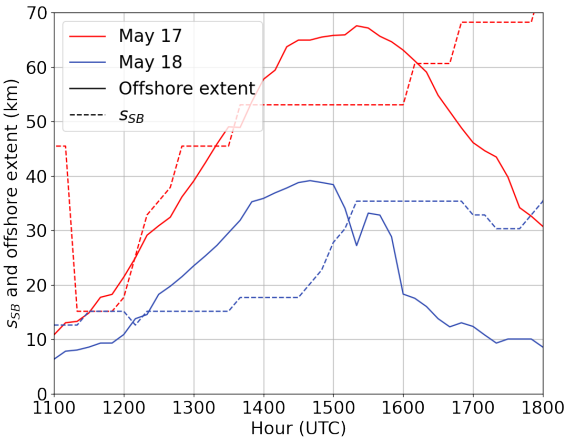

FIGURE 3.12 – Comparison between the SB offshore extent and s_{SB}.

and with Steele et al. (2013) who found a lower expansion speed for larger land synoptic wind. It is possible that other factors are influencing the SB development in the present case, such as the offshore stability that is different between May 17 and May 18 (Section 3.2.5).

It can be seen in Figure 3.10, that at 1600 UTC and 1800 UTC, *WD* has rotated and is mainly along the coast, so that the cross-coast wind component U_c is low. Thus, the decrease in SB extent after 1600 UTC is related to the rotation of the SB, i.e. the increase of the deviation angle δ_{SB} likely caused by the Coriolis force. This is in agreement with the linear theory of Rotunno (1983) that states that the Coriolis frequency has a strong influence on the SB extent (Arritt, 1989).

table of content

table of content

3.2 Interactions of local sea breezes during initiation near a peninsula

In the previous section, it was shown that the wind field during the SB initiation in the studied area was highly heterogeneous and featured several local SBs. In this section, the focus is first made on the May 17 case (Sections 3.2.1, 3.2.2, 3.2.3, 3.2.4) when an atmospheric undular bore, resulting from the interaction between two local SBs, has been observed. Then, Section 3.2.5 investigates the absence of bore on May 18. Part of the results presented hereafter is published in Landreau et al. (2025b).

3.2.1 Local sea breezes and secondary interfaces

The wind field at small-scale during the SB initiation on May 17 is illustrated in Figures 3.13b to 3.13f, which shows the distribution of *WD* at 21 m high between 0900 and 1200 UTC. At 1030 UTC, the study area is divided into 5 zones. Zone E represents the land area outside the breeze circulation, while Zones A to D correspond to the initial stages of local breezes associated with the four coastline segments shown in Figure 3.13a. These four segments are clearly filtered out in the 20-km coastline displayed in Figure 3.2a so that the correct s_{SB} at this time is qualitatively closer to 5 km (Figure 3.2b). The development of the local breeze in each zone depends on the orientation of the coastline relative to the initial northeasterly wind : in Zone A, the local breeze is backdoor with an initial clockwise rotation of the wind vector, in Zone B, the SB is pure, *WS* decreases first and then reverses at 1000 UTC, and in Zone C, the SB is corkscrew, with a counterclockwise rotation of the wind vector, shifting from N-NE at 0900 UTC to NW at 1100 UTC. According to the coast orientation defined in Figure 3.13a, the SB in Zone D is backdoor but it seems to be a more advanced local SB which explains why the wind direction is from the sea at 1030 UTC.

Interfaces between zones in Figure 3.13 are depicted as either solid or dashed lines, indicating whether the wind field is horizontally convergent or divergent, respectively. Interface with Zone E represents the main SBF, which is convergent. Other interfaces are referred to as *secondary*, as they separate local breezes. The secondary B-C interface orthogonal to the coastline is convergent and particularly distinct. At 0930 UTC, *WS* is very low in the area. Over time, convergence intensifies so that at 1200 UTC, the wind speed perpendicular to the interface is about 5 $\mathrm{m.s^{-1}}$ in Zone C and almost zero in Zone B. The B-C front moves northward over time, such that at 1200 UTC, it intersects the LiDAR measurement area, which then lies entirely within Zone B (Figure 3.13). The C-D interface appears divergent, as suggested by the wind vector field, so that its position is inherently imprecise.

The mechanism behind convergent and divergent interfaces can be synthesized by the schematic in Figure 3.14a. A simplified 3-part coastline is represented with a

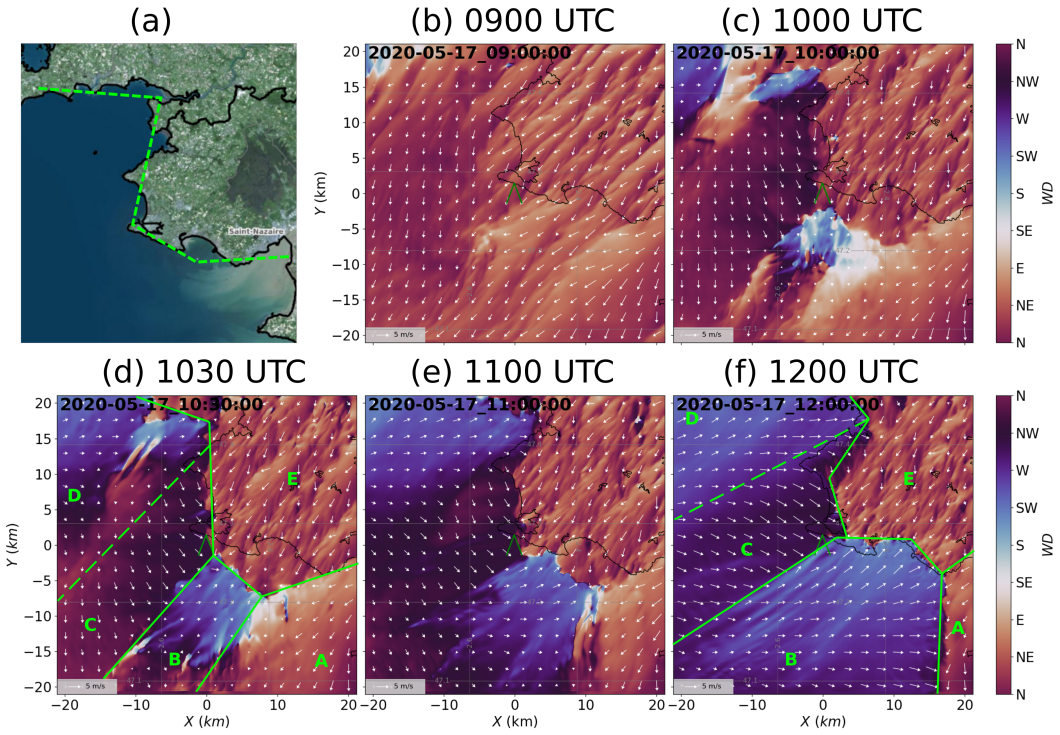

FIGURE 3.13 – (a) Map of the Guérande peninsula where the four dashed green lines are coastal segments mentioned in the text. (b-f) Color plot of the 21 m *WD* on May 17 based on d05 results. White arrows show the 21 m wind. Green thin lines near coord. (0,0) correspond to the LiDAR measurement area. Bold green lines are (solid) convergent and (dashed) divergent interfaces separating different areas, letters are explained in the text.

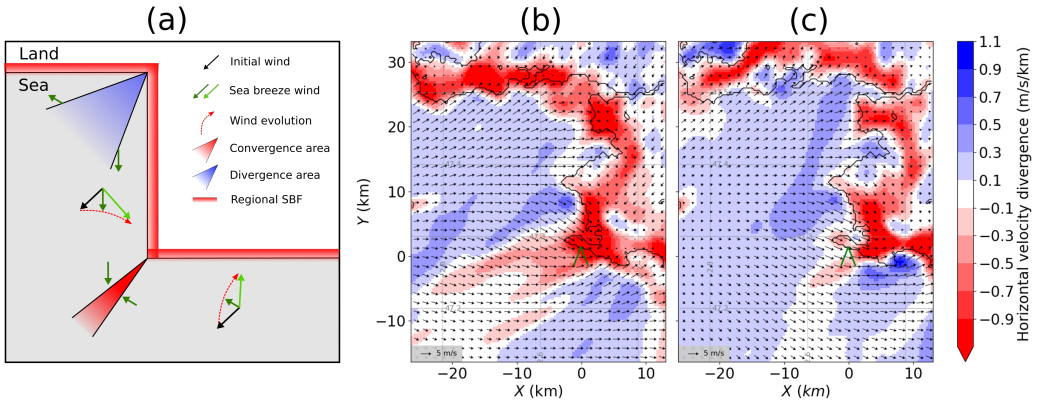

FIGURE 3.14 – (a) Schematic to explain the convergence area leading to a secondary front between two local SB, and (b-c) Horizontal wind divergence based on d04 results at 10 m high (1st cell) on (b) May 17 and (c) May 18. Before computing the divergence, velocity fields are 1-km filtered and averaged over 2 hours between 1100 and 1300 UTC.

right-angle bay and a right-angle peninsula. Under north-east initial wind (represented by the black arrow), due to the baroclinic pressure gradient at sea-breeze initiation (not shown), the wind direction near the west coast (sea to the west

and land to the east) gradually shifts from northwest to northeast, while near the two other coasts, it shifts from northwest to south. In an intermediate stage, the horizontal wind diverges in the bay area and converges towards the tip of the peninsula. The convergent area (marked in red) rapidly collapses into a frontal line. On the opposite, the divergent area (marked in blue) spreads horizontally.

The schematic aligns well with the pattern of horizontal wind divergence ($\frac{\partial U}{\partial X} + \frac{\partial V}{\partial Y}$) near the surface at 1200 UTC on May 17 and May 18 displayed in Figures 3.14b and 3.14c. Offshore, the horizontal wind divergence is predominantly positive, which is a classical feature of SBs (Section 1.3). The convergent area along the coastline (in red) corresponds to the SBF. Another convergent area, corresponding to the B-C secondary front, is identified at the tip of the peninsula. The convergence is observed on both days and is more pronounced on May 17 when it extends up to 20 km offshore. In the bay area, the divergence is positive, especially on May 18.

3.2.2 Evidence of an undular bore in WRF results

In Figure 3.13 at 1200 UTC, oscillations in WD start to be visible in Zone B, to the south of the B-C frontal line. The wave signature is better revealed by the map of W at 150 m high at 1200 UTC, displayed in Figure 3.15a. Above land, the daytime CBL is characterized by strong updrafts and downdrafts. The land and sea areas are separated by the SBF, a continuous line of updrafts along the coastline. Above the sea, W is significantly lower, except at the B-C frontal line, oriented perpendicular to the coastline, where W is greater than 1 m.s^{-1}. This interface is revealed by the wind field at 150 m high (black arrows) while at 550 m (green arrows) there is a nearly uniform wind from northeast. South of this line, the alternation of updrafts and downdrafts parallel to the front shows the presence of gravity waves (GW).

The black line in Figure 3.15a shows the direction that crosses the front and GW. The coordinate X_{GW} and the velocity component U_{GW} across the GW are defined as positive toward the southeast (Zone B). Figures 3.16a, 3.16b, and 3.16c show U_{GW}, θ_v and Ri (Equation 1.29), respectively, in this cross-section at 1200 UTC.

The distribution of U_{GW} (Figure 3.16a) shows convergence near the surface (about 5 m.s^{-1}) that gradually decreases with height up to 250 m. Figure 3.16b shows a horizontal gradient of θ_v across the front. The potential temperature is lower in Zone B, indicating a higher density. θ_v generally increases with height so that the ABL is thermally stable, which is confirmed by the positive values of Ri (Figure 3.16c) throughout most of the cross-section. A convective layer is present below 50 m, due to a sea-surface temperature slightly higher than that of the air. Thus, the B-C front separates two strongly stratified layers with different

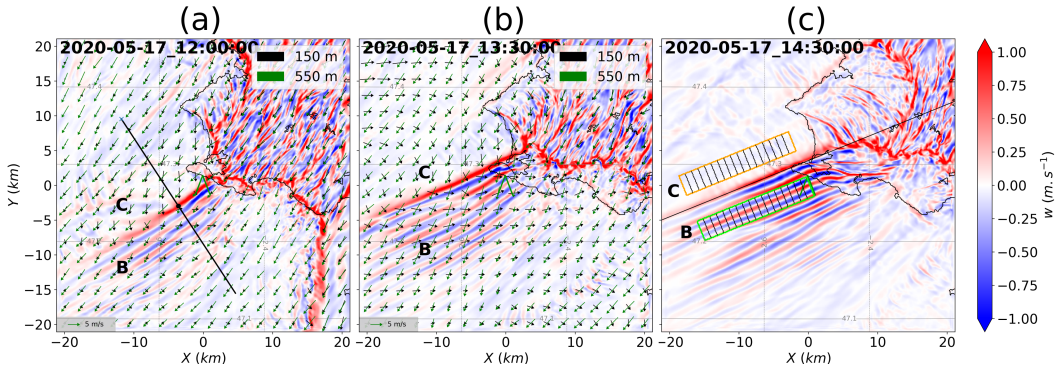

FIGURE 3.15 – Horizontal cross-section of W at 150 m at (a) 1200, (b) 1330, and (c) 1430 UTC on May 17 based on d05 results. Arrows represent the horizontal velocity at (black) 150 m and (green) 550 m. The black line in (a) indicates the vertical cross-section used in Figure 3.16 and the black dot corresponds to X_{GW}=0. The black line and the black and green rectangles in (c) are used to study the GW characteristics.

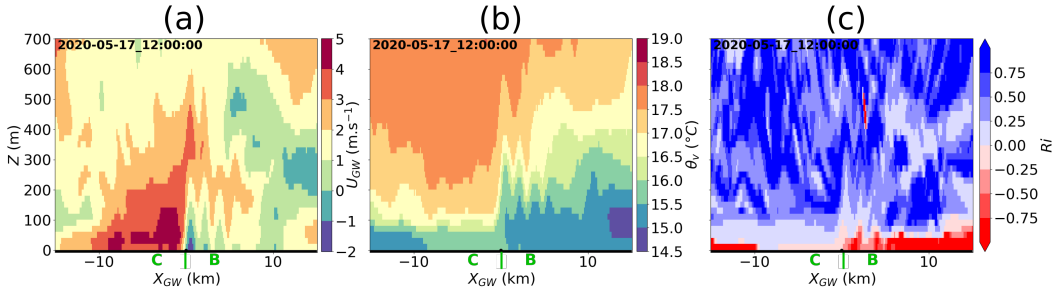

FIGURE 3.16 – Vertical cross-section of (a) U_{GW}, (b) θ_v, and (c) Ri based on d05 results at 1200 UTC on May 17. The position of the vertical cross-section is shown in Figure 3.15a.

densities. In the reference frame of layer C, layer B behaves like a gravity current that propagates beneath layer C, as shown in the works of White and Helfrich (2012) and Rottman and Simpson (1989) (see Section 1.5.3). The front between these two layers generates a perturbation in W, which propagates within and above layer B as gravity waves, thus classifying this phenomenon as an "atmospheric undular bore". The presence of an atmospheric undular bore can generally be revealed by the observation of cloud bands. Unfortunately, no cloud were observed this day on satellite observations (from the Suomi National Polar-orbiting Partnership at 1240 UTC). However, wave patterns being clearly discernible close to the surface, LiDAR data are analyzed in Section 3.2.3 to confirm the presence of GW.

3.2.3 Evidence of gravity waves in LiDAR measurements

Two types of LiDAR scans are used to reveal the presence of GW, horizontal PPI scans at 21 m (Figure 3.17), and vertical scans of W (Figure 3.18a).
The SBF passage is observed in Figure 3.17 during the period from 0931 to 0947

UTC, as a significant separation between positive *RWS* values (away from the LiDAR) in the northern part of the area, and negative *RWS* values (toward the LiDAR) in the southern part. The SBF progresses northward and reaches the LiDAR location around 0950 UTC. At this time, the updrafts related to the SBF passage are observed in Figure 3.18a up to 650 m high, and the first *WD* shift is observed in Figure 2.10 (shift to southwest).
Between 1020 UTC and 1050 UTC, horizontal variations in *RWS* become apparent in Figure 3.17. There is an alternation between highly negative values and low negative or positive values, forming northeast-southwest oriented stripes. Between 1020 and 1028 UTC, the most negative stripe remains stationary at the LiDAR location, while another weaker stripe extends from coordinates (-1 km, -1.5 km) to (0.5 km, 0 km). Between 1028 UTC and 1044 UTC, the main stripe moves toward the southeast. An alternation of updrafts and downdrafts is observed in Figure 3.18a up to 400 m high during the same period, confirming that they are the signature of GW.
At 1100 UTC, *RWS* is positive almost everywhere, and the wind vectors shows that the wind comes from the northwest. This time corresponds to the second *WD* shift observed in Figure 2.10 (shift to northwest). After that, no more oscillation of *W* is observed in Figure 3.18a.

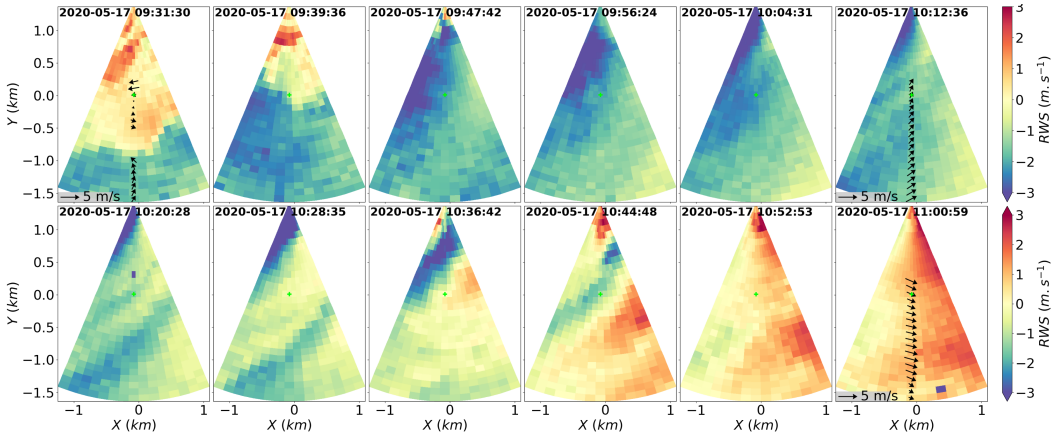

FIGURE 3.17 – *RWS* measured by the LiDAR at 21 m high on May 17 between 0931 and 1100 UTC. The time step between consecutive figures is approximately 7 minutes. For clarity, black arrows represent the wind vector reconstructed at several ranges based only on the instantaneous data. The virtual mast position corresponds to (X, Y) = (0, 0)

Based on the joint analysis of Figures 3.13, 3.17, and 3.18, it is likely that the discrepancies in *WD* between WRF simulations and LiDAR measurements during Phase 3 (Figure 2.11) result from a misrepresentation of the secondary front (B-C interface) position. In WRF-LES results, the local SB of Zone C (associated with northwest winds) arrives at the LiDAR location before the local SB of Zone B (associated with southwest winds). This explains why *WD* shifts first to the northwest and then to the southwest in Figure 2.11. In the LiDAR observations, the wind

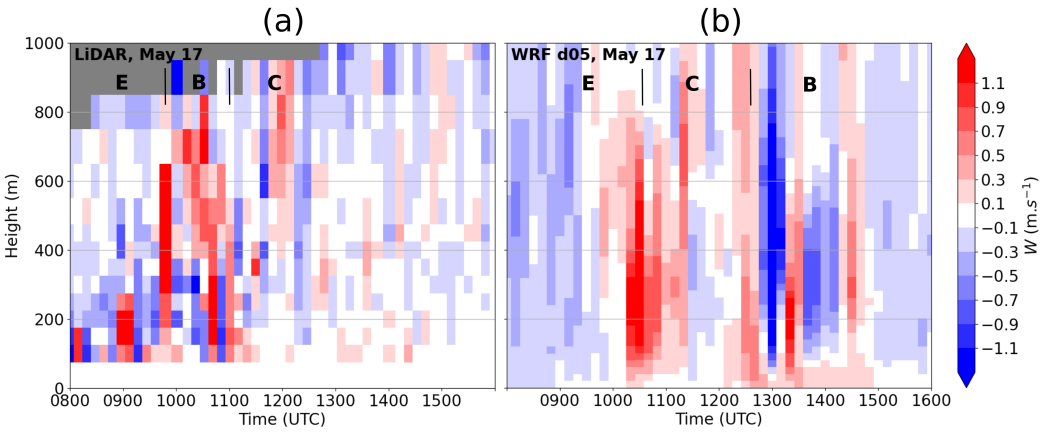

FIGURE 3.18 – Time-height plot of W on May 17 at LiDAR location in LiDAR measurements (a) and in WRF d05 results (b). WRF results are averaged over 10-min windows whereas LiDAR measurements are taken only during 5 seconds. The grey area indicates discarded data due to a poor CNR. Letters, corresponding to the zones defined in Figure 3.13, are explained in the text

initially shifts toward the southwest before turning northwest, suggesting that the local SB from Zone B arrived at the LiDAR first. This is consistent with the fact that the GW are observed between the two *WD* shifts in LiDAR measurements (Figure 3.17 and 3.18) and that they move southwest (Figure 3.17). After 1100 UTC, measurements reveal features from Zone C, i.e. a northwest wind direction and no GW.

Knowing this, it is easier to compare the evolution of W between measurements (Figure 3.18a) and WRF results (Figure 3.18b) at the LiDAR position. In WRF results, the SBF passage can be identified at 1030 UTC by the strong updrafts up to 700 m high. Then, between 1100 and 1200 UTC, no oscillations are observed because Zone C is over the LiDAR position. Finally an alternation of updrafts and downdrafts up to 800 m high is observed between 1200 and 1500 UTC, after the passage of the secondary front. Notably, the oscillations of W in Figure 3.18 extend to higher altitudes in the simulation (1 km) than in the measurements (400 m). It is possible that the difference in GW depth between the WRF results at 1300 UTC and the LiDAR measurements at 1030 UTC is primarily due to differences in the size of the local breeze in Zone B at these times. Indeed, the behavior of gravity waves is strongly influenced by atmospheric stability, and in a SB configuration, the interface between the gravity current (sea wind) and the return current (land wind) is characterized by a stable layer, driven by the temperature difference between the two air masses. Therefore, the shallower SB at 1030 UTC could explain the shallower gravity waves observed at that time. Despite the differences between simulations and measurements, all these observations are coherent with the presence of the atmospheric bore and gravity waves.

table of content

3.2.4 Evolution of the gravity waves characteristics

The main GW characteristics, i.e. the wavelength (λ_{GW}), the amplitude of W oscillations (A_W), the wave speed (S_{GW}), and its direction (α_{GW}), are computed based on the distribution of W at 300 m high in a rectangular region defined in Zone B for X_{GW} between 2 and 5 km behind the front (green box in Figure 3.15c). α_{GW} is determined using the mean direction of the horizontal gradients of W, indicating a direction perpendicular to the front and the waves (i.e. direction of X_{GW} in meteo convention). The wavelength λ_{GW} is calculated from an autocorrelation of W. The wave propagation speed S_{GW} is obtained from a correlation of W between two successive simulation output. Finally, A_W is calculated in each computational cell using the spatial standard deviation of W as

$$A_W = \sqrt{2(\widetilde{W^2} - \widetilde{W}^2)} \tag{3.3}$$

where the tilde notation $\widetilde{\cdot}$ represents a horizontal Gaussian filter with a standard deviation of 1 km. This expression corresponds to the amplitude of a sine wave where the filtering is used as a spatial averaging operator.

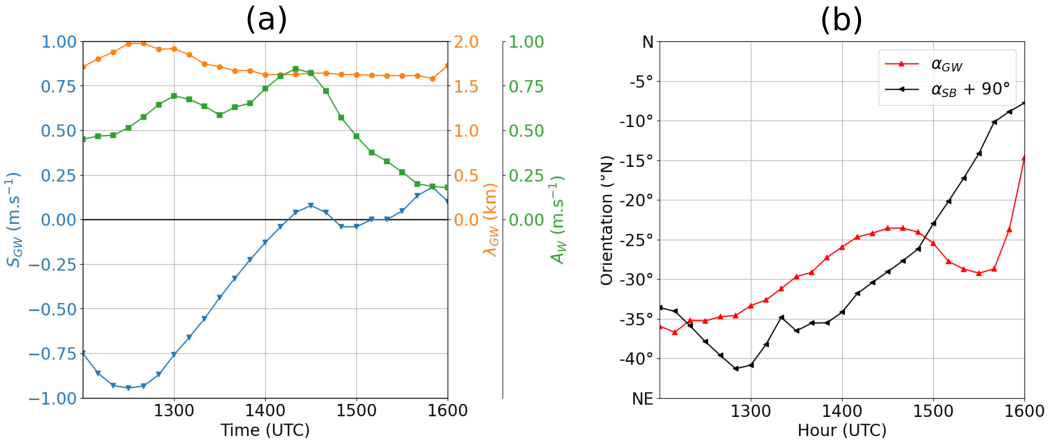

FIGURE 3.19 – (a) Temporal evolution of the gravity wave characteristics between 1200 and 1600 UTC on May 17 : (blue) S_{GW}, (orange) λ_{GW}, and (green) A_W. (b) Same as (a) for (red) α_{GW} and (black) α_{SB}

Figure 3.19a shows the time evolution of S_{GW}, λ_{GW}, and the amplitude A_W, averaged over the green-box region. The wavelength varies only slightly : it reaches a maximum of about 2 km at 1230 UTC, then decreases to 1.6 km at 1400 UTC and remains constant afterward. A_W grows slowly in the early afternoon, peaking around 0.8 m.s^{-1} at 1420 UTC, before decreasing sharply to nearly zero at 1600 UTC. The front moves to the northwest, reaching a maximum speed of 0.95 m.s^{-1} at 1230 UTC. This speed gradually decreases and becomes negligible after 1400 UTC.

Figure 3.19b shows the comparison between α_{GW} and α_{SB}, computed with the method defined in Section 3.1.3 based on the averaged wind profile in the green-box

table of content

region. Interestingly, both α_{GW} and α_{SB} rotate clockwise during the afternoon, so that the cross-GW direction is always oriented perpendicular to the SB direction (within 15 °). As the bore is generated by the convergence between two local SBs, it is not surprising that it rotates simultaneously with the local SB.

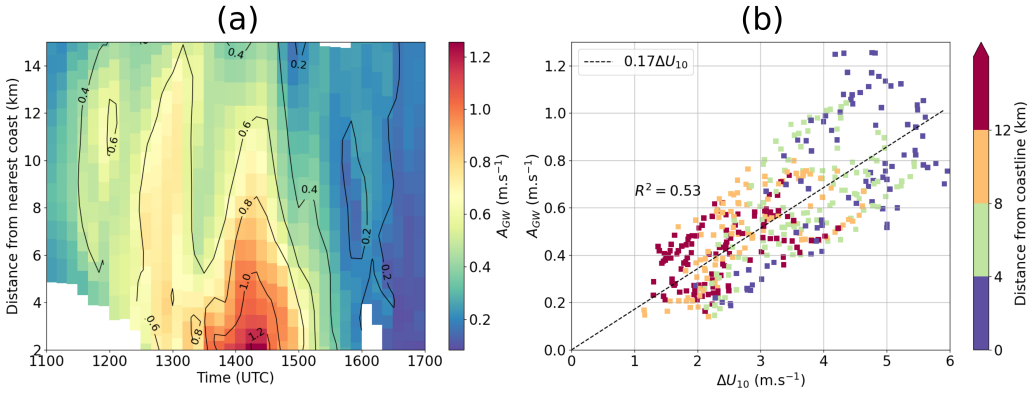

FIGURE 3.20 – (a) Color plot and isocontours of the gravity wave amplitude (A_{GW}) as a function of time and distance from the coast on May 17. (b) A_{GW} as a function of the normal wind speed difference across the front at 10 m, ΔU_{10}. A_{GW} is the maximum value of the A_W profile. Colors indicate the distance from the coast.

The wave amplitude A_W varies in both space and time. To study this variation, the green-box region in Figure 3.15c is subdivided into 1km-wide blocks (approximately 220 cells per block) along the front. The vertical profile of A_W is averaged in each block, and the maximum value in the profile is referred to as A_{GW}. Figure 3.20a shows the evolution of A_{GW} as a function of time and distance from the coast. The amplitude decreases with distance, regardless of the time of day. It also tends to increase over time until 1420 UTC and then decreases, regardless of the distance. As for A_W in Figure 3.19 a second maximum is observed at 1300 UTC between 4 and 14 km from the coastline, followed by a minimum at 1330 UTC. The reason for this minimum appears to be a perturbation in the GW near coordinates (-10 km, -5 km) that lies within the studied region (see Figure 3.15b).

In Figure 3.15c, an orange-box region is defined outside the GW (in Zone C) for X_{GW} between -2 and -5 km (symmetrical of the green-box region with respect to the front). It is also subdivided into blocks, that enable to calculate ΔU_{10}, the difference of U_{GW} at 10 m between each pair of blocks, which is related to the convergence across the front. Figure 3.20b illustrates the evolution of A_{GW} as a function of ΔU_{10} for every pair of blocks between 1200 and 1600 UTC. An approximately linear relationship between A_W and ΔU_{10} is found for all distances. The dashed line represents a linear fit to the scatter plot, with a slope of 0.17. This result shows that the amplitude of the perturbations is linked to the horizontal convergence across the front. The correlation between convergence and wave amplitude can be explained as follows : the convergence generates a vertical velocity component at

the front, through the principle of mass conservation, that serves as the disturbance that initiates the wave.
The correlation between A_{GW} and ΔU_{10} suggest that the spatio-temporal variations of A_{GW} are related to the evolution of the local SBs in Zones B and C. The increase of A_{GW} between 1100 and 1420 UTC is probably related to the strengthening of the local SBs on either side of the front. Afterward, as the SB scale increases (Figure 3.8a), the local effect of the coast diminishes, the front becomes less significant, and the local SBs merge into a regional SB, explaining the decrease of A_{GW} after 1420 UTC. The decrease in amplitude with increasing offshore distance can be attributed to WS_{SB} (Figure 3.9), and therefore the convergence, also decreasing with offshore distance.

3.2.5 Absence of gravity waves on May 18

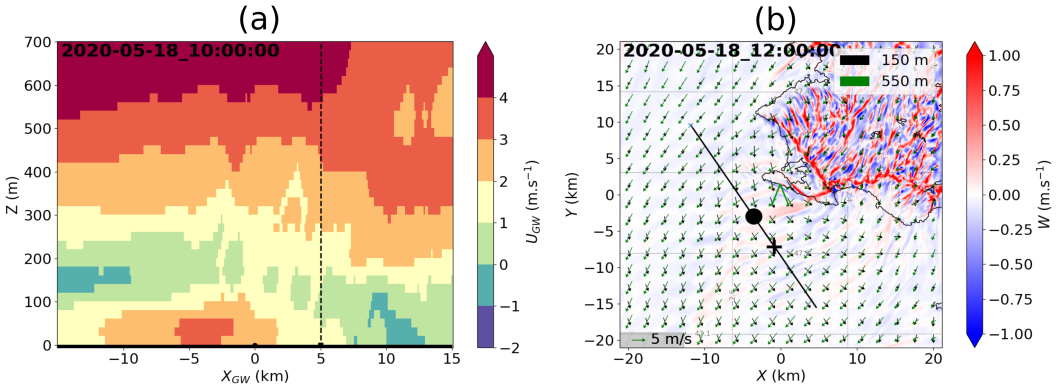

FIGURE 3.21 – (a) Same as Figure 3.16a at 1000 UTC on May 18 and (b) same as Figure 3.15a on May 18

On the next day (May 18), the synoptic wind conditions are approximately similar to those of May 17, with a slightly lighter synoptic wind from the northeast (Figure 2.8). Evidence of SB initiation is provided in Figure 2.11 and in Figure 3.21a where the vertical cross-section of U_{GW} reveals the presence of convergence near the surface at 1000 UTC on May 18. Surprisingly, no gravity waves are observed on this day, neither in LiDAR measurements (not shown) nor in WRF results in Figure 3.21b. Near the LiDAR location, around coordinates (0, 0), the 150 m wind field (black arrows) shows a continuous rotation from north (to the northwest of the LiDAR) to west (to the southeast of the LiDAR) instead of the abrupt transition across the front observed on the previous day.

The offshore θ_v profiles displayed between 0700 and 1200 UTC, on May 17 and May 18 in Figures 3.22a and 3.22b, respectively, show significant differences between the two days. On May 17, the temperature profile consistently increases with height (i.e., the ABL is stably stratified) between 100 m and 700 m, whereas on

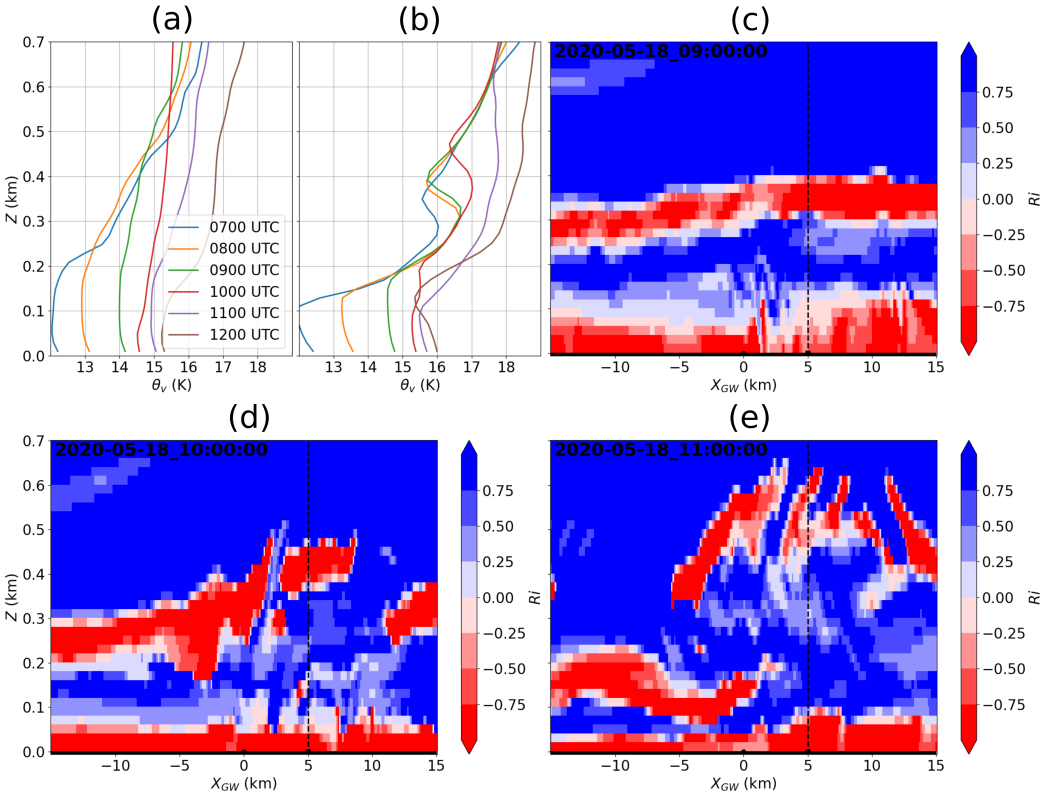

FIGURE 3.22 – Comparison of the offshore θ_v profiles on (a) May 17 and (b) May 18 and vertical cross-section of Ri at (c) 0900 UTC, (d) 1000 UTC, and (e) 1100 UTC on May 18. The line of the cross section is shown in Figure 3.21b and the location of the profiles is indicated with a "+" in Figure 3.21b and with a dashed vertical line in (c), (d), (e), and Figure 3.21a.

May 18, an unstable layer is observed around 350 m between 0700 and 1000 UTC (also visible in Figure 3.22c). At 1000 and 1100 UTC (Figure 3.22d and 3.22e), the thermally unstable layer seems to be destabilized by the convergence that triggers its mixing with the surrounding stable layers. The mixing is also revealed by the more homogeneous profiles of θ_v after 1100 UTC (Figure 3.22b). The mixing of the unstable layer seems to have annihilated the converging front and, consequently, any possibility for a bore and GW to be generated.

The origin of the unstable layer has been investigated by computing backward trajectories (see Section 2.4.4), starting at different vertical levels at 0900 UTC at the same location as temperature profiles. These trajectories, computed from domain d03 results are shown in Figure 3.23. On May 17, all the trajectories are inland. The temperature tends to decrease over time during the night in the ABL with larger θ_v at higher altitude, as expected in the nocturnal SBL. On May 18, the trajectories reveal that the history of the air parcels strongly depends on the height. Below 300 m, the trajectories are from land, resulting in a stable layer between 0 and 300 m high. Above 300 m, the air parcels come from the Channel and are initially colder

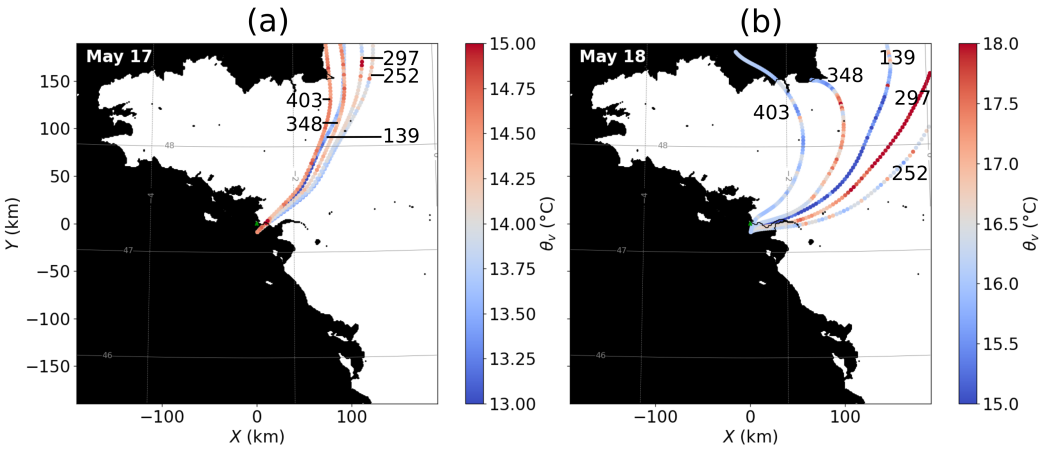

FIGURE 3.23 – Backward trajectories ending at different heights at 0900 UTC on (a) May 17 and (b) May 18 close to Le Croisic. The color shows the evolution of θ_v in the trajectory and the final height (in m) of each trajectories is written in black. The first point of the trajectories (if still in the domain) is at 1500 UTC on the previous day.

than inland. The 348-m air parcels warms up a little in the late afternoon but cools down during the night, while the 403-m air parcel remains colder than the 348-m and 297-m air parcels, explaining the presence of the unstable layer around 350 m high in the morning.

The fact that the trajectories depend on height is a direct consequence of the heterogeneity with height of the wind velocity. Close to the Channel coast, this heterogeneity is probably triggered by the thermally-induced baroclinic pressure gradient. Moreover, the presence of a LLJ at night in this area (Section 5.3), in which by definition the wind varies with height, further explains that the trajectories vary with height. Overall, the comparison between May 17 and May 18 suggests that the presence, or not, of a bore and gravity waves at small scale at Le Croisic is influenced by the wind field on the previous day over the large-scale Brittany peninsula.

3.3 Conclusion of the chapter

In this chapter, an analysis of two SBs near the Southern Brittany coast is presented. Overall, the time evolution of the SB can be summarized as follows. In the morning, several local SBs initiate over several local-scale coast segments. The interface between these SBs is divergent in bays and convergent near peninsulas. At the convergent interface, an undular bore can be generated, depending on the stability conditions. Over time, the local SBs merge into a regional SB, the orientation of which is governed by the coast orientation at larger scale. The SB orientation progressively deviates clockwise from the coast orientation. The offshore extent increases linearly over time until the deviation angle become so large that the wind

direction is mainly parallel to the coast.

As the Southern Brittany coast is complex at several scales, a method is proposed to calculate the coast orientation based on the filtering of the land-sea mask. This method has several advantages : (i) the orientation depends on a scale parameter, (ii) it is defined locally within a certain area, (iii) the method could be applied to any coastline, and (iv) the orientation is defined objectively so that it is reproducible.

The spatial distribution of the SB orientation is studied to quantify the evolving SB scale, i.e. the scale at which the coastline influences the SB orientation. The SB orientation is decomposed into the sum of the coast orientation at a given scale, and a deviation angle. A simple assumption is formulated that the SB scale and the deviation angle are constant over space and depend only on time. Under this assumption, the SB scale and deviation are calculated, and it is found that both the scale and the (clockwise) deviation increase with time. This result is in agreement with the qualitative observation, and with previous studies : the increase of the scale of the coast "felt" by the SB has been mentioned by Simpson (1996), and the clockwise rotation, likely under Coriolis force, is a classical feature of the SB life time (Miller et al., 2003).

The evolution of the SB extent is strongly dissymmetric with a faster expansion offshore than inland. The offshore expansion speed is constant during a few hours, as found by Finkele (1998). However, contrary to the results of Finkele (1998) and Steele et al. (2013), a faster expansion is observed on May 17 when the land synoptic wind was stronger than on May 18. A deeper analysis of the space-time evolution of the pressure forcing, as initiated by Tijm and van Delden (1999), is probably a necessary step toward a better understanding of the increase of the SB extent.

These results must be analyzed with caution as the assumptions are obviously simplistic, and several arbitrary choices were made throughout the calculation (e.g. the method to calculate α_{SB}, the chosen area to compute the standard deviation of δ). In addition, a broader meteorological dataset with SB events at several locations is needed to generalize the conclusion. However, the agreement between the calculation and the observation described in this study and in Simpson (1996), give some in the method. Thus, this study provides an original approach to perform analysis of the SB near a complex coastline, which constitutes a first step toward a unified description of the SB characteristics over different sites. This approach could help, for example, improving the wind forecast during SB events that are currently poorly resolved by the forecasting models (Short, 2020).

During SB initiation on May 17, an atmospheric undular bore and gravity waves are observed near the Guérande peninsula. Despite a few discrepancies between the WRF results and the LiDAR measurements, the direct observation of gravity waves with roughly the same wavelength and orientation gives confidence in the realism of the modeling, thus allowing for a deeper analysis of the bore and the gravity waves

using the simulation results.

The mechanism behind the bore requires (i) a predominantly stable offshore ABL, allowing for the existence of a bore and gravity waves, (ii) conditions for the development of a SB, (iii) a small-scale peninsula-shaped coastline, responsible for the convergence between local SBs. It is suggested that the light synoptic wind from land also helps the existence of the bore by moving the whole SB cell offshore Finkele (1998) where the ABL can be stable. On May 18, conditions (ii) and (iii) are still verified but an unstable layer in the offshore ABL inhibits the formation of the bore, thus confirming the necessity of condition (i) for the presence of a bore.

A similar phenomenon is observed in Australia by Thomsen and Smith (2006) and Noonan and Smith (1986) where a bore is generated after the collision between two SBFs. In these events, the degenerate SBFs collide during the evening, and the bore subsists until the next morning, thus it is referenced as a "Morning glory". In contrast, in the present case, the bore exists only during the early afternoon when the local SBs are still in their development phase, and vanishes before the end of the regional SB event. The GW observed in the present case are also different from the one presented by Rotunno (1983) (Section 1.3.5), that can exist only in equatorial latitudes and can be generated near rectilinear coastlines whereas the present GW are triggered by the peninsula shape at mid-latitudes. Moreover, Rotunno's waves orientation is parallel to the coast while the GW are perpendicular to the coast in the present case. The main characteristics of the present bore also differ in many ways from other bore previously reported in the literature.

— In our case, the bore is almost stationary. Its absolute speed is always lower than 1 $m.s^{-1}$ which is low compared to cold-pool generated bores, e.g. around 17 $m.s^{-1}$ for Martin and Johnson (2008). This low propagation speed suggests that the two local SBs almost neutralize each other so that their convergence line is nearly stationary.

— The wavelength is between 1.5 and 2 km, which is an order of magnitude lower than the typical bore wavelength according to Johnson et al. (2018). This small wavelength is related to the low cross-front wind speed U_{GW} (less than 4 $m.s^{-1}$ in Figure 3.16a), as these two quantities are linked through the GW intrinsic frequency.

— The longitudinal extent of the bore is about 20 km, which is again quite small compared to the few hundreds of kilometers for other studied bores generated by cold pools (Johnson et al., 2018; Zhang et al., 2022) or degenerate SBF (Thomsen and Smith, 2006) in the nocturnal ABL. This width is governed by the SB offshore extent in general because the SB convergence is the main driver of the bore.

— The GW amplitude evolves with time and distance from the coastline. It is related to the convergence across the frontal line which diminishes with the increasing offshore distance. The convergence tends to increase before 1430 UTC as the SB strengthens and diminishes afterward. The decrease of GW

amplitude after 1430 UTC is likely related to the increasing scale of the SB which becomes regional. Consequently, the local SBs merge together and the convergence line vanishes.

Overall, the originality of this bore lies in its generation mechanism, its size, and its timing.

The present chapter provided a description of several phenomena and features related to the SB development involving a large range of scales. In the next chapter, an even smaller scale is investigated through a study of the turbulence within the SB.

table of content

Chapitre 4

Turbulence characteristics in a sea breeze and influence of gravity waves

Introduction

In this chapter, an analysis of the turbulence, and more particularly the TKE, within a SB is presented, based on the LES results. As stated in Section 1.3.6, the turbulence within the offshore part of the SB is not well documented in the literature. Therefore, the first objective is to characterize the offshore TKE profiles within the SB and to determine the mechanisms that drive this TKE.
On May 17, the atmospheric undular bore described in the previous chapter is present during most of the SB lifetime. However, the interaction between GW and turbulence in the ABL, out of the breaking processes, is still poorly documented. Thus, the second objective of the chapter is to study the evolution of turbulence within the GW.
Finally, in Section 1.3.5, it was explained that the evolution of TKE in the return current has almost never been studied directly. However, some analytical models exist to describe the decay of turbulence in a residual layer. Thus, the third objective is to assess the ability of these models to describe the TKE decay in the return current.
Section 4.1 introduces the chapter by describing the wind, temperature and TKE profiles in domain d06 as a function of time and distance from the coastline. In Section 4.2, the turbulence in the middle of the SB cell is analyzed on May 18, when no GW are observed. Then, in Section 4.3, the influence of the GW on the TKE profiles (May 17) is investigated. Finally, an analysis of the turbulence in the return current is provided in Section 4.4.

4.1 Wind and TKE profiles in the sea-breeze

In this section, the TKE is analyzed on May 18, when no GW are observed. To study the TKE as a function of the distance from the coast, the domain d06 is divided into several areas depicted in Figure 4.1. These areas are 3-km long in the direction perpendicular to the 1-km-filtered coastline (red line). The profiles presented in the next figures are averaged over each area.

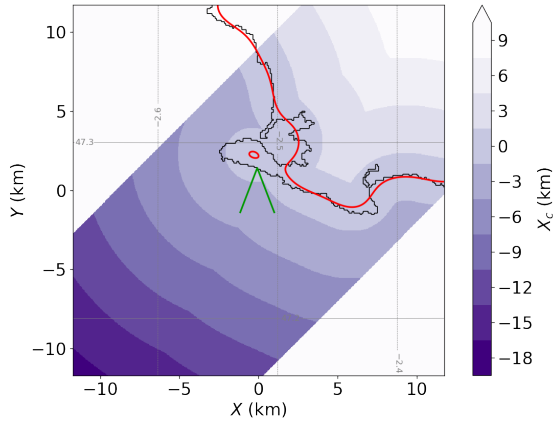

FIGURE 4.1 – Division of the domain d06 into different zones based on the distance from the 1-km coastline shown as a red line. The zones are 3 km long.

4.1.1 Wind profiles in the sea-breeze

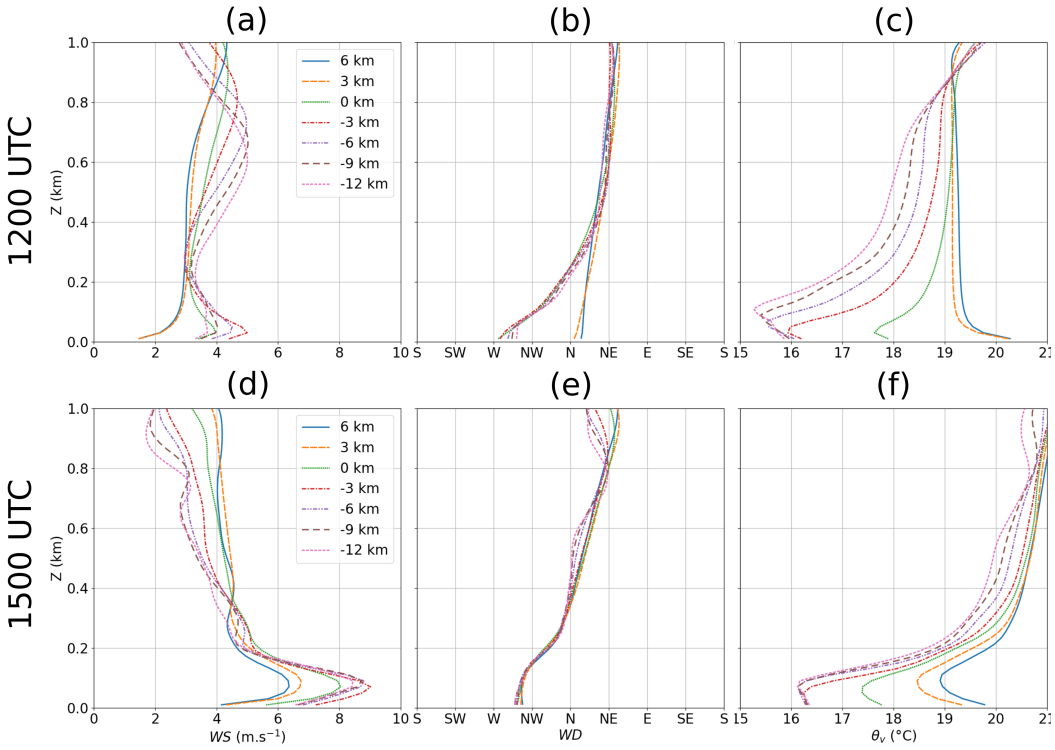

FIGURE 4.2 – Evolution of the profiles of (a, d) *WS*, (b, e) *WD* and (c, f) θ_v as a function of the distance from coastline (X_c in km) on May 18 at (a, b, c) 1200 UTC and (d, e, f) 1500 UTC.

Before studying the TKE profiles, a description of the mean quantities is provided in Figure 4.2, which displays the wind and temperature profiles at 1200 and 1500

table of content

UTC on May 18. At 1200 UTC, the wind direction inland (Figure 4.2b, X_c = 3 and 6 km) evolves only a little between north and northeast but remains from land at every height, indicating that the SB is still mainly offshore. The well-mixed *WS* and θ_v profiles inland (Figure 4.2a and 4.2c) correspond to those of a CBL (Section 1.1.2). Offshore, the shallow SB gravity current is depicted by the westerly winds near the surface. The maximal *WS* in the gravity current (Figure 4.2a) decreases with increasing offshore distance from 5 m.s^{-1} at X_c = -3 km down to 3.5 m.s^{-1} at X_c = -12 km. The θ_v profile shows that the ABL is mainly stable offshore, meaning that the unstable layer at 300 m high described in Section 3.2.5 (Figure 3.22) is not present anymore. The capping inversion can be identified close to 0.9 km high as a larger vertical gradient of θ_v. At 1500 UTC, the *WD* profiles indicate that the SB is present in the whole domain. Inland, the large negative gradient of θ_v below 50 m shows the presence of the convective TIBL, that enhances mixing in the gravity current and causes a *WS* lower than offshore.

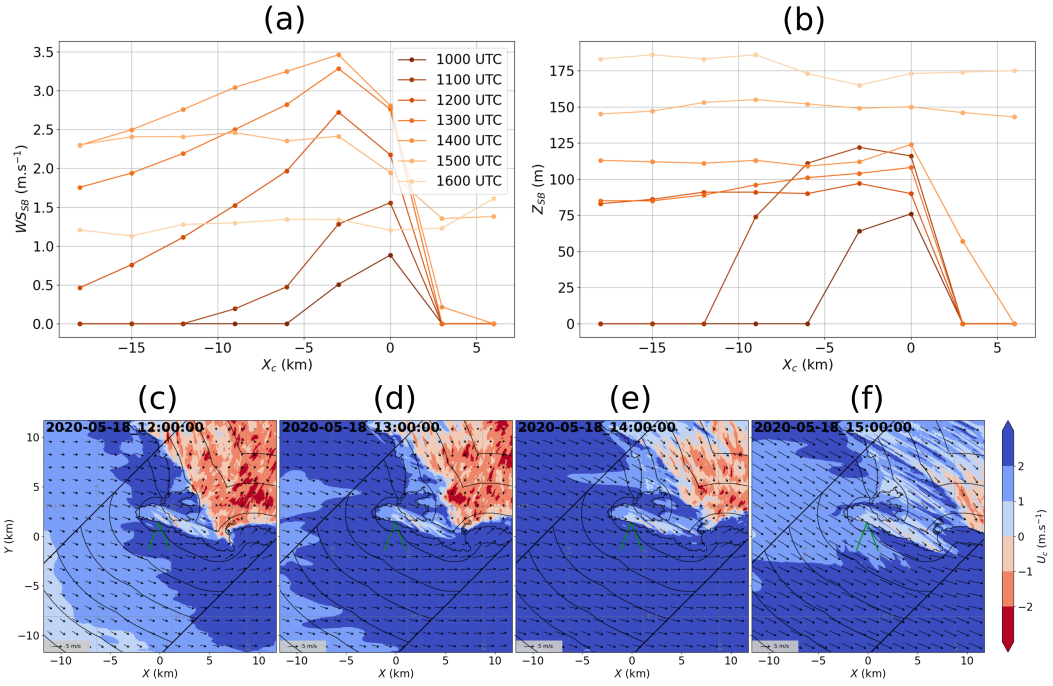

FIGURE 4.3 – Evolution of (a) WS_{SB} and (b) Z_{SB} as a function of X_c at different times on May 18. (c-f) Spatial distribution of U_c at 10 m high in d06 at (c) 1200, (d) 1300, (e) 1400, and (f) 1500 UTC.

The SB characteristics WS_{SB} and Z_{SB} are calculated from the average wind profile with α_c from southwest, which corresponds to the coast orientation at the LiDAR virtual mast for the scale s between 20 and 60 km (Figure 3.3). They are displayed in Figure 4.3a and 4.3b, respectively, as a function of X_c between 1000 and 1600 UTC. The area where $WS_{SB} > 1$ m.s^{-1} illustrates the SB extent. In addition, the spatial distribution of U_c in d06 between 1200 and 1500 UTC is shown in Figures

4.3c to 4.3f. At 1200 UTC, the SB is located mainly offshore. The offshore extent increases quickly and at 1300 UTC it is already larger than 18 km, whereas the SBF is stuck near the coast until 1400 UTC. Between 1400 and 1500 UTC, the SBF progresses rapidly toward the east-southeast so that it covers almost all the domain at 1500 UTC (Figure 4.3f). WS_{SB} at X_c = -3 km progressively increases over time between 1000 UTC and 1400 UTC (Figure 4.3a). During this period, WS_{SB} is decreasing with increasing offshore distance. After 1400 UTC, WS_{SB} decreases over time, because WD has rotated clockwise (Figures 4.2e and 4.3f). All these findings are in agreement with the description of the SB extent in Section 3.1.5. Z_{SB} increases monotonically over time except for an anomaly at 1100 UTC when it is larger than at 1200 UTC at X_c = -3 km (Figure 4.3b). This anomaly is likely caused by the strong mixing enhanced by the unstable layer described in Section 3.2.5. After 1100 UTC, Z_{SB} is homogeneous offshore.

4.1.2 TKE profiles in the sea-breeze

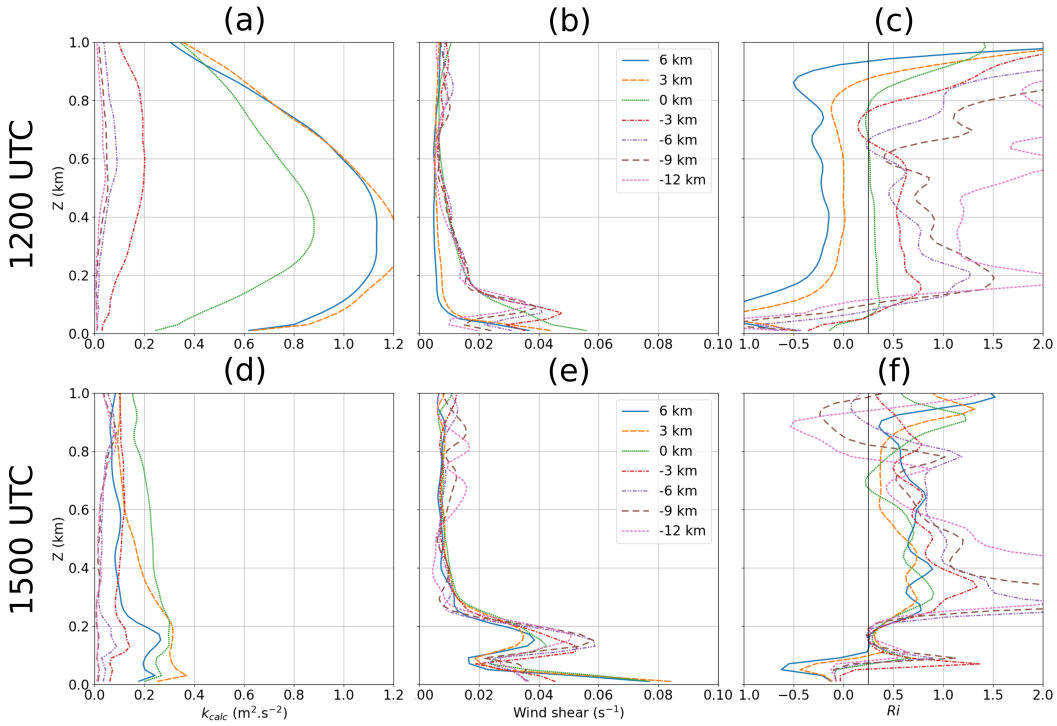

FIGURE 4.4 – Same as Figure 4.2 but for (a, d) k_{calc}, (b, e) the wind shear and (c, f) Ri.

The resolved TKE (k_{calc}) profiles as a function of the offshore distance at 1200 and 1500 UTC are displayed in Figures 4.4a and 4.4d, respectively.
At 1200 UTC, the inland k_{calc} exhibits a rounded profile with low values close to the surface and at the top of the ABL, and a maximum value between 0.8 and 1.3 $m^2.s^{-2}$ at 350 m high. Offshore, k_{calc} is much lower and decreases with increasing

distance. It also exhibits a maximum around 600 m high. At this moment, the SB has not reached the land areas yet. Thus the large TKE inland is caused by the mixing in the CBL. This is confirmed by the negative Ri shown in Figure 4.4c. Offshore, Ri is positive and mostly larger than 0.25 (black line), indicating stable conditions with low turbulence. Thus, the larger TKE at X_c = -3 km than farther offshore is likely a residual turbulence advected from the CBL.
At 1500 UTC, the SB covers most of the domain so that k_{calc} is significantly lower at every location. Below 100 m, a larger value is found inland because of the convective TIBL, that is revealed by the highly negative Ri (around -0.5 in Figure 4.4f). Interestingly, another maximum of k_{calc} is found at 150 m high where the shear is the largest (Figure 4.4e) and where Ri reaches a local minimum close to 0.25. This large shear is caused by the SB gravity current and the return current moving in opposing direction, which is confirmed by the height of the k_{calc} peak matching well with Z_{SB} shown in Figure 4.3b. This peak of TKE will be analyzed in the next section.

4.2 Analysis of the turbulence in the center of the sea-breeze cell

4.2.1 Height and occurrence of the turbulence peak

In this section, the peak of resolved TKE in the middle of the SB cell is analyzed with a focus on its occurrence, the mechanism behind it, and the characteristics of turbulence at this height. To obtain a more precise information on the occurrence of the peaks, the areas used in Section 4.1 are subdivided into several blocks, depicted in Figure 4.5a. Each block is composed of at least 1000 computational cells, and is about 1 km long in the cross-coast direction and 3 km wide in the along-coast direction. At every time step, the k_{tot} profile is averaged in each block and a peak is searched below 400 m. Peaks with a prominence (SciPy, 2025) lower than 0.03 $m^2.s^{-2}$ are discarded and, when multiple peaks are found, the one with the largest k_{tot} is selected. Figure 4.5b shows the distribution of the detected peak within the SB as a function of X_c and the hour on May 18. Inland, a peak is detected in almost every k_{tot} profile because large values of k_{tot} are triggered by convection in the TIBL. Offshore, the presence of a peak is intermittent. Notably, between 1600 UTC and 1700 UTC, a peak with a value larger than 0.1 $m^2.s^{-2}$ is detected in many blocks, whereas at 1700 UTC no peak is found.

The comparison between Z_{SB} and the height of the peaks for X_c < -2 km, shown in Figures 4.5c and 4.5d, reveals that more than half of the peaks are found within 50 m of Z_{SB} (between the dashed lines). A significant amount of peaks are detected below 50 m, in the atmospheric surface layer. Out of the most intense peaks (larger than 0.5 $m^2.s^{-2}$), the majority are found between -2 and -8 km (77 %, Figure 4.5c) and between 1600 and 1700 UTC (93%, Figure 4.5d).

table of content

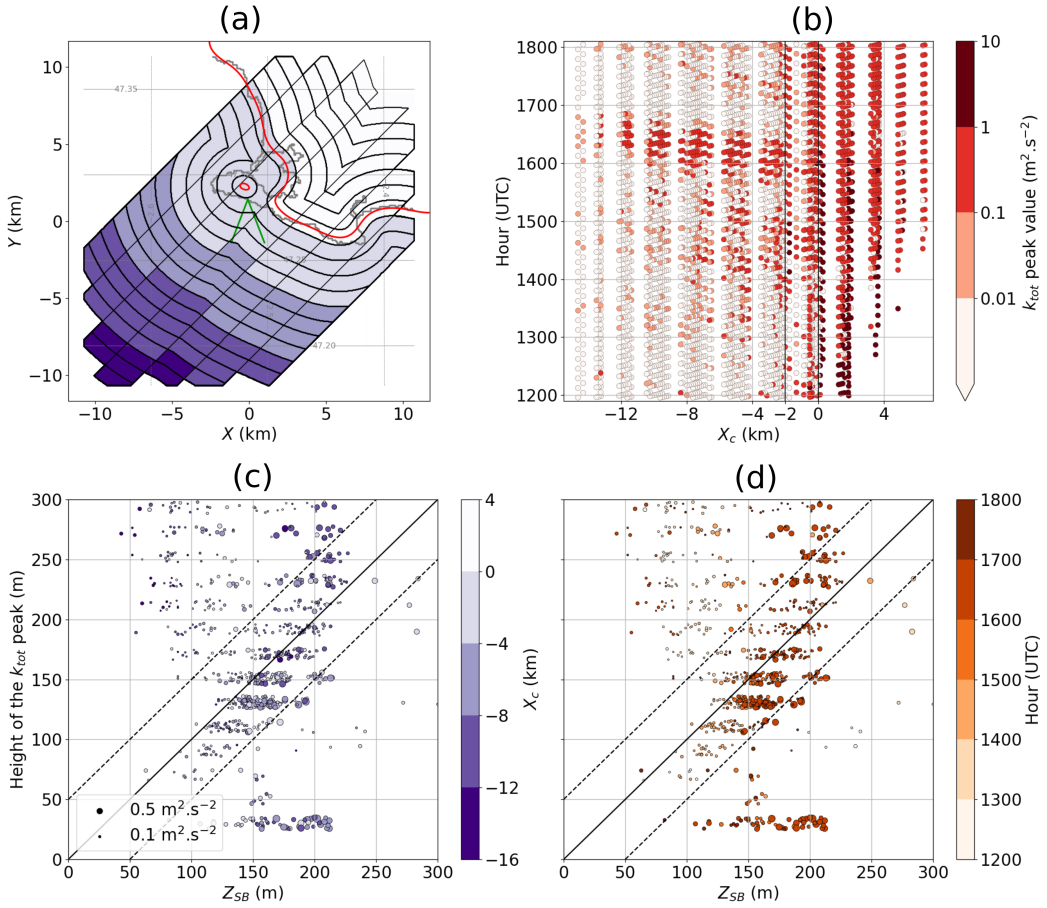

FIGURE 4.5 – (a) Division of the domain d06 into 122 blocks based on the distance from the 1-km coastline (red line). (b) Time-distance plot of the detected peaks in the k_{tot} profiles on May 18. The color indicates the peak value and white dots correspond to the absence of a peak. The position of the dots is slightly shifted to improve readability, and no dot is shown where there is no SB (bottom right). (c,d) Scatter plot of the height of the detected peaks of k_{tot} as a function of Z_{SB} for blocks that are located at least 2 km offshore. The color indicates the distance from coastline in (a, c) and the hour of the day in (d). The size of the dots is proportional to the intensity of the peak as shown in the legend of (c). The dashed lines correspond to Z_{SB} +/- 50 m.

The intermittent nature of k_{tot} is observable in its spatial distribution shown in Figure 4.6. Inland, the large k_{tot} is caused by convective structures in the TIBL, which is out of the scope of this section. Offshore, its value is below 0.1 m^2.s^{-2} except for a few patches, highlighted by black circles, where it is larger. A first patch is shown at 1510 UTC, being about 8 km wide. Larger patches are observed at 1610 UTC and 1620 UTC where k_{tot} exceeds 0.5 m^2.s^{-2}. The similar extent between the two latter patches suggest a continuity between them. This would mean that the patch is moving toward south-southeast and that the amplitude of k_{calc} is decreasing.

Two squares, within and outside the patch, are defined in Figure 4.6c where the

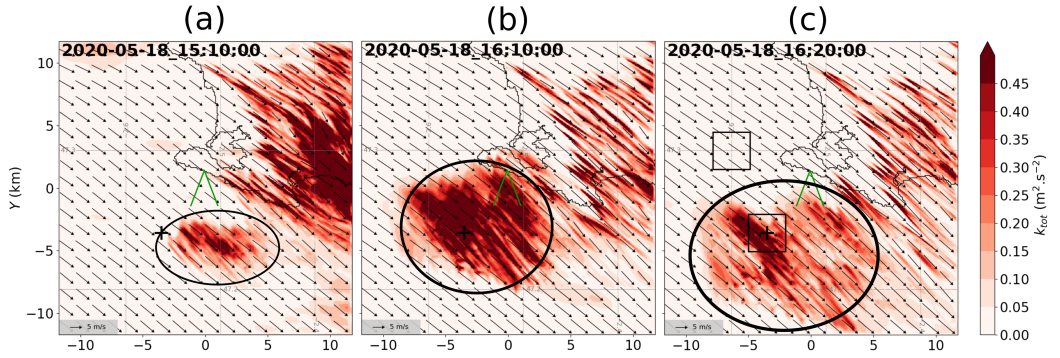

FIGURE 4.6 – Spatial distribution of k_{tot} in d06 at 130 m high, at (a) 1510 UTC, (b) 1610 UTC and (c) 1620 UTC. The circles denotes the position of the offshore patches. The "+" is referred to in Figure 4.10. The squares are used to average the profiles at 1620 UTC shown in Figure 4.7.

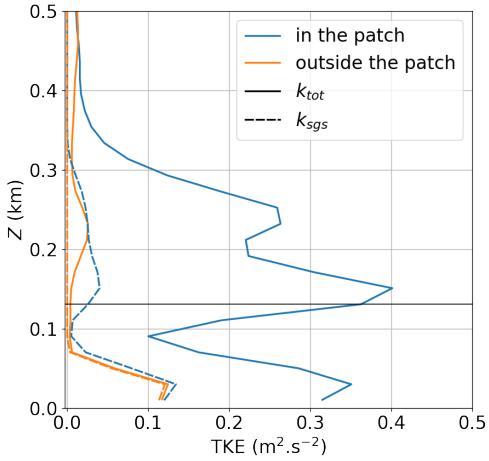

FIGURE 4.7 – Comparison of the TKE profiles within and outside the patch (the two squares in Figure 4.6) at 1620 UTC on May 18. The horizontal line shows the height of the cross-section in Figure 4.6

average profiles of k_{tot} and k_{sgs} at 1620 UTC are shown in Figure 4.7. Below 50 m, a significant maximum of k_{tot} is observed in both areas, which is fully subgrid out of the patch whereas more than 50 % of it is resolved in the patch. More interestingly, within the patch, the k_{tot} profile exhibits a peak at 150 m high where k_{tot} is ten times larger than outside the patch. A peak is also observed outside the patch at 230 m high, but with a lower amplitude (0.03 m^2.s^{-2}).

To determine the relative importance of these strongly turbulent events in the average k_{tot}, the maximum in the k_{tot} profile between 130 and 210 m high is taken in each computational cell located more than 2 km offshore and at each time step between 1200 and 1800 UTC. Figure 4.8 shows the proportion of the average k_{tot} generated by the most turbulent events. Almost half of the average k_{tot} is generated

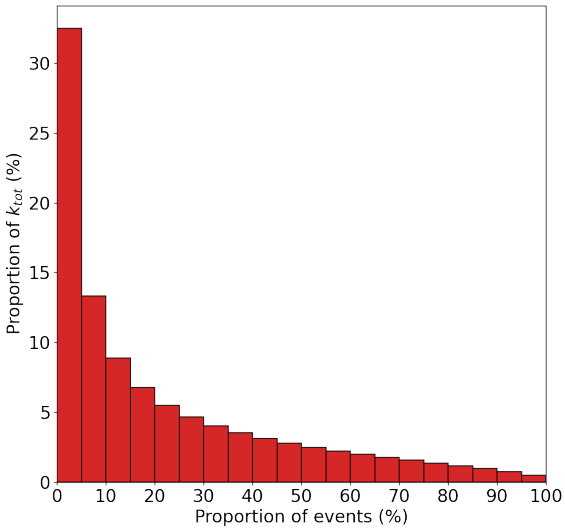

FIGURE 4.8 – Proportion of the total TKE generated by the most turbulent events.

by the 10 % most turbulent events while the 40 % least turbulent events generates only 10 % of the average k_{tot}. This figure emphasizes the strong heterogeneity of k_{tot} in the center of the SB cell.

Thus, the peak in the k_{tot} profile in the center of the SB cell shown in Figure 4.4d is mostly due to a minority of strongly turbulent patches. In the next section, these patches are more closely investigated.

4.2.2 Kelvin-Helmholtz instability

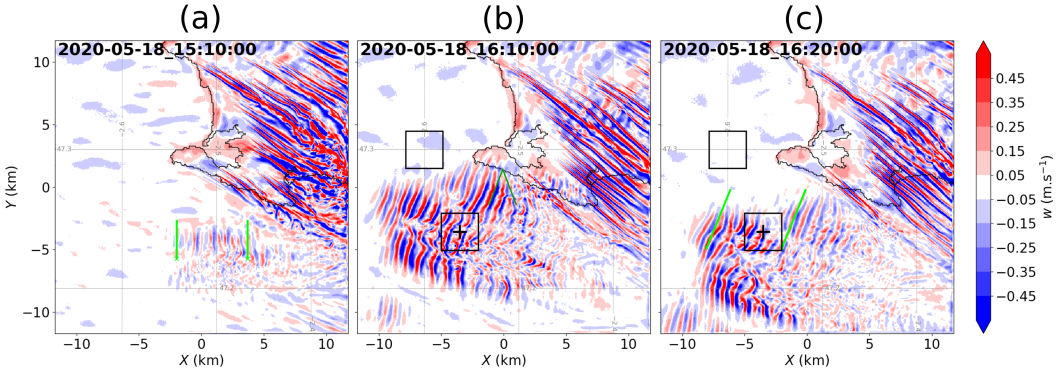

FIGURE 4.9 – Spatial distribution of the instantaneous vertical wind speed w in d06 at 130 m high, at (a) 1510 UTC, (b) 1610 UTC and (c) 1620 UTC. The "+" is referred to in Figure 4.10. The squares are used to average the profiles shown in Figures 4.7 and 4.12. The green lines are used to determine λ_{KH} and α_{KH}

table of content

To investigate the nature of the patch, the distribution of the instantaneous vertical velocity field (w) is displayed in Figures 4.9a to 4.9c. Oscillations of w are identified offshore, revealing the wave nature of the patch. At 1620 UTC, a part of the waves is disturbed and breaks down near coordinates (0, -7 km). It is recalled here that the 10-minute statistics presented at 1620 UTC (e.g. k_{tot} in Figure 4.6c) are computed between 1610 UTC and 1620 UTC. Thus, Figures 4.9b and 4.9c show that the southern squared area is located within the waves between 1610 and 1620 UTC, while the other one is outside the waves for the same period.

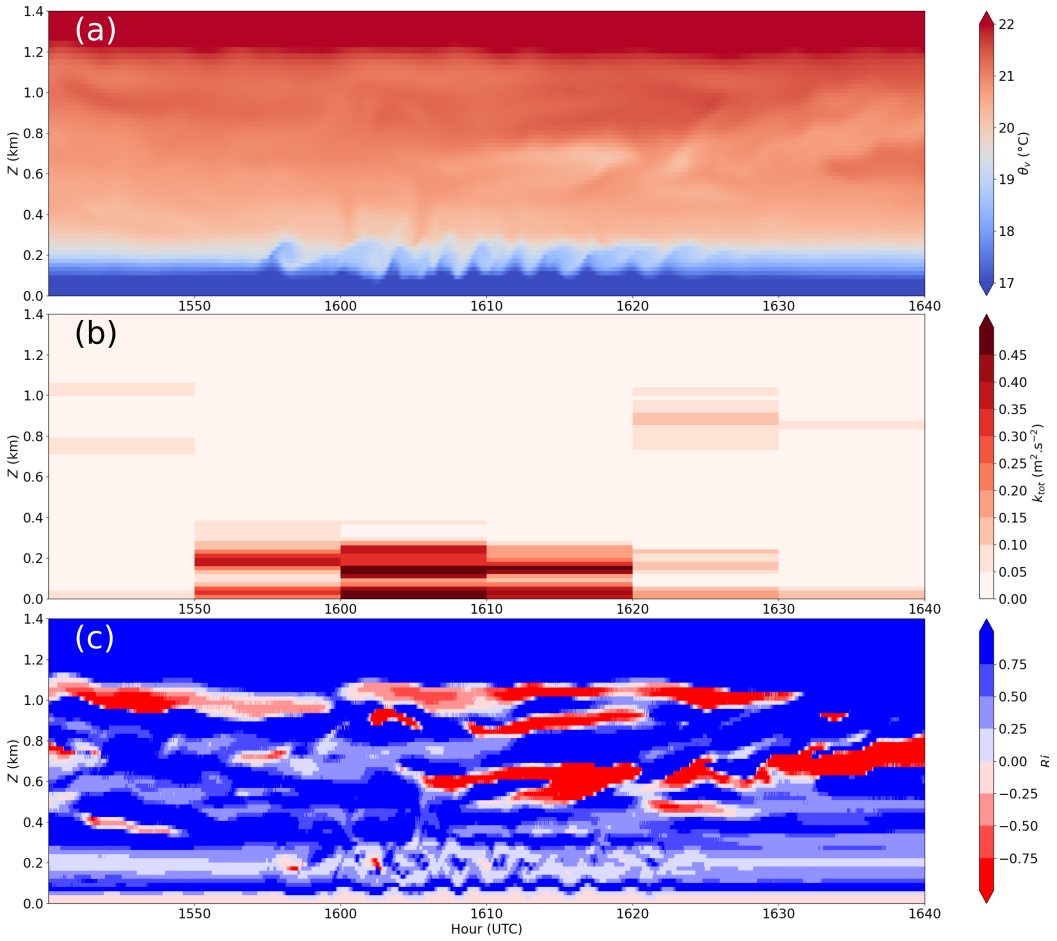

FIGURE 4.10 – Time-height evolution of (a) the instantaneous θ_v, (b) k_{tot}, and (c) the instantaneous Ri, at the location of the "+" shown in Figure 4.6.

The waves are detected in the distribution of w (instantaneous) but not in that of W (10-minute averaged, not shown), indicating that they are filtered out by the 10-minute averages. For that reason, Figure 4.10a shows the time evolution of the instantaneous θ_v profile between 1500 and 1640 UTC (saved with the *wrf_timeseries* feature), at the location of the "+" in Figures 4.6 and 4.9. At 1540, the θ_v profile shows a cold layer below 200 m, corresponding to the SB gravity current and a

warmer layer between 200 and 1.2 km high, corresponding to the SB return current. The stable discontinuity at 1.2 km high corresponds to the capping inversion. Waves are discernible between 1555 and 1625 UTC at 150 m high, which is consistent with the one described in Figures 4.9b and 4.9c. Again, the location of the waves matches with that of the largest k_{tot} shown in Figure 4.10b. Figure 4.10c shows Ri calculated with the instantaneous shear and temperature gradient. At the height of the waves, Ri is below the critical value of 0.25. Moreover the waves have billow shapes (Figure 4.10a), well-pronounced at 1555 UTC. All these statements indicate that the waves are generated by Kelvin-Helmholtz-like instabilities (see Section 1.5.1) that develops when the shear is strong enough to overcome the stability.

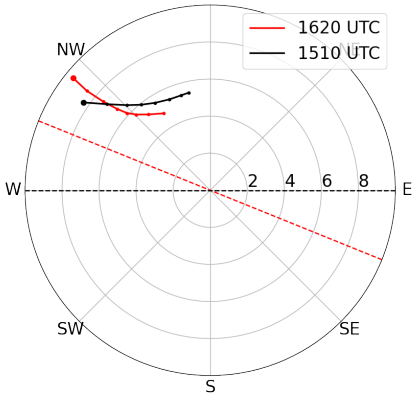

FIGURE 4.11 – Hodograph of the wind profile between the green lines of Figure 4.9a and 4.9c, from 110 m high (biggest dot) to 250 m high. The dotted lines show the waves direction, perpendicular to the green lines.

Their wavelength λ_{KH} and orientation α_{KH} are determined at 1510 UTC and 1610 UTC by placing two lines parallel to the waves as shown in Figures 4.9a and 4.9b. It is found that $\lambda_{KH} = 628$ m at 1510 UTC and 928 m at 1610 UTC, which is consistent with other KH studies during SB events (Section 1.3.5). Their aspect ratio, being about 4, is larger but of the same order of magnitude than the 1.7 proposed by Simpson and Britter (1980). Figure 4.11 presents the hodograph of the wind profiles from 110 to 250 m high, where the orientation of the profile indicates the direction of the vertical wind shear. This direction corresponds well to that of α_{KH} depicted by the dashed lines, which comfort the fact that the waves are generated by KH instability.

4.2.3 Turbulence in the Kelvin-Helmholtz billows

The components of k_{calc} at 1620 UTC within and outside the KH waves (KHW) are displayed in Figure 4.12a and 4.12b, respectively, with u_{KH} the velocity com-

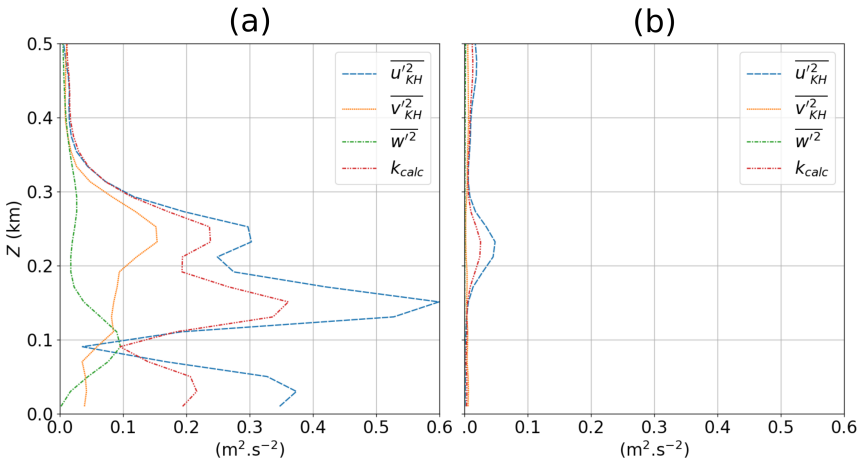

FIGURE 4.12 – Profiles of $\overline{u'^2_{KH}}$, $\overline{v'^2_{KH}}$, $\overline{w'^2}$, and k_{calc} averaged over the squares, shown in Figure 4.9c, (a) within and (b) outside of the KH waves, at 1620 UTC on May 18.

ponent in the direction crossing the waves (direction of α_{KH} and direction of the shear) and v_{KH} the component in the direction along the waves, parallel to the green lines in Figure 4.9c. Within the KHW, $\overline{u'^2_{KH}}$ is the largest velocity variance almost at every height, and is the major contribution to k_{calc}. At 150 m high, it is about 6 times larger than $\overline{v'^2_{KH}}$. Around 100 m high, $\overline{w'^2}$ exhibits a peak of 0.1 $m^2.s^{-2}$ and $\overline{u'^2_{KH}}$ a minimum of 0.05 $m^2.s^{-2}$. Out of the waves, k_{calc} is very small except at 230 m high, as also observed in Figure 4.7, where the main component is also $\overline{u'^2_{KH}}$, the component in the shear direction.

The time-height evolution of u_{KH} at the same location as in Figure 4.10 is shown in Figure 4.13a. The same wave pattern as in the evolution of θ_v (Figure 4.10a) is observed at 151 m high. This is more clearly visible in Figure 4.13b where u_{KH} at 151 m high shows a nearly harmonic evolution between 1608 and 1622 UTC. Interestingly, u_{KH} at 30 m high also displays a wave pattern that explains the large TKE observed near the surface in Figure 4.12a. These oscillations are out of phase compared to that at 151 m high, whereas the oscillations of w at the two heights are in phase (not shown), indicating that they are due to the interaction between the KHW and the surface. Indeed, close to the surface, the amplitude of the w oscillations is lower than at 100 m high so that the vertical gradient of w is positive in the ascending phase and negative in the descending phase of the wave. Thus, the mass continuity implies a horizontal convergence (divergence) in the ascending (descending) phase, resulting in oscillations of u_{KH}. A similar mechanism may generate rotors below orographic GW (Ralph et al., 1997).

It seems important to discuss the definition of turbulence as it is clear from Figure 4.13b that the oscillations of u_{KH} are caused by the passage of the waves. Thus, k_{calc} includes the variances induced by the motion of the KHW. The ratio of

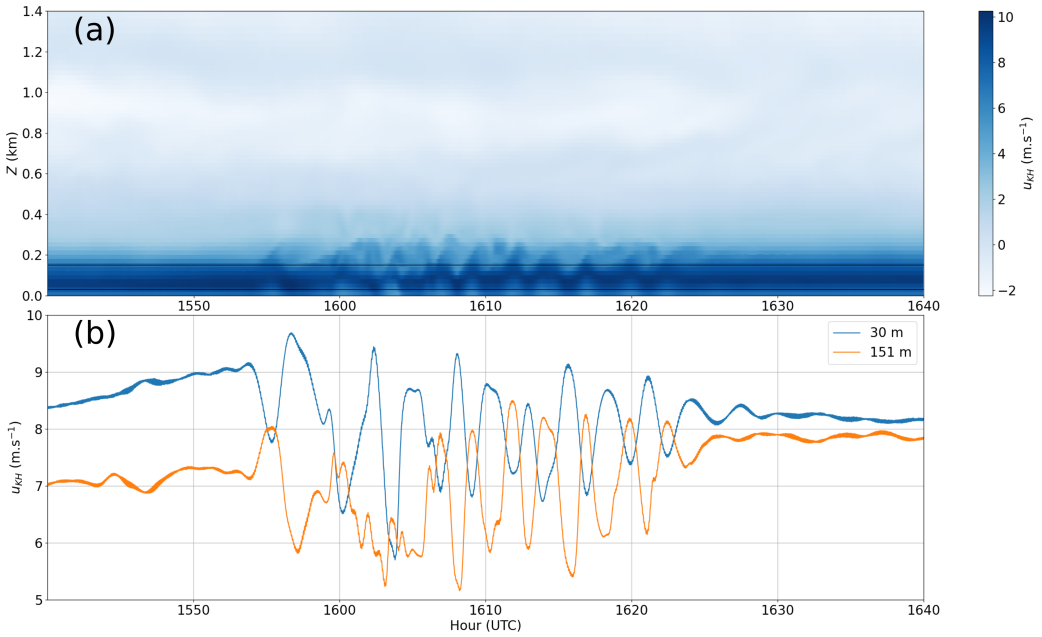

FIGURE 4.13 – (a) Same as Figure 4.10 for u_{KH}, and (b) time evolution of u_{KH} at 30 m and 151 m high at the same location. The two horizontal lines in (a) are at 30 m and 151 m high.

the "real" TKE to k_{calc} corresponds to the LIST indicator (Section 1.1.5). In Figure 4.13b between 1610 and 1620 UTC, the oscillations of u_{KH} related to the KHW have a much larger amplitude than the turbulent fluctuations, suggesting that the LIST is small, which means that the intermittency is strong (Ren et al., 2019). A few kilometers to the southeast of the location of the time series (Figure 4.9b), where the KHW break up, the turbulence is likely more intense and the LIST larger.

In the next section, the turbulence within the GW observed on May 17 (Section 3.2) is analyzed and a method is proposed to estimate the velocity variance induced by the GW motion. This method cannot be applied to the present KHW as they are moving too fast and are too much dirty (following the terminology of Mahrt (2014)) compared to the GW.

4.3 Impact of gravity waves on the turbulent kinetic energy

Understanding the interaction between waves and other sub-mesoscale motions with turbulence is a key challenge for the stable layers modeling (Sun et al., 2015b) (Section 1.1.5). However, the impact of gravity waves on turbulence is not well documented in the literature. This section presents a study of the TKE within and outside the bore and gravity waves observed on May 17 (Section 3.2.2), in order to

assess the extent to which their presence can modify the TKE profiles in a SB. This study was initially based on a previous simulation with only 5 domains (Landreau et al., 2025c). In this chapter, the same analysis is conducted using the results from domain d06.

4.3.1 Turbulence out of the gravity waves

The same regions as in Figure 3.15c are shown in Figure 4.14 for domain d06. The region outside the GW for X_{GW} (cross-GW coordinate) between -5 and -2 km is shown in orange, and the region within the GW for X_{GW} between 2 and 5 km is shown in green. These regions are divided into blocks of 1 km (black rectangles) so that each block is composed of more than 1000 cells.

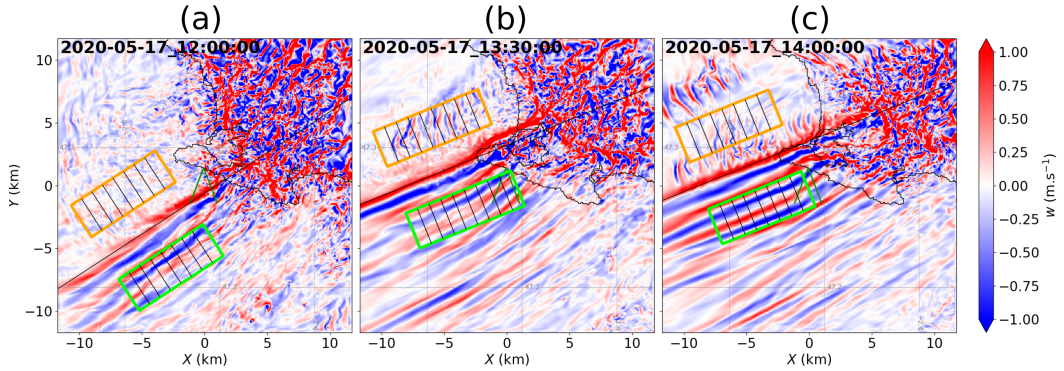

FIGURE 4.14 – Spatial distribution of the instantaneous w at 150 m high in d06 at (a) 1200, (b) 1330, and (c) 1400 UTC on May 17. The rectangles depict the regions and blocks used in this section.

We first focus on the total TKE (k_{tot}) profile outside the gravity waves. Figure 4.15a compares the k_{tot} profiles at 1200 UTC and 1400 UTC on May 17 spatially averaged within two blocks located 3 and 7 km from the coast. The profiles exhibit the same structure as on May 18 at 1500 UTC (Figure 4.4d) with the presence of a peak around 100 m high, close to Z_{SB} (dashed line). Such a peak is searched in each block and at each time step using the same method as in Section 4.2.1. Figure 4.15b displays the scatter plot of the peak height as a function of Z_{SB}. A good correlation between these two quantities is observed, although the peaks tend to be located slightly higher than Z_{SB} in average. This correlation suggests that the mechanism behind the peak of k_{tot} is similar to that analyzed in Section 4.2, i.e. the development and breaking of KHW. The oscillations of w in the orange-box at 1330 UTC in Figure 4.14b further confirm the presence of KHW. At 1200 UTC (Figure 4.14a), the more random variations of w are maybe caused by KHW breaking.

table of content

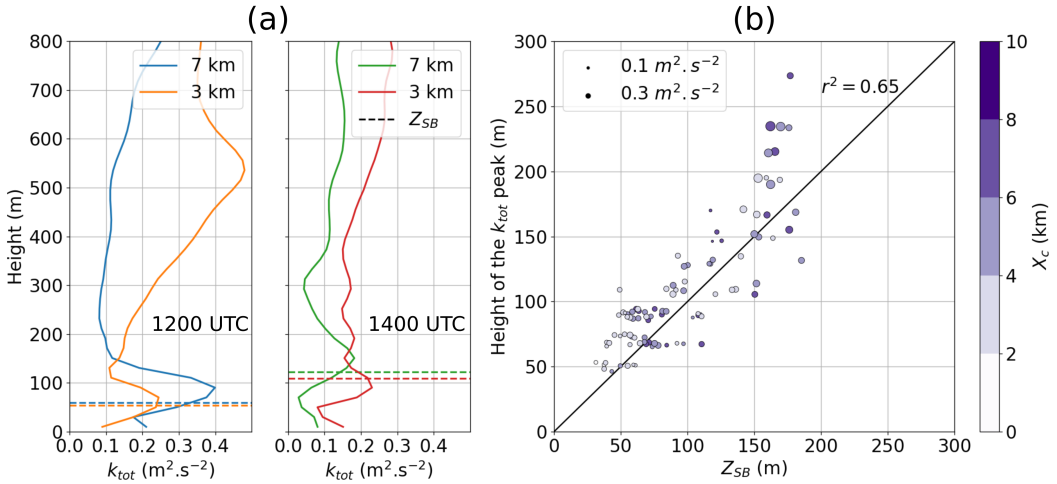

FIGURE 4.15 – (a) k_{tot} profile at (left) 1200 and (right) 1400 UTC, in two different blocks in the region without gravity waves shown in Figure 4.14. (b) Evolution of the height of the detected peaks in the k_{tot} profile (as described in the text) as a function of Z_{SB}. The size of the markers is proportional to k_{tot} at the peak and the color indicates the distance from the coastline. A bit of randomness, between -5 and +5 m, is added to both heights to improve readability.

4.3.2 Variance induced by the waves' motion

Before comparing the TKE profiles within and outside the GW, the impact of the gravity-waves' motion on k_{tot} is considered. It has been shown earlier that the GW move horizontally with a maximum speed of 1 m.s^{-1} (Section 3.2.4). Thus, the waves motion influences the variance calculated over time at a given location (Section 1.1.5) so that k_{calc}, and thus k_{tot}, include kinetic energy induced by the GW motions (denoted as G). With the aim of eliminating G, a method is given in Appendix C and the main steps are briefly described below. Knowing G, it is possible to deduce the real turbulent kinetic energy k as

$$k = k_{tot} - G \tag{4.1}$$

To determine the local value of G, each wind velocity component in the GW is approximated by a sinusoidal function with the amplitude determined by Equation 3.3. The phase for W is determined based on W and its partial derivative along X_{GW}, and the phases for U and V are then deduced from this computation (90 ° out of phase compared to W). Then, the theoretical variances induced by the sine-waves' motion (G_U, G_V, and G_W) are calculated. Finally G is computed as

$$G = \frac{1}{2}(G_U + G_V + G_W). \tag{4.2}$$

An evaluation of U_{sine} and W_{sine}, the sine-wave reconstruction of U and W, at 300 m high and at 1300 UTC is presented in Figure 4.16a. W_{sine} is very close to W. Some differences are observed between U and U_{sine} at the extrema, mainly due to the wave not being perfectly harmonic, but the amplitude and the wavelength

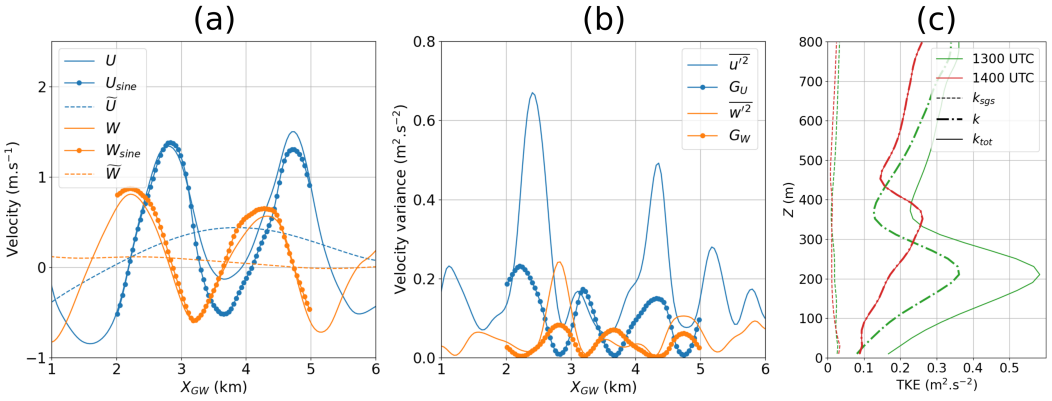

FIGURE 4.16 – (a) W and U as a function of X_{GW} at 300 m on the same cross-section as in Figure 3.16 at 1300 UTC. The solid line represents the WRF output, the dashed line is the spatially-filtered output, and the dotted solid line is the sine-wave reconstruction. (b) Variance of W and U on the same section as (a). The solid line is the WRF output and the dotted solid line is the GW related variance. (c) TKE contribution profiles at 1300 and 1400 UTC averaged over the green-box region defined in Figure 4.14.

are well represented. Figure 4.16b shows the comparison between the calculated variances ($\overline{u'^2}$ and $\overline{w'^2}$) and the GW related variances (G_U and G_W) of U and W. As expected, the positions of the variance peaks are not the same for U and W due to the phase difference between the two variables. It is worth noting that the peaks of $\overline{u'^2}$ ($\overline{w'^2}$) are located at the same position as the peaks of G_U (G_W). $\overline{u'^2}$ is larger than $\overline{w'^2}$ because the thermally stable stratification of the layer tends to suppress fluctuations of W. This is why, in this cross-section, G_W accounts for 56 % of $\overline{w'^2}$ whereas G_U accounts for only 42 % of $\overline{u'^2}$.

Figure 4.16c shows the vertical profile of k_{sgs}, k_{tot}, and k, averaged over the green-box region at 1300 and 1400 UTC. In average, k_{sgs} is about one order of magnitude lower than k_{tot}, so that most of the turbulence is resolved. At 1300 UTC, G (the difference between the solid curve and the dashed dotted curve) is significant compared to k_{tot}, indicating that k_{tot} is an overestimation of the real turbulent kinetic energy k. At 1400 UTC, G is almost negligible because the GW are approximately stationary ($S_{GW} \approx 0$ in Figure 3.19). After subtracting G from k_{tot} (Equation 4.1), a peak of k (dashed-dotted lines) is still observable between 200 and 400 m high with a value between 0.2 and 0.35 $\mathrm{m}^2.\mathrm{s}^{-2}$.

4.3.3 Turbulence within the gravity waves

Because the height of the peak varies over time and space, due to the evolution of the SB (Figure 4.15) and the vertical displacement induced by the GW (not shown), any spatial or temporal averaging would tend to smooth the k profile. This is why it has been chosen to study the TKE as a function of Z^*_{SB}. Outside the GW, Z^*_{SB} is simply defined as the height normalized by Z_{SB}. In the presence of GW, the

height of a volume of air oscillates around an equilibrium altitude Z_0 that represents its mean height. For each altitude of each cell composing a block, the equilibrium altitude Z_0 is found by interpolating the local value of θ_v onto the average θ_v profile of the block. Finally, Z^*_{SB} is defined as

$$Z^*_{SB} = \frac{Z_0}{Z_{SB0}} \tag{4.3}$$

where Z_{SB0} is the equilibrium SB characteristic height. This method is summarized in Figure 4.17a for an arbitrary point A, represented with a green dot. This point is placed in a trough where its real altitude $Z_{(A)}$ is lower than its equilibrium altitude $Z_{0(A)}$. The SB characteristic height at this location ($Z_{SB(A)}$, the one that nullifies the cross-coast velocity) and the corresponding equilibrium height ($Z_{SB0(A)}$) are depicted with a red dot.

Figure 4.17b shows the k profile as a function of Z^*_{SB}, averaged between 1230 and 1430 UTC within and outside the GW. Within the GW, the averaging is conditioned by the phase of W (see the calculation in Appendix C). The same kind of profile is observed within the GW as outside, with a peak at $Z^*_{SB} = 1.1$ for each phase. However, the peak value depends on the phase. Higher values are reached at the crests than at the troughs. For $Z^*_{SB} = 1.1$, there is a difference of 50% between k at the crests and at the troughs. The maximum value is reached during the ascending phase just before the crests.
Figures 4.17c and 4.17d shows the profiles of k and k_{tot} averaged between 1230 and 1330 UTC when the GW motion speed is the largest (Figure 3.19). When no correction is applied (Figure 4.17d) the largest k_{tot} is in phases A and D where the horizontal gradient of the wind speed is the largest so that the variances induced by the waves motion are the largest. When applying the correction (subtracting G, Figure 4.17c), the results are similar to that between 1340 and 1430 UTC (Figure 4.17e) when the GW are not moving, with the highest TKE near the crests. This illustrates the importance of subtracting the GW motion variance to study the evolution of the TKE within the GW.

For the rest of this section, the calculation of the covariances is needed. However, correcting the covariance, i.e. estimating the part of the covariance induced by the GW motion, is much more complex. Thus, in the rest of the section, only the period between 1340 and 1430 UTC, when the GW are stationary, is considered.

Figure 4.18 displays the 3 components of k_{calc} in the referential frame related to the GW. The profiles within the GW and outside are similar for each component. Around $Z^*_{SB} = 1$, the $\overline{v'^2_{GW}}$ components (Figure 4.18b) clearly dominates over the two others, indicating a significant anisotropy.

table of content

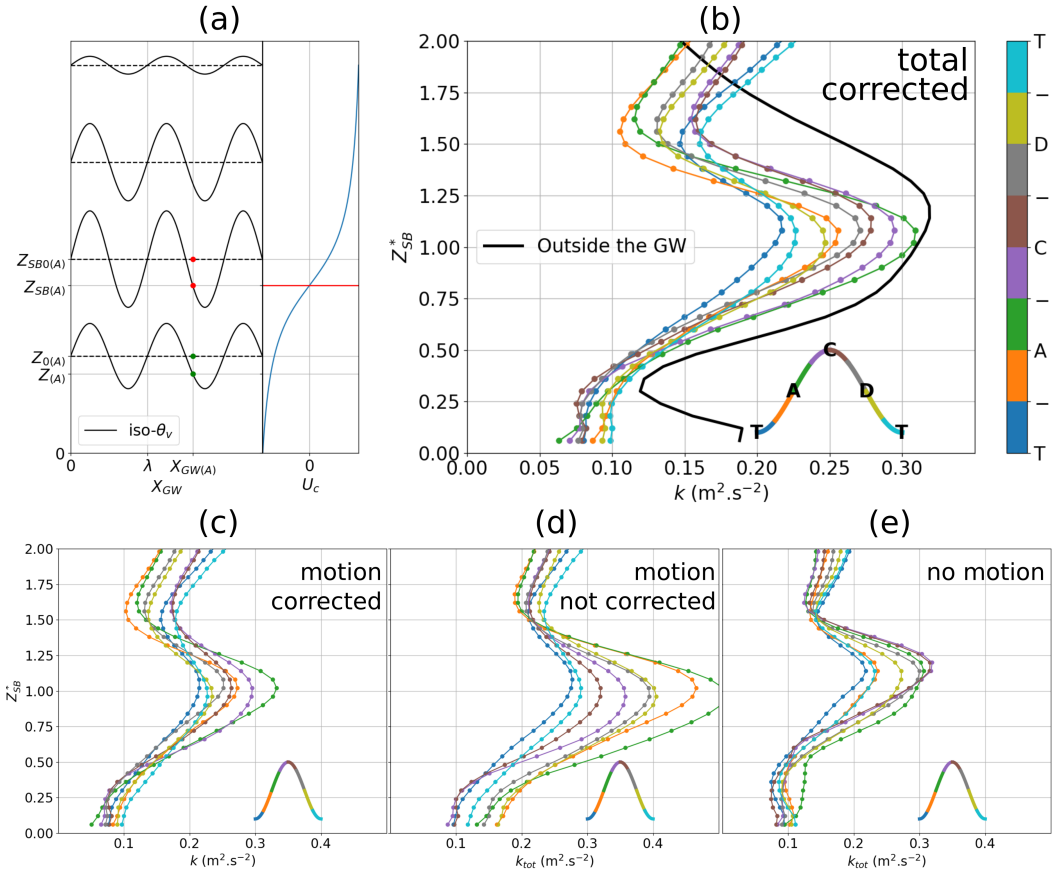

FIGURE 4.17 – (a) Schematic explaining the calculation of Z_0, Z_{SB}, Z_{SB0} and Z^*_{SB}. Details are in the text. (b) k profiles as a function of Z^*_{SB} and the GW phase, averaged between 1230 and 1430 UTC in the green-box region depicted in Figure 4.14. As shown in the wave diagram in the bottom right corner, orange and green represent the ascending phases (A), purple and brown correspond to the crests (C), grey and olive represent the descending phases (D), and light and dark blues correspond to the troughs (T). The black line shows the same profile averaged over the region outside the GW. (c-e) Same as (b) for (c) k between 1230 and 1330 UTC, (d) k_{tot} between 1230 and 1330 UTC, (e) k_{tot} between 1340 and 1430 UTC.

4.3.4 Turbulent kinetic energy budget within the gravity waves

To better understand the distribution of k within the GW, the TKE budget is computed following Equation 2.6, and is averaged between 1340 and 1430 UTC. Figure 4.19a displays k_{tot} and the iso-contours of k over the same period. The contours match the colors, which confirms that, during this period, $k_{tot} = k$ because the GW are stationary. Since the subgrid TKE is much lower than the resolved one (Figure 4.16), one can consider that $k_{calc} = k_{tot} = k$, so that the budget of k_{calc} is also the budget of k.

Five budget terms are shown in Figures 4.19b to 4.19f. Around $Z^*_{SB} = 1$, k is the largest around the crests, which is consistent with Figure 4.17e. Surprisingly,

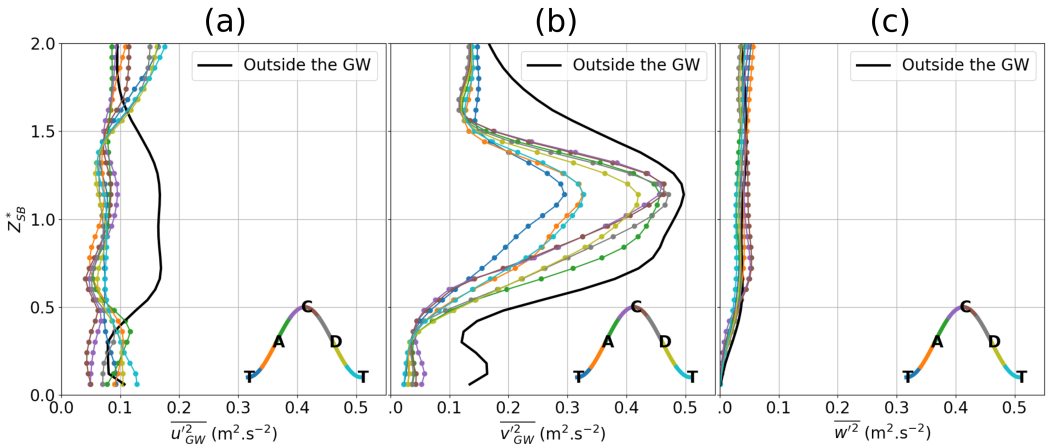

FIGURE 4.18 – Same as 4.17b for (a) $\overline{u'^2_{GW}}$, (b) $\overline{v'^2_{GW}}$, and (c) $\overline{w'^2}$. The time averaging is realized between 1340 and 1400 UTC when the GW are stationary.

the location of this maximum does not match with that of the largest P (Figure 4.19b). Instead, the maximum P is found in the ascending phase, i.e., upwind of the k maximum, where it is nearly compensated by A (Figure 4.19d) while the other terms are less significant. This means that the k pattern does not result from a local equilibrium between the production and dissipation terms. The k budget can be studied from a Lagrangian point of view : k progressively increases in the ascending phase, where P is positive, thus reaching a maximum just before the crests. The maximum of k remains all along the crests because P is balanced by B and ε. In the descending phase and at the troughs, P becomes negative while the contribution of ε remains important. As a consequence, k is progressively lost and a minimum is found at the troughs.

The two major components of P are P_{23} and P_{11} defined as :

$$P_{23} = -\overline{v'_{GW} w'} \frac{\partial V_{GW}}{\partial Z} \tag{4.4}$$

$$P_{11} = -\overline{u'^2_{GW}} \frac{\partial U_{GW}}{\partial X_{GW}}. \tag{4.5}$$

Their distribution are displayed in Figures 4.20a and 4.20b. For $Z^*_{SB} < 0.5$ and $Z^*_{SB} > 1.5$, P is governed by P_{11} (Figure 4.20b), and shows a specific pattern that can be analyzed. Near the surface (below $Z^*_{SB} = 0.5$), it is positive in the ascending phase, and negative in the descending phase. In the ascending phase, W equals 0 at the surface and is positive at $Z^*_{SB} = 0.5$, so that the continuity requires a horizontal deceleration ($\frac{\partial U_{GW}}{\partial X_{GW}} < 0$), shown by the vectors. As $\overline{u'^2_{GW}}$ is necessarily positive, P_{11} is negative. In contrast, in the descending phase, the acceleration is positive and the production is negative. In the upper layer (above $Z^*_{SB} = 1.5$), the opposite pattern is observed because the amplitude of W decreases with height (not shown) : in the ascending phase, $W > 0$, the vertical gradient of W is negative and the mass conservation implies that the horizontal acceleration is positive, so that P_{11} is negative. Near the

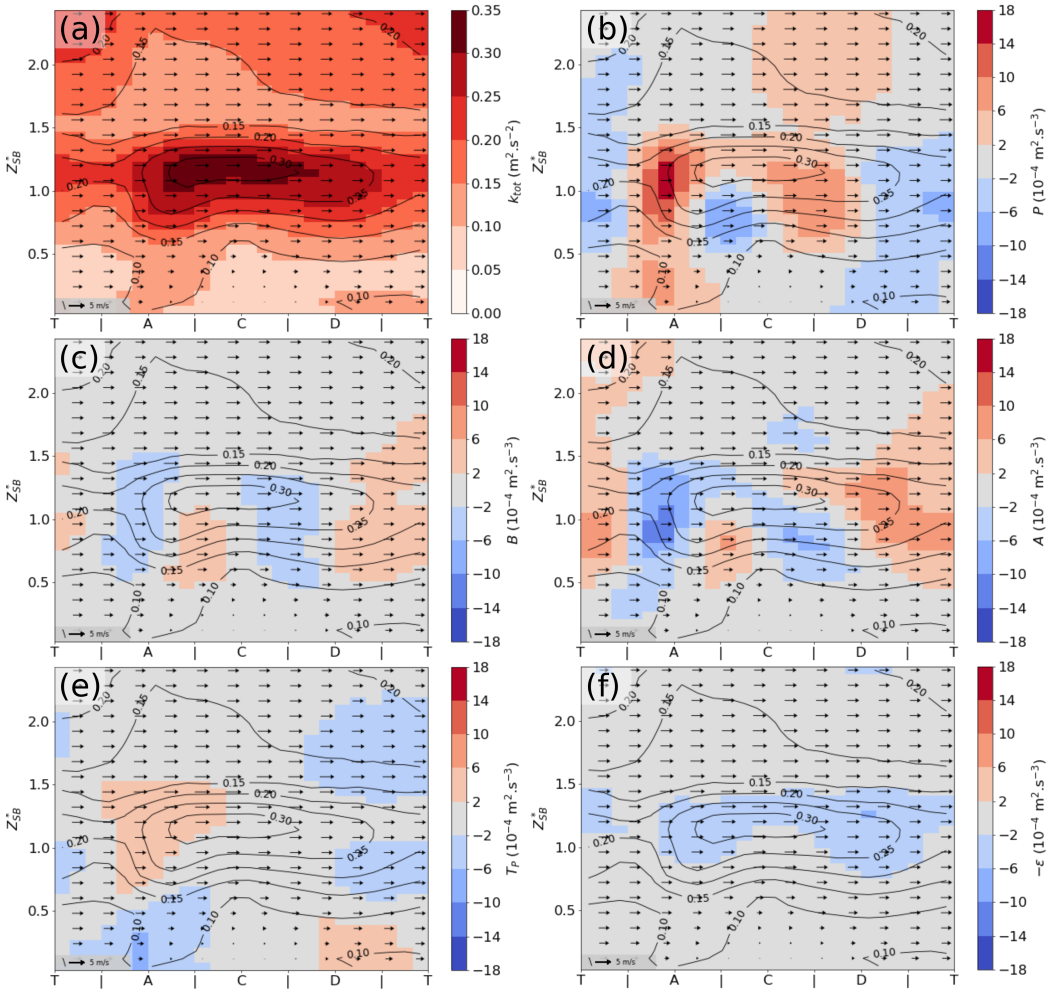

FIGURE 4.19 – Evolution of (a) k_{tot}, (b) P, (c) B, (d) A, (e) T_P, and (f) $-\varepsilon$ as a function of Z^*_{SB} and the GW phase, averaged between 1340 and 1430 UTC in the green-box region shown in Figure 4.14. iso-k lines and U_{GW} vectors are shown in each figure.

surface, P_{11} is almost exclusively compensated by T_P (Figure 4.19e), that seem to transport the TKE between $Z^*_{SB} < 0.5$ and $Z^*_{SB} > 0.5$, contributing to the growth of the TKE peak in the ascending phase and to its weakening in the descending phase.

Around $Z^*_{SB} = 1$, the most important contribution to P is P_{23} (Figure 4.20a). Its distribution shows oscillations with a wavelength that is twice smaller than the GW wavelength. The extrema are localized between the defined phases, e.g. a minimum between phases A and C or a maximum between C and D, except for the largest maximum that is slightly shifted toward the ascending phase. The SB wind profile induces a large vertical gradient of V_{GW} (the along-GW component is roughly cross-coast), that does not change sign within the GW. Thus, according to Equation 4.4, the variations of P_{23} are caused by the oscillations of $\overline{v'_{GW}w'}$ within the GW. Interestingly, this distribution is similar but with opposite sign compared

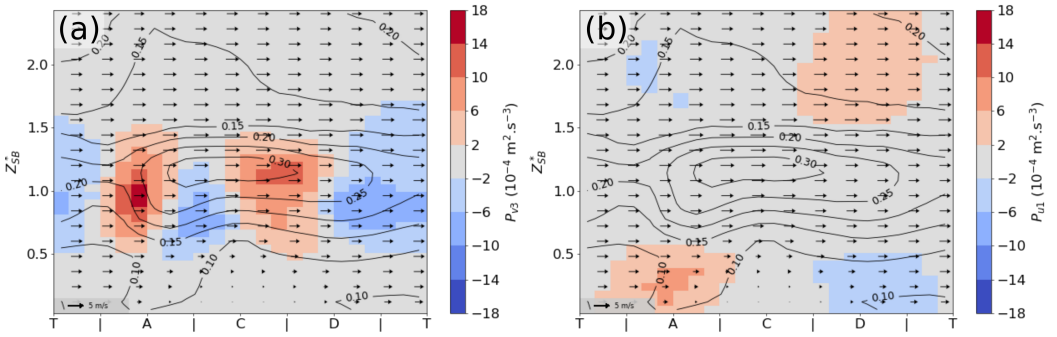

FIGURE 4.20 – Same as Figure 4.19 for (a) P_{23}, and (b) P_{11}.

to that of B (Figure 4.19c), i.e. to that of $\overline{w'\theta'_v}$.

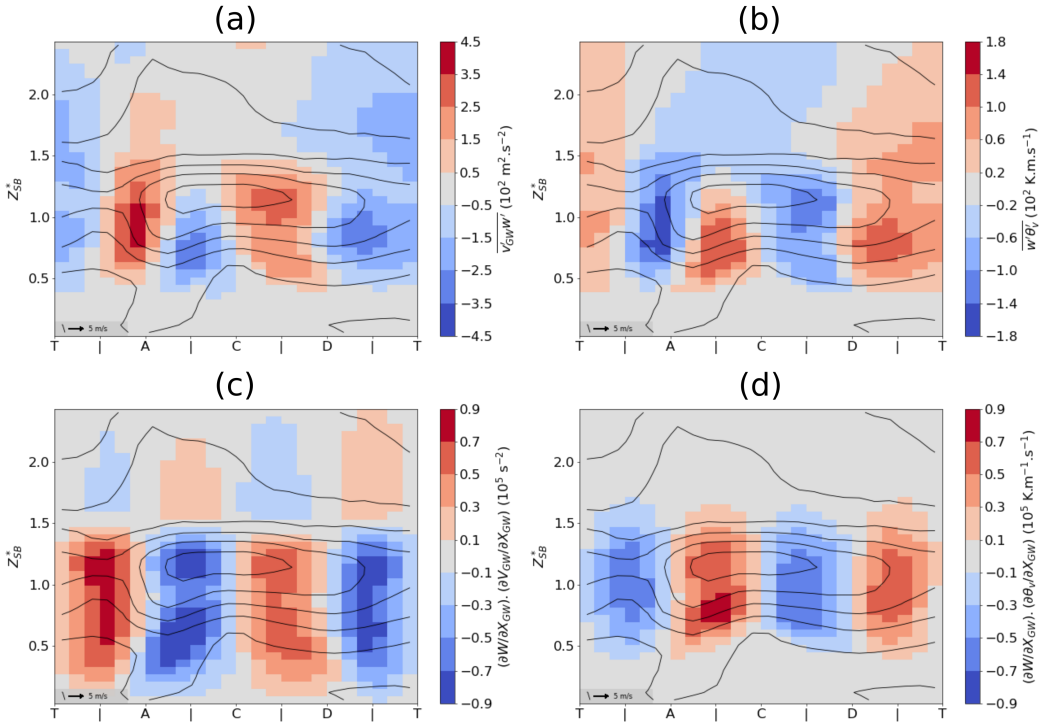

FIGURE 4.21 – Same as Figure 4.19 for (a) $\overline{v'_{GW}w'}$, (b) $\overline{w'\theta'_v}$, (c) $\frac{\partial W}{\partial X_{GW}}\frac{\partial V_{GW}}{\partial X_{GW}}$, and (d) $\frac{\partial W}{\partial X_{GW}}\frac{\partial \theta_v}{\partial X_{GW}}$.

To understand the oscillations of $\overline{v'_{GW}w'}$ and $\overline{w'\theta'_v}$ within the GW, we can build an argumentation similar to that of Grachev et al. (2016). Assuming that the turbulent moments are caused by the vertical turbulent transport of velocity or temperature, they explain the sign of the turbulent covariances in a stable sheared layer as follows : "an upward air parcel ($w' > 0$) ends up being slower ($u' < 0$) and cooler ($\theta' < 0$) than its surroundings, while a downward ($w' < 0$) moving air parcel is faster ($u' > 0$) and warmer ($\theta' > 0$) [so that] $\overline{w'\theta'} < 0$, $\overline{u'w'} < 0$, and $\overline{u'\theta'} > 0$". This assumption works pretty well as the vertical gradients of the mean quantities are

generally larger than the horizontal ones. However, in the present case the horizontal gradients of the mean quantities are of the same order of magnitude as the vertical gradients. Moreover, the horizontal fluctuations are larger than the vertical ones (Figure 4.18). Thus, we can build a similar argumentation driven by horizontal fluctuations. In the area between C and D, an air parcel traveling from D to C ($u'_{GW} < 0$) ends up being warmer ($\theta'_v > 0$ because $\frac{\partial \theta_v}{\partial X_{GW}} > 0$), moving downward ($w' < 0$ because $\frac{\partial W}{\partial X_{GW}} < 0$) and with a lower transverse velocity component ($v'_{GW} < 0$ because $\frac{\partial V_{GW}}{\partial X_{GW}} < 0$) compared to its surroundings, so that $\overline{w'\theta'_v} < 0$ and $\overline{v'_{GW}w'} > 0$. Such an argument rely on the assumption that

$$\overline{w'\theta'_v} = c_\theta \frac{\partial W}{\partial X_{GW}} \frac{\partial \theta_v}{\partial X_{GW}} \tag{4.6}$$

$$\overline{v'_{GW}w'} = c_v \frac{\partial W}{\partial X_{GW}} \frac{\partial V_{GW}}{\partial X_{GW}} \tag{4.7}$$

where c_θ and c_v are coefficients (in m^2) related to the horizontal mixing of θ_v and v_{GW}, respectively. Figure 4.21 displays the two terms of each equation. Except for the extremum located between T and A, the same oscillation is found for each covariance and its associated product of horizontal gradients, which gives some credit to the horizontal transport assumption.Moreover, this argument can also explain the opposite sign between B and P_{23}. Assuming that V_{GW} and θ_v are vertically displaced by the GW, their horizontal gradient can be expressed as a function of that of the vertical displacement η as

$$\frac{\partial \theta_v}{\partial X_{GW}} = -\frac{\partial \theta_v}{\partial Z} \frac{\partial \eta}{\partial X_{GW}} \tag{4.8}$$

$$\frac{\partial V_{GW}}{\partial X_{GW}} = -\frac{\partial V_{GW}}{\partial Z} \frac{\partial \eta}{\partial X_{GW}} \tag{4.9}$$

Combining with Equations 4.4 to 4.7, one can find that

$$\frac{B}{P_{23}} = -\frac{c_\theta}{c_v} \frac{\frac{g}{\theta_v}\frac{\partial \theta_v}{\partial Z}}{(\frac{\partial V_{GW}}{\partial Z})^2} = -\frac{c_\theta}{c_v} Ri \tag{4.10}$$

Since Ri, c_θ, and c_v are positive, this model explains why B and P_{23} have opposite signs.

Finally, the ratio c_θ/c_v is a kind of inverse Prandtl number as it compares the heat exchange to the momentum exchange. Thus, Equation 4.10 is similar to the classical relationship in a horizontally homogeneous atmosphere that is

$$Ri_f = Pr^{-1} Ri \tag{4.11}$$

where Ri_f is the Richardson flux number, ratio of $-B$ to P, and Pr is the Prandtl number, ratio of the eddy viscosity to the turbulent thermal diffusivity. It is interesting to note that, whereas the stable stratification inhibits the vertical mixing, the periodic vertical displacement induced by the GW allows for horizontal mixing with properties that are similar to the classical theories in the ABL.

table of content

4.4 Analysis of the turbulence in the sea-breeze return current

It was shown in Section 4.1 that at 1200 UTC, k_{calc} was decreasing with increasing offshore distance (Figure 4.4a). It was suggested that this particular TKE is produced in the inland CBL, out of the SB, and is progressively decaying while being advected toward the sea. As stated in Section 1.3.5, the decay of turbulence in the return current has already been observed but the modeling of this decay is still poorly documented. In this section, the evolution of k_{calc} in the return current as a function of the distance from the SBF is investigated, and is fitted with the three analytical models introduced in Section 1.3.5 to assess their ability to describe the turbulent decay in the SB return current. Then, a comparison of the best-fit parameters of the models is presented and compared to the parametrization proposed by Nieuwstadt and Brost (1986).

4.4.1 Evolution of the turbulence with offshore distance

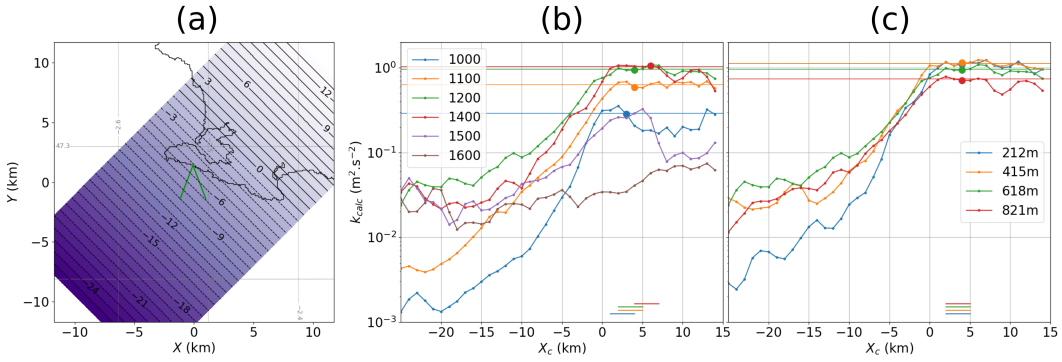

FIGURE 4.22 – (a) Map of d06 showing the rectangular zones in which k_{calc} is averaged in (b) and (c). The lines show iso values of X_c which is positive inland and negative offshore. (b,c) Evolution of k_{calc} as a function of X_c on May 18 (b) at 618 m high at different times and (c) at 1200 UTC at different heights. The circle indicates X_{SBF}. The horizontal lines shows k_0, the average k_{calc} between X_{SBF} - 2 and X_{SBF} + 1, as depicted by the short lines at the bottom.

Domain d06 is divided into several zones shown in Figure 4.22a in which the k_{calc} profile is averaged at each time step from 1000 to 1600 UTC on May 18. Figures 4.22b and 4.22c show the evolution of k_{calc} as a function of the distance from the coastline X_c at various time and height. The bigger circles depict the position where half of the zone lies in the CBL (U_c at 10 m high is negative, as shown in Figure 4.3) and thus shows the average position of the SBF, X_{SBF}. At 1500 and 1600 UTC, the SBF from the west has covered most of the domain d06 so that X_{SBF} is out of the domain (Figure 4.3f). In each curve, k_{calc} is decaying with distance after a certain location. Far offshore ($X_c <$ - 10 km), the decay is less intense. The location where the decay starts, called X_0, moves over time from $X_c = 0$ km at 1200 UTC to more

than 15 km at 1600 UTC. X_0 is located about 4 km to the southwest of X_{SBF}. This difference between X_{SBF} and X_0 is related to the fact that the SBF is not parallel to the zones defined in Figure 4.22a. Thus, in a few zones to the southwest of X_{SBF}, the TKE can be maintained by a small portion of CBL.

4.4.2 Performance of the models

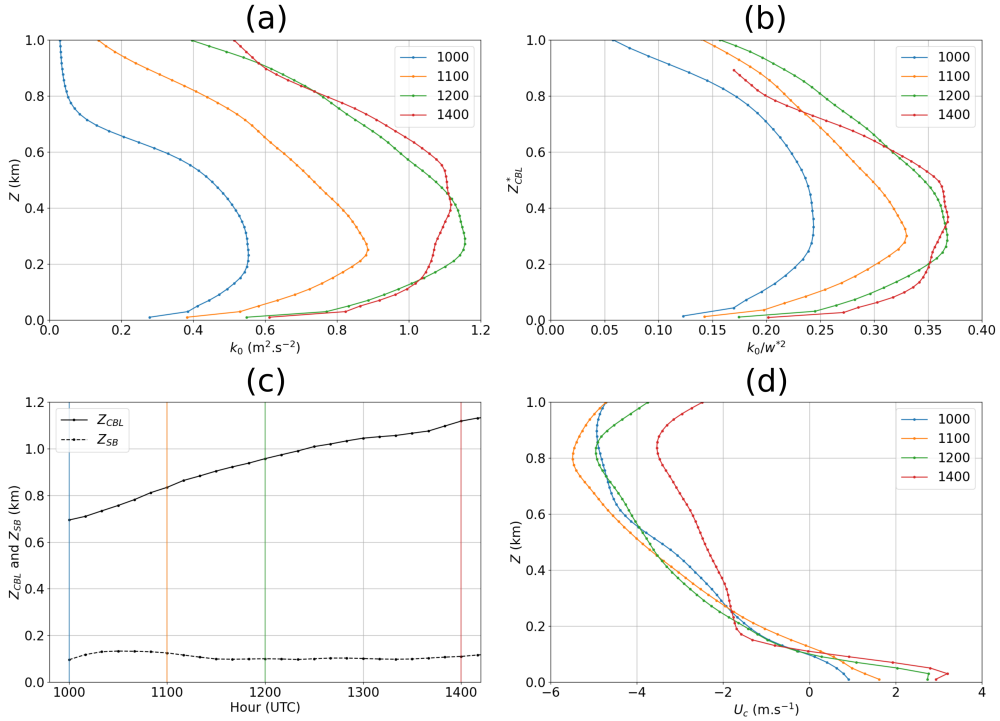

FIGURE 4.23 – (a) Profiles of k_0 at different times. (b) Same as (a) where the height and k_0 are normalized with Z_{CBL} and w^{*2}, respectively. (c) Time evolution of Z_{CBL} and Z_{SB} where Z_{SB} is determined based on the profile of U_c at X_c = -5 km shown in (d).

Before fitting the decay with the models introduced in Section 1.3.5, a few external parameters are defined and displayed in Figure 4.23. The initial TKE before the decay, called k_0, is calculated as the average k_{calc} between X_{SBF} - 2 and X_{SBF} + 1. The profile of k_0 at different times is shown in the dimensional form in Figure 4.23a and in the non-dimensional form in Figure 4.23b. The 4 profiles are quite similar and resemble that of a classical CBL, with a maximum at $Z^*_{CBL} \approx 0.3$. Interestingly, k_0 is almost steady between 1200 and 1400 UTC. The evolution of Z_{SB} and Z_{CBL} is shown in Figure 4.23c. Z_{CBL} increases linearly with time while Z_{SB} is roughly constant as previously shown in Figure 4.3b. From these two heights, the SB return-current normalized height is defined as $Z^*_{RC} = (Z - Z_{SB})/(Z_{CBL} - Z_{SB})$, being equal to 0 at $Z = Z_{SB}$ and 1 at $Z = Z_{CBL}$. The following analysis is based only on the points where $0.2 < Z^*_{RC} < 1$ so that U_c, displayed in Figure 4.23d, is

between -1.5 and -6 m.s^{-1}.

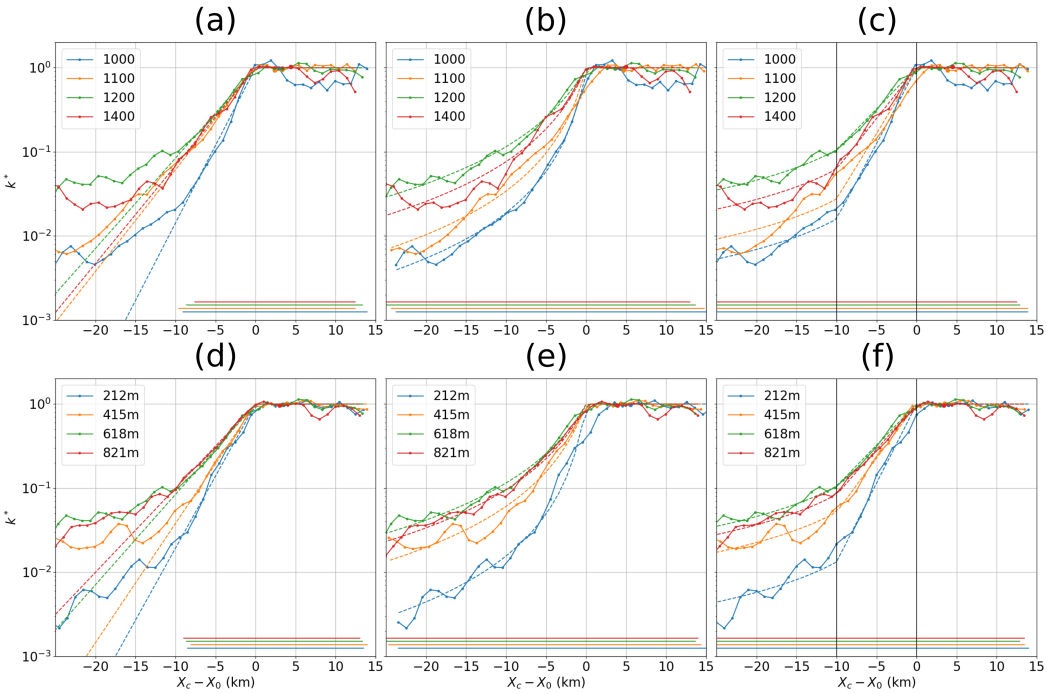

FIGURE 4.24 – Fit of $\log(k^*)(X_c - X_0)$ at the same time and height than in (a, b, c) Figure 4.22b and (d, e, f) Figure 4.22c with (a, d) model 1, (b, e) model 2, and (c, f) model 3. The area where the fit is made is depicted by the horizontal lines at the bottom. and the vertical lines in (c, f) separate the 3 parts of model 3.

To fit the TKE decay with the three models introduced in Section 1.3.5, it is assumed that the flow is quasi-stationary, i.e. that the time scale of the variations of the CBL parameters is large compared to the advection time scale, so that the time since the decoupling can be replaced by $(X_c - X_0)/U_c$. This assumption will be discussed later. The fit is made on the logarithm of $k^* = k_{calc}/k_0$ as a function of X_c and each model has two parameters, which are the position of the decay X_{0i} and a constant c_i. Based on the development made in Appendix D, one can find that model 1 writes

$$\log(k^*) = \begin{cases} -c_1(X_c - X_{01}) & \text{if } X_c < X_{01} \\ 0 & \text{if } X_{01} < X_c \end{cases} \tag{4.12}$$

and model 2 writes

$$\log(k^*) = \begin{cases} -2\log(1 + c_2(X_c - X_{02})) & \text{if } X_c < X_{02} \\ 0 & \text{if } X_{02} < X_c \end{cases} \tag{4.13}$$

For model 3, the $t^{*-1.2}$ decay observed by Nieuwstadt and Brost (1986) does not occur immediately at $X_c = X_0$, but starts around $t^* = 1$. For that reason, the

$t^{*-1.2}$ is fitted only farther than a certain distance ΔX_3 from X_0. Between X_0 and $X_0 - \Delta X_3$, the continuity is maintained by a linear function of $\log(k^*)(X_c)$, corresponding to an exponential decay of k^* as in model 1. Then, model 3 writes

$$\log(k^*) = \begin{cases} -1.2\log(c_3(X_c - X_{03})) & \text{if } X_c < X_{03} - \Delta X_3 \\ -1.2\log(c_3\Delta X_3)\frac{X_c - X_{03}}{\Delta X_3} & \text{if } X_{03} - \Delta X_3 < X_c < X_{03} \\ 0 & \text{if } X_{03} < X_c \end{cases} \tag{4.14}$$

The value of ΔX_3 is constrained to 10 km (model 3a) and 5 km (model 3b).

The resulting fits, computed using the Scipy library, are shown in Figure 4.24 for the same curves as in Figure 4.22. Model 1 (Figures 4.24a and 4.24d) is linear in the log plot. It is able to represent the first portion of the decay, within 10 km of X_0, that is approximately linear. Thus, the fit is realized on this portion. Farther offshore, the decay is too fast and k^* is strongly underestimated. Models 2 and 3 better capture the decay at every distance.

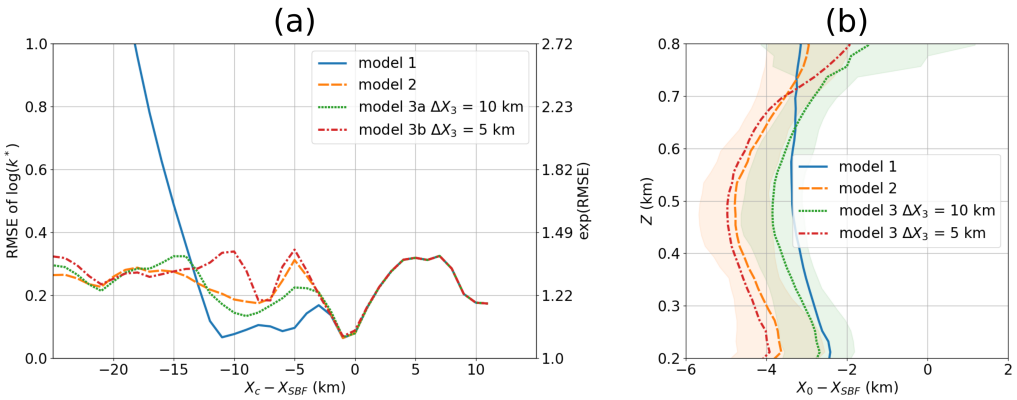

FIGURE 4.25 – (a) Comparison of the RMSE of the modeled $\log(k^*)$ compared to the simulated one, as a function of $X_c - X_{SBF}$. The right axis shows the exponential of this RMSE which represents the average factor between the modeled k^* and the simulated one. (b) Profile of $X_0 - X_{SBF}$, averaged between 1000 and 1400 UTC, for each model. The shaded area shows +/- the standard deviation.

The ability of the models to describe the decay is highlighted by Figure 4.25a, that shows the RMSE of the fit of $\log(k^*)$ computed over every height as a function of $X_c - X_{SBF}$. For $X_c - X_{SBF} > 0$, $X_c - X_0 > 0$, and every model gives $\log(k^*) = 0$, resulting in a similar RMSE between the models. Between 0 and -10 km, model 1 gives the best results. Moreover, model 3a performs better than the 3b, meaning that the decay is close to exponential at the beginning. Farther than -12 km, the first model diverges whereas for the other models, the RMSE of $\log(k^*)$ are about 0.3. There, the performance of model 3 is not sensitive to ΔX_3. All along the area, the RMSE of model 2 and 3a remain below 0.3, meaning that the difference between the modeled k^* and the simulated one is less than 40% in average.

table of content

4.4.3 Comparison of the parameters

The profiles of $X_0 - X_{SBF}$ obtained from the different models are compared in Figure 4.25b. For every model, the fitted X_0 is lower than X_{SBF}, as observed earlier in Figure 4.22. It is expected that X_0 is not sensitive to Z, as the decoupling is supposed to occur at the same location all along the profile. With model 1, X_0 is indeed almost constant in the profile. It is slightly closer to X_{SBF} at 300 m high than above, suggesting that the upper air "feels" the effects of the decoupling a little bit later than at lower level. For models 2, 3a, and 3b, X_0 varies more significantly with Z. Model 3a is closer to model 1 whereas in models 2 and 3b, X_0 is 1 km farther to the south-west. The reason for this difference can be understood by looking more closely at the fit of the 212 m curve at 1200 UTC displayed in Figures 4.24d and 4.24e. With model 2, (Figure 4.24e), the slope close to $X_c = X_0$ is larger than with model 1, so that for X_0 farther to the southwest, the fit is better.

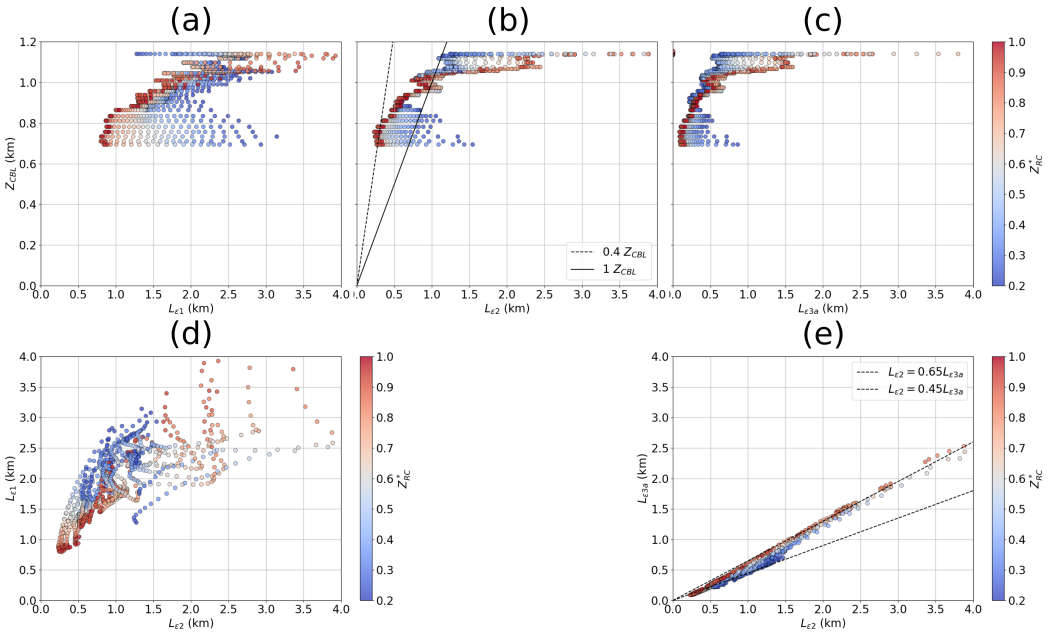

FIGURE 4.26 – Comparison of the various length scales for each fit between 1000 and 1400 UTC : (a) $L_{\varepsilon 1}$ and Z_{CBL}, (b) $L_{\varepsilon 2}$ and Z_{CBL}, (c) $L_{\varepsilon 3a}$ and Z_{CBL}, (d) $L_{\varepsilon 2}$ and $L_{\varepsilon 1}$, and (e) $L_{\varepsilon 2}$ and $L_{\varepsilon 3a}$. The color indicates Z^*_{RC}

A length scale parameter $L_{\varepsilon i}$ can be deduced from the parameter c_i of each model (see Appendix D) as

$$L_{\varepsilon 1} = \frac{w^*}{c_1 U_c} \tag{4.15}$$

$$L_{\varepsilon 2} = \frac{w^*}{2 c_2 U_c} \tag{4.16}$$

$$L_{\varepsilon 3} = \frac{w^*}{c_3 U_c} \tag{4.17}$$

table of content

A small length scale corresponds to a faster decay of turbulence. According to Nieuwstadt and Brost (1986), $L_{\varepsilon 3}$ should be proportional to Z_{CBL}. Thus, the length scales are compared to Z_{CBL} in Figures 4.26a to 4.26c. $L_{\varepsilon 3b}$ is not represented as it is very close to $L_{\varepsilon 3a}$.
The three length scales increase with Z_{CBL}. However, this increase is non-linear, i.e. the length scales are not proportional to Z_{CBL}, which means that the similarity based on the CBL characteristics is not achieved. For $Z^*_{RC} > 0.5$, the length scales do not significantly depend on Z^*_{RC}, whereas for $Z^*_{RC} < 0.5$, there is a larger dispersion, which can be caused by an interaction with the center of the SB cell (Section 4.2). The larger dispersion can also be attributed to the larger advection time due to the lower magnitude of U_c (Figure 4.23d) so that the quasi-stationary hypothesis cannot be applied. Moreover, the largest dispersion is observed for Z_{CBL} below 900 m, which correspond to the time between 1000 and 1130 UTC when k_0 is the less stationary (Figure 4.23a).

Figures 4.26d and 4.26e show the comparison between the length scale parameters. The comparison reveals that the length scales of models 2 and 3 (Figure 4.26e) are well correlated with a linear relationship with a coefficient between 0.65 and 0.45.

4.5 Conclusion of the chapter

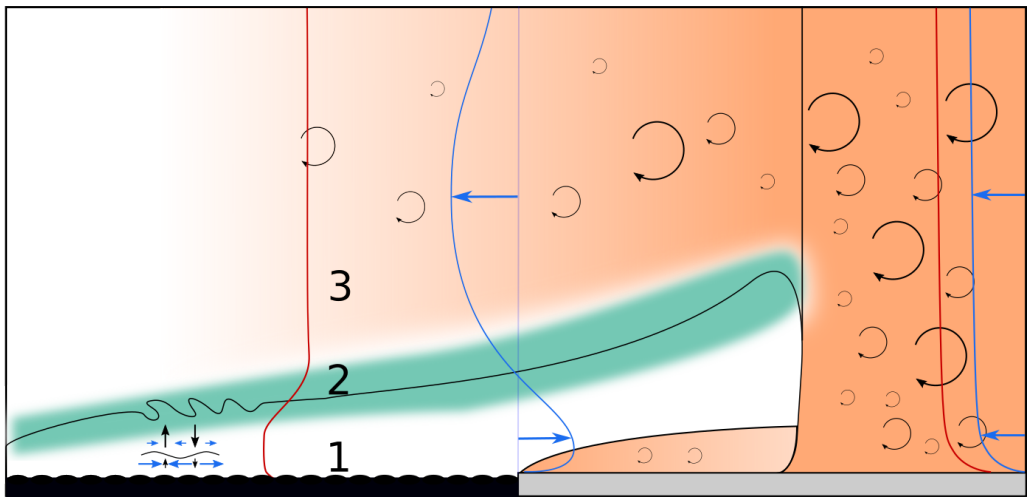

FIGURE 4.27 – Schematic of the offshore turbulence within the SB in this case study. Numbered layers correspond to (1) the near-surface gravity current offshore, influenced by the waves from above, (2) the center of the SB cell featuring KHW, and (3) the return current where the turbulence is a residual from the CBL. The blue and red lines are profiles of U_c and θ_v, respectively.

In this chapter, the resolved-TKE profile in the offshore side of the SB is described using the LES results. This profile can be divided into three layers, labeled 1, 2, and 3 in Figure 4.27, corresponding to the gravity current close to the surface, the center of

the cell, and the return current, respectively. The focus is made on the center of the SB cell (2), first without GW and then within the GW, and on the return current (3).

In the center of the SB cell, both the wind shear and the vertical gradient of temperature are large. For that reason, the distribution of the TKE is heterogeneous, featuring a few patches of large TKE that develop where the shear production dominates, on a homogeneous background where the buoyancy inhibition dominates. The TKE patches are generated by the Kelvin-Helmholtz instability, and take first the form of waves that are oriented according to the shear, the shear direction being across the waves. The wind fluctuations in this direction are by far the largest contribution to the TKE, so that the turbulence is strongly anisotropic. The vertical fluctuations are very low, likely inhibited by the buoyancy effect.

KH billows were observed during SB events in many occurrences (Section 1.5.1). However, these observations were made just behind the SBF (Reible et al., 1993; Wood et al., 1999). In the present study, the waves seem to be generated spontaneously several kilometers away from the SBF. During the two KH events presented in Section 4.2.2, the SBF is even out of the domain d06. These events resemble that observed in stable layers out of the SB, either inland (Merrill, 1977) or offshore (Busack and Brümmer, 1988), in terms of height (120 m, 360 m) and wavelength (420 m, 650 m).

Within waves, the TKE calculation must be carried out carefully as a significant part of k_{calc} is due to their motion which is not a turbulent motion (Ren et al., 2025). The KHW have a too small wavelength and are moving too fast to determine the proportion of the calculated variances that is related to their motion. However, the time series of u_{KH} (Figure 4.13b) suggest that, where the KHW are well established, most of the resolved TKE is due to their motion while the "real" turbulence is low. It is likely that the breaking of KHW (that can be identified e.g. in Figure 4.9b) generates turbulence. It is generally hard to isolate the turbulent fluctuations from the sub-mesoscale structures as their respective scales may overlap Mahrt (2014). A few attempts are reported by Ren et al. (2025), e.g. based on the Huang-Hilbert transform applied on high-frequency measurements (Wei et al., 2021). In the present case, a method is proposed to subtract the variances induced by the motion of the GW observed on May 17 from the total variance. Without this correction, the conclusion is very dependent on the GW motion speed, with higher TKE in the ascending and descending phases when the GW motion speed is large.

Applying the proposed correction, the study shows that the TKE profiles within and outside the GW are similar. However, the GW do have an impact on the TKE peak, which is more intense at the crests than at troughs. The distribution of TKE is mainly governed by a combination of production and advection : the TKE is produced in the ascending phase, is advected toward the crest where it reaches the maximum, and is lost in the descending phase and at the troughs where it reaches a

minimum.
Roy et al. (2021) also observed a higher TKE at crests during a measurement campaign within orographic GW. However, it is difficult to compare the two studies since their measurements were taken at 10 m high, where the flow is highly influenced by the surface. In contrast, Martin and Johnson (2008) and Rottman and Simpson (1989) found that the highest turbulent region within an undular bore was located in the descending phase of the leading edge. A possible explanation for the difference between their results and the present results is that, in the present case, the TKE peak is related to the SB generated shear approximately directed *along* the GW, whereas in their case, turbulence is enhanced by the shear oriented *across* the GW and associated to the velocity difference between the gravity current and the ambient air. The oscillation of turbulent statistics within the GW was also pointed out by Sun et al. (2015a). In their study, the turbulence is locally influenced by the variation of mean horizontal wind speed within the GW : the phase with the highest wind speed has a higher bulk shear and is more turbulent. However, in the present study, it is found that the phase with the highest TKE does not match with the phase with the highest shear production but is instead between the positive and the negative production area, because the TKE produced at a given location is advected by the mean flow.

The TKE budget within the GW is analyzed in 3 distinct layers ($Z^*_{SB} < 0.5$, $Z^*_{SB} \approx 1$, and $Z^*_{SB} > 1.5$), roughly equivalent to the three layers shown in Figure 4.27. In layers 1 and 3, the shear production oscillates under the action of the mean wind speed oscillations related to the GW. In layer 1, this production is compensated by the pressure transport that seems to exchange TKE with the peak, thus helping the growth of the peak in the ascending phase. In layer 2, the production pattern results from the interaction between the SB-induced shear and the oscillations of vertical eddy covariance within the GW. An hypothesis is formulated that the oscillations of the covariance is caused by the horizontal turbulent transport of velocity and temperature within the waves. This hypothesis is comforted by the oscillations of both the production and the buoyancy terms, with opposite signs. This hypothesis differs from the classical ABL framework (MOST in Section 1.1.2) where the horizontal gradients are generally low and the vertical transport dominates. In the present case, the combination of large horizontal gradients and low $\overline{w'^2}$ makes the horizontal transport dominate over the vertical one.

The TKE in the SB gravity current close to the surface (layer 1 in Figure 4.27) is not specifically investigated in this chapter. However, it is observed that near the surface, the amplitude of the oscillations of the vertical velocity associated with both KHW (Section 4.2.3) and GW (Section 3.2.2) increase with height. This induces strong oscillations of the horizontal wind speed near the surface through the principle of mass conservation, as illustrated by the arrows in Figure 4.27. This mechanism is well-known for cases with orographic gravity waves. Over the sea, it is possible that the wind oscillations at low levels would interact with the sea-surface waves that

are not simulated by the current model. A more realistic sea-surface modeling is necessary to study the interaction between the SB gravity current and the sea surface.

In the return current (layer 3 in Figure 4.27), the TKE is a residual TKE from the land CBL that is decaying within a few tens of kilometers of the SBF. Three analytical models, based on previous studies, are compared with the TKE calculated from the simulation results.
In model 1, the time variation of the TKE is proportional to the TKE itself, which corresponds to an exponential decay. This model reproduces well the decay within 10 km of the SBF but strongly underestimates the TKE farther offshore.
In model 2, the time variation of the TKE is proportional to the TKE to the power 3/2, whereas model 3 is an empirical model where the scaling is based on the CBL parameters. Models 2 and 3 reproduce well the decay within the whole domain (up to 20 km). They show the same performance with an average difference below 40 % between the model and the simulation results. A noticeable difference of more than 1 km is found in the value of X_0 between models 2 and 3a, which is caused by the larger slope of the decay close to the decoupling with model 2 than with model 3a. Although it was a very different case, this is in agreement with El Guernaoui et al. (2019) who found that the modeling of the decay is sensitive to the choice of the initial time.
The comparison between the length scale parameters shows that models 2 and 3 are strongly related to each other. Despite a dependency of the length scales on Z_{CBL}, the relationship is not linear as in the ideal case of Nieuwstadt and Brost (1986), which means that the similarity based on the CBL characteristics is not achieved. For $Z^*_{RC} > 0.5$, the length scales do not depend on Z^*_{RC}, whereas for $Z^*_{RC} < 0.5$, there is a larger dispersion that is attributed either to the interaction with the center of the SB cell or to an advection time scale too large to meet the quasi-stationary assumption.
These results constitute a step toward building a model for the decay of turbulence in the return current.

This chapter gave some insights on the behavior of the offshore turbulence within a SB. Moreover, several results of this study might be applicable to other situations : the KHW observed in Section 4.2 resemble that of other stable layers, the influence of the GW in the turbulence in layers 1 and 3 is apparently not related to the SB, and the decay of turbulence in the SB return current likely resemble that above the stable TIBL that can develop during daytime at the land-sea transition under land wind. Thus, these results could be used, for example, to parameterize the turbulence in coastal areas in a RANS simulation or to estimate the turbulence offshore under land winds based on inland measurements.

table of content

Chapitre 5

Analysis of the low-level jet around the land-sea transition

Introduction

The wind profiles during nighttime (Figure 2.12d) revealed the presence of a pronounced LLJ at Le Croisic, i.e. at the coastline, coming from the land side (Figure 2.12e). This phenomenon is of high interest for wind-energy applications as it can drive large wind speed and important wind shear.
As reported in Section 1.4.2, different mechanisms can generate a LLJ in coastal areas. However, the observation at a single location is not sufficient to determine which one is involved in the present case. Thus, the first objective is to investigate the mechanism responsible for the initiation of the LLJ using the spatial information of the simulation results.
Section 1.4.5 reported some studies of LLJs in coastal areas. However, they were mostly long-term statistical analysis or single-location studies. Therefore, the second objective is to investigate how the LLJ characteristics (e.g. height, speed) change after crossing the coastline from land to sea.
Although the turbulence in a LLJ has been studied by several authors (Section 1.4.4), they focused mainly on inertial LLJs located either inland (Banta, 2008) or far offshore (Smedman et al., 1993). The present LES results give the opportunity to study the impact of the land-sea transition on the LLJ turbulence, which has not been studied yet. Thus, the third objective is to analyze the turbulence around the coastline during the LLJ event.

Section 5.1 presents the method used to characterize the LLJ, a comparison between WRF results and the LiDAR data, and the nature of the transition from the daytime SB to the nocturnal LLJ observed at Le Croisic. Then, the LLJ initiation mechanism is analyzed in Section 5.2 by studying the evolution of the air mass in the Lagrangian frame. Section 5.3 describes the evolution of the LLJ mean characteristics around the land-sea transition. Then, the offshore TKE in the LLJ is analyzed within the first kilometers of the coast in Section 5.4. Finally, several organized structures present in the LLJ are identified and described in Section 5.5.

table of content

5.1 Nocturnal low-level jet at Le Croisic

5.1.1 Detection and definition of the LLJ characteristics

For the LiDAR data, the LLJ detection method is based on Visich and Conan (2025) and Aird et al. (2022). It uses the function *find_peak* from the Scipy library (version 1.7.3) to search valid peaks in the WS profile at each time step, following these steps :

1. The surface point ($Z = 0,\ WS = 0$) is added in the WS profile below the lowest height of the profile (explanation for this is given hereafter).
2. Peaks in the WS profile are searched using the *find_peak* function. This function searches the local maxima in the profile, and, for each maximum, calculates its prominence and width. Briefly, the prominence of a peak is the difference between the peak value and the minimum value (called base) that is found before reaching a larger peak (SciPy, 2025). A base is found on both sides of the peak (above and below), and the difference between the peak value and the largest base is the prominence. Then, the closest distance needed to decrease by half of the prominence is calculated on both sides, and the sum of these two distances is the peak width.
3. Peaks with a width lower than 50 m are discarded to avoid false detections due to measurement errors.
4. A peak is kept only if its prominence is at least 2 $\mathrm{m.s^{-1}}$ or simultaneously larger than 1 $\mathrm{m.s^{-1}}$ and than 20 % of its velocity value.
5. Finally the profile is considered a LLJ if only one valid peak is found in the profile. The LLJ core speed (WS_{LLJ}) is the value of the peak. The LLJ core height (Z_{LLJ}) is determined by calculating the vertical gradient of WS just above and below the peak, and using a linear interpolation to find the height at which this gradient equals 0. With this method, Z_{LLJ} can take values between two grid points.

The addition of the surface point ($Z = 0,\ WS = 0$) is necessary to detect very low-level peaks, because their bottom base is the lowest point of the profile (20 m for the LiDAR). Therefore, the prominence would be highly underestimated if the velocity at the lowest measurement height is close to the peak velocity. Adding the surface point makes the detection method less dependent on the lowest measurement height.

For the simulation results, the same method is applied. For the purpose of continuity and noise attenuation, the peak detection is realized on the wind speed filtered (Section 2.4.3) with a standard deviation of 10 times the horizontal grid size of the domain ($\widetilde{WS} = \sqrt{\widetilde{U}^2 + \widetilde{V}^2}$). The $\widetilde{WS}$ profile up to 1 km high is used for the peak prominence and width calculation and an additional step is added to discard peaks above 500 m.

table of content

5.1.2 Comparison of the LLJ characteristics at Le Croisic

The evolution of the LLJ core height (Z_{LLJ}), core speed (WS_{LLJ}), core direction (WD_{LLJ}), width, and prominence, in LiDAR measurements and WRF results at the virtual mast location, is shown in Figure 5.1. The domain d06 is not shown as its results are very close to that of the domain d05. The LLJ characteristics can be analyzed using the same 5 Phases as in Figures 2.10 and 2.11.

Phase 1 : In LiDAR measurements during the late night, WS_{LLJ} reaches a maximum around 10 m.s^{-1} with a northeast direction, at a height between 100 and 200 m. In WRF results, the direction is well reproduced, the height is slightly overestimated, and WS_{LLJ} tends to decrease with time. WS_{LLJ} is significantly lower in RANS domains than in LES domains and in LiDAR measurements.

Phase 2 : In the early morning, while the wind direction is roughly constant from east-northeast (land), WS_{LLJ} decreases and Z_{LLJ} increases rapidly. The increase of Z_{LLJ} is closely related to that of Z_{CBL} (dashed grey line), indicating that the modification of the LLJ is caused by the development of the CBL. A similar behavior is observed by Djath et al. (2022) in the morning.

Phase 3 : On May 17, this phase (SB initiation) matches with the disappearance of the LLJ of Phase 2, and at the end, the Phase 4 LLJ starts. On May 18, a LLJ is observed in LES results with a low core speed (below 4 m.s^{-1} and at low altitude (below 50 m) whereas in LiDAR measurements, there is a competition between two low-speed peaks : the higher one being the late Phase 2 LLJ, and the lower one matches the early Phase 4 LLJ characteristics of the LES results.

Phase 4 : A LLJ is detected in both datasets with WS_{LLJ} increasing with time up to at least 8 m.s^{-1}. The core height also increases from 50 to 150 m high, and the wind direction veers from southwest to northwest (as in Figure 2.11). WS_{LLJ} is larger in finer domains (as in Phase 1), and is overestimated on May 18 compared to the LiDAR results (as WS in Figure 2.11). In Chapter 3, it was shown that a SB develops during this phase. As Z_{LLJ} remains below Z_{SB} (blueish dashed line) until 1900 UTC, it is clear that the detected LLJ corresponds to the SB gravity current. The increase of WS_{LLJ} and Z_{LLJ} and the veering of WD_{LLJ} are in agreement with this statement. After 1600 UTC, Z_{SB} decreases because of the SB rotation but Z_{LLJ} continues to increase.

Phase 5 : This phase is characterized by a rapid shift in WD_{LLJ} from northwest to northeast in both domains. Simultaneously, a minimum of WS_{LLJ} is noticeable in fine WRF domains (d03 to d05) and only on May 18 in LiDAR measurements while Z_{LLJ} reaches a maximum of about 200 m in both datasets.

For all phases, the evolution of the prominence (Figure 5.1e) is correlated with that of WS_{LLJ} with a significantly larger prominence during Phase 1 than during Phase 4 for equivalent values of WS_{LLJ}. The width (Figure 5.1d) shows the largest differences between the LiDAR data and the simulation results, especially during Phase 1 when the simulation overestimates it by 100 m.

Overall, the comparison between the LiDAR and the WRF LLJ characteristics

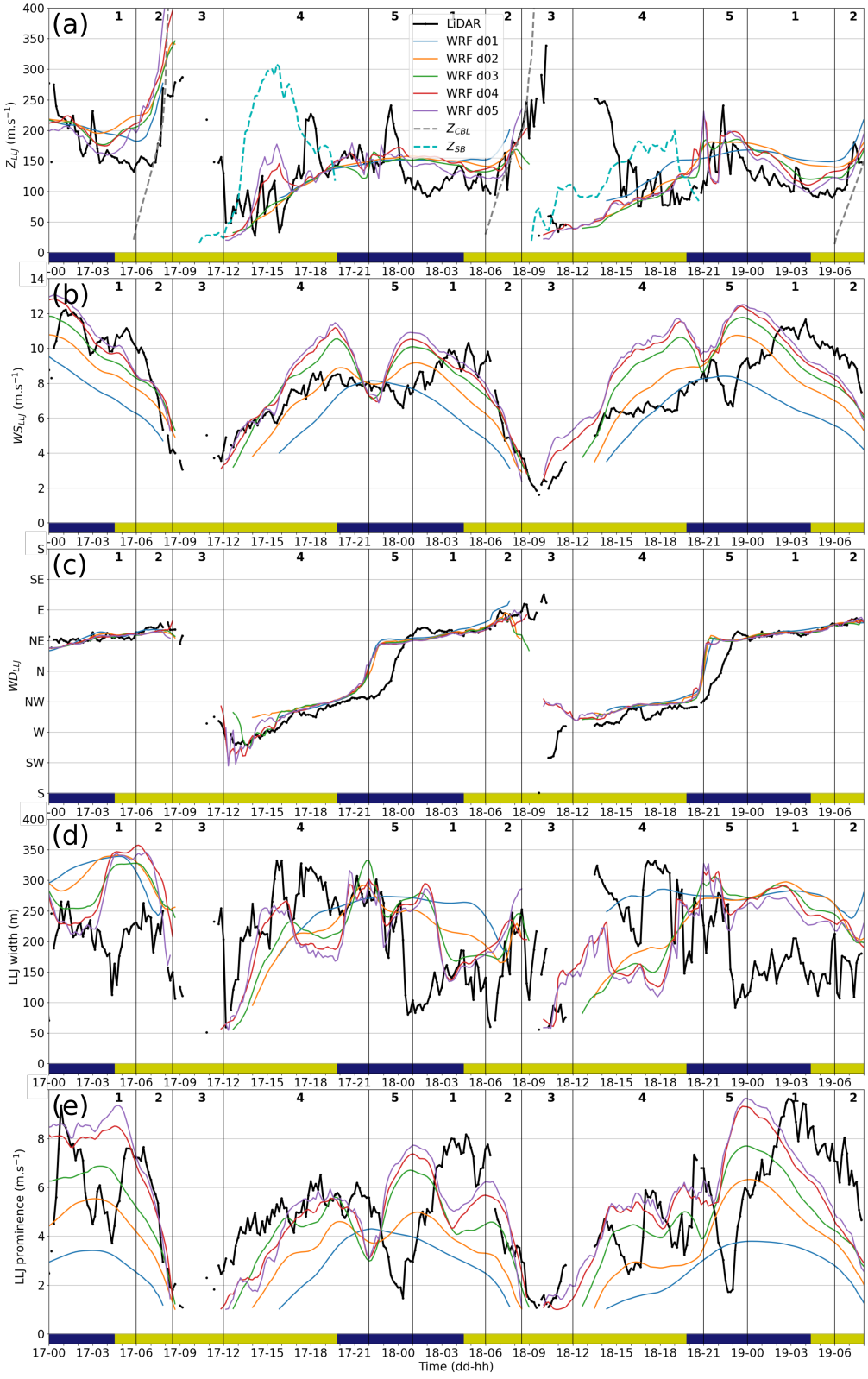

FIGURE 5.1 – Evolution of (a) Z_{LLJ}, (b) WS_{LLJ}, (c) WD_{LLJ}, (d) the LLJ width, and (e) the LLJ prominence, on May 17 and 18.

table of content

is satisfying. The nature of the LLJ from Phase 1 and the transition in Phase 5 are however not clear and will be investigated in the next sections.

5.1.3 Transition from sea breeze to low-level jet

To investigate the Phase 5 in the WRF results, Figure 5.2 displays the evolution of θ_v and the horizontal wind curl, two quantities that can be used to detect atmospheric fronts (Parfitt et al., 2017), at 100 m high between 1800 UTC on May 17 and 0300 UTC on May 18. The wind curl is calculated as $\frac{\partial \widetilde{V}}{\partial X} - \frac{\partial \widetilde{U}}{\partial Y}$ where U and V are filtered at a scale of 10 km (about 10 times the horizontal grid size, see Section 2.4.3).

At 1800 UTC, the domain d03 is divided into 3 zones, labeled E, F, and G. Zone E corresponds to the far-inland area unaffected by coastal flows. There, the air is warm due to the strong daytime heating of the land surface, and the wind direction is persistently from northeast. Zone F, to the west of the domain, represents the late regional sea breeze, where wind is blowing from northwest because it has turned clockwise during Phase 4 under the influence of the Coriolis force (Figure 2.11). All along the Atlantic coastline, the strongly positive curl, opposed to the negative synoptic curl (anticyclone in Figure 2.8), reveals the location of the SBF. To the north of the domain, in Zone G, the wind is mainly from north-northwest (coming from the Channel), and the temperature increases with distance inland. The wind field in this area is probably influenced by a baroclinic pressure force associated to the Channel coast. The E-G interface is characterized by horizontal convergence, as shown by the wind vectors, whereas the curl is close to 0.

From 1800 UTC to 0300 UTC, the SBF weakens and moves toward southwest, crossing the LiDAR location at coordinates (0, 0) around 2200 UTC (not shown), i.e. during Phase 5. Thus, the transition observed at the LiDAR location during Phase 5 corresponds to the passage of the F-G interface over the LiDAR position.

Figures 5.3a and 5.3b show the horizontal distribution of WS_{LLJ} and Z_{LLJ}, respectively, at 0300 UTC on May 18 (i.e. during Phase 1 at Le Croisic). Interestingly, the area of presence of the LLJ (non grey area) is very broad but is roughly restricted to Zones F and G, with a maximum in WS_{LLJ} of about 9 m.s^{-1} in each zone. It is noticeable that the LLJ is absent in Zone E, except in the South of France but this area has a complex topography and will not be analyzed here.

Overall, this Section showed that the nocturnal LLJ observed during Phase 1 at Le Croisic results from the advection of air from the Channel coast. In the next Section, the mechanism responsible for the generation of this LLJ is investigated

table of content

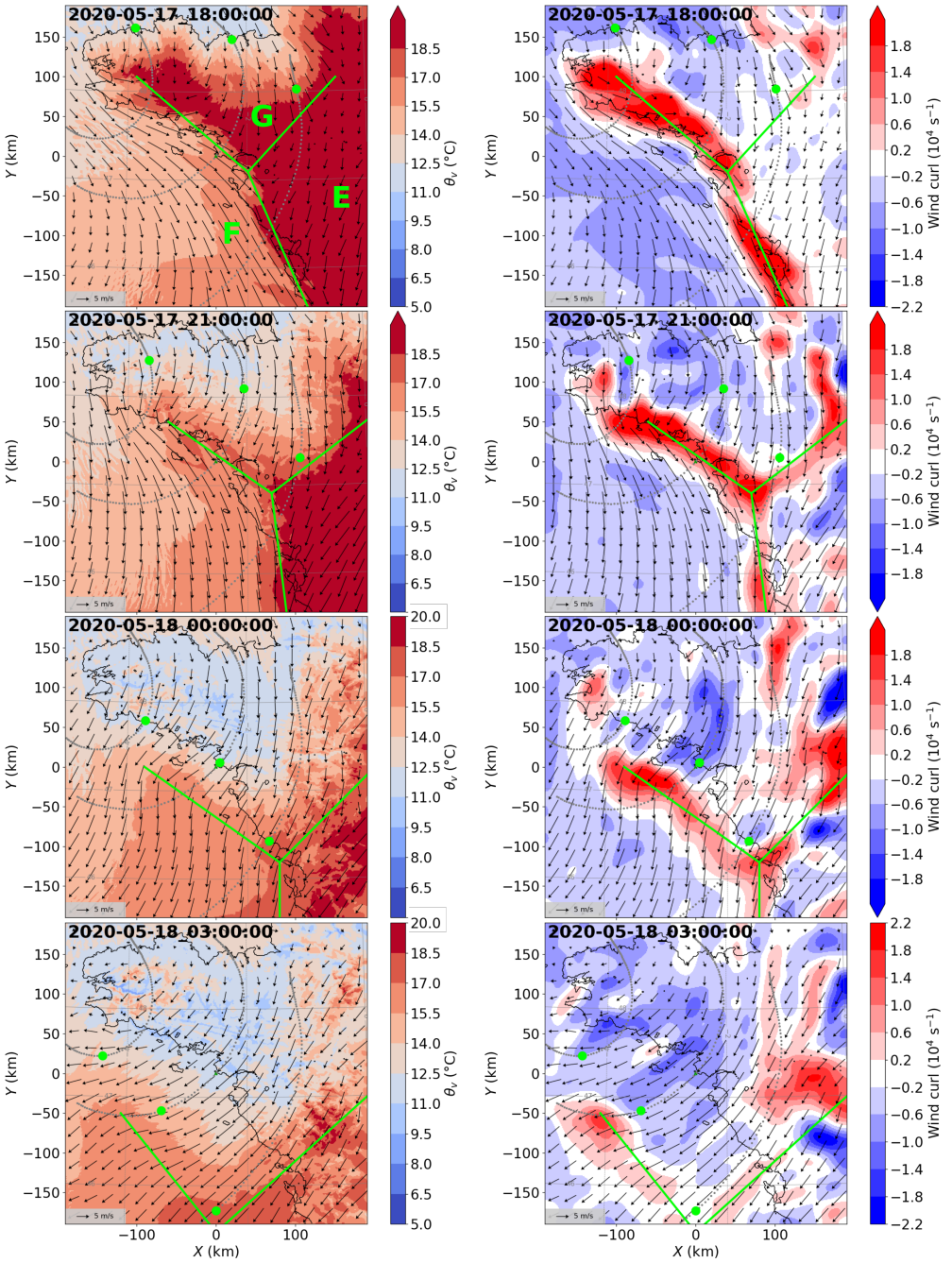

FIGURE 5.2 – Evolution of (left) θ_v and (right) the horizontal wind curl at 100 m high between 1800 UTC on May 17 and 0300 UTC on May 18 based on d03 results. The curl is computed with U and V horizontally filtered with a 10-km Gaussian filter. Lines separates Zones E, F, and G explained in the text. Grey dots correspond to the trajectories introduced later in Figure 5.4 and the big green dot is the location of the air mas at the time indicated on the Figure.

table of content

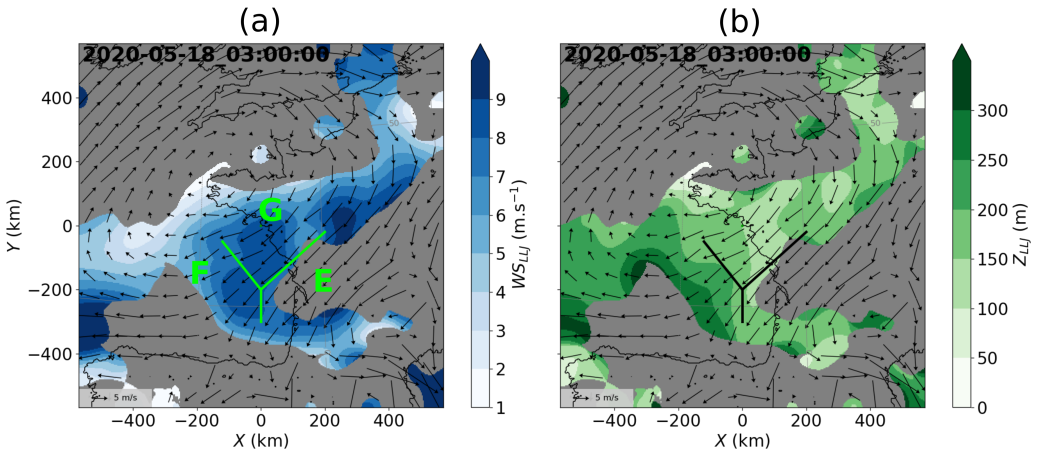

FIGURE 5.3 – Spatial distribution of (a) WS_{LLJ} and (b) Z_{LLJ} on May 18 at 0300 UTC based on WRF d02. No LLJ is detected in the grey area. The arrows indicate the 150 m wind vector and the green lines delimits the three Zones defined in Figure 5.2.

5.2 Initiation of the nocturnal low-level jet

As shown in the previous section, the LLJ at Le Croisic results from air that is advected from the Channel coast, i.e. over a few hundreds of kilometers. The advection time associated with a wind speed around 9 $m.s^{-1}$ is more than 6 hours. This time scale is too close to that of the thermal forcing (daily cycle) to study the LLJ initiation in the Eulerian frame. Therefore, the LLJ history is analyzed in a Lagrangian frame, i.e. following trajectories computed in post-processing (Section 2.4.4) based on the wind field filtered at 10 km.

Three trajectories named T1, T2, and T3 are computed, from three coastal location where a LLJ is observed at 0000 UTC (the virtual mast is at T2). From each initial location, both the forward and backward trajectories are computed. The hourly WS, WD, and θ_v profiles, only in the backward trajectories, are displayed in Figures 5.4a to 5.4i, and the corresponding trajectories are shown in Figure 5.4j. The evolution of the profiles along T2 are analyzed first, and then compared with T1 and T3.

Along T2, between 1500 UTC and 1700 UTC on May 17, the WS profile (dark blue curve in Figure 5.4b) already features a maximum with a north-northwest WD (Figures 5.4e). This maximum is located below 200 m in a shallow convective mixed layer as depicted by the θ_v profiles (Figures 5.4h), whereas above the mixed layer, the atmosphere is stratified. Between 1800 and 2000 UTC (blue), WS increases up to 6 $m.s^{-1}$ below 600 m but remains low above. Meanwhile, a stable layer starts to develop below 100 m high. From 2100 UTC to 0000 UTC (light green before 0000 UTC and olive at 0000 UTC), while progressively getting closer to the Atlantic coast, WS at 180 m rapidly increases, forming a narrow peak. Near the surface, the wind veers progressively over time. At 800 m high, WD shows a 90° counter-clockwise

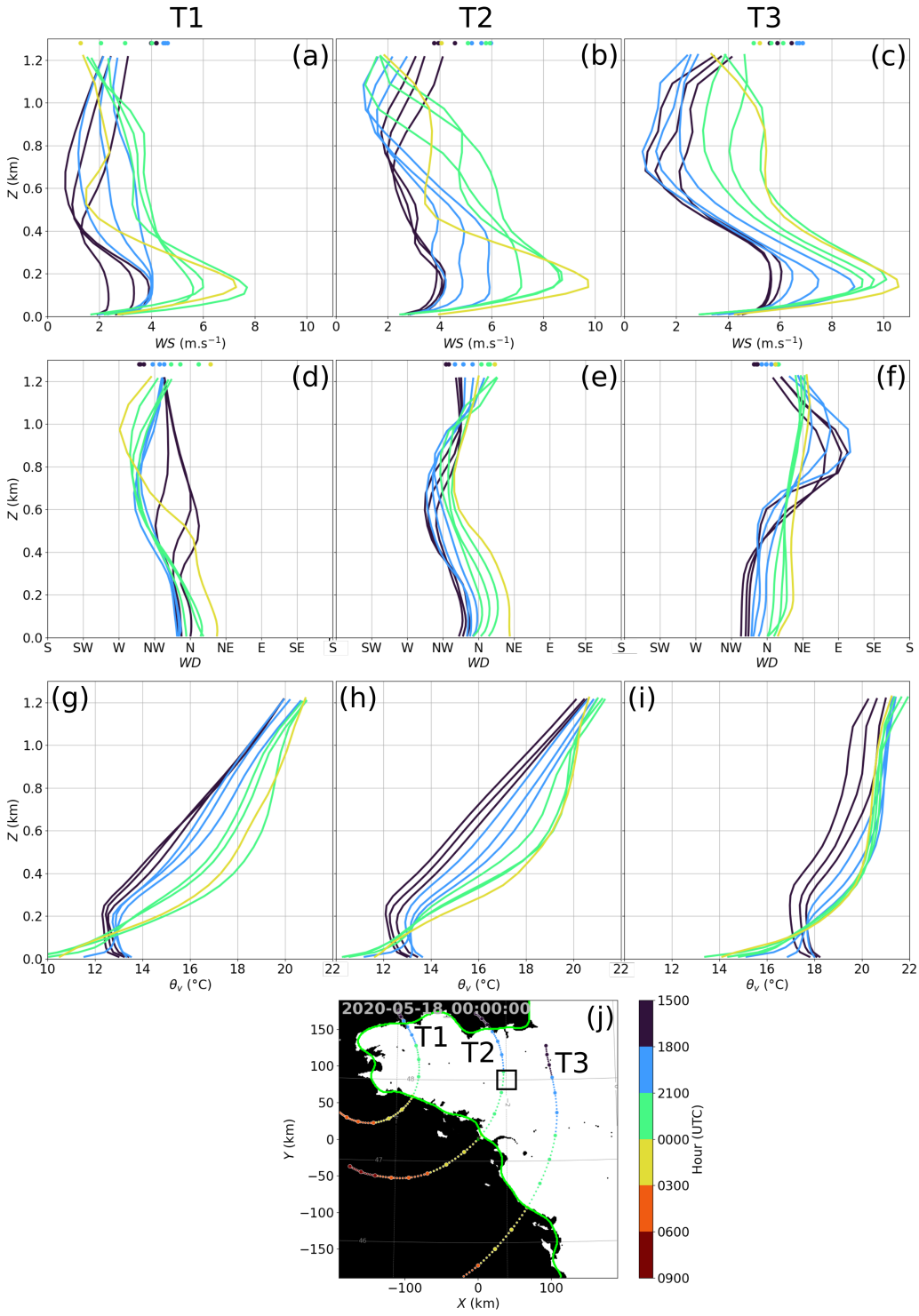

FIGURE 5.4 – Profiles of *WS* (a-c), *WD* (d-f), and θ_v (g-i) on the three trajectories shown in (j), based on domain d03 results. The color indicates the hour of the day. The three trajectories crosses the green smoothed coastline at 0000 UTC on May 18, and corresponds from top-left to bottom-right to (a, d, g), (b, e, h), and (c, f, i). The dots at the top of (a-f) show the value at 2000 m high.

table of content

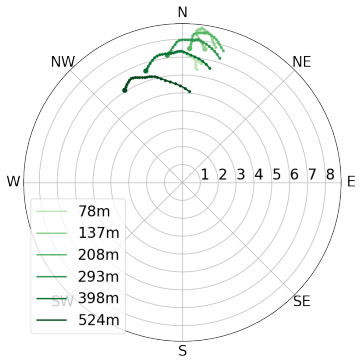

FIGURE 5.5 – Hodographs of the wind over time between 2100 UTC (large dot) and 0100 UTC, at several heights, in the black rectangle shown in Figure 5.4j.

departure compared to near the surface. The θ_v profiles show that the whole ABL is stably stratified.
The profiles on trajectories T1 and T3 show nearly the same evolution with the presence of a slow LLJ at 1500 UTC that accelerates all along the path while the ABL becomes fully stable.

The three trajectories are also reported in the distribution of θ_v at 100 m high shown in Figure 5.2. This figure reveals that, all along the trajectories, the air parcels are located in an area with a horizontal gradient of temperature, i.e. a baroclinic area. During daytime, the Channel coast induces baroclinicity, responsible for the LLJ profiles at 1500 UTC. Notably, a SB return current can be identified by the change in *WD* at 800 m high in T3 (Figure 5.4f). Then, the advection of the cold northerly wind from the Channel that progressively warms up inland, maintains this thermal gradient during daytime. After the sunset, the ABL progressively cools down but the thermal difference remains. Finally the air mass reaches the Atlantic coast at night when the sea surface is warmer than the land surface, which maintains the favorable baroclinicity. Therefore, the persistence of the baroclinicity whereas the land-sea temperature difference changes of sign (Figure 2.9) is a consequence of the advection over the large-scale Brittany peninsula.

The acceleration of the jet at 2100 UTC matches with the development of the near-surface nighttime SBL, suggesting that the jet accelerates due to frictional decoupling (Section 1.4.2). In Figure 5.5, wind rotation over time is observed at different heights inland between 2100 and 0100 UTC. This rotation is likely the manifestation of IO initiated by the frictional decoupling (see Section 1.2.3).

Overall, the LLJ is influenced both by the persistent baroclinicity and the frictional decoupling. The acceleration of the LLJ after sunset suggests that the wind speed at Z_{LLJ} before the decoupling, although it was already a LLJ, was lower than the equilibrium wind speed. One can conclude that the equilibrium wind has a

jet-like profile that is very likely caused by the baroclinicity. Thus, the persistent baroclinicity appears to be the primary mechanism for the presence of the LLJ, whereas the frictional decoupling contributes to the LLJ acceleration as a secondary mechanism.

5.3 Evolution of the low-level jet characteristics around the land-sea transition

The trajectories can be used to analyzed the evolution of the LLJ characteristics around the land-sea transition. Figures 5.6 shows the evolution of WS_{LLJ} and the prominence over several trajectories crossing the coastline at 0000 UTC (Figures 5.6a and 5.6c) and 0200 UTC (Figures 5.6b and 5.6d).

The southeastern part of the domain where no LLJ is detected (grey area), corresponds to Zone E where the absence of LLJ was already noticed in Figure 5.3. In the LLJ, WS_{LLJ} (Figures 5.6a and 5.6b) reaches a maximum at the Atlantic coastline. This maximum is significantly lower at the northwest of the domain where the synoptic wind speed is also lower. To the north of Le Croisic, the LLJ prominence (5.6c and 5.6d) is found to be at least 3 m.s^{-1} larger at the coastline than 50 km inland, while WS_{LLJ} only increases by about 1 m.s^{-1}. This result illustrates the simultaneous increase of the peak velocity and decrease of the minimum velocity above when approaching to the coast. This is consistent with the baroclinic mechanism proposed in Section 5.2, that generates opposite pressure forcing close to the surface and aloft (Section 1.2.1). For trajectories to the south of Le Croisic, there is no clear increase of the LLJ prominence at the coastline. Instead, a significant maximum of prominence is found earlier, around coordinates (100, 50 km).
Offshore, both WS_{LLJ} and the prominence decrease with increasing distance from the coastline. For trajectories crossing the coastline at 0000 UTC, the decrease in WS_{LLJ} starts roughly 3 hours and 50 km after crossing the coastline while the decrease in the prominence is more pronounced close to the coastline. For that crossing the coastline at 0200 UTC, both quantities decrease gradually with increasing offshore distance.

The core height distribution, displayed in Figures 5.7a and 5.7b reveals that Z_{LLJ} is roughly the lowest at the coastline (especially at 0200 UTC with values below 150 m) and increases with distance offshore. There are also significant variations in the alongshore direction. The evolution of the width, shown in Figures 5.7c and 5.7d is quite similar.

To pursue the analysis of the LLJ characteristics offshore, the evolution of the N^2_{BV} profile along the trajectory T2 (Figure 5.2j) is shown in Figure 5.8a. As the land surface is colder than the sea surface at night (Figure 2.9), a convective TIBL

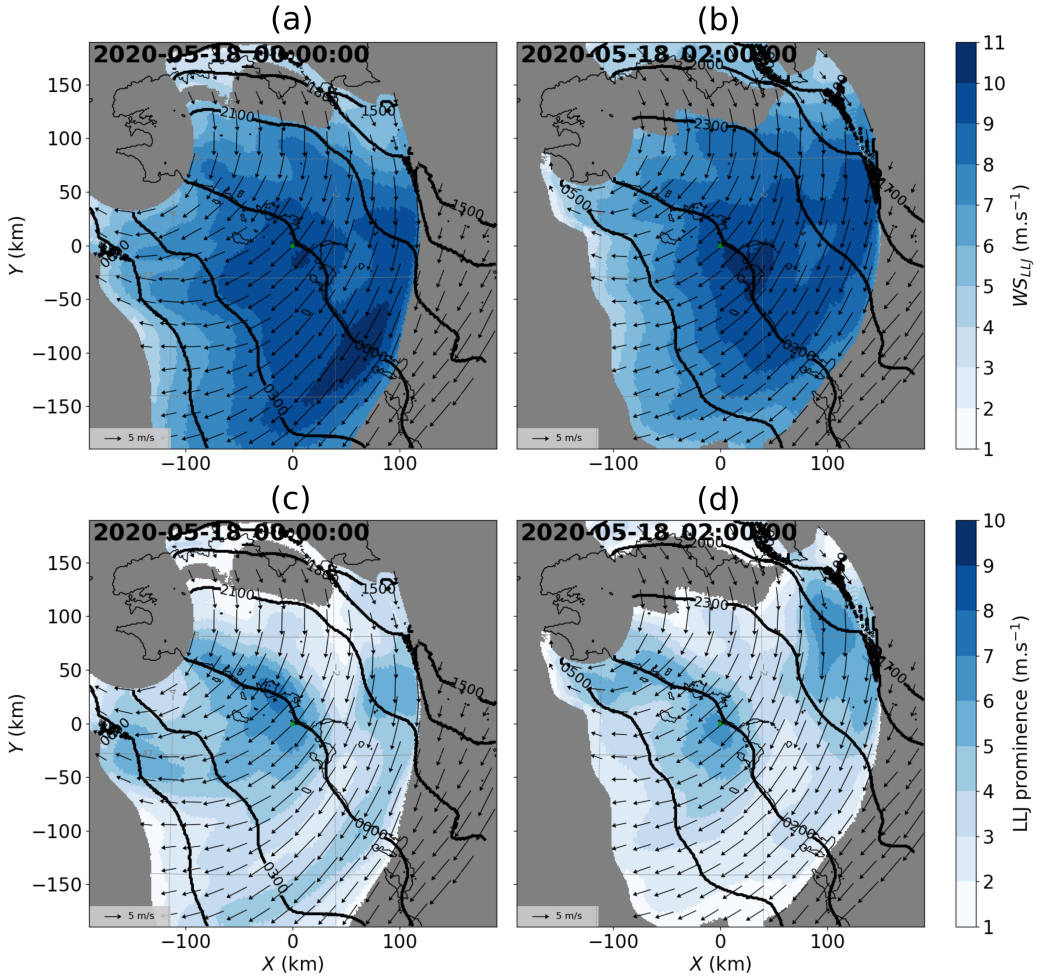

FIGURE 5.6 – Spatial evolution of (a, b) WS_{LLJ} and (c, d) the LLJ prominence on the trajectories that crossed the coastline at (a, c) 0000 UTC and (b, d) 0200 UTC on May 18, based on domain d03 results. Isolines of time are shown every 3 hours in black.

develops over the sea, depicted by negative values of N^2_{BV} close to the surface. The top of this TIBL (Z_{TIBL}), defined with the threshold $N^2_{BV} = 10^{-4}$ s^{-2}, is depicted by a red line. The TIBL thickens with the increasing offshore distance while its growth rate is decreasing, which is in agreement with previous studies over land (Calmet and Mestayer, 2015) and over a lake (Chang and Braham, 1991). The LLJ core, depicted by the green line, remains always above Z_{TIBL} so that Z_{LLJ} also increases with increasing offshore distance. Figure 5.8b shows a scatter plot to compare Z_{TIBL} and Z_{LLJ} on several trajectories. It appears that Z_{TIBL} acts as a lower boundary for the LLJ core.

To better understand the interaction between the TIBL and the LLJ, the evolution of the wind and temperature profiles after crossing the coastline is shown in Figure 5.9 on the same three trajectories as in Figure 5.4, i.e. T1, T2, and T3.

table of content

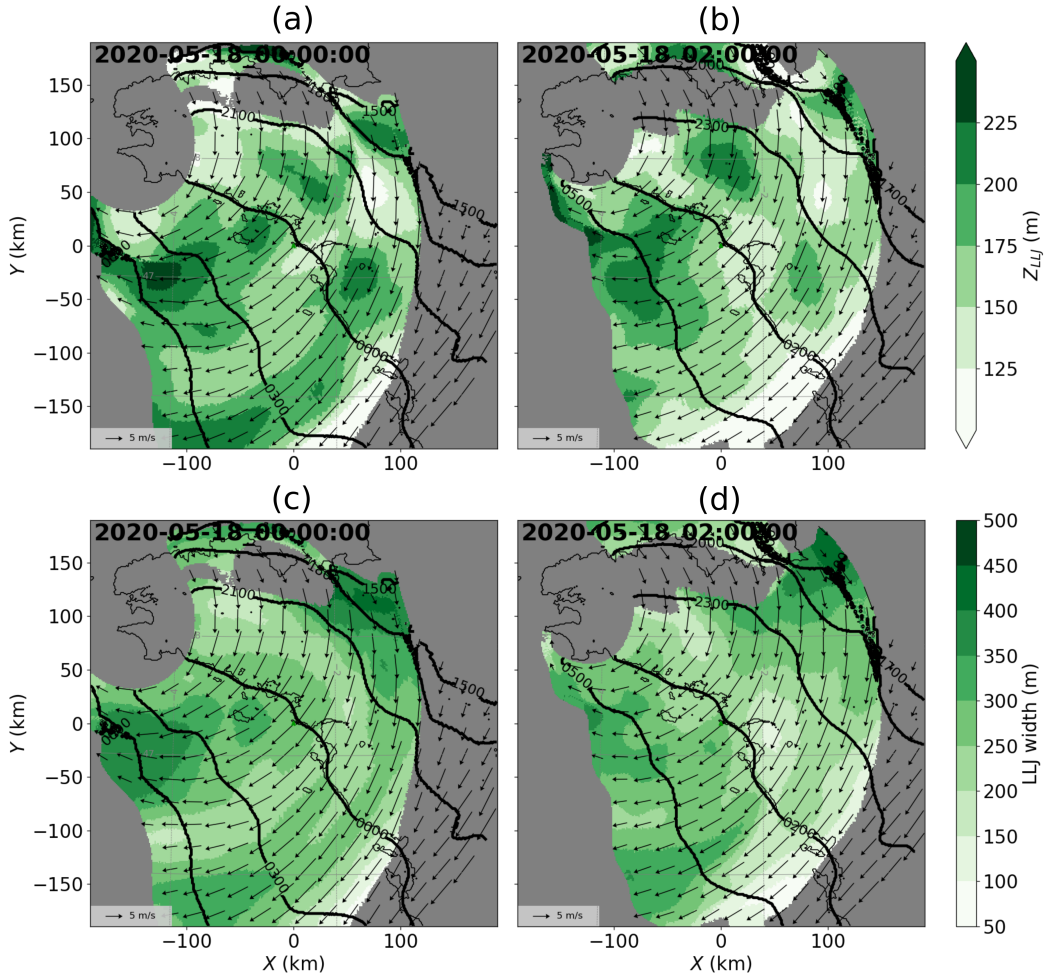

FIGURE 5.7 – Same as Figure 5.6 for (a, b) Z_{LLJ} and (c, d) the LLJ width

For the three trajectories, the θ_v profiles (Figures 5.9g to 5.9i) have a negative vertical gradient near the sea surface, revealing the development of the TIBL, that thickens with increasing distance. Below 50 m, in the surface layer, *WS* increases at first which can be associated both to the convective TIBL (Hara et al., 2009) and to the rough-smooth IBL as suggested by Barthelmie et al. (1996). Meanwhile, at the core height, WS_{LLJ} decreases. As a result, the vertical gradient of *WS* between 50 and 150 m high decreases with time, especially along T2.

Above Z_{LLJ}, along T1 and T2 (Figures 5.9a and 5.9b), *WS* also decreases until *WD* switches from land wind to sea wind. Along T1, this switch occurs at the coastline at 0000 UTC whereas along T2, it occurs around 0300 UTC at 100 km offshore. T3 shows a different behavior : *WS* remains larger than 5 m.s^{-1} and *WD* is constant with height.

table of content

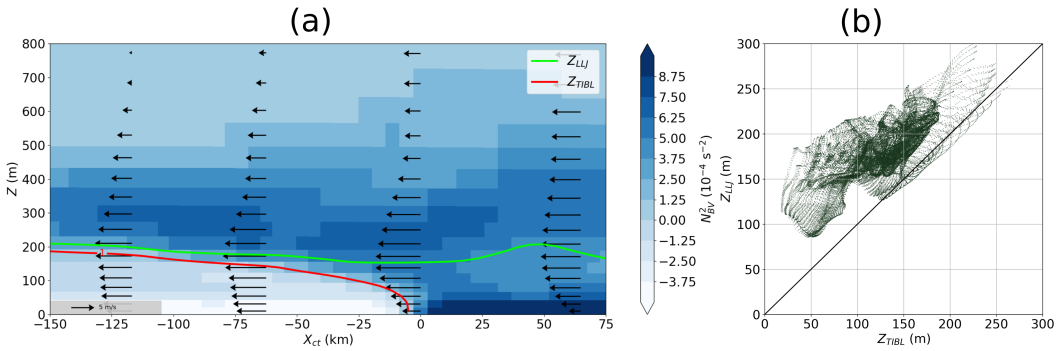

FIGURE 5.8 – (a) Evolution of the ${N_{BV}}^2$ profile as a function of the distance from the coast along the trajectory T2 (X_{ct}, negative in the offshore direction). The green and red curves show Z_{LLJ} and the TIBL height Z_{TIBL}, respectively. (b) Scatter plot of Z_{LLJ} as a function of Z_{TIBL} on all the trajectories used to draw Figures 5.6 and 5.7.

As shown in Figure 5.2g, at 0300 UTC a horizontal gradient of temperature at 100 m high is observable offshore, which is due to a combination of two mechanisms : (i) air over land cools down in the nocturnal ABL (see Figure 2.9) and is progressively advected offshore, and (ii) after crossing the coastline, the air is warmed up in the TIBL near the surface. Thus, the switch in WD above 600 m high along T1 and T2 corresponds to a weak land-breeze return current, caused by the baroclinicity. The baroclinicity should be favorable to a reinforcement of the land gravity current (i.e. the LLJ) near the surface. Thus, the decrease of WS_{LLJ} with increasing offshore distance is likely caused by the mixing in the convective TIBL. The decrease in WS is more pronounced just below the jet core (i.e. close to Z_{TIBL}), than just above it, which explains the increase of Z_{LLJ} along T2 and T3.

These results suggest that the evolution of the LLJ offshore is mostly influenced by the development of the TIBL, which contributes to its weakening and its rise. Despite this negative contribution, the LLJ sustains farther than 100 km offshore (along T2). In the next section, the focus is made on the first kilometers after the land-sea transition to study the interaction between the LLJ, the TIBL and the turbulence.

5.4 TKE in the low-level jet around the land-sea transition

To study the TKE as a function of the distance from the coast (X_c), the domain d06 is divided into the same areas as depicted in Figure 4.1 where the various profiles presented hereafter are averaged as in Section 4.1. This section focuses on the few kilometers around the land-sea transition, so that the associated advection time scale is much smaller than in the previous sections, enabling the following analysis to be carried out in an Eulerian frame.

table of content

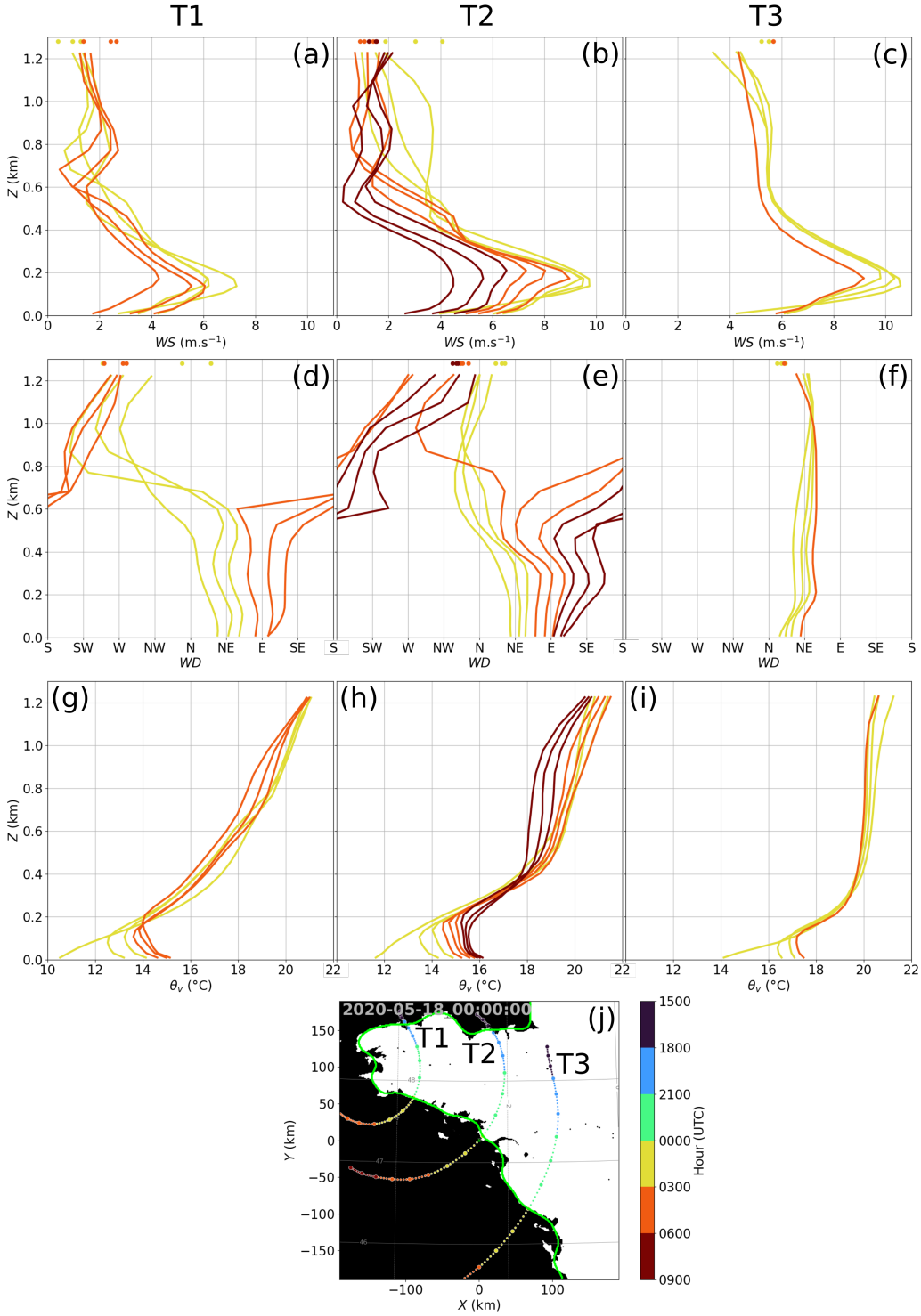

FIGURE 5.9 – Same as Figure 5.4, offshore

table of content

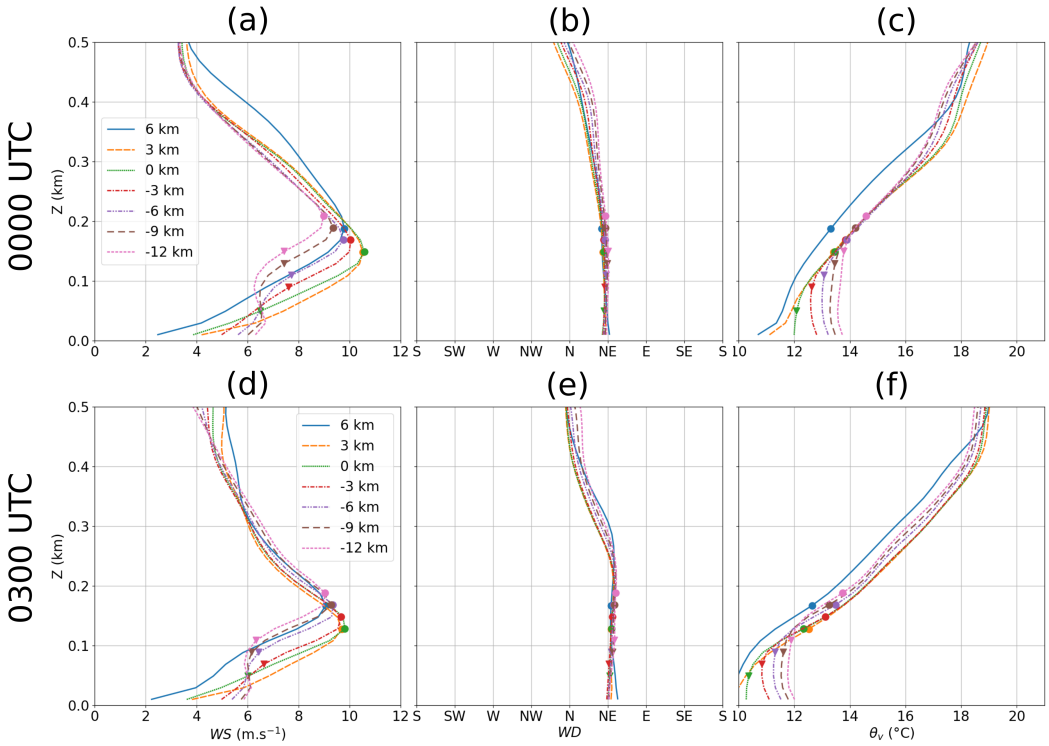

FIGURE 5.10 – Evolution of the profiles of (a, d) WS, (b, e) WD and (c, f) θ_v as a function of the distance from coastline (X_c in km) on May 18 at (a, b, c) 0000 UTC and (d, e, f) 0300 UTC, based on domain d06 results. The circles indicate Z_{LLJ} and the triangles indicate Z_{TIBL}.

Before studying the TKE profiles, a description of the mean quantities is provided in Figure 5.10 which displays the wind and temperature profiles at 0000 and 0300 UTC on May 18 at various distance from the coast. The profiles at 0000 UTC and at 0300 UTC are very similar. The WS profiles have a LLJ shape while WD is from land (north-northeast) throughout the profile. The θ_v profiles show that the ABL is stable except for a well-mixed layer corresponding to the TIBL. With increasing offshore distance, the TIBL grows, WS below 50 m increases, WS_{LLJ} decreases, and Z_{LLJ} increases. All these findings are in agreement with the observations made in Section 5.3.

The LLJ characteristics WS_{LLJ} and Z_{LLJ} are displayed in Figures 5.11a and 5.11b, respectively, as a function of X_c between 0000 and 0400 UTC. Starting from the coast and going offshore ($X_c < 0$), the decrease rate of WS_{LLJ} is about 0.1 $\mathrm{m.s^{-1}.km^{-1}}$ while the growth rate of Z_{LLJ} is between 5 and 10 $\mathrm{m.km^{-1}}$. The two characteristics vary by 10 to 20 % over time during the 4-hour period.

The resolved TKE profiles as a function of the offshore distance at 0000 and 0300 UTC are displayed in Figures 5.12a and 5.12d, respectively. Above Z_{LLJ}, k_{calc} is very low (< 0.02 $\mathrm{m^2.s^{-2}}$), except for a small maximum of 0.03 $\mathrm{m^2.s^{-2}}$ at 450 m

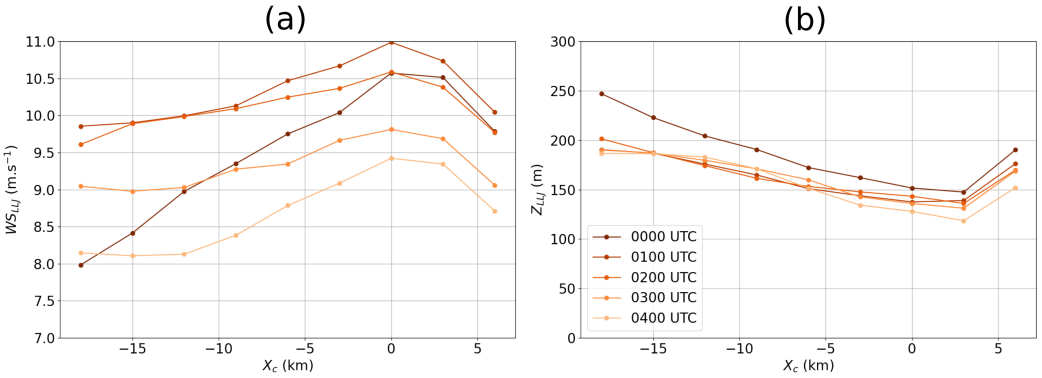

FIGURE 5.11 – Evolution of (a) WS_{LLJ} and (b) Z_{LLJ} as a function of X_c at different times on May 18, based on domain d06 results.

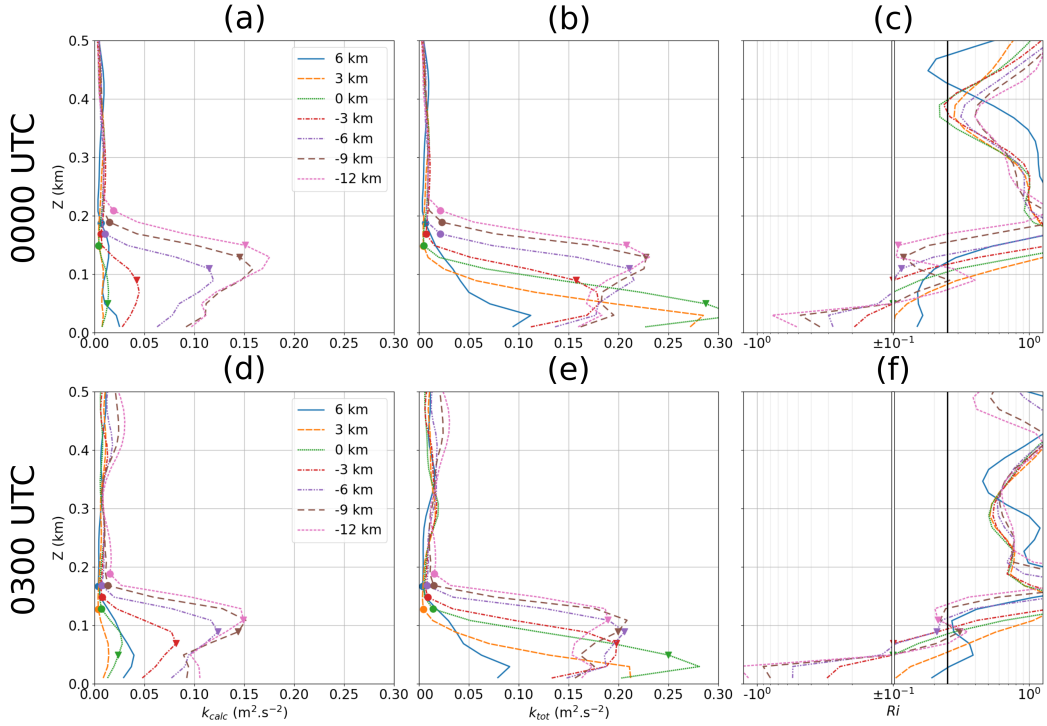

FIGURE 5.12 – Same as Figure 5.10 for (a, d) k_{calc}, (b, e) k_{tot} and (c, f) Ri where the vertical black line indicates 0.25.

high at 0300 UTC. Below Z_{LLJ}, it exhibits a maximum which increases with offshore distance, located at the top of the TIBL (triangles) where the shear is intense. In the TIBL, k_{calc} also increases with offshore distance but less and less rapidly so that, between -9 and -12 km, it is constant and even slightly decreasing at 0000 UTC.

The profiles of Ri displayed in Figures 5.12c and 5.12f, can help understanding the distribution of k_{calc}. For $X_c <$ -3 km, the negative values of Ri below 50 m suggest that k_{calc} is produced by the positive buoyancy effect in the TIBL. Around

Z_{TIBL} (triangles), Ri is positive but lower than the 0.25 critical value, indicating that the shear production dominates over the buoyancy inhibition. At Z_{LLJ} (circles), the shear goes to 0 so that Ri becomes infinite, which explains the very low TKE. Above Z_{LLJ}, Ri is mostly larger than 0.5 so that k_{calc} is inhibited by buoyancy effect.

The comparison between k_{calc} and k_{tot} (Figures 5.12b and 5.12e) reveals that, close to the coastline (for X_c = 3, 0, and -3 km), k_{calc} is less than half of k_{tot}, meaning that most of the TKE is subgrid. This behavior is exacerbated near the surface. The evolution of k_{tot} with distance is no longer consistent with that of k_{calc} in the transition region. The fact that the maximum k_{tot} is the greatest where the atmosphere is stable could be the result of a poor subgrid-scale modeling. Farther offshore (for X_c = -6, -9, and -12 km), k_{calc} is the largest contribution to k_{tot}, i.e. most of the TKE is resolved.

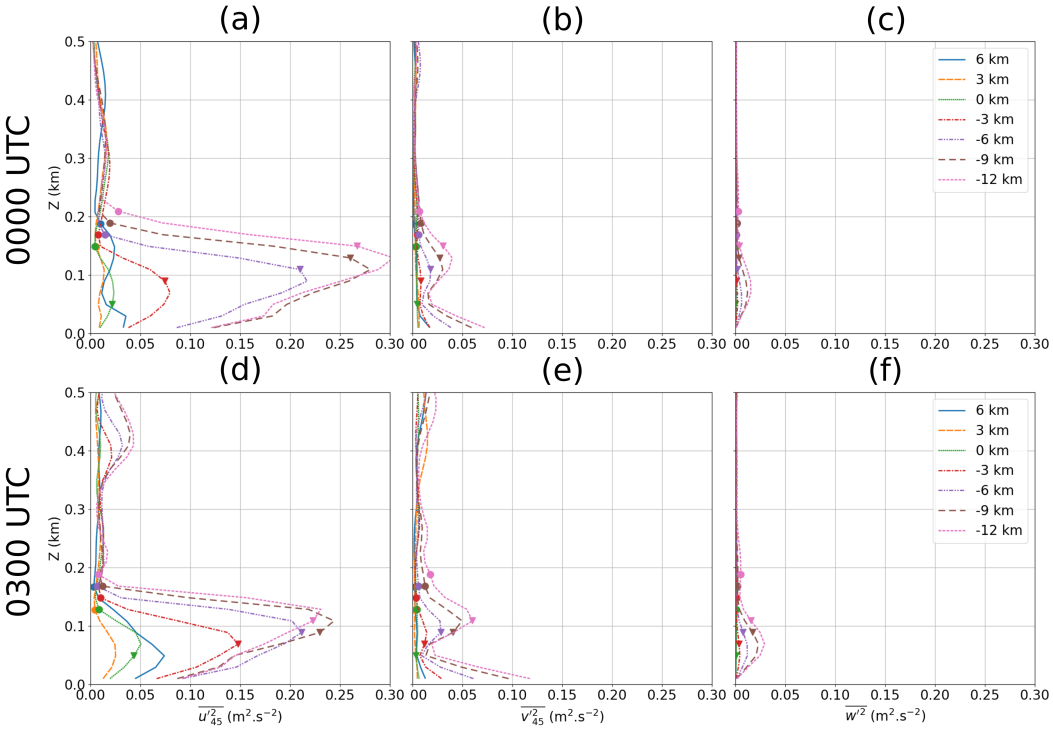

FIGURE 5.13 – Same as Figure 5.12 but for (a, d) $\overline{u'^2_{45}}$, (b, e) $\overline{v'^2_{45}}$ and (c, f) $\overline{w'^2}$.

Figure 5.13 displays the three contributions to k_{calc} in a referential frame rotated at 45°, so that $\overline{u'^2_{45}}$ is roughly the variance along the LLJ wind direction (Figure 5.10b and 5.10e) and $\overline{v'^2_{45}}$, the variance in the transversal direction. Below Z_{LLJ}, $\overline{u'^2_{45}}$ (Figures 5.13a and 5.13d) is the largest at all heights, which is likely because it is in the direction of the shear related to the LLJ. The profiles of $\overline{v'^2_{45}}$ (Figures 5.13b and 5.13c) show a particular behavior with two maxima, the first one close to the surface and the second near the top of the TIBL, while $\overline{w'^2}$ exhibits a maximum in between.

table of content

Above Z_{LLJ}, $\overline{w'^2}$ nearly equals 0, while the two other components are around 0.01 $m^2.s^{-2}$, except for the peak of $\overline{u'^2_{45}}$ at 0300 UTC at 400 m high previously observed in the k_{calc} profile (Figure 5.12d). It will be shown in Section 5.5 that the particular profiles of $\overline{v'^2_{45}}$, and $\overline{w'^2}$ in the TIBL are related to the presence of longitudinal rolls, and that the small peak of $\overline{u'^2_{45}}$ at 400 m high is caused by the presence of KHW.

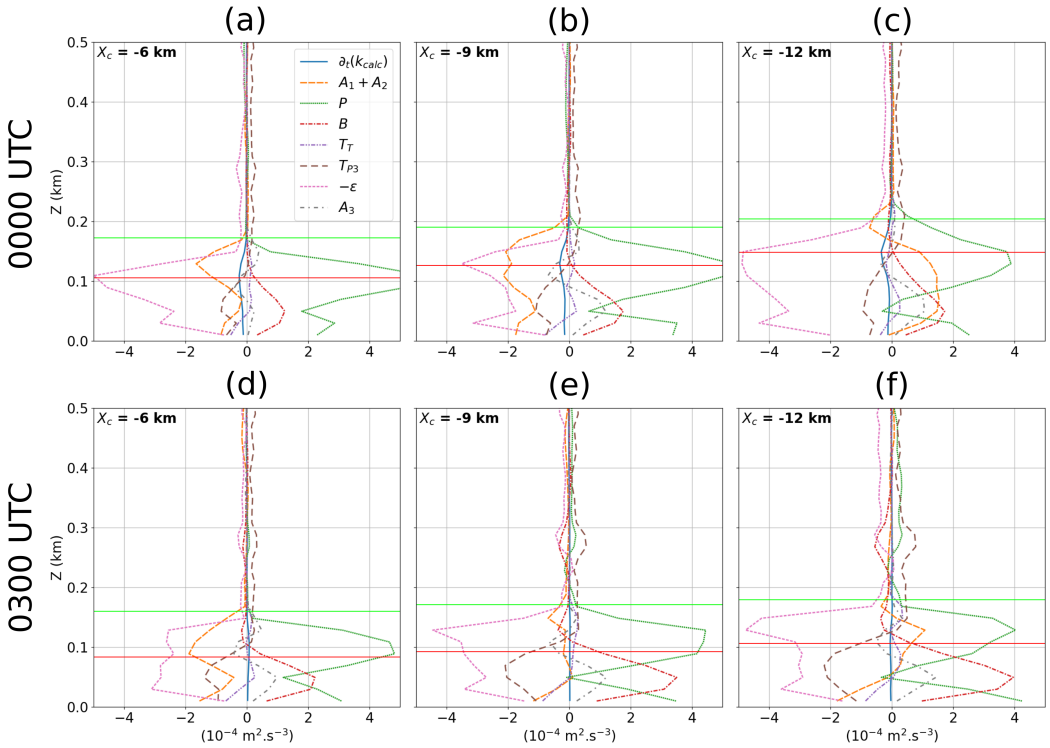

FIGURE 5.14 – TKE budget at X_c = (a, d) -6, (b, e) -9, and (c, f) -12 km at (a, b, c) 0000 and (d, e, f) 0300 UTC, based on domain d06 results. The horizontal green and red lines indicate Z_{LLJ} and Z_{TIBL}, respectively. The advection term A is separated into the horizontal advection (A_1 + A_2) and the vertical advection (A_3). Due to their suspicious behavior the horizontal pressure terms are discarded and are not taken into account in the calculation of ε. Only the vertical pressure term T_{p3} is shown.

To further investigate the distribution of the resolved TKE, its budget (Equation 2.6) is calculated offshore at X_c = -6, -9, and -12 km, and shown at 0000 UTC in Figures 5.14a to 5.14c and at 0300 UTC in Figures 5.14d to 5.14f. Note that the horizontal components of T_P exhibit a non-physical behavior so that T_P is replaced by its vertical component T_{P3}.

In the middle of the TIBL, at 50 m high, B is positive and dominates over P (except at 0000 UTC at X_c = -6 km in Figure 5.14a). T_{P3} partially compensates B by transferring energy above the TIBL. Both the turbulent transport T_T and the vertical advection A_3 are positive around 50 m high, indicating a transport of TKE to the center of the TIBL. It is compensated by negative values close to the surface for T_T, and near Z_{TIBL} for A_3. $A_1 + A_2$ is lower at X_c = -6 km where k_{calc} increases

with offshore distance than at X_c = -12 km where it does not (Figure 5.12).
Between Z_{TIBL} and Z_{LLJ}, P is by far the major contribution to the production of k_{calc}, and is mostly compensated by ε. The term A_3 is slightly positive, indicating some transport of k_{calc} from the TIBL. $A_1 + A_2$ is negative because, in this layer, k_{calc} increases with increasing offshore distance, except at X_c = -12 km at 0300 UTC (Figure 5.12).
Finally, above Z_{LLJ}, all the terms are an order of magnitude lower than below.
These budgets confirm the explanation formulated based on the Ri profile with the presence of 3 distinct layers : The TIBL where buoyancy production dominates, the layer between Z_{TIBL} and Z_{LLJ} where dynamical production dominates, and the layer above the jet where the TKE is negligible. The fact that A_3 transport TKE roughly the same way as T_T is the signature of some organized convective structures that are not completely filtered out by the 10-minute averaging. These structures will be investigated in the next section.

5.5 Organized structures in the low-level jet

The previous section focused on the vertical and cross-coast variations of the averaged profiles of k_{calc}. However, as already stated in Sections 4.2 and 4.3, k_{calc} also includes the energy of a various amount of organized structures such as the GW and the KHW, for example. Figure 5.15a, showing the horizontal distribution of k_{calc} in domain d06 at 110 m high at 0040 UTC, reveals that k_{calc} is very heterogeneous offshore. The horizontal cross-sections of w, at 50, 110, and 410 m high shown in Figure 5.15b, 5.15c, and 5.15d, respectively, show the presence of several organized structures with various orientations and scales which are likely at the origin of the heterogeneous distribution of k_{calc}.

This section aims at determining the nature of these structures, their characteristics, and their influence on the LLJ and the ABL. In Sections 5.5.1, 5.5.2, and 5.5.3, three different types of oscillations are investigated, using horizontal and vertical cross sections of the instantaneous w field and time series of the instantaneous fields available at the two "+" shown in Figure 5.15.

5.5.1 Convective rolls in the TIBL

Figures 5.16a and 5.16b, show the distribution of w^* and u^*, respectively, at 0240 UTC. w^* does not vary significantly with distance and is mainly between 0.36 and 0.42 m.s^{-1}, whereas u^* clearly increases with increasing offshore distance from 0.16 to 0.23. As a result the ratio u^*/w^* (Figure 5.16c) increases with increasing offshore distance from 0.4 to 0.64. According to several studies reported in Section 1.5.4, this range of values indicate that the TIBL is moderately convective and

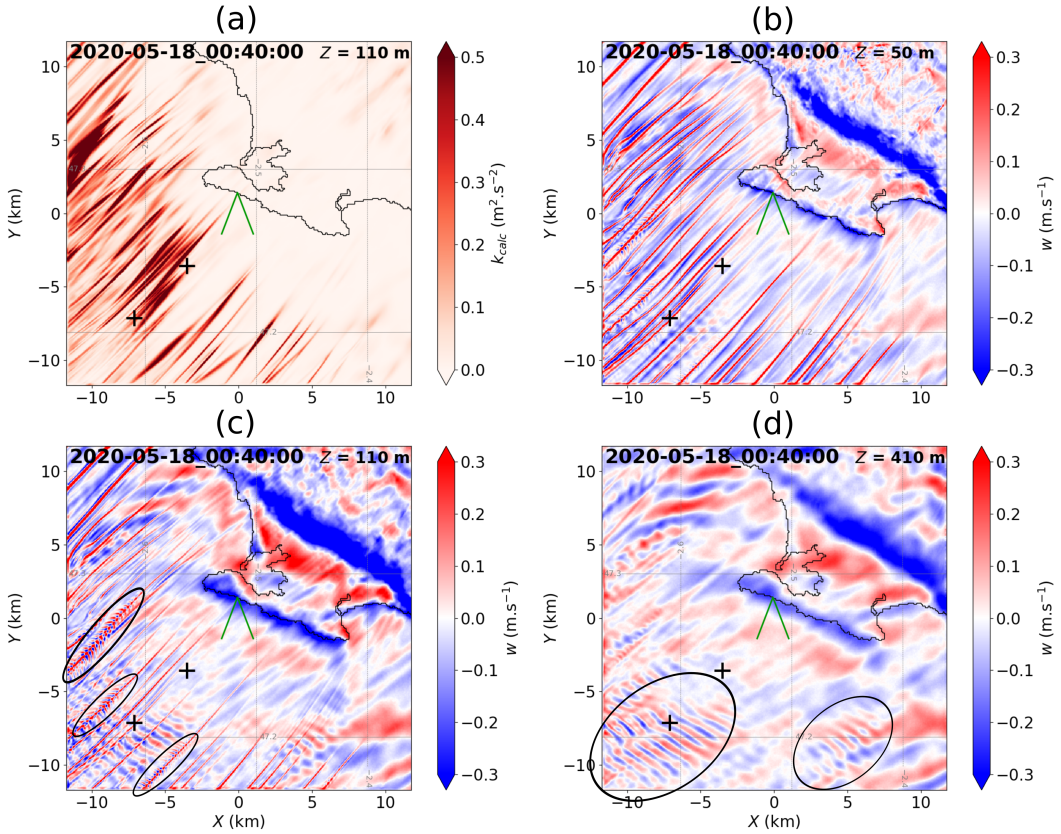

FIGURE 5.15 – Distribution of (a) k_{calc} at 110 m high and (b-d) w at (b) 50 m, (c) 110 m , and (d) 410 m high, at 0040 on May 18, based on domain d06 results.

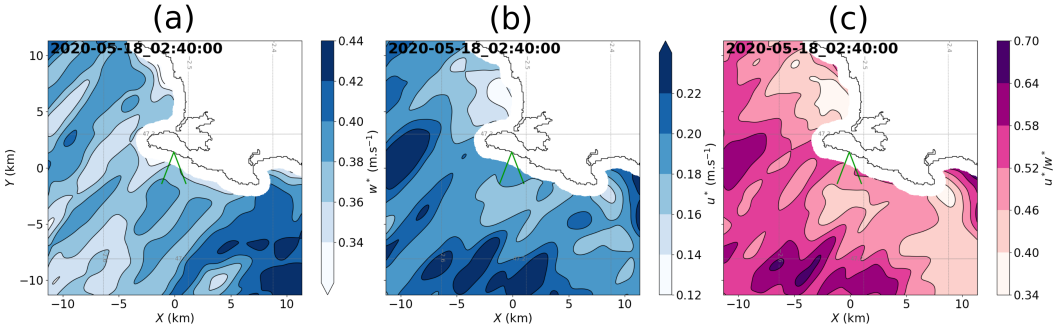

FIGURE 5.16 – Distribution of (a) w^*, (b) u^*, and (c) u^*/w^* at 0240 UTC on May 18 based on domain d06 results. The "+" shows the position of the time series in Figure 5.18.

allows for the presence of horizontal convective rolls (HCR).

Figure 5.17 shows the cross section of w at 50 m high, where several lines of updrafts oriented perpendicular to the coastline, separated by areas of low-amplitude downdrafts. These structures are observed throughout the night and very likely correspond to HCR. Between 0220 and 0300 UTC (Figure 5.17b to 5.17f), they are

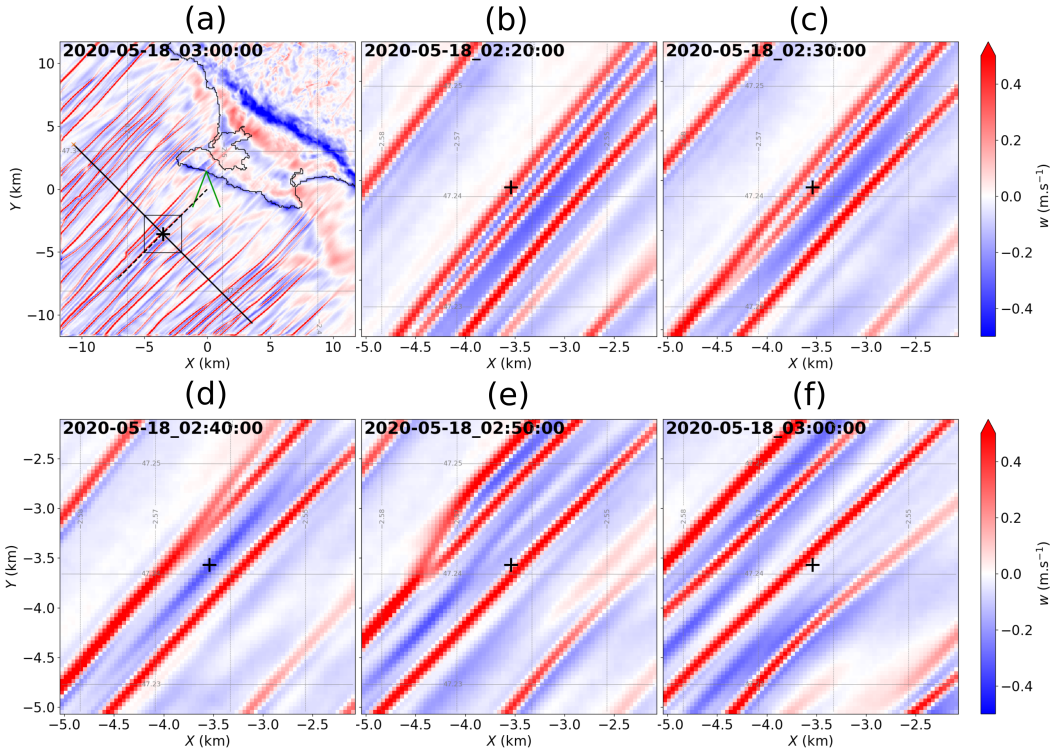

FIGURE 5.17 – Distribution of w at 50 m high at (a) 0300 UTC. (b-e) Same as (a) zoomed over the square area at (b) 0220, (c) 0230, (d) 0240, (e) 0250, and (f) 0300 UTC. The "+" and the lines in (a) are used in Figures 5.18 and 5.19

moving slowly northwest so that a few of them move over the location of the time series (black "+" in the figure).

Figure 5.18 displays the time series of the profiles of w, u_{45} and v_{45} at this location. The passage of the HCR is visible in the w time series (Figure 5.18a), as an alternation of positive (at 0220, 0232 and 0255 UTC) and negative (at 0227 and 0240 UTC) values. The HCR are mainly located below Z_{TIBL} (red line). The u_{45} component is in the direction of the average LLJ wind profile (Figure 5.10e), so that its profile (Figure 5.18b) corresponds to that of a LLJ with a core height around 180 m. Interestingly the v_{45} time series shows some oscillations in the TIBL that are out of phase with that of w. The (v_{45}, w) vector field, depicted by the arrows, reveals the presence of several contra-rotating longitudinal rolls confirming that the structures are HCR. The evolution of u_{45} (Figure 5.18b) shows that the HCR are transporting high wind speed downward (at 0240 UTC) and low wind speed upward (at 0230 and 0255 UTC), thus contributing to the strong mixing that tends to homogenize the wind and temperature profiles in the TIBL (see Figure 5.10).

The vertical cross-section of w across the HCR displayed in Figure 5.19a shows that the updrafts are stronger and their area are narrower compared to the down-

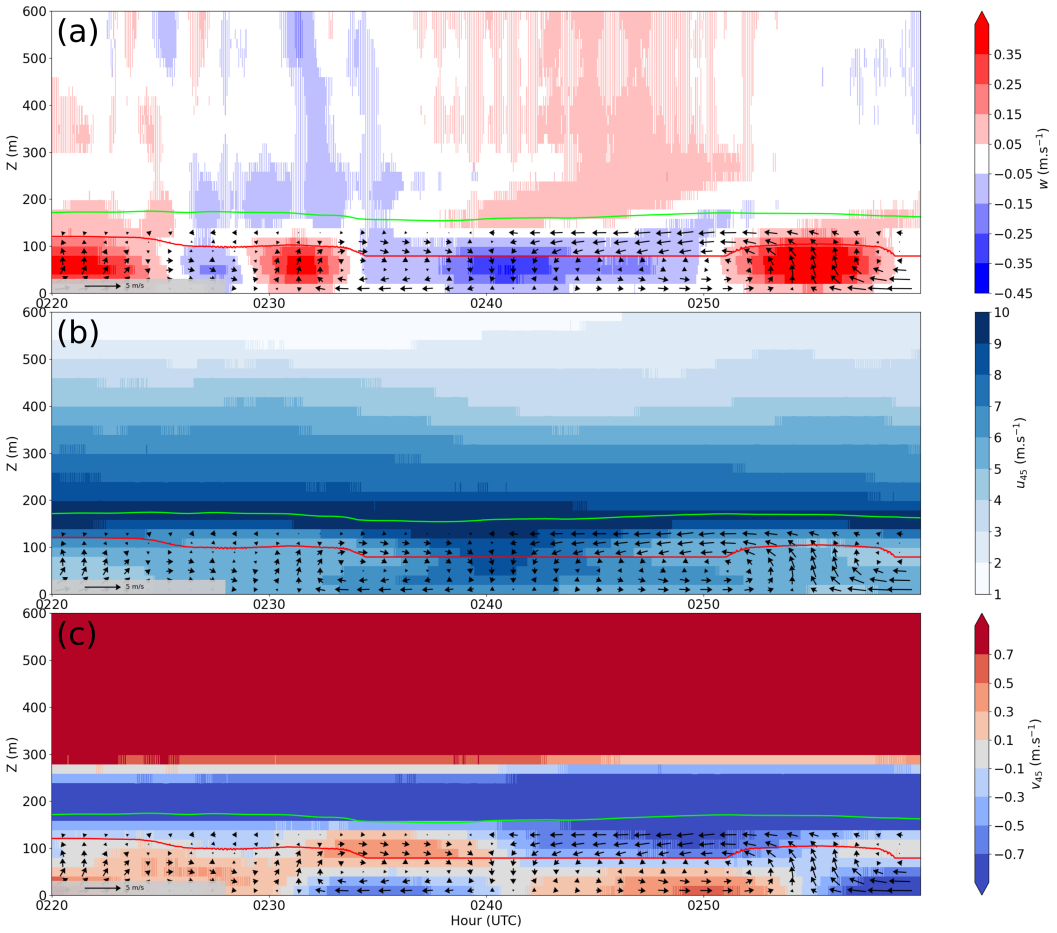

FIGURE 5.18 – Time-height plot of (a) w, (b) u_{45}, and (c) v_{45}, between 0220 and 0300 UTC on May 18, at the location of the "+" in Figure 5.17. The green and red lines correspond to the instantaneous z_{LLJ} and z_{TIBL} (calculated with the instantaneous profiles), respectively. The arrows depict the (v_{45}, w) vector field.

drafts. This particular behavior will be discussed in the conclusion.
The wavelength λ_{HCR}, defined as the distance between two updrafts, is variable between 200 m and 2 km so that the aspect ratio (λ_{HCR}/Z_{TIBL}) ranges from 2 to 15. This range of aspect ratio is in agreement with the observations referenced by Young et al. (2002). It must be reminded that the rolls are still in their development phase because only the first kilometers after the land-sea transition are studied so that, farther offshore, the aspect ratio might be lower.
The hodograph of the wind profile, displayed in Figure 5.19b, shows that, at 0300 UTC, the along-HCR direction matches with WD below 50 m. Thus, the HCR are oriented in the streamwise direction which is in agreement with the definition of the phenomenon (Jayaraman and Brasseur, 2021).

table of content

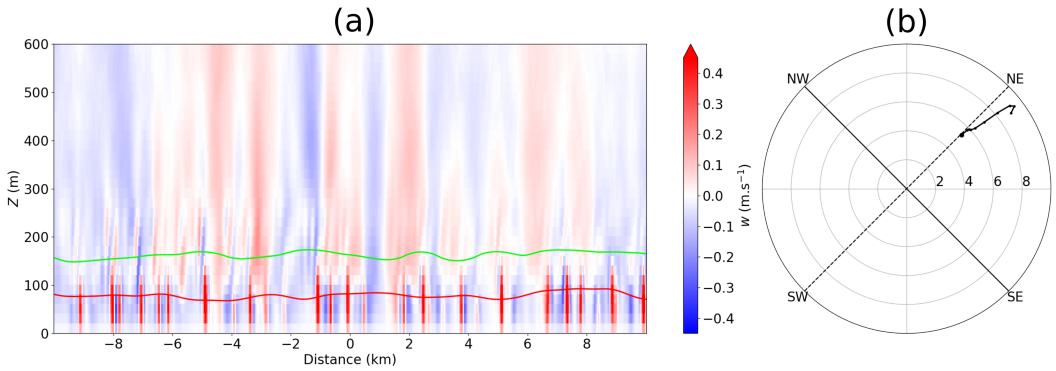

FIGURE 5.19 – (a) Vertical cross section of w along the solid black oriented northwest-southeast shown in Figure 5.17c at 0300 on May 18. The green and red lines correspond to Z_{LLJ} and Z_{TIBL}, respectively. (b) Hodograph of the wind profile between 10 (large dot) and 190 m high, averaged in the square shown in Figure 5.17c, at 0300 UTC. The solid and dashed lines have the same orientation as in Figure 5.17c.

5.5.2 Kelvin-Helmholtz waves above the jet core

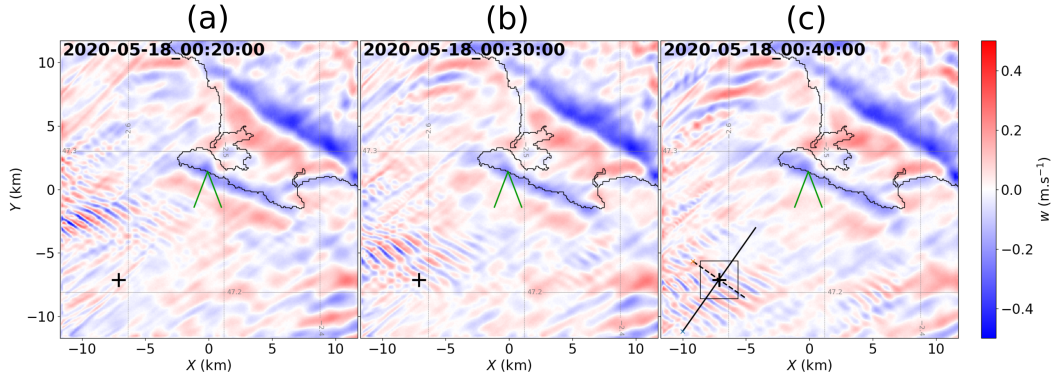

FIGURE 5.20 – Distribution of w at 410 m high at (a) 0020, (b) 0030, and (c) 0040 UTC on May 18 based on domain d06 results. The "+", the square and the lines are used in Figures 5.21 and 5.22.

Figure 5.20, showing the horizontal distribution of w at 410 m high, highlights the presence of a patch of waves oriented parallel to the coastline. Several patches are observed during the night but, unlike the HCR, their presence is intermittent. This specific patch is studied because it is moving southward from (-7, -2 km) at 0020 to (-7, -7 km) at 0040 UTC, so that, at the latter time, it is located at the location position where time series are available (black "+").

The time series of w shown in Figures 5.21a indicate that these oscillations occur between 150 m (z_{TIBL}) and 600 m high. Notably, a phase shift is observed at 400 m high. At this height, the time series of θ_v reveal the presence of billows, similar to that observed in Figure 4.10a. The location of the billows also matches with that of a layer of $Ri < 0.25$, displayed in Figure 5.21c, indicating that the waves are generated by the KH instability at 400 m high. The KHW enhance oscillations of

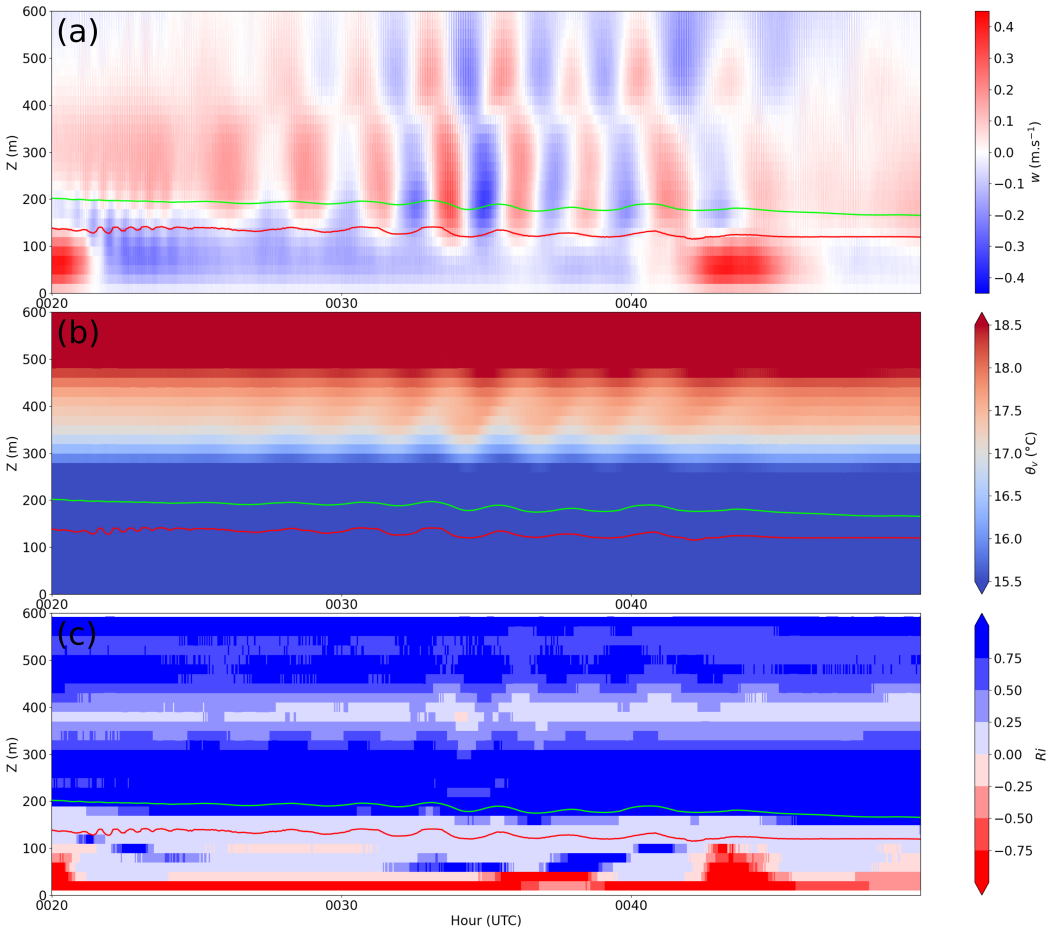

FIGURE 5.21 – Time-height plot of (a) w, (b) θ_v, and (c) the instantaneous Ri, between 0020 and 0050 UTC on May 18, at the location of the "+" in Figure 5.20. The green and red lines correspond to z_{LLJ} and z_{TIBL}, respectively.

the entire stable layer so that z_{LLJ} (green line) oscillates with an amplitude of about 30 m and a period of less than 3 minutes.

Figure 5.22a displays the vertical cross-section of w across the waves at 0040 UTC, allowing for the calculation of their wavelength $\lambda_{KH} \approx 800$ m. This wavelength is quite similar to that of the KHW observed during the SB event in Section 4.2.1. Figure 5.22b shows the hodograph of the wind profile averaged in the square of Figure 5.20c. The direction across the waves (solid line) corresponds well with the direction of the shear around 400 m high (highlighted in red), confirming that the waves are induced by the shear, which is in agreement with the KH instability.

table of content

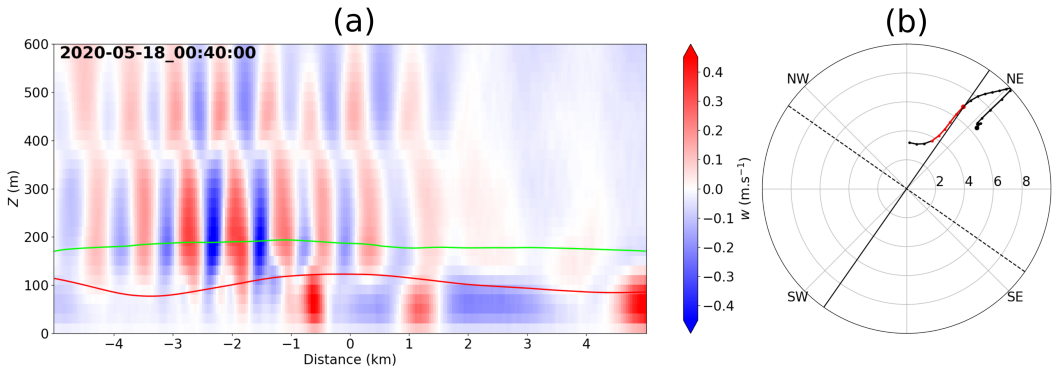

FIGURE 5.22 – (a) Vertical cross section of w along the solid black oriented northwest-southeast shown in Figure 5.20c at 0040 on May 18. The green and red lines correspond to Z_{LLJ} and Z_{TIBL}, respectively. (b) Hodograph of the wind profile between 10 and 510 m high (black), and between 330 and 430 m high (red), averaged in the square shown in Figure 5.20c, at 0040 UTC. The solid and dashed lines have the same orientation as in Figure 5.20c.

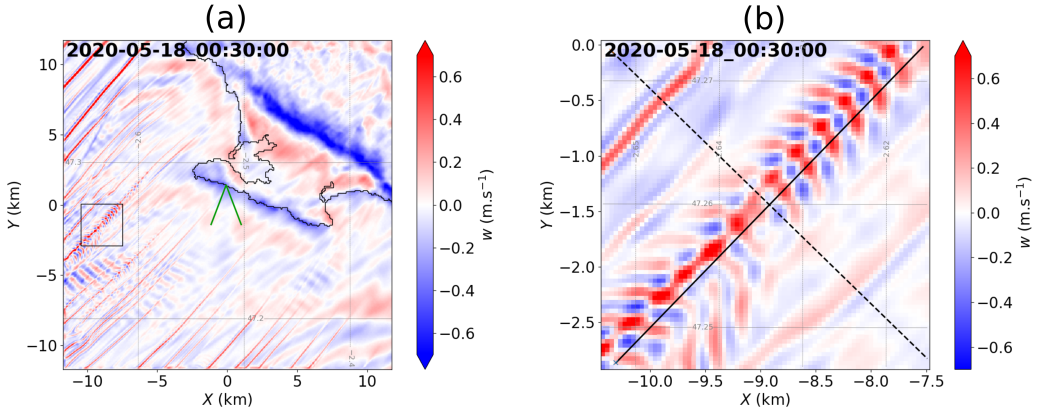

FIGURE 5.23 – (a) Distribution of w at 110 m high at 0030 UTC. (b) Same as (a) but zoomed on the square region shown in (a). The lines are used in Figure 5.24.

5.5.3 Kelvin-Helmholtz waves below the jet core

Another kind of waves is observed in the distribution of w at 110 m high shown in Figure 5.23. Three occurrences of these waves are highlighted by circles in Figure 5.15c. In each case, the waves are located just around a HCR updrafts line.

Figure 5.24a and 5.24b displays the average Ri profile and the distribution of w in the solid-line section shown in Figure 5.23b. The w distribution shows oscillations between 50 and 300 m high with a phase shift around 180 m high (highlighted by the black lines). This phase shift is similar to that of KHW observed in Figures 5.21a and 5.22a. Moreover, at this height, Ri is below the critical value of 0.25. These two observations suggest that the waves are generated by a KH instability, caused by the high shear below the jet core. The wavelength, $\lambda_{KH} \approx 300$ m, is lower than for the KHW identified at higher altitude (Section 5.5.2).

table of content

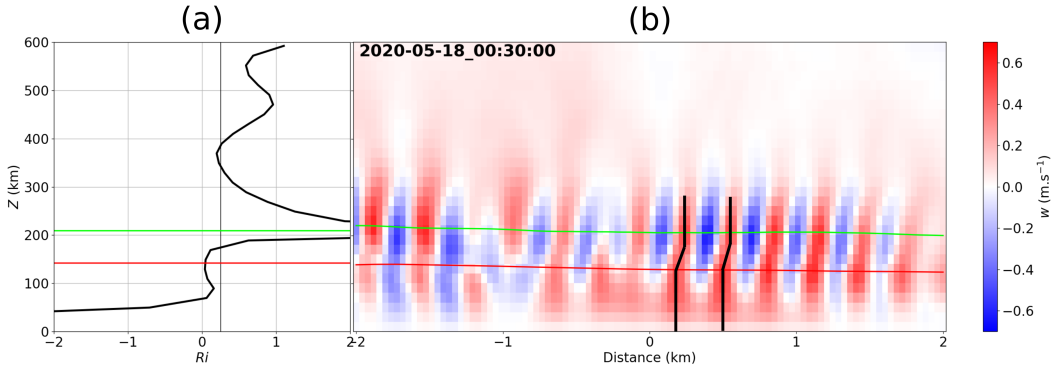

FIGURE 5.24 – (a) Profile of Ri in the square region shown in Figure 5.23a and (b) vertical cross section of w along the solid black oriented northeast-southwest shown in Figure 5.23b at 0030 on May 18. The green and red lines correspond to Z_{LLJ} and Z_{TIBL}, respectively.

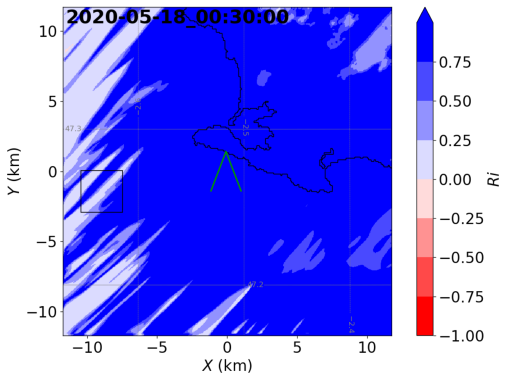

FIGURE 5.25 – Distribution of Ri at 170 m high at 0030 UTC. The square is the same as in Figure 5.23a.

The presence of these waves only close to the HCR updraft lines can be explained by looking more closely at Figure 5.18b : at the top of the updraft region (e.g. at 0230 UTC), the wind shear seems to be much larger than during the downdraft passage (at 0240 UTC). Indeed, the distribution of Ri at 170 m high at 0030 UTC displayed in Figure 5.25 shows some area where Ri is positive but lower than the 0.25 critical value. The comparison with Figure 5.23a confirm that these area are found close to updraft lines.

As shown in Figure 5.23, the orientation of these KHW varies in space : at the center of the waves, the cross-wave direction is oriented along the HCR updraft, whereas on both side of the HCR updraft, it deviates by 30 to 45°. The orientation of the KHW is governed by the direction of the wind curl vector WC. In previous sections (Sections 4.2.3 and 5.5.2), it has been shown that the direction across the KHW is that of the vertical shear, because the vertical shear was much larger than the horizontal wind gradients. However, in the HCR, the wind components also

vary horizontally (Figure 5.18). In the 45° rotated referential frame, WC writes

$$WC = \begin{pmatrix} \frac{\partial W}{\partial Y_{45}} - \frac{\partial V_{45}}{\partial Z} \\ \frac{\partial U_{45}}{\partial Z} - \frac{\partial W}{\partial X_{45}} \\ \frac{\partial V_{45}}{\partial X_{45}} - \frac{\partial U_{45}}{\partial Y_{45}} \end{pmatrix} \tag{5.1}$$

where X_{45} and U_{45} are oriented along the HCR lines and Y_{45} and V_{45} are oriented across the HCR lines. The derivatives along X_{45} are likely negligible as the HCR length is much larger than their wavelength. At the center of the updrafts line, $V_{45}(Z) = 0$ and the derivatives in Y_{45} also equal 0 so that

$$WC = \begin{pmatrix} 0 \\ \frac{\partial U_{45}}{\partial Z} \\ 0 \end{pmatrix}, \tag{5.2}$$

where $\frac{\partial U_{45}}{\partial Z}$ is the shear below the LLJ, resulting in KH billows oriented across the HCR lines. However, on both sides of the updraft line, V_{45} and the derivatives in Y_{45} are non-negligible so that

$$WC = \begin{pmatrix} \frac{\partial W}{\partial Y_{45}} - \frac{\partial V_{45}}{\partial Z} \\ \frac{\partial U_{45}}{\partial Z} \\ \frac{\partial U_{45}}{\partial Y_{45}} \end{pmatrix}, \tag{5.3}$$

which explains why the orientation of the KHW is not purely across the HCR lines.

Overall, this section showed the presence of 3 kind of perturbations, located in three different layers : HCR in the TIBL, a first type of KHW between Z_{TIBL} and Z_{LLJ}, and a second type of KHW above Z_{LLJ}.

5.6 Conclusion of the chapter

In this chapter, the characteristics of a nocturnal low-level jet before, and more particularly after the land-sea transition are investigated. Its main characteristics are determined with a classical method based on the research of a peak in the WS profile. A good agreement is found between the LiDAR measurements and the WRF results so that the rest of the analysis is based on WRF results.

The LLJ extends over several hundreds of kilometers. The advection time scale associated with such large distances is of several hours, which is comparable to the time scale of the external forcing variations (daily thermal cycle). For that reason, the large-scale evolution of the LLJ is investigated following trajectories at a given level. However, in a LLJ, the air column is not transported with a vertically-uniform speed. Therefore, the evolution of the profiles must be analyzed carefully. In this case, this method is very useful as the LLJ is advected over a heterogeneous area and the forcing changes during its long lifetime.

table of content

As in Wagner et al. (2019), both the baroclinicity and the frictional decoupling influence a coastal LLJ. In the present case, the baroclinicity is the primary mechanism behind the LLJ initiation. Despite the inversion of the land-sea temperature difference after the sunset, a favorable horizontal temperature gradient remains all along the trajectory due to the advection over the large-scale Brittany peninsula : during daytime, the baroclinicity near the Channel coastline initiates the LLJ (sea-breeze mechanism) which is advected during the afternoon so that, during nighttime, the baroclinicity near the Atlantic coastline reinforce the LLJ (land-breeze mechanism). This two-coast mechanism has, to the author's knowledge, never been reported in the literature. It emphasizes the need to use a Lagrangian framework because the location of the favorable temperature gradient changes during the LLJ lifetime. The frictional-decoupling mechanism is of secondary importance, but it significantly modifies the LLJ characteristics : a noticeable acceleration and wind rotation (suggesting IO) are observed after the sunset.

While it is advected offshore, the LLJ is mainly impacted by the development of a convective TIBL below its core. Below 50 m, an acceleration is observed within the first 50 kilometers of the coastline that can be attributed to the rough-smooth transition or to the increase of mixing in the TIBL (Barthelmie et al., 1996). In a long-term analysis, Djath et al. (2022) observed the evolution of the wind speed at 10 m high after crossing the coastline, and separated the cases when WS increases and those when WS decreases with distance from the coastline. They hypothesized that the decrease of WS after the land-sea transition could be related to the interaction of a LLJ from land with the marine TIBL. The present results, i.e. the acceleration of WS at 10 m after the land-sea transition caused by the interaction with the TIBL, disagree with their hypothesis. Above 50 m high, the wind speed homogenizes due to the mixing in the TIBL, so that WS decreases below Z_{LLJ}. As a result, Z_{LLJ} increases so that the LLJ core is always located above the TIBL. The simultaneous increase of Z_{LLJ} and decrease of WS_{LLJ} with the development of an underlying convective layer is also identified when the land CBL develops during Phase 2 in Figure 5.1. Djath et al. (2022) observed a similar behavior in a coastal area in the morning. Despite the LLJ deceleration caused by the mixing in the underlying TIBL, the LLJ sustains at least 150 km offshore.

The resolved TKE, its budget, and the organized structures identified in the offshore LLJ emphasize the presence of 3 distinct layers depicted in Figure 5.26. Below Z_{TIBL} (in the TIBL), the TKE is significant with a maximum around Z_{TIBL} and increases with offshore distance within the first ten kilometers of the coast. Its main component is the horizontal variance in the direction of the wind. Its budget is governed by the buoyancy production and the shear production, while the advection and the vertical pressure transport are also non-negligible. The TIBL is moderately convective which enhances the generation of HCR that transport large wind speeds downward and low wind speeds upward. The HCR are responsible for the largest $\overline{v_{45}'^2}$ near the surface and around Z_{TIBL} and for the largest $\overline{w'^2}$ in the middle of the

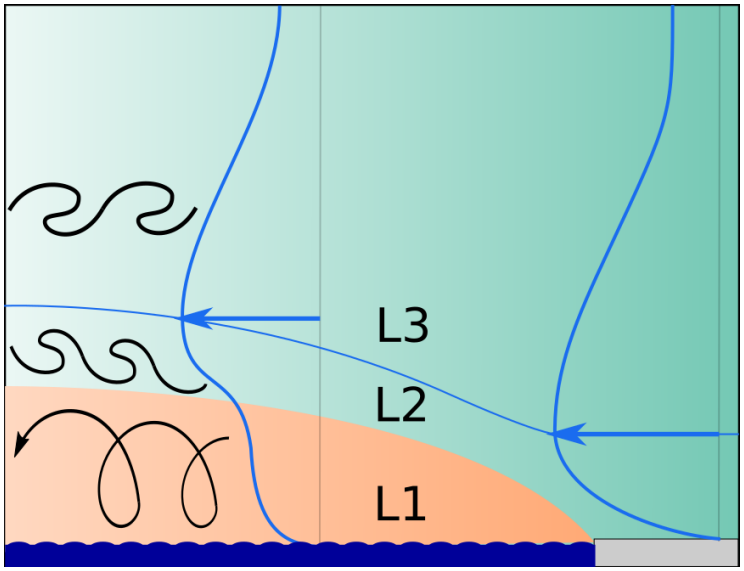

FIGURE 5.26 – Schematic summarizing the structure of the offshore ABL during the LLJ event. The blue curves show the LLJ wind profile. Layers L1, L2, and L3 correspond respectively to the TIBL, the intermediate layer between the TIBL and the LLJ core, and the layer above the LLJ core.

TIBL.
Between Z_{TIBL} and Z_{LLJ}, the TKE also increases with offshore distance but decreases with height from its maximum at Z_{TIBL} to a minimum value around Z_{LLJ}. The budget is governed by a balance between P and ε. A particular type of KHW are observed at the top of the HCR updrafts, where the Richardson is the lowest. The KHW orientation vary horizontally which is likely due to the horizontal wind variations (related to the HCR) modifying the local wind curl vector.
Above Z_{LLJ}, the TKE is an order of magnitude lower than in the two other layers, and the Richardson number is larger than the critical value of 0.25 almost everywhere, indicating that the buoyancy inhibition dominates over the shear production. A few patches of KHW are generated in this layer.
The three types of perturbation generate vertical oscillations of the whole LLJ layer with an amplitude of 10 to 30 m. Although it has not been demonstrated, it is possible that each type of KHW favors the development of the other one through these vertical oscillations.

The several conclusions of Banta (2008) on the scaling of the LLJ characteristics, i.e. WS_{LLJ} increases with Z_{LLJ}, $\overline{u'^2}$ scales with WS_{LLJ} (see Section 1.4.4), do not apply in this case. The obvious reason for the different conclusions between the two studies is the fact that he studied inertial LLJs in the SBL whereas the present case deals with a baroclinic LLJ influenced by the underlying convective TIBL. This shows that there is no unique scaling for all the LLJ but different categories of LLJ exist. Some findings are however similar to other studies such as the mi-

nimum TKE at Z_{LLJ} where Ri becomes infinite (Smedman et al., 1993; Banta, 2008).

The HCR observed in this case form lines that are particularly smooth compared to other studies (Moeng and Sullivan, 1994; Jayaraman and Brasseur, 2021). Such nice HCR might be caused by a too coarse vertical grid size (20 m) compared to the small depth of the TIBL (100 m). Thus, it is possible that small-scale perturbations that would destabilize the HCR are not properly resolved.
In this study, the HCR updrafts are narrower and with a larger amplitude than the downdrafts (Figure 5.19). This feature can be identified in Bhimireddy and Bhaganagar (2018) (IOP5) or in Cheung et al. (2024) (their Figure 3), but not clearly in other studies (LeMone, 1973; Sykes and Henn, 1989; Rakesh et al., 2017). This feature might be related to a particular regime of HCR but a direct observation is needed to confirm the realism of this statement.
The observation of KHW at the top of HCR updrafts has rarely been reported. KHW were already observed below a LLJ core by Newsom and Banta (2003), with a similar wavelength (around 320 m) but these KHW were not related to HCR. The interaction between HCR and KHW in a LLJ has been studied by Nakanishi et al. (2014). However, their HCR do not have the same origin, and the KHW are not observed at a specific phase of the HCR. A case that is closer to the present study is that of KHW generated by HCR at the top of the CBL (Rayment and Readings, 1974; Deardorff et al., 1980). Notably, Kallistratova et al. (2013) measured the growing morning CBL for a year and observed KHW events 45 % of the days, showing that their presence is a common feature of the CBL top boundary.

Overall, the TIBL has a strong influence on the offshore characteristics of the LLJ through the action of convective rolls that enhance mixing, reduce the jet speed, increase the jet height, and trigger KH waves in the LLJ stable layer. It is, to the author's knowledge, the first analysis of the interaction between a LLJ and a TIBL that develop over the sea. These results have significant implications for offshore wind energy, as will be discussed in Section 6.4.

Chapitre 6

General conclusions and perspectives

This chapter presents general conclusions of this work. Section 6.1 concludes about the methodology employed and more precisely the simulation set-up and the analysis tools developed through the thesis. Then, Section 6.2 summarizes the impact of the multiscale coastline on the state of the ABL during the studied period. Section 6.3 compares the various waves and their interaction with turbulence in the SBs and the LLJs. Implications of these results for offshore wind farms are discussed in Section 6.4. Finally, perspectives for future research are presented in Section 6.5.

6.1 On the methodology

To perform realistic simulations at turbulence-permitting scales (Bauer et al., 2020) while taking into account mesoscale processes, a progressive downscaling was used. With this method, the daily cycle observed by the LiDAR (alternation of SBs and LLJs) was pretty well reproduced by the simulation (Section 2.5). In the land CBL, the TKE budget was similar to that of idealized simulations performed by other authors, showing that the turbulent fluxes were properly resolved. In addition, the resolution of the undular bore, a phenomenon also identified by the LiDAR measurements, gives strong credit to the realism of the simulation.
With this method, some intermediate domains had resolution in the grey zone. In very stable layers, even the domain with the smallest grid size (d06, $\Delta_X = 39$ m) was in the grey zone so that the subgrid and the resolved TKE were of the same order of magnitude (e.g. in the LLJ inland in Section 5.4). However, the simulation reached the current technical limits in terms of computational time and storage. For illustration, the simulation ran during 2 weeks on 96 CPUs, and the results took about 7 TB of storage. Therefore, an increase of the resolution of the smallest domain must be compensated by a decrease of its horizontal extent. Since coastal flows are heterogeneous and depend on the offshore distance, such a smaller extent is not desirable.
Another downscaling method consisting of a large jump between the mesoscale and the microscale resolutions could have been used to avoid the grey zone and directly reach resolutions for which the LES models are designed for, i.e. at which the grid size is in the inertial range of turbulence (Section 1.6.2). Again, with the current computational limits, such a microscale domain would have a small horizontal

extent so that the bore and the waves studied here wouldn't have enough space to develop. These structures with wavelength between a few hundred meters and a few kilometers need an extent of several times their wavelength, and a grid size at least an order of magnitude lower than their wavelength to be resolved. Therefore, using the "jump" method, these structures would not have been resolved. Thus, considering the currently available computational power, the progressive downscaling method, including the grey-zone resolutions, used in this study is necessary to resolve all the structures of coastal flows.

An interesting feature of LES is the resolution of the large turbulent eddies so that the TKE budget can be estimated. In some studies, this budget is studied at a single location using the *wrf_timeseries* feature (Rohanizadegan et al., 2025). However, this method allows neither for the calculation of the TKE at every location, nor for that of the complete budget (the horizontal gradients are missing). Thus, the calculation of statistics was implemented in WRF so that the TKE budget can be computed at every location in post-processing (Section 2.4). This represents a significant improvement for WRF-LES.
It was shown in Section 2.5.4, that this budget must be computed with care in WRF because the Boussinesq approximation gave unusual results in the CBL, whereas the WRF budget gave more realistic results. This budget was very helpful to investigate the mechanism at the origin of turbulence in a SB in the presence of GW. Unfortunately, in the LLJ, where the ABL is very stable and the TKE is quite low, the horizontal pressure terms showed a non-physical behavior, i.e. a persistent negative value at all levels. The reason for this behavior has been investigated but no answer was found. Possible explanations for this result include a bug in the computation, or an additional term that should be considered in the horizontal pressure terms maybe related to the acoustic time step (Skamarock et al., 2019). Despite this doubtful horizontal pressure term, this work provided the calculation of statistics in WRF and built the first stage toward the implementation of the TKE budget.

This thesis deals with a complex multiscale coastline which has an impact on the wind field. In a majority of studies, either coastlines have been assimilated to a straight line, or the results have been described qualitatively. To improve this analysis, a Gaussian filter was applied on the land-sea mask to quantitatively describe the coast orientation (Section 3.1.2). This method has several advantages : (i) the description depends on a scale parameter so that lakes, islands, bays, and peninsulas are filtered out at large scale, (ii) the coast orientation is defined locally within a certain area, (iii) the method could be applied to any coastline, (iv) the orientation is defined objectively so that it is reproducible. The filtering analysis could be extended to describe other quantities than the coast orientation such as its curvature or its tortuosity. This method could be applied to various coastal analysis to help the comparison between different sites.

The interaction between sub-mesoscale motions and turbulence was identified by

Sun et al. (2015b) as a key aspect of the SBL. In this study, a method was proposed to decompose the TKE from the energy of the GW motion (in the bore during the SB event in Section 4.3). However, this method is limited to specific cases : (i) the waves should be nearly-harmonic, (ii) they should move at low speed, and (iii) it requires a spatial information of the waves. For the various KHW observed in this study, however, the energy related to their motion is harder to estimate, and no method has been proposed. Therefore, improvements are needed to separate the more general sub-mesoscale motions from turbulence in simulation results.

6.2 On the impact of a multiscale coastline on the ABL

The first objective of this thesis was to assess how a complex coastline influences the wind field and the main characteristics of the SBs and LLJs. It was shown that the multiscale heterogeneity of the coastline can influence the ABL in several complex ways. At a scale of about 20 km (Guérande Peninsula), the baroclinicity near bays and peninsulas induces wind divergence and convergence, respectively, near the surface during SB initiation. The convergence near the Guérande peninsula generates an atmospheric undular bore on May 17 when the ABL is stable, and triggers a strong mixing on May 18 when an unstable layer is present (Section 3.2). At the scale of about 100 km (Brittany Peninsula), the advection of air from different directions (from land or from the Channel) causes the aforementioned unstable layer. Moreover, the advection of air over the Brittany peninsula maintains the baroclinic LLJ during more than 12 hours despite the inversion of the land-sea temperature difference (Section 5.2). Therefore, this study highlights the large variety of phenomena that can occur around a multiscale coastline and emphasizes the difficulty of predicting and modeling the coastal ABL.

As suggested by Simpson (1996), the shape of the coastline has an impact on the rotation of the SB (Section 3.1) : at the initiation, the SB direction is oriented according to the small-scale coast orientation, and over time it progressively depends on the coast orientation at a larger scale. Simultaneously, this SB direction deviates clockwise, likely under the action of the Coriolis force. To quantify the evolution of the SB scale and deviation, a simple model assuming that the two quantities varies in time but are homogeneous in space was proposed. The results obtained with this model are in agreement with the qualitative observations. Despite the few limitations of this method, it gives some first keys to model the development of SB near complex coastlines.

The local SB initiation near a peninsula generates convergence that results on May 17, when the ABL is stable, in an atmospheric bore lasting for a few hours (Section 3.2). Such an offshore atmospheric undular bore generated by convergence has, to the author's knowledge, never been reported. The bore differs from other

atmospheric bores by its generation mechanism, its size (small extent, small speed, and small wavelength), and its timing. Considering the conditions of its existence (baroclinicity near a peninsula under light synoptic wind and an initially stable layer), it is possible that this phenomenon is not so infrequent. Thus, a better knowledge of this kind of bore could help interpreting field observations of wind and turbulence and analyzing micrometeorology for several types of applications.

6.3 On the waves and turbulence in a coastal area

The second objective of this thesis was to document the nature and intensity of turbulence within the offshore CABL during SB and LLJ events. It was shown that the offshore part of these two events is divided into several layers with different properties related to stability and shear. In addition, several organized structures were observed in these layers. These structures and their main characteristics are summarized in Table 6.1.

	Location	Orientation	λ	Period
GW	around Z_{SB}	along α_{SB} the shear	1.8 km	$>$ 25 min
KHW1	around Z_{SB}	across α_{SB} the shear	600-900 m	3 min
HCR	$Z < Z_{TIBL}$	along WD the shear	0.2-2 km	$>$ 10 min
KHW2	$Z_{TIBL} < Z < Z_{LLJ}$ above HCR updrafts	across the HCR the shear	300 m	1 min
KHW3	$Z_{LLJ} < Z$	across WD the shear	800 m	2 min

TABLE 6.1 – Characteristics of the waves and oscillations detected the study where the KHW in the SB, below, and above the jet core are numbered 1, 2, and 3, respectively. The period related to their passage at a fixed location is estimated by dividing the wavelength by their speed for GW, or the wind speed for the KHW2. For the HCR, the KHW1, and the KHW3, it is estimated from Figures 5.18, 4.13, and 5.21, respectively.

Two sheared stable layers were encountered in this work, the layer above the LLJ, and the center of the SB cell. In both layers, intermittent KHW (KHW1 and KHW3) are responsible for the major part of the resolved TKE (Sections 4.2 and 5.5.2). This energy is produced locally and the layers are decoupled from the surface so that they can be qualified as *very stable* (Sun et al., 2015b).
Below the LLJ core (Section 5.5.3), it was shown that the KHW2 are triggered by the underlying updrafts related to the HCR in the TIBL. Thus, the turbulence there is coupled with the surface.

table of content

The interaction between the GW and the turbulence was investigated in Section 4.3 by calculating the TKE and its budget in the different phases of the waves. The GW induce significant oscillations of the TKE within the SB with a peak of TKE at the waves crests. Interestingly, a periodic change of sign of the buoyancy and the shear production is found. This periodic variation suggest that the turbulent fluxes in the GW are governed by predominant horizontal transport rather than the classical vertical transport that generally prevails in the ABL. The non-negligible horizontal transport should probably be taken into account to build turbulence models in stable layers.

Recent work of Stiperski and Calaf (2018) showed that the scaling laws in the ASL are influenced by the anisotropy. This result was obtained without an exact knowledge of the structures associated with a specific anisotropy. Thus, it seems interesting to document the degree of anisotropy associated with a various range of motions. The three components of the resolved TKE were studied in different conditions : in the SB with and without the KHW (Section 4.2.3), in the GW (Section 4.3), and in the LLJ (Section 5.4).
Figure 6.1 compares the degree of anisotropy under different conditions and at different heights. In the CBL (stars), the turbulence is very isotropic (3C) except in the ASL (below 100 m) where the vertical velocity variance is lower than the two other components. In the three other cases (LLJ, SB with KHW, and SB without KHW), the turbulence has one dominant component (1C) almost everywhere. In the LLJ, near the core height (200 m), the turbulence has two dominant components (2C) but the TKE there is very low. In the SB within KHW, a nearly-isotropic turbulence is found at 50 m, where the vertical oscillations caused by the KHW are important. Near 400 m high, the turbulence is also isotropic but the TKE is quite low.
It was shown that, when the turbulence has one dominant component, the main component is that in the direction of the shear, which, for the SB, is not generally the wind direction (Section 3.1.3).

The decay of the residual turbulence in the return current is investigated and the ability of existing analytical model to describe this decay is evaluated (Section 4.4). Two analytical models are able to fit correctly the decay, among which, one is simply assuming that the variation rate of k_{calc} is proportional to $k_{calc}^{3/2}$. The best-fit length-scale parameters of these models are compared to the commonly used Z_{CBL}. Despite a monotonic relationship between these length scales and Z_{CBL}, the expected linear relationship is not retrieved, suggesting either that the assumptions used in this study show some limitations, or that the return current is not a purely residual layer as it may interact with the center of the SB cell. Thus, the correct parametrization of the models still requires some work. It is possible that such a model could be applied to thermal decoupling after the land-sea transitions during daytime even without a SB, which occur very frequently and is likely governing the

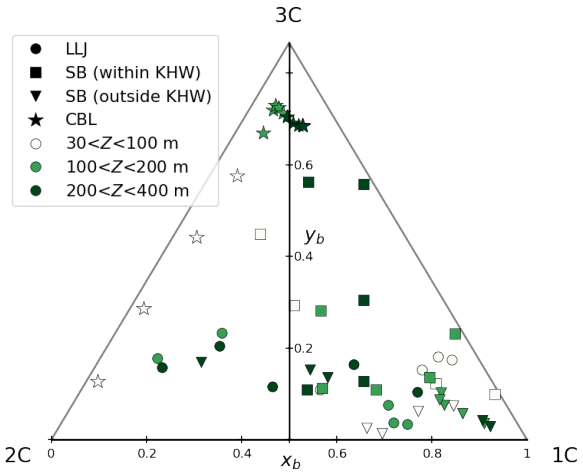

FIGURE 6.1 – Turbulence anisotropy as a function of the height and the state of the ABL, visualized on a barycentric map where x_b and y_b are the coordinates (Stiperski and Calaf, 2018), and where 1C, 2C, and 3C correspond to a turbulence dominated by one component, by two components, and to an isotropic turbulence, respectively. The LLJ profile is taken at X_c = -9 at 0300 UTC (Figure 5.13), the SB profiles with and without KH are those of Figure 4.12. The CBL profiles are averaged in the same period and area as the TKE budget terms in Section 2.5.4.

turbulence in the offshore coastal ABL.

6.4 On the implications for wind energy

Several aspects of this work have implications for wind energy. The SBs and LLJs studied here extend more than 50 km offshore, so that they are of importance for wind farms as most of them are located within 50 km of the coastline (Díaz and Guedes Soares, 2020). Moreover, the St-Nazaire wind farm (80 wind turbines with a hub area between 25 and 175 m high) was built at 15 kilometers from Le Croisic in 2022, i.e. 2 years after the studied period. Therefore, it is of interest to discuss these implications.

The bore front generated during SB initiation separates two zones featuring different wind speeds (Section 3.2). This heterogeneity likely make the power production hard to predict in this area. Although this front moves quite slowly, an hypothetical passage over a wind farm would result in a noticeable wind power ramp (Gallego-Castillo et al., 2015). The transition from SB to LLJ at a given location also takes the form of a frontal line, that results, for a fixed point, in a 90 ° rotation within an hour (Section 5.1). These two mesoscale fronts would enhance heterogeneity of the production within the farm.

table of content

The impact of LLJ and wind shear on wind turbines has been studied by several authors (Eggers et al., 2003; Gutierrez et al., 2017; Murphy et al., 2020; Gadde and Stevens, 2021; Paulsen et al., 2025). However, in this case, the LLJ interacts with the TIBL, which significantly modifies its property : the shear is reduced in the TIBL, and the turbulence increases below the jet. As the jet height is close to a wind-turbine hub height (between 100 and 200 m), a hypothetical wind turbine in the LLJ would benefit from a large wind speed, but experience a significant shear (around 0.03 s^{-1}) with a non-negligible turbulence intensity (around 6.3 %) in the lower half of the hub, and negative shear with very low turbulence in the upper half.

The GW and KHW may also have consequences for wind farms which have been discussed in the WESC2025 conference (Landreau et al., 2025a).
The various waves induce spatial oscillations of the wind speed. Moreover, it was shown that the GW induce oscillations of the TKE, and Cheung et al. (2024) found that HCR also induce variations of TKE. As their wavelengths (between a few hundred meters and a few kilometers in Table 6.1) are of the same order than the distance between the turbines in a farm, two turbines could experience different inflow conditions. In a recent study, Cheung et al. (2024) found that wakes recover faster in the updraft of the HCR, where the wind speed is smaller, than in the downdraft region. Ollier and Watson (2023) studied the influence of trapped lee waves with a wavelength of about 10 km on a wind farm production, and found that the power production depends on the phase of the wave at the location of the farm. As the waves move, they induce oscillations of the inflow for an hypothetical wind turbine. The period of these oscillations is estimated between 1 minutes for the KHW2 and more than 25 minutes for the GW (Table 6.1). For each wave, this period is larger than the rotor time scale defined as the rotor diameter divided by the wind speed (about 20 s in this case) (Gao et al., 2020), so that the passage of the KHW would enhance fluctuations of the power production. Even the KHW above the jet core (KHW3), that are located above the hub area (around 400 m high), induce oscillations of the whole LLJ and thus, would influence the wind turbine production.
Variations of the inflow can also modifies the wake. Small-scale turbulence is known to affect the wake recovery while the variations at scales larger than twice the rotor diameter passively transport the wake in meandering movement (Porté-Agel et al., 2020). In this case, all the wavelengths are larger than twice the St-Nazaire wind turbines' rotor diameter (150 m) so that the waves would likely induce wake meandering.
The break-up process of KHW can involve several types secondary instability (Thorpe, 2012) which likely induce periodic oscillations and turbulence at smaller scales. Such structures could generate fatigue and influence the wake recovery.

table of content

6.5 Perspectives

In this thesis, the turbulence resolved by the simulation was validated in the CBL through comparison with the literature and by extension was considered valid in the rest of the domain. Several sonic anemometers, performing turbulence measurements, are located at the top of offshore lighthouse in the studied area. During the studied period, chosen based on the phenomena observed with the LiDAR, no sonic data was not available. Thus, a perspective for the methodology assessment would be perform a simulation at another date when the conditions are similar (SB and LLJ) and when the sonic anemometers are available, to compare the turbulence resolved by the simulation with the sonic measurements. In addition, it would be useful to assess the sensitivity of the resolved turbulence and the HCR to the vertical grid size, since it has been suggested that this resolution could be responsible for the very smooth HCR.

In the simulation, the description of the sea-surface temperature (SST) was simplistic : it changed only once a day, and its spatial distribution was quite homogeneous (forced with ERA5 at $\Delta_X = 31$ km). Such a smooth distribution is unrealistic, especially in coastal areas and near river deltas where small-scale variations of temperature are generally observed. The SST have an impact on the development of thermal winds like the SBs and LLJs studied here. More particularly, the initiation of the local SBs could be influenced by the small-scale variations of SST. Thus, it would be interesting to assess the sensitivity of these phenomena to the SST distribution.

In simulations with low resolutions (e.g. grid size larger than 5 km), the coastline is necessarily smooth so that the development of the local SBs is neglected. This raises some questions about the impact of the local SBs on the development of the regional SB. Idealized simulations over coastline with complexities at different scales could be performed to assess the sensitivity of the SB development to the coast complexity. If this influence is non-negligible, it could be parameterized through a coastal subgrid model, similar to the existing GW drag subgrid models.

An idealized simulation over a rectangular peninsula with similar wind and temperature forcing could also be used to validate the suggested mechanism for the initiation of the bore. Such a simulation could then be used to assess the sensitivity of the bore characteristics to various parameters such as the shape of the coastline, or the background wind.

Based on the present results, it seems that on a sunny day, under light synoptic wind from land, near a 20-km rectangle peninsula, there are significant chances to observe a similar bore (the last condition being a stable ABL offshore). Thus, the presence of a bore within a few days could be predicted based on the meteorological forecast. Moreover, it lasts for several hours during which it is nearly stationary. These two characteristics give some opportunities for direct observations. At short

term, GW could be detected using the LiDAR data, to assess the frequency of this event over the six months of measurements. At longer term, another measurements campaign could be realized to observe the evolution of the GW and their interaction with turbulence over several hours, which is not possible with other bores reported in the literature.

Then, since the studied KHW are responsible for most of the turbulence in the very stable layers, it would be interesting to generalize on their presence in the SB and in the LLJ, and to understand the factors that trigger their generation. Above the LLJ and in the SB, the presence of an external destabilization was not demonstrated but is a possible cause for the generation of KHW there. Indeed, the KHW in the SB could be triggered by the residual turbulence in the return current, and that above the LLJ core by the KHW or HCR below the LLJ core that are shown to generate oscillation of the whole LLJ layer. Another mechanism that can explain the intermittent nature of the KHW is a cyclic behavior observed by Van der Linden et al. (2020) : when the shear exceeds a critical value, KHW develop, break, and generate turbulence that reduce the shear, then the turbulence decays, allowing for the increase of the shear and the generation of new series of KHW. This second hypothesis does not involve an external factor and is referred to as *internal* by Ren et al. (2025).
Again, investigating the frequency and origin of the KHW would require long-term offshore field measurements. The sonic anemometers described earlier could be used to detect the presence of KHW. As shown in this study, although the KHW are located in the center of the SB cell and above the LLJ, they induce wind oscillations near the surface that could be detected with anemometers.

Finally, the possible consequences of the observed phenomena for wind farms were discussed, considering the wind conditions at a given location (Section 6.4). However, wind farms also modify the ABL through wake effects. Thus, a last perspective is to determine the retroaction of the wind farm on the observed phenomena. Does the mixing induced by the farm influence the SB development ? Does it inhibit the development of the bore, the GW and the KHW ? Those questions could be investigated by doing a simulation including a model for the influence of wind farms and by performing measurements near the St-Nazaire wind farm that is now in activity in the studied area.

Bibliographie

Abbs, D. J. and Physick, W. L. (1992). Sea-breeze observations and modelling : A review. (Cited in page 10.)

Aird, J. A., Barthelmie, R. J., Shepherd, T. J., and Pryor, S. C. (2021). WRF-simulated low-level jets over Iowa : Characterization and sensitivity studies. *Wind Energy Science*, 6(4) :1015--1030. (Cited in page 37.)

Aird, J. A., Barthelmie, R. J., Shepherd, T. J., and Pryor, S. C. (2022). Occurrence of Low-Level Jets over the Eastern U.S. Coastal Zone at Heights Relevant to Wind Energy. *Energies*, 15(2) :445. (Cited in pages 6, 17, 18, 19, 20 et 114.)

Angevine, W. M., Bazile, E., Legain, D., and Pino, D. (2014). Land surface spinup for episodic modeling. *Atmospheric Chemistry and Physics*, 14(15) :8165--8172. (Cited in page 35.)

Antonelli, M. and Rotunno, R. (2007). Large-Eddy Simulation of the Onset of the Sea Breeze. *Journal of the Atmospheric Sciences*, 64(12) :4445--4457. (Cited in page 11.)

Aparna, M., Shetye, S. R., Shankar, D., Shenoi, S. S. C., Mehra, P., and Desai, R. G. P. (2005). Estimating the seaward extent of sea breeze from QuikSCAT scatterometry. *Geophysical Research Letters*, 32(13). (Cited in page 13.)

Arritt, R. W. (1989). Numerical modelling of the offshore extent of sea breezes. *Quarterly Journal of the Royal Meteorological Society*, 115(487) :547--570. (Cited in pages 12, 13, 14, 16, 64 et 66.)

Arritt, R. W. (1993). Effects of the Large-Scale Flow on Characteristic Features of the Sea Breeze. *Journal of Applied Meteorology and Climatology*, 32(1) :116--125. (Cited in pages 11 et 13.)

Baker, R. D., Lynn, B. H., Boone, A., Tao, W.-K., and Simpson, J. (2001). The Influence of Soil Moisture, Coastline Curvature, and Land-Breeze Circulations on Sea-Breeze-Initiated Precipitation. *Journal of Hydrometeorology*, 2(2) :193--211. (Cited in page 12.)

Baki, H., Basu, S., and Lavidas, G. (2025). Modeling frontal low-level jets and associated extreme wind power ramps over the North Sea. *Wind Energy Science*, 10(8) :1575--1609. (Cited in page 18.)

Banta, R. M. (2008). Stable-boundary-layer regimes from the perspective of the low-level jet. *Acta Geophysica*, 56(1) :58--87. (Cited in pages 17, 18, 19, 20, 113, 141 et 142.)

table of content

Banta, R. M., Pichugina, Y. L., and Brewer, W. A. (2006). Turbulent Velocity-Variance Profiles in the Stable Boundary Layer Generated by a Nocturnal Low-Level Jet. *Journal of the Atmospheric Sciences*, 63(11) :2700--2719. (Cited in page 19.)

Barthelmie, R., Courtney, M., Lange, B., Nielsen, M., Sempreviva, A., Svenson, J., Olsen, F., and Christensen, T. (1999). Offshore wind resources at Danish measurement sites : 1999 European Wind Energy Conference and Exhibition. *Wind energy for the next millennium. Proceedings*, pages 1101--1104. (Cited in page 6.)

Barthelmie, R. J., Grisogono, B., and Pryor, S. C. (1996). Observations and simulations of diurnal cycles of near-surface wind speeds over land and sea. *Journal of Geophysical Research : Atmospheres*, 101(D16) :21327--21337. (Cited in pages 124 et 140.)

Bauer, H.-S., Muppa, S. K., Wulfmeyer, V., Behrendt, A., Warrach-Sagi, K., and Späth, F. (2020). Multi-nested WRF simulations for studying planetary boundary layer processes on the turbulence-permitting scale in a realistic mesoscale environment. *Tellus A : Dynamic Meteorology and Oceanography*, 72(1) :1--28. (Cited in pages 28, 36 et 143.)

Bauer, H.-S., Späth, F., Lange, D., Thundathil, R., Ingwersen, J., Behrendt, A., and Wulfmeyer, V. (2023). Evolution of the Convective Boundary Layer in a WRF Simulation Nested Down to 100 m Resolution During a Cloud-Free Case of LAFE, 2017 and Comparison to Observations. *Journal of Geophysical Research : Atmospheres*, 128(8) :e2022JD037212. (Cited in page 37.)

Beare, R. J., Macvean, M. K., Holtslag, A. A. M., Cuxart, J., Esau, I., Golaz, J.-C., Jimenez, M. A., Khairoutdinov, M., Kosovic, B., Lewellen, D., Lund, T. S., Lundquist, J. K., Mccabe, A., Moene, A. F., Noh, Y., Raasch, S., and Sullivan, P. (2006). An Intercomparison of Large-Eddy Simulations of the Stable Boundary Layer. *Boundary-Layer Meteorology*, 118(2) :247--272. (Cited in page 28.)

Bhimireddy, S. R. and Bhaganagar, K. (2018). Performance Assessment of Dynamic Downscaling of WRF to Simulate Convective Conditions during Sagebrush Phase 1 Tracer Experiments. *Atmosphere*, 9(12) :505. (Cited in page 142.)

Blackadar, A. K. (1957). Boundary Layer Wind Maxima and Their Significance for the Growth of Nocturnal Inversions. *Bulletin of the American Meteorological Society*, 38(5) :283--290. (Cited in pages 9 et 17.)

Briere, S. (1987). Energetics of Daytime Sea Breeze Circulation as Determined from a Two-Dimensional, Third-Order Turbulence Closure Model. *Journal of the Atmospheric Sciences*, 44(11) :1455--1474. (Cited in page 14.)

Britter, R. E. and Simpson, J. E. (1978). Experiments on the dynamics of a gravity current head. *Journal of Fluid Mechanics*, 88(2) :223--240. (Cited in page 14.)

Burk, S. D. and Thompson, W. T. (1996). The Summertime Low-Level Jet and Marine Boundary Layer Structure along the California Coast. *Monthly Weather Review*, 124(4) :668--686. (Cited in pages 18 et 19.)

Busack, B. and Brümmer, B. (1988). A case study of Kelvin-Helmholtz waves within an off-shore stable boundary layer : Observations and linear model. *Boundary-Layer Meteorology*, 44(1) :105--135. (Cited in page 110.)

Calmet, I. and Mestayer, P. (2015). Study of the Thermal Internal Boundary Layer during sea-breeze events in the complex coastal area of Marseille. *Theoretical and Applied Climatology*, 123. (Cited in pages 16 et 123.)

Calmet, I., Mestayer, P. G., van Eijk, A. M. J., and Herlédant, O. (2018). A Coastal Bay Summer Breeze Study, Part 2 : High-resolution Numerical Simulation of Sea-breeze Local Influences. *Boundary-Layer Meteorology*, 167(1) :27--51. (Cited in page 12.)

Céspedes, J., Kotthaus, S., Preissler, J., Toupoint, C., Thobois, L., Drouin, M.-A., Dupont, J.-C., Faucheux, A., and Haeffelin, M. (2024). The Paris low-level jet during PANAME 2022 and its impact on the summertime urban heat island. *Atmospheric Chemistry and Physics*, 24(20) :11477--11496. (Cited in pages 19 et 20.)

Chang, S. S. and Braham, R. R. (1991). Observational Study of a Convective Internal Boundary Layer over Lake Michigan. *Journal of the Atmospheric Sciences*, 48(20) :2265--2279. (Cited in page 123.)

Charnock, H. (1955). Wind stress on a water surface. *Quarterly Journal of the Royal Meteorological Society*, 81(350) :639--640. (Cited in pages 6 et 38.)

Cheung, L., Yalla, G., Brown, K., deVelder, N., Hsieh, A., Herges, T., Houck, D., Maniaci, D., Sakievich, P., and Abraham, A. (2024). Modification of wind turbine wakes by large-scale, convective atmospheric boundary layer structures. *Journal of Renewable and Sustainable Energy*, 16(6) :063304. (Cited in pages 142 et 149.)

Choi, H.-J. and Hong, S.-Y. (2015). An updated subgrid orographic parameterization for global atmospheric forecast models. *Journal of Geophysical Research : Atmospheres*, 120(24) :12445--12457. (Cited in page 39.)

Christakos, K., Varlas, G., Reuder, J., Katsafados, P., and Papadopoulos, A. (2014). Analysis of a Low-level Coastal Jet off the Western Coast of Norway. *Energy Procedia*, 53 :162--172. (Cited in page 20.)

Clarke, R. H. (1984). Colliding sea-breezes and the creation of internal atmospheric bore waves : Two-dimensional numerical studies. *Autralian Meteorological Magazine*, 32(4) :207--226. (Cited in page 11.)

table of content

Clarke, R. H., Smith, R. K., and Reid, D. G. (1981). The Morning Glory of the Gulf of Carpentaria : An Atmospheric Undular Bore. *Monthly Weather Review*, 109(8) :1726--1750. (Cited in page 25.)

Colle, B. A. and Novak, D. R. (2010). The New York Bight Jet : Climatology and Dynamical Evolution. *Monthly Weather Review*, 138(6) :2385--2404. (Cited in page 18.)

Conzemius, R. J. and Fedorovich, E. (2006). Dynamics of Sheared Convective Boundary Layer Entrainment. Part I : Methodological Background and Large-Eddy Simulations. *Journal of the Atmospheric Sciences*, 63(4) :1151--1178. (Cited in page 51.)

Cosgrove, B. A., Lohmann, D., Mitchell, K. E., Houser, P. R., Wood, E. F., Schaake, J. C., Robock, A., Sheffield, J., Duan, Q., Luo, L., Higgins, R. W., Pinker, R. T., and Tarpley, J. D. (2003). Land surface model spin-up behavior in the North American Land Data Assimilation System (NLDAS). *Journal of Geophysical Research : Atmospheres*, 108(D22). (Cited in page 35.)

Crosman, E. T. and Horel, J. D. (2010). Sea and Lake Breezes : A Review of Numerical Studies. *Boundary-Layer Meteorology*, 137(1) :1--29. (Cited in pages 10 et 12.)

Cuxart, J. and Jiménez, M. A. (2007). Mixing Processes in a Nocturnal Low-Level Jet : An LES Study. *Journal of the Atmospheric Sciences*, 64(5) :1666--1679. (Cited in pages 19 et 20.)

Cuxart, J., Jiménez, M. A., Prtenjak, M. T., and Grisogono, B. (2014). Study of a Sea-Breeze Case through Momentum, Temperature, and Turbulence Budgets. *Journal of Applied Meteorology and Climatology*, 53(11) :2589--2609. (Cited in pages 11, 12 et 14.)

Deardorff, J. W. (1980). Stratocumulus-capped mixed layers derived from a three-dimensional model. *Boundary-Layer Meteorology*, 18(4) :495--527. (Cited in pages 5 et 37.)

Deardorff, J. W., Willis, G. E., and Stockton, B. H. (1980). Laboratory studies of the entrainment zone of a convectively mixed layer. *Journal of Fluid Mechanics*, 100(1) :41--64. (Cited in page 142.)

Díaz, H. and Guedes Soares, C. (2020). Review of the current status, technology and future trends of offshore wind farms. *Ocean Engineering*, 209 :107381. (Cited in page 148.)

Dixit, C. M. and Nicholson, J. R. (1964). The Sea Breeze at and near Bombay. *MAUSAM*, 15(4) :603--608. (Cited in page 13.)

table of content

Djath, B., Schulz-Stellenfleth, J., and Cañadillas, B. (2022). Study of Coastal Effects Relevant for Offshore Wind Energy Using Spaceborne Synthetic Aperture Radar (SAR). *Remote Sensing*, 14(7) :1688. (Cited in pages 20, 115 et 140.)

Drobinski, P. and Foster, R. C. (2003). On the Origin of Near-Surface Streaks in the Neutrally-Stratified Planetary Boundary Layer. *Boundary-Layer Meteorology*, 108(2) :247--256. (Cited in page 26.)

Durden, D. J., Nappo, C. J., Leclerc, M. Y., Duarte, H. F., Zhang, G., Parker, M. J., and Kurzeja, R. J. (2013). On the impact of wave-like disturbances on turbulent fluxes and turbulence statistics in nighttime conditions : A case study. *Biogeosciences*, 10(12) :8433--8443. (Cited in page 40.)

Dy, C. and Fung, J. (2016). Updated Global Soil Map for the WRF Model and Soil Moisture Initialization for the Noah LSM : SOIL MAP AND SOIL MOISTURE. *Journal of Geophysical Research : Atmospheres*. (Cited in page 37.)

Eggers, A. J., J., Digumarthi, R., and Chaney, K. (2003). Wind Shear and Turbulence Effects on Rotor Fatigue and Loads Control. *Journal of Solar Energy Engineering*, 125(4) :402--409. (Cited in page 149.)

El Guernaoui, O., Reuder, J., Esau, I., Wolf, T., and Maronga, B. (2019). Scaling the Decay of Turbulence Kinetic Energy in the Free-Convective Boundary Layer. *Boundary-Layer Meteorology*, 173(1) :79--97. (Cited in pages 16 et 112.)

Elliott, W. P. (1958). The growth of the atmospheric internal boundary layer. *Eos, Transactions American Geophysical Union*, 39(6) :1048--1054. (Cited in page 8.)

European Environment Agency (2016). EU-DEM (raster) - version 1.1, Apr. 2016. (Cited in page 38.)

European Environment Agency (2019). CORINE Land Cover 2018 (raster 100 m), Europe, 6-yearly - version 2020_20u1, May 2020. (Cited in page 38.)

European Union's Copernicus Land Monitoring Service information (2017a). Fraction of Green Vegetation Cover 1999-2020 (raster 1 km), global, 10-daily -- version 1. (Cited in page 38.)

European Union's Copernicus Land Monitoring Service information (2017b). Leaf Area Index 2014-present (raster 300 m), global, 10-daily -- version 1. (Cited in page 38.)

Fang, J. and Du, Y. (2022). A global survey of diurnal offshore propagation of rainfall. *Nature Communications*, 13(1) :7437. (Cited in page 14.)

Finkele, K. (1998). Inland and Offshore Propagation Speeds of a Sea Breeze from Simulations and Measurements. *Boundary-Layer Meteorology*, 87(2) :307--329. (Cited in pages xv, 12, 13, 14, 64, 65, 66, 79 et 80.)

Finkele, K., Hacker, J. M., Kraus, H., and Byron-Scott, R. A. D. (1995). A complete sea-breeze circulation cell derived from aircraft observations. *Boundary-Layer Meteorology*, 73(3) :299--317. (Cited in page 13.)

Fu, S., Rotunno, R., Chen, J., Deng, X., and Xue, H. (2021). A large-eddy simulation study of deep-convection initiation through the collision of two sea-breeze fronts. *Atmospheric Chemistry and Physics*, 21(12) :9289--9308. (Cited in page 12.)

Gadde, S. N. and Stevens, R. J. A. M. (2021). Effect of low-level jet height on wind farm performance. *Journal of Renewable and Sustainable Energy*, 13(1) :013305. (Cited in page 149.)

Gahmberg, M., Savijärvi, H., and Leskinen, M. (2010). The influence of synoptic scale flow on sea breeze induced surface winds and calm zones. *Tellus A : Dynamic Meteorology and Oceanography*, 62(2) :209. (Cited in pages 11 et 12.)

Gallego-Castillo, C., Cuerva-Tejero, A., and Lopez-Garcia, O. (2015). A review on the recent history of wind power ramp forecasting. *Renewable and Sustainable Energy Reviews*, 52 :1148--1157. (Cited in page 148.)

Gao, L., Yang, S., Abraham, A., and Hong, J. (2020). Effects of inflow turbulence on structural response of wind turbine blades. *Journal of Wind Engineering and Industrial Aerodynamics*, 199 :104137. (Cited in page 149.)

Giannakopoulou, E.-M. and Nhili, R. (2014). WRF Model Methodology for Offshore Wind Energy Applications. *Advances in Meteorology*, 2014 :e319819. (Cited in page 37.)

Göbel, M. (2024). WRFlux : V1.7.0. (Cited in page 39.)

Gowan, T. (2019). Trajectories : Python code for calculating 'offline' trajectories using u, v, and w wind components from NWP model output. https ://github.com/tomgowan/trajectories/tree/master. (Cited in page 42.)

Grachev, A. A., Leo, L. S., Sabatino, S. D., Fernando, H. J. S., Pardyjak, E. R., and Fairall, C. W. (2016). Structure of Turbulence in Katabatic Flows Below and Above the Wind-Speed Maximum. *Boundary-Layer Meteorology*, 159(3) :469--494. (Cited in page 102.)

Grau, A., Jiménez, M. A., and Cuxart, J. (2021). Statistical characterization of the sea-breeze physical mechanisms through in-situ and satellite observations. *International Journal of Climatology*, 41(1) :17--30. (Cited in pages 11 et 45.)

Grell, A. G. A., Dudhia, A. J., and Stauffer, A. D. (1994). A description of the fifth-generation Penn State/NCAR Mesoscale Model (MM5). *University Corporation for Atmospheric Research*. (Cited in page 27.)

table of content

Gutierrez, W., Ruiz-Columbie, A., Tutkun, M., and Castillo, L. (2017). Impacts of the low-level jet's negative wind shear on the wind turbine. *Wind Energy Science*, 2(2) :533--545. (Cited in page 149.)

Haghi, K. R., Geerts, B., Chipilski, H. G., Johnson, A., Degelia, S., Imy, D., Parsons, D. B., Adams-Selin, R. D., Turner, D. D., and Wang, X. (2019). Bore-ing into Nocturnal Convection. *Bulletin of the American Meteorological Society*, 100(6) :1103--1121. (Cited in page 25.)

Hallgren, C., Aird, J. A., Ivanell, S., Körnich, H., Barthelmie, R. J., Pryor, S. C., and Sahlée, E. (2023). Brief communication : On the definition of the low-level jet. *Wind Energy Science*, 8(11) :1651--1658. (Cited in page 17.)

Hara, T., Ohya, Y., Uchida, T., and Ohba, R. (2009). Wind-Tunnel and Numerical Simulations of the Coastal Thermal Internal Boundary Layer. *Boundary-Layer Meteorology*, 130(3) :365--381. (Cited in page 124.)

Haurwitz, B. (1947). COMMENTS ON THE SEA-BREEZE CIRCULATION. *Journal of the Atmospheric Sciences*, 4(1) :1--8. (Cited in page 11.)

Hersbach, H., Bell, B., Biavati, G., Horányi, A., Muñoz Sabater, J., Nicolas, J., Peubey, C., Radu, R., Rozum, I., Schepers, D., Simmons, A., Soci, C., Dee, D., and Thépaut, J.-N. (2023). ERA5 hourly data on pressure levels from 1940 to present. (Cited in page 34.)

Högström, U. and Smedman-Högström, A.-S. (1984). The wind regime in coastal areas with special reference to results obtained from the Swedish wind energy program. *Boundary-Layer Meteorology*, 30(1) :351--373. (Cited in page 17.)

Holton, J. R. (1967). The diurnal boundary layer wind oscillation above sloping terrain1. *Tellus*, 19(2) :199--205. (Cited in page 18.)

Holtslag, M. (2016). *Far Offshore Wind Conditions in Scope of Wind Energy*. Dissertation (TU Delft). (Cited in page 6.)

Holtslag, M. C., Bierbooms, W. a. a. M., and van Bussel, G. J. W. (2016). Wind turbine fatigue loads as a function of atmospheric conditions offshore. *Wind Energy*, 19(10) :1917--1932. (Cited in page 17.)

Honnert, R., Efstathiou, G. A., Beare, R. J., Ito, J., Lock, A., Neggers, R., Plant, R. S., Shin, H. H., Tomassini, L., and Zhou, B. (2020). The Atmospheric Boundary Layer and the ''Gray Zone'' of Turbulence : A Critical Review. *Journal of Geophysical Research : Atmospheres*, 125(13) :e2019JD030317. (Cited in page 28.)

Huang, L., Bai, L., and Zhang, Y. (2024a). Analysis of Uncertainties in Convection-Permitting Ensemble Simulations of Land Breeze and Nocturnal Coastal Rainfall in South China. *Journal of Meteorological Research*, 38(6) :1047--1063. (Cited in page 6.)

table of content

Huang, L., Zhang, S., Xu, X., Huang, H., and Xu, F. (2024b). An Atmospheric Bore Formed from the Collision Between Gust Front and Sea Breeze and Its Role in the Convection Initiation. (Cited in pages 14 et 25.)

Iacono, M. J., Delamere, J. S., Mlawer, E. J., Shephard, M. W., Clough, S. A., and Collins, W. D. (2008). Radiative forcing by long-lived greenhouse gases : Calculations with the AER radiative transfer models. *Journal of Geophysical Research : Atmospheres*, 113(D13). (Cited in page 39.)

Iwai, H., Ishii, S., Tsunematsu, N., Mizutani, K., Murayama, Y., Itabe, T., Yamada, I., Matayoshi, N., Matsushima, D., Weiming, S., Yamazaki, T., and Iwasaki, T. (2008). Dual-Doppler lidar observation of horizontal convective rolls and near-surface streaks. *Geophysical Research Letters*, 35(14). (Cited in page 26.)

Janjić, Z. I. (1994). The Step-Mountain Eta Coordinate Model : Further Developments of the Convection, Viscous Sublayer, and Turbulence Closure Schemes. *Monthly Weather Review*, 122(5) :927--945. (Cited in page 36.)

Jayaraman, B. and Brasseur, J. G. (2021). Transition in atmospheric boundary layer turbulence structure from neutral to convective, and large-scale rolls. *Journal of Fluid Mechanics*, 913 :A42. (Cited in pages 26, 134 et 142.)

Jiang, Q. and Wang, Q. (2021). Characteristics and Scaling of the Stable Marine Internal Boundary Layer. *Journal of Geophysical Research : Atmospheres*, 126(21) :e2021JD035510. (Cited in page 8.)

Jiang, Q., Wang, S., and O'Neill, L. (2010). Some Insights into the Characteristics and Dynamics of the Chilean Low-Level Coastal Jet. *Monthly Weather Review*, 138(8) :3185--3206. (Cited in page 18.)

Johnson, A. and Wang, X. (2019). Multicase Assessment of the Impacts of Horizontal and Vertical Grid Spacing, and Turbulence Closure Model, on Subkilometer-Scale Simulations of Atmospheric Bores during PECAN. *Monthly Weather Review*, 147(5) :1533--1555. (Cited in page 25.)

Johnson, A., Wang, X., Haghi, K. R., and Parsons, D. B. (2018). Evaluation of Forecasts of a Convectively Generated Bore Using an Intensively Observed Case Study from PECAN. *Monthly Weather Review*, 146(9) :3097--3122. (Cited in pages 22, 37 et 80.)

Jourdier, B. (2020). Evaluation of ERA5, MERRA-2, COSMO-REA6, NEWA and AROME to simulate wind power production over France. In *Advances in Science and Research*, volume 17, pages 63--77. Copernicus GmbH. (Cited in page 32.)

Juliano, T. W., Kosović, B., Jiménez, P. A., Eghdami, M., Haupt, S. E., and Martilli, A. (2022). ''Gray Zone'' Simulations Using a Three-Dimensional Planetary Boundary Layer Parameterization in the Weather Research and Forecasting Model. *Monthly Weather Review*, 150(7) :1585--1619. (Cited in page 28.)

table of content

Kaimal, J. and Finnigan, J. (1994). *Atmospheric Boundary Layer Flows*. Oxford University Press, oxford university press edition. (Cited in pages 8, 14 et 51.)

Kallistratova, M. A., Kouznetsov, R. D., Kramar, V. F., and Kuznetsov, D. D. (2013). Profiles of Wind Speed Variances within Nocturnal Low-Level Jets Observed with a Sodar. *Journal of Atmospheric and Oceanic Technology*, 30(9) :1970--1977. (Cited in page 142.)

Kallistratova, M. A., Petenko, I. V., Kouznetsov, R. D., Kuznetsov, D. D., Lyulyukin, V. S., and Perepelkin, V. G. (2019). Kelvin-Helmholtz billows in rising morning inversions. *IOP Conference Series : Earth and Environmental Science*, 231(1) :012025. (Cited in page 22.)

Kalverla, P. C., Duncan Jr., J. B., Steeneveld, G.-J., and Holtslag, A. A. M. (2019). Low-level jets over the North Sea based on ERA5 and observations : Together they do better. *Wind Energy Science*, 4(2) :193--209. (Cited in page 18.)

Kitada, T. (1987). Turbulence structure of sea breeze front and its implication in air pollution transport --- Application of k-ε turbulence model ---. *Boundary-Layer Meteorology*, 41(1) :217--239. (Cited in page 14.)

Kitamura, Y. and Nishizawa, S. (2019). Estimation of energy dissipation caused by odd order difference schemes for an unstable planetary boundary layer. *Atmospheric Science Letters*, 20(6) :e905. (Cited in page 53.)

Kosović, B., Basu, S., Berg, J., Berg, L. K., Haupt, S. E., Larsén, X. G., Peinke, J., Stevens, R. J. A. M., Veers, P., and Watson, S. (2025). Impact of atmospheric turbulence on performance and loads of wind turbines : Knowledge gaps and research challenges. *Wind Energy Science Discussions*, pages 1--67. (Cited in pages 17 et 27.)

Kraus, H., Hacker, J. M., and Hartmann, J. (1990). An observational aircraft-based study of sea-breeze frontogenesis. *Boundary-Layer Meteorology*, 53(3) :223--265. (Cited in page 10.)

Lafore, J. P., Stein, J., Asencio, N., Bougeault, P., Ducrocq, V., Duron, J., Fischer, C., Héreil, P., Mascart, P., Masson, V., Pinty, J. P., Redelsperger, J. L., Richard, E., and Vilà-Guerau de Arellano, J. (1998). The Meso-NH Atmospheric Simulation System. Part I : Adiabatic formulation and control simulations. *Annales Geophysicae*, 16(1) :90--109. (Cited in page 27.)

Landreau, M., Calmet, I., and Conan, B. (2025a). Impact of gravity waves and sea breeze on offshore wind resource : A case study. In *WESC 2025*, Nantes, France. Wind Energy Science Conference. (Cited in page 149.)

Landreau, M., Conan, B., Luce, B., and Calmet, I. (2025b). Observation and Large-Eddy Simulation of an Offshore Atmospheric Undular Bore During Sea-Breeze Initiation. *Journal of Geophysical Research : Atmospheres*, 130(19) :e2025JD043852. (Cited in page 68.)

table of content

Landreau, M., Conan, B., Luce, B., and Calmet, I. (2025c). Observation and LES modeling of an offshore atmospheric undular bore generated during sea-breeze initiation near a peninsula. (Cited in page 95.)

Laprise, R. (1992). The Euler Equations of Motion with Hydrostatic Pressure as an Independent Variable. *Monthly Weather Review*, 120(1) :197--207. (Cited in page 175.)

LeMone, M. A. (1973). The Structure and Dynamics of Horizontal Roll Vortices in the Planetary Boundary Layer. *Journal of the Atmospheric Sciences*, 30(6) :1077--1091. (Cited in pages 26 et 142.)

Liu, H., He, M., Wang, B., and Zhang, Q. (2014). Advances in low-level jet research and future prospects. *Journal of Meteorological Research*, 28(1) :57--75. (Cited in page 17.)

Liu, Y., Liu, Y., Muñoz-Esparza, D., Hu, F., Yan, C., and Miao, S. (2020). Simulation of Flow Fields in Complex Terrain with WRF-LES : Sensitivity Assessment of Different PBL Treatments. *Journal of Applied Meteorology and Climatology*, 59(9) :1481--1501. (Cited in pages 28, 37, 38 et 39.)

Luce, H., Kantha, L., Hashiguchi, H., Doddi, A., Lawrence, D., and Yabuki, M. (2020). On the Relationship between the TKE Dissipation Rate and the Temperature Structure Function Parameter in the Convective Boundary Layer. *Journal of the Atmospheric Sciences*, 77(7) :2311--2326. (Cited in page 51.)

Luiz, E. W. and Fiedler, S. (2024). Global Climatology of Low-Level-Jets : Occurrence, Characteristics, and Meteorological Drivers. *Journal of Geophysical Research : Atmospheres*, 129(9) :e2023JD040262. (Cited in pages 17 et 20.)

Ma, J., Xu, H., and Dong, C. (2016). Seasonal variations in atmospheric responses to oceanic eddies in the Kuroshio Extension. *Tellus A : Dynamic Meteorology and Oceanography*, 68(1) :31563. (Cited in page 6.)

Mahrt, L. (2014). Stably Stratified Atmospheric Boundary Layers. *Annual Review of Fluid Mechanics*, 46(1) :23--45. (Cited in pages 23, 94 et 110.)

Mahrt, L., Vickers, D., and Andreas, E. L. (2014). Low-Level Wind Maxima and Structure of the Stably Stratified Boundary Layer in the Coastal Zone. *Journal of Applied Meteorology and Climatology*, 53(2) :363--376. (Cited in pages 8, 18 et 19.)

Martin, E. R. and Johnson, R. H. (2008). An Observational and Modeling Study of an Atmospheric Internal Bore during NAME 2004. *Monthly Weather Review*, 136(11) :4150--4167. (Cited in pages 80 et 111.)

Merrill, J. T. (1977). Observational and Theoretical Study of Shear Instability in the Airflow near the Ground. *Journal of the Atmospheric Sciences*, 34(6) :911--921. (Cited in page 110.)

table of content

Mestayer, P. G., Calmet, I., Herlédant, O., Barré, S., Piquet, T., and Rosant, J.-M. (2018). A Coastal Bay Summer Breeze Study, Part 1 : Results of the Quiberon 2006 Experimental Campaign. *Boundary-Layer Meteorology*, 167(1) :1--26. (Cited in pages 11, 12 et 16.)

Miller, S. T. K., Keim, B. D., Talbot, R. W., and Mao, H. (2003). Sea breeze : Structure, forecasting, and impacts. *Reviews of Geophysics*, 41(3). (Cited in pages 10, 12 et 79.)

Mirocha, J. D., Simpson, M. D., Fast, J. D., Berg, L. K., and Baskett, R. L. (2016). Investigation of boundary-layer wind predictions during nocturnal low-level jet events using the Weather Research and Forecasting model. *Wind Energy*, 19(4) :739--762. (Cited in page 36.)

Moeng, C.-H. and Sullivan, P. P. (1994). A Comparison of Shear- and Buoyancy-Driven Planetary Boundary Layer Flows. *Journal of the Atmospheric Sciences*, 51(7) :999--1022. (Cited in pages 5, 26 et 142.)

Monin, A. S. and Obukhov, A. M. (1954). Basic laws of turbulent mixing in the surface layer of the atmosphere. (Cited in page 3.)

Munoz-Esparza, D., Kosovic, B., Mirocha, J. D., and van Beeck, J. (2014). Bridging the Transition from Mesoscale to Microscale Turbulence in Numerical Weather Prediction Models. *Boundary-Layer Meteorology*, vol. 153. (Cited in page 28.)

Murphy, P., Lundquist, J. K., and Fleming, P. (2020). How wind speed shear and directional veer affect the power production of a megawatt-scale operational wind turbine. *Wind Energy Science*, 5(3) :1169--1190. (Cited in page 149.)

Nakanishi, M., Shibuya, R., Ito, J., and Niino, H. (2014). Large-Eddy Simulation of a Residual Layer : Low-Level Jet, Convective Rolls, and Kelvin--Helmholtz Instability. *Journal of the Atmospheric Sciences*, 71(12) :4473--4491. (Cited in pages 20, 22 et 142.)

Newsom, R. K. and Banta, R. M. (2003). Shear-Flow Instability in the Stable Nocturnal Boundary Layer as Observed by Doppler Lidar during CASES-99. *Journal of the Atmospheric Sciences*, 60(1) :16--33. (Cited in pages 20, 22 et 142.)

Nieuwstadt, F. T. M. (1984). Some aspects of the turbulent stable boundary layer. *Boundary-Layer Meteorology*, 30(1) :31--55. (Cited in page 5.)

Nieuwstadt, F. T. M. and Brost, R. A. (1986). The Decay of Convective Turbulence. *Journal of the Atmospheric Sciences*, 43(6) :532--546. (Cited in pages 14, 15, 16, 104, 106, 109 et 112.)

Noonan, J. A. and Smith, R. K. (1986). Sea-Breeze Circulations over Cape York Peninsula and the Generation of Gulf of Carpentaria Cloud Line Disturbances. *Journal of the Atmospheric Sciences*, 43(16) :1679--1693. (Cited in pages 14, 25 et 80.)

table of content

Nunalee, C. G. and Basu, S. (2014). Mesoscale modeling of coastal low-level jets : Implications for offshore wind resource estimation. *Wind Energy*, 17(8) :1199--1216. (Cited in pages 16 et 36.)

Ollier, S. J. and Watson, S. J. (2023). Modelling the impact of trapped lee waves on offshore wind farm power output. *Wind Energy Science*, 8(7) :1179--1200. (Cited in page 149.)

Parfitt, R., Czaja, A., and Seo, H. (2017). A simple diagnostic for the detection of atmospheric fronts. *Geophysical Research Letters*, 44(9) :4351--4358. (Cited in page 117.)

Paskin, L., Conan, B., Perignon, Y., and Aubrun, S. (2022). Evidence of Ocean Waves Signature in the Space--Time Turbulent Spectra of the Lower Marine Atmosphere Measured by a Scanning LiDAR. *Remote Sensing*, 14(13) :3007. (Cited in pages xiii et 30.)

Paul, F. P., S., R., T.j., A., Bala Subrahamanyam, D., and Ramachandran, R. (2021). Numerical simulation of sea-breeze circulation over the Arabian Sea during the passage of a cyclonic storm OCKHI using a regional atmospheric model COSMO. *Dynamics of Atmospheres and Oceans*, 96 :101265. (Cited in page 10.)

Paulsen, J., Schneemann, J., Steinfeld, G., Theuer, F., and Kühn, M. (2025). The impact of low-level jets on the power generated by offshore wind turbines. (Cited in page 149.)

Pino, D. and Vilà-Guerau De Arellano, J. (2008). Effects of shear in the convective boundary layer : Analysis of the turbulent kinetic energy budget. *Acta Geophysica*, 56(1) :167--193. (Cited in pages xiv, 5, 14, 50 et 52.)

Plant, R. S. and Keith, G. J. (2007). Occurrence of Kelvin-Helmholtz Billows in Sea-breeze Circulations. *Boundary-Layer Meteorology*, 122(1) :1--15. (Cited in pages 14 et 22.)

Pollak, D. A., Nygaard, N. G., Jiménez, M. M., Wagner, R., and Sathe, A. (2014). Characterization of Ambient Offshore Turbulence Intensity from Analysis of Nine Offshore Meteorological Masts in Northern Europe. 2014 :GC42B--02. (Cited in page 6.)

Porté-Agel, F., Bastankhah, M., and Shamsoddin, S. (2020). Wind-Turbine and Wind-Farm Flows : A Review. *Boundary-Layer Meteorology*, 174(1) :1--59. (Cited in page 149.)

Quint, D., Lundquist, J. K., and Rosencrans, D. (2025). Simulations suggest offshore wind farms modify low-level jets. *Wind Energy Science*, 10(1) :117--142. (Cited in pages 18 et 19.)

table of content

Rai, R. K., Berg, L. K., Pekour, M., Shaw, W. J., Kosovic, B., Mirocha, J. D., and Ennis, B. L. (2017). Spatiotemporal Variability of Turbulence Kinetic Energy Budgets in the Convective Boundary Layer over Both Simple and Complex Terrain. *Journal of Applied Meteorology and Climatology*, 56(12) :3285--3302. (Cited in pages 40, 41 et 182.)

Rakesh, P., Sandeepan, B., Venkatesan, R., and Baskaran, R. (2017). Observation and numerical simulation of submesoscale motions within sea breeze over a tropical coastal site : A case study. *Atmospheric Research*, 198 :205--215. (Cited in page 142.)

Ralph, F. M., Neiman, P. J., Keller, T. L., Levinson, D., and Fedor, L. (1997). Observations, Simulations, and Analysis of Nonstationary Trapped Lee Waves. *Journal of the Atmospheric Sciences*, 54(10) :1308--1333. (Cited in page 93.)

Rayment, R. and Readings, C. J. (1974). A case study of the structure and energetics of an inversion. *Quarterly Journal of the Royal Meteorological Society*, 100(424) :221--233. (Cited in page 142.)

Reible, D. D., Simpson, J. E., and Linden, P. F. (1993). The sea breeze and gravity-current frontogenesis. *Quarterly Journal of the Royal Meteorological Society*, 119(509) :1--16. (Cited in page 110.)

Reimann, L., Vafeidis, A. T., and Honsel, L. E. (2023). Population development as a driver of coastal risk : Current trends and future pathways. *Cambridge Prisms : Coastal Futures*, 1 :e14. (Cited in page 1.)

Ren, Y., Zhang, H., Wei, W., Wu, B., Cai, X., and Song, Y. (2019). Effects of turbulence structure and urbanization on the heavy haze pollution process. *Atmospheric Chemistry and Physics*, 19(2) :1041--1057. (Cited in pages 5 et 94.)

Ren, Y., Zhang, H., Zhang, X., Cai, X., Song, Y., Liang, J., Zhang, L., Zhu, T., and Huang, J. (2025). Research progress and current application of weak turbulence and turbulence intermittency in stable boundary layers. *Earth-Science Reviews*, 262 :105062. (Cited in pages 5, 40, 110 et 151.)

Rizza, U., Miglietta, M. M., Anabor, V., Degrazia, G. A., and Maldaner, S. (2015). Large-eddy simulation of sea breeze at an idealized peninsular site. *Journal of Marine Systems*, 148 :167--182. (Cited in pages 10 et 14.)

Rohanizadegan, M., Petrone, R. M., Pomeroy, J. W., and Kosovic, B. (2025). Analysis of Turbulence and Turbulence Kinetic Energy Dynamics in Complex Terrain. *Journal of Geophysical Research : Atmospheres*, 130(5) :e2023JD040558. (Cited in pages 40 et 144.)

Rottman, J. W. and Simpson, J. E. (1989). The formation of internal bores in the atmosphere : A laboratory model. *Quarterly Journal of the Royal Meteorological Society*, 115(488) :941--963. (Cited in pages xiii, 23, 24, 71 et 111.)

table of content

Rotunno, R. (1983). On the Linear Theory of the Land and Sea Breeze. *Journal of the Atmospheric Sciences*, 40(8) :1999--2009. (Cited in pages 12, 14, 22, 66 et 80.)

Roy, S., Sentchev, A., Schmitt, F. G., Augustin, P., and Fourmentin, M. (2021). Impact of the Nocturnal Low-Level Jet and Orographic Waves on Turbulent Motions and Energy Fluxes in the Lower Atmospheric Boundary Layer. *Boundary-Layer Meteorology*, 180(3) :527--542. (Cited in pages 22 et 111.)

Sathe, A., Gryning, S.-E., and Peña, A. (2011). Comparison of the atmospheric stability and wind profiles at two wind farm sites over a long marine fetch in the North Sea. *Wind Energy*, 14(6) :767--780. (Cited in page 6.)

SciPy (2025). Peak_prominences --- SciPy v1.16.2 Manual. https ://docs.scipy.org/doc/scipy/reference/generated/scipy.signal.peak_prominences.html. (Cited in pages 87 et 114.)

Scorer, R. S. (1949). Theory of waves in the lee of mountains. *Quarterly Journal of the Royal Meteorological Society*, 75(323) :41--56. (Cited in page 22.)

Segura, R., Badia, A., Ventura, S., Gilabert, J., Martilli, A., and Villalba, G. (2021). Sensitivity study of PBL schemes and soil initialization using the WRF-BEP-BEM model over a Mediterranean coastal city. *Urban Climate*, 39 :100982. (Cited in page 37.)

Seity, Y., Brousseau, P., Malardel, S., Hello, G., Bénard, P., Bouttier, F., Lac, C., and Masson, V. (2011). The AROME-France Convective-Scale Operational Model. *Monthly Weather Review*, 139(3) :976--991. (Cited in page 32.)

Sha, W., Kawamura, T., and Ueda, H. (1991). A Numerical Study on Sea/Land Breezes as a Gravity Current : Kelvin--Helmholtz Billows and Inland Penetration of the Sea-Breeze Front. *Journal of the Atmospheric Sciences*, 48(14) :1649--1665. (Cited in page 14.)

Shao, Y., Hacker, J. M., and Schwerdtfeger, P. (1991). The structure of turbulence in a coastal atmospheric boundary layer. *Quarterly Journal of the Royal Meteorological Society*, 117(502) :1299--1324. (Cited in page 14.)

Shen, L. and Zhao, C. (2020). Dominance of Shortwave Radiative Heating in the Sea-Land Breeze Amplitude and its Impacts on Atmospheric Visibility in Tokyo, Japan. *Journal of Geophysical Research : Atmospheres*, 125(8) :e2019JD031541. (Cited in page 12.)

Sheridan, L., Krishnamurthy, R., and Gaudet, B. (2021). Assessment of Model Hub Height Wind Speed Performance Using DOE Lidar Buoy Data. Technical Report PNNL--30840, 1779495. (Cited in page 34.)

table of content

Sheridan, L. M., Krishnamurthy, R., Gustafson Jr., W. I., Liu, Y., Gaudet, B. J., Bodini, N., Newsom, R. K., and Pekour, M. (2024). Offshore low-level jet observations and model representation using lidar buoy data off the California coast. *Wind Energy Science*, 9(3) :741--758. (Cited in page 20.)

Shin, H. H. and Hong, S.-Y. (2011). Intercomparison of Planetary Boundary-Layer Parametrizations in the WRF Model for a Single Day from CASES-99. *Boundary-Layer Meteorology*, 139(2) :261--281. (Cited in page 35.)

Short, E. (2020). Verifying Operational Forecasts of Land--Sea-Breeze and Boundary Layer Mixing Processes. *Weather and Forecasting*, 35(4) :1427--1445. (Cited in page 79.)

Simpson, J. E. (1994). *Sea Breeze and Local Winds*. Cambridge University Press. (Cited in pages 10 et 13.)

Simpson, J. E. (1996). Diurnal Changes in Sea-Breeze Direction. *Journal of Applied Meteorology and Climatology*, 35(7) :1166--1169. (Cited in pages 12, 16, 55, 57, 79 et 145.)

Simpson, J. E. and Britter, R. E. (1980). A laboratory model of an atmospheric mesofront. *Quarterly Journal of the Royal Meteorological Society*, 106(449) :485--500. (Cited in pages 14 et 92.)

Skamarock, C., Klemp, B., Dudhia, J., Gill, O., Liu, Z., Berner, J., Wang, W., Powers, G., Duda, G., Barker, D., and Huang, X.-y. (2019). A Description of the Advanced Research WRF Model Version 4.1. (Cited in pages xiv, 27, 32, 36, 37, 144 et 175.)

Smedman, A.-S. (1988). Observations of a multi-level turbulence structure in a very stable atmospheric boundary layer. *Boundary-Layer Meteorology*, 44(3) :231--253. (Cited in page 20.)

Smedman, A.-S., Bergström, H., and Högström, U. (1995). Spectra, variances and length scales in a marine stable boundary layer dominated by a low level jet. *Boundary-Layer Meteorology*, 76(3) :211--232. (Cited in page 20.)

Smedman, A.-S., Tjernström, M., and Högström, U. (1993). Analysis of the turbulence structure of a marine low-level jet. *Boundary-Layer Meteorology*, 66(1) :105--126. (Cited in pages 19, 20, 113 et 142.)

Sorbjan, Z. (1997). DECAY OF CONVECTIVE TURBULENCE REVISITED. *Boundary-Layer Meteorology*, 82(3) :503--517. (Cited in pages 14 et 16.)

Staquet, C. and Sommeria, J. (2002). INTERNAL GRAVITY WAVES : From Instabilities to Turbulence. *Annual Review of Fluid Mechanics*, 34(Volume 34, 2002) :559--593. (Cited in page 22.)

table of content

Steele, C. J., Dorling, S. R., Von Glasow, R., and Bacon, J. (2013). Idealized WRF model sensitivity simulations of sea breeze types and their effects on offshore windfields. *Atmospheric Chemistry and Physics*, 13(1) :443--461. (Cited in pages 11, 12, 13, 66 et 79.)

Steele, C. J., Dorling, S. R., von Glasow, R., and Bacon, J. (2015). Modelling sea-breeze climatologies and interactions on coasts in the southern North Sea : Implications for offshore wind energy. *Quarterly Journal of the Royal Meteorological Society*, 141(690) :1821--1835. (Cited in page 12.)

Stensrud, D. J. (1996). Importance of Low-Level Jets to Climate : A Review. *Journal of Climate*, 9(8) :1698--1711. (Cited in page 18.)

Stevenson, RE. (1969). The ocean and its atmosphere as seen from gemini spacecraft. *Ann. Meteor., Offenbach.*, 4 :195--199. (Cited in page 13.)

Stiperski, I. and Calaf, M. (2018). Dependence of near-surface similarity scaling on the anisotropy of atmospheric turbulence. *Quarterly Journal of the Royal Meteorological Society*, 144(712) :641--657. (Cited in pages xxii, 147 et 148.)

Stoll, R., Gibbs, J. A., Salesky, S. T., Anderson, W., and Calaf, M. (2020). Large-Eddy Simulation of the Atmospheric Boundary Layer. *Boundary-Layer Meteorology*, 177(2) :541--581. (Cited in page 5.)

Stull, R. B. (2017). *Practical Meteorology : An Algebra-Based Survey of Atmospheric Science*. Dept. of Earth, Ocean & Atmospheric Sciences, University of British Columbia, Vancouver, BC, Canada, version 1.02b edition. (Cited in pages xiii, 4, 8, 9, 10, 23 et 51.)

Subrahamanyam, D. B., Gupta, K. S., Ravindran, S., and Krishnan, P. (2001). Study of sea breeze and land breeze along the west coast of Indian sub-continent over the latitude range 15°N to 8°N during INDOEX IFP-99 (SK-141) cruise. *Current Science*, 80 :85--88. (Cited in page 13.)

Sun, J., Mahrt, L., Nappo, C., and Lenschow, D. H. (2015a). Wind and Temperature Oscillations Generated by Wave--Turbulence Interactions in the Stably Stratified Boundary Layer. *Journal of the Atmospheric Sciences*, 72(4) :1484--1503. (Cited in pages 22 et 111.)

Sun, J., Nappo, C. J., Mahrt, L., Belušić, D., Grisogono, B., Stauffer, D. R., Pulido, M., Staquet, C., Jiang, Q., Pouquet, A., Yagüe, C., Galperin, B., Smith, R. B., Finnigan, J. J., Mayor, S. D., Svensson, G., Grachev, A. A., and Neff, W. D. (2015b). Review of wave-turbulence interactions in the stable atmospheric boundary layer. *Reviews of Geophysics*, 53(3) :956--993. (Cited in pages 1, 5, 21, 94, 145 et 146.)

table of content

Svensson, N., Arnqvist, J., Bergström, H., Rutgersson, A., and Sahlée, E. (2019). Measurements and Modelling of Offshore Wind Profiles in a Semi-Enclosed Sea. *Atmosphere*, 10(4) :194. (Cited in page 20.)

Sykes, R. I. and Henn, D. S. (1989). Large-Eddy Simulation of Turbulent Sheared Convection. *Journal of the Atmospheric Sciences*, 46(8) :1106--1118. (Cited in pages 26 et 142.)

Talbot, C., Bou-Zeid, E., and Smith, J. (2012). Nested Mesoscale Large-Eddy Simulations with WRF : Performance in Real Test Cases. *Journal of Hydrometeorology*, 13(5) :1421--1441. (Cited in pages 37 et 39.)

Taylor, K. E. (2001). Summarizing multiple aspects of model performance in a single diagram. *Journal of Geophysical Research : Atmospheres*, 106(D7) :7183--7192. (Cited in page 50.)

Teixeira, M. A. C. (2014). The physics of orographic gravity wave drag. *Frontiers in Physics*, 2. (Cited in page 22.)

Thomasson, A. (2021). *Turbulence Intensity During Low-Level Jets in the Baltic Sea*. Department of earth sciences, uppsala university edition. (Cited in page 20.)

Thomsen, G. L. and Smith, R. K. (2006). Simulations of low-level convergence lines over north-eastern Australia. *Quarterly Journal of the Royal Meteorological Society*, 132(616) :691--707. (Cited in pages 14, 25 et 80.)

Thorpe, S. A. (2012). On the Kelvin--Helmholtz route to turbulence. *Journal of Fluid Mechanics*, 708 :1--4. (Cited in pages 22 et 149.)

Tijm, A. B. C. and van Delden, A. J. (1999). The role of sound waves in sea-breeze initiation. *Quarterly Journal of the Royal Meteorological Society*, 125(558) :1997--2018. (Cited in page 79.)

Tsiringakis, A., Theeuwes, N. E., Barlow, J. F., and Steeneveld, G.-J. (2022). Interactions Between the Nocturnal Low-Level Jets and the Urban Boundary Layer : A Case Study over London. *Boundary-Layer Meteorology*, 183(2) :249--272. (Cited in page 19.)

Turner, J. S. (1979). *Buoyancy Effects in Fluids*. Cambridge University Press. (Cited in page 22.)

Udina, M., Montornès, À., Casso, P., Kosović, B., and Bech, J. (2020). WRF-LES Simulation of the Boundary Layer Turbulent Processes during the BLLAST Campaign. *Atmosphere*, 11(11) :1149. (Cited in page 36.)

Van de Wiel, B. J. H., Moene, A. F., Steeneveld, G. J., Baas, P., Bosveld, F. C., and Holtslag, A. a. M. (2010). A Conceptual View on Inertial Oscillations and Nocturnal Low-Level Jets. *Journal of the Atmospheric Sciences*, 67(8) :2679--2689. (Cited in pages xiii, 9, 17, 18 et 19.)

table of content

Van der Linden, S. J. A., Van de Wiel, B. J. H., Petenko, I., Van Heerwaarden, C. C., Baas, P., and Jonker, H. J. J. (2020). A Businger Mechanism for Intermittent Bursting in the Stable Boundary Layer. *Journal of the Atmospheric Sciences*, 77(10) :3343--3360. (Cited in page 151.)

Veers, P., Dykes, K., Basu, S., Bianchini, A., Clifton, A., Green, P., Holttinen, H., Kitzing, L., Kosovic, B., Lundquist, J. K., Meyers, J., O'Malley, M., Shaw, W. J., and Straw, B. (2022). Grand Challenges : Wind energy research needs for a global energy transition. *Wind Energy Science*, 7(6) :2491--2496. (Cited in page 1.)

Vihma, T., Uotila, J., and Launiainen, J. (1998). Air-sea interaction over a thermal marine front in the Denmark Strait. *Journal of Geophysical Research : Oceans*, 103(C12) :27665--27678. (Cited in page 18.)

Visich, A. and Conan, B. (2025). Measurement and analysis of high altitude wind profiles over the sea in a coastal zone using a scanning doppler LiDAR : Application to offshore wind energy. *Ocean Engineering*, 325 :120749. (Cited in pages 17, 31 et 114.)

Vogel, J., Afshari, A., Chockalingam, G., and Stadler, S. (2022). Evaluation of a novel WRF/PALM-4U coupling scheme incorporating a roughness-corrected surface layer representation. *Urban Climate*, 46 :101311. (Cited in page 38.)

Wacławczyk, M., Ma, Y.-F., Kopeć, J. M., and Malinowski, S. P. (2017). Novel approaches to estimating turbulent kinetic energy dissipation rate from low and moderate resolution velocity fluctuation time series. (Cited in page 53.)

Wagner, D., Steinfeld, G., Witha, B., Wurps, H., and Reuder, J. (2019). Low Level Jets over the Southern North Sea. *Meteorologische Zeitschrift*. (Cited in pages 17, 18, 19, 20 et 140.)

Waleffe, F. and Kim, J. (1998). How streamwise rolls and streaks self-sustain in a shear flow. II. In *29th AIAA, Fluid Dynamics Conference*, Albuquerque,NM,U.S.A. American Institute of Aeronautics and Astronautics. (Cited in pages 25 et 26.)

Wei, Z., Zhang, L., Ren, Y., Wei, W., Zhang, H., Cai, X., Song, Y., and Kang, L. (2021). Characteristics of the turbulence intermittency and its influence on the turbulent transport in the semi-arid region of the Loess Plateau. *Atmospheric Research*, 249 :105312. (Cited in page 110.)

White, B. L. and Helfrich, K. R. (2012). A general description of a gravity current front propagating in a two-layer stratified fluid. *Journal of Fluid Mechanics*, 711 :545--575. (Cited in pages xiii, 23, 25 et 71.)

Wood, R., Stromberg, I. M., and Jonas, P. R. (1999). Aircraft observations of sea-breeze frontal structure. *Quarterly Journal of the Royal Meteorological Society*, 125(558) :1959--1995. (Cited in pages 14, 16 et 110.)

table of content

Wyngaard, J. C. (2004). Toward Numerical Modeling in the ‘‘Terra Incognita’’. *Journal of the Atmospheric Sciences*, 61(14) :1816--1826. (Cited in page 28.)

Xia, G., Draxl, C., Optis, M., and Redfern, S. (2022). Detecting and characterizing simulated sea breezes over the US northeastern coast with implications for offshore wind energy. *Wind Energy Science*, 7(2) :815--829. (Cited in page 39.)

Xue, M., Droegemeier, K. K., and Wong, V. (2000). The Advanced Regional Prediction System (ARPS) -- A multi-scale nonhydrostatic atmospheric simulation and prediction model. Part I : Model dynamics and verification. *Meteorology and Atmospheric Physics*, 75(3) :161--193. (Cited in page 27.)

Young, G. S., Kristovich, D. A. R., Hjelmfelt, M. R., and Foster, R. C. (2002). ROLLS, STREETS, WAVES, AND MORE : A Review of Quasi-Two-Dimensional Structures in the Atmospheric Boundary Layer. *Bulletin of the American Meteorological Society*, 83(7) :997--1002. (Cited in pages 25, 26 et 134.)

Zhang, S., Parsons, D. B., Xu, X., Huang, H., Xu, F., Wu, T., Chen, G., Abulikemu, A., Zhao, Y., Zhang, S., and Tang, Y. (2024). The Development of Atmospheric Bores in Non-Uniform Baroclinic Environments and Their Roles in the Maintenance, Structure, and Evolution of an MCS. *Journal of Geophysical Research : Atmospheres*, 129(1) :e2023JD039319. (Cited in page 25.)

Zhang, S., Parsons, D. B., Xu, X., Sun, J., Wu, T., Xu, F., Wei, N., and Chen, G. (2022). Bores Observed During the Warm Season of 2015--2019 Over the Southern North China Plain. *Geophysical Research Letters*, 49(15) :e2022GL099205. (Cited in page 80.)

Zhong, S. and Takle, E. S. (1992). An Observational Study of Sea- and Land-Breeze Circulation in an Area of Complex Coastal Heating. *Journal of Applied Meteorology and Climatology*, 31(12) :1426--1438. (Cited in pages 12 et 13.)

Appendices

table of content

Annexe A

WRF referential frame and prognostic equations

This appendix presents the WRF prognostic equations. First, the WRF referential frame is introduced in Section A.1, and then, the transformation of the Navier-Stokes equations into the WRF framework is detailed in Section A.2.

A.1 WRF referential frame

A.1.1 notation

The classical referential frame for a regional study is the Cartesian referential frame

$$R_c = (t, x, y, z) \tag{A.1}$$

The partial derivatives in R_c are :

$$\partial_{x_i} = (\partial_{t_c}, \partial_{x_c}, \partial_{y_c}, \partial_z) \tag{A.2}$$

In WRF (Skamarock et al., 2019) (hereafter SK19), the vertical coordinate is a terrain-following dry-hydrostatic-pressure-based coordinate η (Laprise, 1992). The WRF referential frame is

$$R_w = (t, x, y, \eta) \tag{A.3}$$

The partial derivatives in R_w are

$$\partial_{\chi_i} = (\partial_{t_w}, \partial_{x_w}, \partial_{y_w}, \partial_\eta) \tag{A.4}$$

A.1.2 Jacobian

The Jacobian matrix for coordinate change is

$$J_{ij} = \partial_{\chi_j}(x_i) = \begin{bmatrix} 1 & 0 & 0 & 0 \\ 0 & 1 & 0 & 0 \\ 0 & 0 & 1 & 0 \\ z_t & z_x & z_y & z_\eta \end{bmatrix} \tag{A.5}$$

table of content

with

$$z_t = \partial_{t_w}(z) \tag{A.6}$$
$$z_x = \partial_{x_w}(z) \tag{A.7}$$
$$z_y = \partial_{y_w}(z) \tag{A.8}$$
$$z_\eta = \partial_\eta(z) \tag{A.9}$$

and its inverse matrix is

$$J_{ij}^{-1} = \partial_{x_j}(\chi_i) = \begin{bmatrix} 1 & 0 & 0 & 0 \\ 0 & 1 & 0 & 0 \\ 0 & 0 & 1 & 0 \\ \eta_t & \eta_x & \eta_y & \eta_z \end{bmatrix} \tag{A.10}$$

with

$$\eta_t = \partial_{t_c}(\eta) \tag{A.11}$$
$$\eta_x = \partial_{x_c}(\eta) \tag{A.12}$$
$$\eta_y = \partial_{y_c}(\eta) \tag{A.13}$$
$$\eta_z = \partial_z(\eta) \tag{A.14}$$

Then, from J_{ij} and J_{ij}^{-1}, it is found that

$$z_t = -z_\eta \eta_t \qquad \eta_t = -\eta_z z_t \tag{A.15}$$
$$z_x = -z_\eta \eta_x \qquad \eta_x = -\eta_z z_x \tag{A.16}$$
$$z_y = -z_\eta \eta_y \qquad \eta_y = -\eta_z z_y \tag{A.17}$$
$$z_\eta = (\eta_z)^{-1} \qquad \eta_z = (z_\eta)^{-1} \tag{A.18}$$

and since derivatives in the same referential frame can commute

$$\partial_\eta(z_t) = \partial_{t_w}(z_\eta) \qquad \partial_z(\eta_t) = \partial_{t_c}(\eta_z) \tag{A.19}$$
$$\partial_\eta(z_x) = \partial_{x_w}(z_\eta) \qquad \partial_z(\eta_x) = \partial_{x_c}(\eta_z) \tag{A.20}$$
$$\partial_\eta(z_y) = \partial_{y_w}(z_\eta) \qquad \partial_z(\eta_y) = \partial_{y_c}(\eta_z) \tag{A.21}$$

A.1.3 partial derivatives

The relation between partial derivatives of R_c and R_w is obtained with the Jacobian matrix

$$\partial_{\chi_j} = \partial_{x_i}.J_{ij} = \begin{bmatrix} \partial_{t_w} \\ \partial_{x_w} \\ \partial_{y_w} \\ \partial_\eta \end{bmatrix} = \begin{bmatrix} \partial_{t_c} + & z_t\partial_z \\ \partial_{x_c} + & z_x\partial_z \\ \partial_{y_c} + & z_y\partial_z \\ & z_\eta\partial_z \end{bmatrix} \tag{A.22}$$

and

$$\partial_{x_j} = \partial_{\chi_i}.J_{ij}^{-1} = \begin{bmatrix} \partial_{t_c} \\ \partial_{x_c} \\ \partial_{y_c} \\ \partial_z \end{bmatrix} = \begin{bmatrix} \partial_{t_w} + & \eta_t\partial_\eta \\ \partial_{x_w} + & \eta_x\partial_\eta \\ \partial_{y_w} + & \eta_y\partial_\eta \\ & \eta_z\partial_\eta \end{bmatrix} \tag{A.23}$$

table of content

A.1.4 velocities

The velocity vector in R_c is defined as

$$u_i = \begin{bmatrix} 1 \\ u \\ v \\ w \end{bmatrix} = \begin{bmatrix} \frac{dt}{dt} \\ \frac{dx}{dt} \\ \frac{dy}{dt} \\ \frac{dz}{dt} \end{bmatrix} \tag{A.24}$$

The velocity vector in R_w is defined as

$$v_i = \begin{bmatrix} 1 \\ u \\ v \\ \omega \end{bmatrix} = \begin{bmatrix} \frac{dt}{dt} \\ \frac{dx}{dt} \\ \frac{dy}{dt} \\ \frac{d\eta}{dt} \end{bmatrix} \tag{A.25}$$

From relationship $u_i = J_{ij} v_j$, it is found that

$$w = z_t + u z_x + x z_y + \omega z_\eta \tag{A.26}$$

and

$$\omega = \eta_t + u \eta_x + v \eta_y + w \eta_z \tag{A.27}$$

A.2 WRF prognostic equations

A.2.1 Transforming a flux-form equation from R_c to R_w

A flux-form equation in R_c describing the transport of the scalar ψ can be written as

$$\partial_{x_i}(\rho u_i \psi) = f \tag{A.28}$$

which is equivalent to

$$f = \partial_{t_c}(\rho\psi) + \partial_{x_c}(\rho u \psi) + \partial_{y_c}(\rho v \psi) + \partial_z(\rho w \psi) \tag{A.29}$$

Transforming the derivatives with Equation A.22 gives

$$\begin{aligned} f = \partial_{t_w}(\rho\psi) \quad & + \eta_t \partial_\eta(\rho\psi) \\ & + \partial_{x_w}(\rho u \psi) + \eta_x \partial_\eta(\rho u \psi) \\ & + \partial_{y_w}(\rho v \psi) + \eta_y \partial_\eta(\rho v \psi) \\ & + \eta_z \partial_\eta(\rho w \psi) \end{aligned} \tag{A.30}$$

Then, replacing w by its expression with R_w velocities (eq. A.26) and splitting the derivative of each velocity gives

$$\begin{aligned} f = \partial_{t_w}(\rho\psi) \quad & + \eta_t \partial_\eta(\rho\psi) \quad + \eta_z \partial_\eta(\rho\psi z_t) \\ & + \partial_{x_w}(\rho u \psi) + \eta_x \partial_\eta(\rho u \psi) + \eta_z \partial_\eta(\rho u \psi z_x) \\ & + \partial_{y_w}(\rho v \psi) + \eta_y \partial_\eta(\rho v \psi) + \eta_z \partial_\eta(\rho v \psi z_y) \\ & + \eta_z \partial_\eta(\rho \omega \psi z_\eta) \end{aligned} \tag{A.31}$$

table of content

Decomposing these new terms gives

$$\begin{aligned} f = \partial_{t_w}(\rho\psi) \quad &+ \eta_t\partial_\eta(\rho\psi) \quad + \eta_z\rho\psi\partial_\eta(z_t) \quad + \eta_z z_t\partial_\eta(\rho\psi) \\ &+ \partial_{x_w}(\rho u\psi) + \eta_x\partial_\eta(\rho u\psi) + \eta_z\rho u\psi\partial_\eta(z_x) + \eta_z z_x\partial_\eta(\rho u\psi) \\ &+ \partial_{y_w}(\rho v\psi) + \eta_y\partial_\eta(\rho v\psi) + \eta_z\rho v\psi\partial_\eta(z_y) + \eta_z z_y\partial_\eta(\rho v\psi) \\ &+ \eta_z\partial_\eta(\rho\omega\psi z_\eta) \end{aligned} \tag{A.32}$$

According to Equations A.15 to A.17, the second and fourth terms cancel each other. Then, the 3rd term of each line can be modified with Equations A.19 to A.21, to obtain

$$\begin{aligned} f = \partial_{t_w}(\rho\psi) \quad &+ \eta_z\rho\psi\partial_{t_w}(z_\eta) \\ &+ \partial_{x_w}(\rho u\psi) + \eta_z\rho u\psi\partial_{x_w}(z_\eta) \\ &+ \partial_{y_w}(\rho v\psi) + \eta_z\rho v\psi\partial_{y_w}(z_\eta) \\ &+ \eta_z\partial_\eta(\rho\omega\psi z_\eta) \end{aligned} \tag{A.33}$$

Finally, multiplying by z_η and using Equation A.18 gives

$$z_\eta f = \partial_{t_w}(\rho\psi z_\eta) + \partial_{x_w}(\rho u\psi z_\eta) + \partial_{y_w}(\rho v\psi z_\eta) + \partial_\eta(\rho\omega\psi z_\eta) \tag{A.34}$$

$$z_\eta f = \partial_{\chi_i}(\rho v_i\psi z_\eta) \tag{A.35}$$

A.2.2 Navier-Stokes in WRF referential frame

Starting from here, time derivative and space derivative are treated separately. The flux-form Navier-Stokes equations in R_c is

$$\partial_{t_c}(\rho) + \partial_{x_j}(\rho u_j) = 0 \tag{A.36}$$

$$\partial_{t_c}(\rho_d) + \partial_{x_j}(\rho_d u_j) = 0 \tag{A.37}$$

$$\partial_{t_c}(\rho u_i) + \partial_{x_j}(\rho u_i u_j) + \partial_{x_i}(p) + \rho g\delta_{i3} = f_{u_i} \tag{A.38}$$

$$\partial_{t_c}(\rho q_m) + \partial_{x_j}(\rho u_j q_m) = f_{q_m} \tag{A.39}$$

$$\partial_{t_c}(\rho\theta_m) + \partial_{x_j}(\rho u_j\theta_m) = f_\theta \tag{A.40}$$

with ρ the total density, ρ_d the dry-air density, u_j the cartesian velocity vector (u, v, w), p the pressure, g the gravitational acceleration considered as constant, q_m the mixing ratio of any moisture variable (e.g. vapor, ice, rain), θ_m the moist (or virtual) potential temperature. The right hand side (RHS) of the momentum equation (f_{u_i}) includes the Coriolis term, the curvature term and the diffusion term. The viscous term is often neglected in atmospheric flows. f_{q_m} and f_θ are the forcing terms of respectively the q_m and θ_m equations.

Each equation of this set is of the same form as A.28 with $\psi = 1$, $\psi = 1$ and $\rho = \rho_d$, $\psi = u_i$, $\psi = q_m$ and $\psi = \theta_m$, respectively. Then using the same method,

these equations can be transpose to R_w as

$$\partial_{t_w}(\rho z_\eta) + \partial_{\chi_j}(\rho v_j z_\eta) = 0 \tag{A.41}$$
$$\partial_{t_w}(\rho_d z_\eta) + \partial_{\chi_j}(\rho_d v_j z_\eta) = 0 \tag{A.42}$$
$$\partial_{t_w}(\rho u z_\eta) + \partial_{\chi_j}(\rho u v_j z_\eta) + \partial_{x_c}(p) z_\eta = f_u z_\eta \tag{A.43}$$
$$\partial_{t_w}(\rho v z_\eta) + \partial_{\chi_j}(\rho v v_j z_\eta) + \partial_{y_c}(p) z_\eta = f_v z_\eta \tag{A.44}$$
$$\partial_{t_w}(\rho w z_\eta) + \partial_{\chi_j}(\rho w v_j z_\eta) + \partial_z(p) z_\eta + \rho g z_\eta = f_w z_\eta \tag{A.45}$$
$$\partial_{t_w}(\rho q_m z_\eta) + \partial_{\chi_j}(\rho v_j q_m z_\eta) = f_{q_m} z_\eta \tag{A.46}$$
$$\partial_{t_w}(\rho \theta_m z_\eta) + \partial_{\chi_j}(\rho v_j \theta_m z_\eta) = f_\theta z_\eta \tag{A.47}$$

Transforming the pressure gradient terms with R_w derivatives, the following set of equations is obtained

$$\partial_{t_w}(\rho z_\eta) + \partial_{\chi_j}(\rho v_j z_\eta) = 0 \tag{A.48}$$
$$\partial_{t_w}(\rho_d z_\eta) + \partial_{\chi_j}(\rho_d v_j z_\eta) = 0 \tag{A.49}$$
$$\partial_{t_w}(\rho u z_\eta) + \partial_{\chi_j}(\rho u v_j z_\eta) + \partial_{x_w}(p) z_\eta - \frac{1}{g}\partial_{x_w}(\phi)\partial_\eta(p) = f_u z_\eta \tag{A.50}$$
$$\partial_{t_w}(\rho v z_\eta) + \partial_{\chi_j}(\rho v v_j z_\eta) + \partial_{y_w}(p) z_\eta - \frac{1}{g}\partial_{y_w}(\phi)\partial_\eta(p) = f_v z_\eta \tag{A.51}$$
$$\partial_{t_w}(\rho w z_\eta) + \partial_{\chi_j}(\rho w v_j z_\eta) + \partial_\eta(p) + \rho g z_\eta = f_w z_\eta \tag{A.52}$$
$$\partial_{t_w}(\rho q_m z_\eta) + \partial_{\chi_j}(\rho v_j q_m z_\eta) = f_{q_m} z_\eta \tag{A.53}$$
$$\partial_{t_w}(\rho \theta_m z_\eta) + \partial_{\chi_j}(\rho v_j \theta_m z_\eta) = f_\theta z_\eta \tag{A.54}$$

with the geopotential $\phi = gz$.

Multiplying Equations A.50 to A.54 by $-g\rho_d/\rho$, setting $\mu_d = -g\rho_d z_\eta$ (following SK19 eq.2.6), and combining with Equations A.48 and A.49, gives

$$\partial_{t_w}(\mu_d u) + \partial_{\chi_j}(\mu_d u v_j) + \frac{\mu_d}{\rho}\partial_{x_w}(p) + \frac{\rho_d}{\rho}\partial_{x_w}(\phi)\partial_\eta(p) = f_u \frac{\mu_d}{\rho} \tag{A.55}$$
$$\partial_{t_w}(\mu_d v) + \partial_{\chi_j}(\mu_d v v_j) + \frac{\mu_d}{\rho}\partial_{y_w}(p) + \frac{\rho_d}{\rho}\partial_{y_w}(\phi)\partial_\eta(p) = f_v \frac{\mu_d}{\rho} \tag{A.56}$$
$$\partial_{t_w}(\mu_d w) + \partial_{\chi_j}(\mu_d w v_j) - g(\frac{\rho_d}{\rho}\partial_\eta(p) + \mu_d) = f_w \frac{\mu_d}{\rho} \tag{A.57}$$
$$\partial_{t_w}(\mu_d q_m) + \partial_{\chi_j}(\mu_d v_j q_m) = f_{q_m} \frac{\mu_d}{\rho} \tag{A.58}$$
$$\partial_{t_w}(\mu_d \theta_m) + \partial_{\chi_j}(\mu_d \rho v_j \theta_m) = f_\theta \frac{\mu_d}{\rho} \tag{A.59}$$

These equations correspond to Equations 2.8 to 2.11 and 2.14, respectively, in SK19. Then multiplying Equation A.49 by $-g$ gives

$$\partial_{t_w}(\mu_d) + \partial_{\chi_j}(\mu_d v_j) = 0 \tag{A.60}$$

which corresponds to Equation 2.12 in SK19.

table of content

A.2.3 LES subgrid turbulent mixing

The turbulent mixing term S_i in WRF is evaluated in physical space (Equation 4.2 in SK19)

$$S_i = -\partial_{x_j}(T_{ij}) \tag{A.61}$$

where

$$T_{ij} = -\mu_d K_{h,v}(\partial_{x_i}(u_j) + \partial_{x_j}(u_i)) = -\mu_d \tau_{ij} \tag{A.62}$$

with K_h, and K_v the horizontal and vertical eddy viscosities, respectively. In the TKE1.5 model, the latters are computed based on a prognostic subgrid TKE (k_{sgs}) as

$$K_{h,v} = 0.15 l_{h,v} \sqrt{k_{sgs}} \tag{A.63}$$

with $l_{h,v}$ the horizontal or vertical length scale. The horizontal length scale is the horizontal grid size while the vertical length scale equals the vertical grid size for unstable cases and decreases as a function of $\sqrt{k_{sgs}}/N_{BV}$ for stable cases. k_{sgs} has its own prognostic equation with advection, shear production, buoyancy and dissipation processes.

Annexe B

TKE budget calculation in WRF

To calculate the TKE budget, the momentum equation is written in differential form. In Section A.2.2, it is found that

$$\partial_{t_c}(\rho u_i) + \partial_{x_i}(\rho u_i u_j) = \frac{1}{z_\eta}(\partial_{t_c}(\rho u_i v_j z_\eta) + \partial_{\chi_i}(\rho v_i u_j z_\eta)) \tag{B.1}$$

Transforming the LHS term to differential form (combining with the continuity equation), and the RHS term to the WRF flux-form gives

$$\partial_{t_c}(u_i) + u_j\partial_{x_i}(u_i) = \frac{1}{\mu_d}(\partial_{t_c}(\mu_d u_i v_j) + \partial_{\chi_i}(\mu_d v_i u_j)) \tag{B.2}$$

Thus, neglecting the coriolis force, the following system is obtained

$$\partial_{t_c}(u) + u_j\partial_{x_j}(u) = -\frac{1}{\rho}\partial_{x_w}(p) - \frac{\rho_d}{\rho\mu_d}\partial_{x_w}(\phi)\partial_\eta(p) - \frac{1}{\mu_d}\partial_{x_j}(\mu_d K_{h,v} D_{1j}) \tag{B.3}$$

$$\partial_{t_c}(v) + u_j\partial_{x_j}(v) = -\frac{1}{\rho}\partial_{y_w}(p) - \frac{\rho_d}{\rho\mu_d}\partial_{y_w}(\phi)\partial_\eta(p) - \frac{1}{\mu_d}\partial_{x_j}(\mu_d K_{h,v} D_{2j}) \tag{B.4}$$

$$\partial_{t_c}(v) + u_j\partial_{x_j}(v) = -g(\frac{\rho_d}{\rho\mu_d}\partial_\eta(p) + 1) - \frac{1}{\mu_d}\partial_{x_j}(\mu_d K_{h,v} D_{3j}) \tag{B.5}$$

that can be written as

$$\partial_{t_c}(u_i) + u_j\partial_{x_j}(u_i) = -a_i - b_i \tag{B.6}$$

where

$$a_i = \partial x_i(p) - g\delta_{i3} = \begin{pmatrix} \frac{1}{\rho}\partial_{x_w}(p) + \frac{\rho_d}{\rho\mu_d}\partial_{x_w}(\phi)\partial_\eta(p) \\ \frac{1}{\rho}\partial_{y_w}(p) + \frac{\rho_d}{\rho\mu_d}\partial_{y_w}(\phi)\partial_\eta(p) \\ g(\frac{\rho_d}{\rho\mu_d}\partial_\eta(p) + 1) \end{pmatrix} \tag{B.7}$$

$$b_i = \frac{1}{\mu_d}\partial_{x_j}(\mu_d K_{h,v} D_{ij}) \tag{B.8}$$

Then an averaging operator, denoted by $\langle\cdot\rangle$, is defined so that each variable x can be decomposed as

$$x = X + x' \tag{B.9}$$

where $X = \langle x\rangle$ is the average quantity and x' is the fluctuation. This operator is supposed to have the following properties :

$$\langle x'\rangle = 0 \tag{B.10}$$

$$\langle X.y\rangle = X.Y \tag{B.11}$$

$$\langle\partial_{t_c}(x)\rangle = \partial_{t_c}(X) \tag{B.12}$$

$$\langle\partial_{x_j}(x)\rangle = \partial_{x_j}(X) \tag{B.13}$$

table of content

Thus, applying the operator to B.6 gives the momentum equation for average quantities

$$\partial_{t_c}(U_i) + U_j \partial_{x_j}(U_i) = -A_i - B_i - \langle u_j' \partial_{x_j}(u_i') \rangle \tag{B.14}$$

Subtracting B.14 from B.6 gives the momentum equation for fluctuations

$$\partial_{t_c}(u_i') + U_j \partial_{x_j}(u_i') + u_j' \partial_{x_j}(U_i) + u_j' \partial_{x_j}(u_i') = -a_i' - b_i' + \langle u_j' \partial_{x_j}(u_i') \rangle \tag{B.15}$$

Then, multiplying by u_i' and applying the averaging operator gives the resolved TKE (k_{calc}) budget equation

$$\partial_{t_c}(k_{calc}) + U_j \partial_{x_j}(k_{calc}) = -\langle u_i' u_j' \rangle \partial_{x_j}(U_i) - \langle u_j' \partial_{x_j}({k_{calc}}') \rangle - \langle a_i' u_i' \rangle - \langle b_i' u_i' \rangle \tag{B.16}$$

where $k_{calc} = \langle \frac{1}{2} u_i' u_i' \rangle$ and ${k_{calc}}' = \frac{1}{2} u_i' u_i'$. Finally, it is assumed that $\partial_{x_j} u_j' \approx 0$, so that the equation becomes

$$\partial_{t_c}(k_{calc}) = \underbrace{-U_j \partial_{x_j}(k_{calc})}_{A} \underbrace{-\langle u_i' u_j' \rangle \partial_{x_j}(U_i)}_{P} \underbrace{-\partial_{x_j} \langle u_j' {k_{calc}}' \rangle}_{T_T} \underbrace{-\langle a_i' u_i' \rangle}_{PB} \underbrace{-\langle b_i' u_i' \rangle}_{-D} \tag{B.17}$$

where A is the advection, P the shear production, T_T the turbulent transport, PB the combined pressure and buoyancy effect, and D the exchanged between resolved and subgrid scales that can be considered as a dissipation term (Rai et al., 2017). The buoyancy term B can be calculated separately as

$$B = \frac{g}{\theta_v} \overline{w' \theta_v'} \delta_{i3} \tag{B.18}$$

and the pressure transport T_P can be decoupled from buoyancy by subtracting B from PB. In addition, the advection scheme inevitably generates a numerical dissipation E that should be included in the total dissipation ε so that the final WRF budget is

$$\partial_{t_c}(k_{calc}) = A + P + T_T + \underbrace{PB - B}_{T_P} + B \underbrace{-D - E}_{-\varepsilon} \tag{B.19}$$

Annexe C

Calculation of G

This appendix describes the method used to calculate G, defined in Equation 4.2 as half the sum of the GW related variances (G_U, G_V, and G_W). This equation is similar to a TKE definition. Thus, subtracting G from k_{calc} is equivalent to subtracting the GW related variances from the calculated variances ($\overline{u'^2}$, $\overline{v'^2}$, and $\overline{w'^2}$, respectively). The variance of the sum of GW oscillations and turbulent fluctuation is given for U by :

$$\overline{u'^2} = var_{turb}(U) + G_U + covar_{GW,turb}(U) \tag{C.1}$$

where var_{turb} is the variance related to turbulent fluctuations, and $covar_{GW,turb}$ the covariance between the GW related oscillations and the turbulent fluctuations. Thus, equation 4.2 assumes that the following assumption is verified :

$$covar_{GW,turb}(U, V, W) = 0 \tag{C.2}$$

We assume that the turbulent fluctuations are independent of the GW related oscillations, as they occur at different scales. Thus, averaging the k profiles over a large number of cells and over several time steps reduces the calculated covariance, and the method of subtracting G becomes valid.

The GW related variances are calculated as follows. First, each wind velocity component in the GW is approximated by a sine wave function in space of equation

$$f_{(X_{GW})} = A\sin(\phi_{(X_{GW}=0)} + \frac{2\pi}{\lambda}X_{GW}) = A\sin(\phi_{(X_{GW})}) \tag{C.3}$$

where f is the amplitude at a given location, A is the maximum amplitude, $\phi_{(X_{GW})}$ is the phase at location X_{GW}, and λ is the wavelength. The calculation of A and λ is given in section 3.2.4. The phase ϕ can be calculated using f and its spatial derivative with respect to X_{GW}.

$$\frac{\partial f}{\partial X_{GW}} = \frac{2\pi}{\lambda}A\cos(\phi_{(X_{GW})}) \tag{C.4}$$

Thus, we can calculate ϕ as :

$$\phi_{(X_{GW})} = \arctan(\frac{2\pi}{\lambda}\frac{f}{\frac{\partial f}{\partial X_{GW}}}) \tag{C.5}$$

The phase of W (ϕ_W) is calculated with this method, whereas the phase of U and V is given by $\phi_U = \phi_V = \phi_W - \frac{\pi}{2}$ because the horizontal and vertical velocities are out

of phase within a gravity wave (Figure 4.16a). Then, at a fixed location, the motion of the sine wave in space results in a sine wave in time that can be expressed with

$$f_{(t)} = A\sin(\phi_{(t=0)} + \omega t) = A\sin(\phi_{(t)})$$

where ω is the angular frequency, $\phi_{(t)}$ is the phase at time t. The equivalence between spatial and temporal sine waves gives :

$$\phi_{(t)} = \phi_{(X_{GW})} = \phi \tag{C.6}$$

$$\omega = 2\pi\frac{S_{GW}}{\lambda} \tag{C.7}$$

with S_{GW} the wave motion speed calculated in section 3.2.4. Finally, the GW related variance of f (G_f) over an interval $[t - \frac{\Delta t}{2}, t + \frac{\Delta t}{2}]$ is given by :

$$G_f = \frac{A^2}{2} - \frac{A^2}{4\omega\Delta t}[\sin(2\phi + \omega\Delta t) - \sin(2\phi - \omega\Delta t)] - \left[\frac{A}{\omega\Delta t}\left(\cos\left(\phi + \frac{\omega\Delta t}{2}\right) - \cos\left(\phi - \frac{\omega\Delta t}{2}\right)\right)\right]^2$$

Annexe D

Turbulence decay models in logarithmic form

This appendix describes the transformation of the three models of turbulence decay introduced in Section 1.3.5 to perform the fit in Section 4.4. The models in Section 1.3.5 describe the TKE k as a function of the time since decoupling t while after the transformation, they should describe the logarithm of $k^* = k/k_0$ as a function of $X_c - X_0 = U_c t$.

Model 1 writes

$$k(t) = k_0 \exp^{-\frac{t}{t_{\varepsilon 1}}} \tag{D.1}$$

so that dividing by k_0 and applying the logarithm gives

$$\log(k^*) = -\frac{t}{t_{\varepsilon 1}} \tag{D.2}$$

Then, replacing t gives

$$\log(k^*) = -\frac{X_c - X_0}{U_c t_{\varepsilon 1}} \tag{D.3}$$

$$\log(k^*) = -c_1(X_c - X_0). \tag{D.4}$$

with $c_1 = \frac{1}{U_c t_{\varepsilon 1}}$.

Model 2 writes

$$k(t) = k_0(1 + \frac{C_\varepsilon w^*}{2C_k Z_{CBL}} t)^{-2} \tag{D.5}$$

so that dividing by k_0 and applying the logarithm gives

$$\log(k^*) = -2\log(1 + \frac{C_\varepsilon w^*}{2C_k Z_{CBL}} t) \tag{D.6}$$

Then, replacing t gives

$$\log(k^*) = -2\log(1 + \frac{C_\varepsilon w^*}{2C_k Z_{CBL}} \frac{X_c - X_0}{U_c}) \tag{D.7}$$

$$\log(k^*) = -2\log(1 + c_2(X_c - X_0)). \tag{D.8}$$

with $c_2 = \frac{C_\varepsilon w^*}{2C_k Z_{CBL} U_c}$.

table of content

Model 3 writes

$$\frac{k}{w^{*2}} = c_4(\frac{tw^*}{Z_{CBL}})^{-1.2} \tag{D.9}$$

where c_4 is a proportional constant, so that multiplying by w^{*2}/k_0 gives

$$k^* = \frac{c_4 w^{*2}}{k_0}\left(\frac{tw^*}{Z_{CBL}}\right)^{-1.2} \tag{D.10}$$

$$k^* = \left[\left(\frac{c_4 w^{*2}}{k_0}\right)^{\frac{-1}{1.2}}\frac{tw^*}{Z_{CBL}}\right]^{-1.2} \tag{D.11}$$

Then, applying the logarithm and replacing t gives

$$\log(k^*) = -1.2\log\left(\left(\frac{c_4 w^{*2}}{k_0}\right)^{\frac{-1}{1.2}}\frac{(X_c - X_0)w^*}{U_c Z_{CBL}}\right) \tag{D.12}$$

$$\log(k^*) = -1.2\log(c_3(X_c - X_0)) \tag{D.13}$$

with $c_3 = \left(\frac{c_4 w^{*2}}{k_0}\right)^{\frac{-1}{1.2}}\frac{w^*}{U_c Z_{CBL}}$.

table of content

COLLEGE ED SCIENCES
DOCTORAL DE L'INGENIERIE
PAYS DE LA LOIRE ET DES SYSTEMES

CENTRALE NANTES

Titre : Analyse multi-échelles des brises de mer et des jets de basses couches dans une zone côtière

Mots clés : simulation des grandes-échelles, brise de mer, jet de basses couches, turbulence

Résumé : Malgré son importance pour les activités humaines et le développement de l'éolien en mer, la structuration de la couche limite atmosphérique marine (CLAM) en zone côtière complexe reste encore mal comprise.
À partir de simulations numériques couvrant des processus allant de la méso-échelle aux grandes échelles de la turbulence, ces travaux présentent une analyse détaillée de la CLAM au large de la côte atlantique française, lors de deux journées caractérisées par une alternance de brises de mer et de jets de basses couches, déjà observée par mesures LiDAR.
Pendant l'initiation de la brise de mer, une zone de convergence se forme à proximité de la presqu'île de Guérande, conduisant à la formation d'un bore atmosphérique ondulatoire, un phénomène encore jamais observé dans ces conditions. Par ailleurs, il est montré que le jet de basses couches est créé par la combinaison de vents thermiques et de l'advection d'air au-dessus de la péninsule bretonne.
L'analyse de la turbulence révèle que, dans les brises et les jets, la CLAM se divise en plusieurs couches présentant des conditions de cisaillement et de stabilité différentes. Dans les couches fortement stables et cisaillées, au centre de la cellule de brise et au-dessus du cœur du jet, la turbulence est principalement liée à la présence d'ondes de Kelvin-Helmholtz.
Plus généralement, ces travaux illustrent le potentiel des simulations des grandes échelles réalistes pour l'étude des phénomènes côtiers, contribuent à une meilleure compréhension des vents thermiques en mer et fournissent des outils et méthodes pour approfondir l'analyse de la CLAM à proximité des côtes complexes.

Title : Multiscale analysis of sea breezes and low-level jets in a coastal area

Keywords : large-eddy simulation, sea breeze, low-level jet, turbulence

Abstract : Despite its importance for human activities and the development of offshore wind power, the structure of the marine atmospheric boundary layer in complex coastal areas remains poorly understood.
Based on numerical simulations covering processes ranging from mesoscale to the largest scales of turbulence, this work presents a detailed analysis of the coastal atmospheric boundary layer (CABL) off the French Atlantic coast during two days characterized by alternating sea breezes and low-level jets, as previously observed by LiDAR measurements.
During the sea-breeze initiation, a convergence zone forms near the Guérande peninsula, leading to the formation of an atmospheric undular bore, a phenomenon never before observed under these conditions. Furthermore, it is shown that the low-level jet is created by a combination of thermal winds and air advection over the Brittany peninsula. Analysis of the turbulence reveals that, in breezes and jets, the offshore CABL is divided into several layers with different shear and stability conditions. In highly stable and sheared layers, at the center of the breeze cell and above the core of the jet, turbulence is mainly linked to the presence of Kelvin-Helmholtz waves.
Overall, this work illustrates the potential of realistic large-eddy simulations for studying coastal phenomena, contributes to a better understanding of offshore thermal winds, and provides tools and methods for further analysis of CABL near complex coastlines.